Karlsruher Institut für Technologie

Two-photon Laser Microprinting and Micropatterning of Porous Polymeric Materials

Dissertation 2022

Joël Monti

Two-photon Laser Microprinting and Micropatterning of Porous Polymeric Materials

Zur Erlangung des akademischen Grades eines

DOKTORS DER NATURWISSENSCHAFTEN (Dr. rer. nat.)

von der KIT-Fakultät für Chemie und Biowissenschaften des
Karlsruher Instituts für Technologie (KIT)

genehmigte

Dissertation

von

M. Sc. Joël Monti

Tag der mündlichen Prüfung	18. Juli 2022
Referent	Prof. Mario Ruben
Korreferentin	Jun.-Prof. Eva Blasco

DECLARATION

I, Joël Monti, declare that the work presented in the present dissertation was realised in the context of the PhD-studies at the Institute of Technology of Karlsruhe from the 01.05.2019 to the 01.06.22, under the co-supervision of Prof. Mario Ruben and Jun.-Prof. Eva Blasco. Also, I declare that:

- I have written the present dissertation on my own.
- No material other than that formally cited has been reused.
- Any participation to the presented work from people other than me has been formaly acknowledged.
- The rules for the protection of good scientific practice of the Karlsruhe Institute of Technology were strickly followed.
- The filling and archiving of the primary data, in accordance with §A(6) of the rules for ensuring good scientific practice of KIT has been ensured.
- The electronic version of this work corresponds to the written one.
- I did not undertake any previous doctoral studies or performed the present work while being enrolled in any other doctoral studies.

Karlsruhe, the 1st of June 2022

.....

Joël Monti

DEKLARATION

Ich, Joël Monti, versichere, dass die in der vorliegenden Dissertation vorgestellte Arbeit im Rahmen des Promotionsstudiums am Karlsruher Institut für Technologie vom 01.05.2019 bis zum 01.06.22 unter der Co-Betreuung von Prof. Mario Ruben und Jun.-Prof. Eva Blasco entstanden ist. Außerdem versichere ich, dass:

- ich die Arbeit selbständig angefertigt habe.

- ich keine anderen als die angegebenen Quellen und Hilfsmittel benutzt habe.

- jegliche Beteiligung von anderen Personen an der vorliegenden Arbeit formell anerkannt wurde.

- die Regeln zur Sicherung guter wissenschaftlicher Praxis des Karlsruher Instituts für Technologie strikt eingehalten wurden.

- die Abgabe und Archivierung der Primärdaten gemäß §A(6) der Regeln zur Sicherung guter wissenschaftlicher Praxis des KIT beim Institut gesichert ist.

- die elektronische Version dieser Arbeit mit der schriftlichen übereinstimmt.

- ich keine früheren Promotionsstudien durchgeführt und die vorliegende Arbeit nicht während eines anderen Promotionsstudiums angefertigt habe.

Karlsruhe, den 1. Juni 2022

.....

Joël Monti

PUBLICATIONS

First author publications

Monti, J., Concellón, A., Dong, R., Simmler, M., Münchinger, A., Huck, C., Tegeder, P., Nirschl, H., Wegener, M., Osuji, C., Blasco, E., Two-Photon Laser Microprinting of Highly Ordered Nanoporous Materials Based on Hexagonal Columnar Liquid Crystals. *ACS Applied Materials & Interfaces* **2022**, *14*(29), 33746-33755.

Dong, Z.,[§] **Monti, J.**,[§] Cui, H., Welle, A., Singaraju, S. A., Blasco, E., Levkin, P. A., Material-Independent 3D Patterning Via Two-Photon Lithography and Discontinuous Wetting. *Advanced Materials Technologies* **2022**, 2201268.
[§]Authors contributed equally

Monti, J., Blasco, E., Hierarchical Ordering in Light-Triggered Additive Manufacturing. *Polymer Chemistry* **2020**, *11*(46), 7316-7329.

Other contributions

Münchinger, A., Hahn, V., Beutel, D., Woska, S., **Monti, J.**, Rockstuhl, C., Blasco, E., Wegener, M., Multi-Photon 4D Printing of Complex Liquid Crystalline Microstructures by In Situ Alignment Using Electric Fields. *Advanced Material Technologies* **2022**, *7*(1), 2100944.

ACKNOWLEDGEMENTS

I would like to thank my supervisor, Prof. Eva Blasco for giving me the opportunity to carry out my PhD in her newly built research group. I enjoyed a lot of freedom and was given a broad variety of challenges, which helped me learn a lot. She maintained a close and helpful guidance throughout my entire time at KIT, which I greatly appreciated. My work at KIT was performed in close relation with the group of Prof. Mario Ruben, my co-supervisor, who I would equally like to acknowledge for giving me the opportunity to carry out my doctorate studies at KIT. He and his group have been of great help and friendly company, at and outside INT.

Thank you to the current and past members of the Blasco group with whom I shared my doctorate experience. Our ways separated eventually, which makes me not knowing each of them as much as I wish to, but I am regardless grateful to having spent these years in their company.

I would also like to thank Prof. Martin Wegener and his group, who shared their facilities, expertise and advices, support and guidance, and were moreover really welcoming and friendly. I enjoyed having their different approach on the issues I was facing, as much as I enjoyed sharing about their own issues from a chemist´s point-of-view.

Thereafter, I would like to acknowledge all the people who contributed to the research projects detailed in this dissertation. Dr. Alberto Concellón (MIT) as well as Prof. Chinedum Osuji, his coworkers Dr. Omar Qaboos Imran and Ruiqi Dong (the University of Pennsylvania) for sharing their expertise with columnar liquid crystalline material, and providing determinant advices about their handling. Also, Prof. Hermann Nirschl and his coworkers Mira Simmler, Dr. Julian Ungerer, Manuel Meier and Simon Buchheiser (KIT) who relayed over the year, performing the WAXS experiments presented in my work. Similarly, I would like to acknowledge Dr. Kai Weissenbruch (KIT) for his help with confocal fluorescence microscroscopy as well Prof. Petra Taegeder and Dr. Christian Huck (Heidelberg University) for the FTIR measurement of microstructures. Last, I would like to

thank Prof. Pavel Levkin and Dr. Zheqin Dong for the nice collaboration work that is detailed in chapter 4.

In the regard of the proof-reading of this dissertation, I am grateful to Prof. Eva Blasco, Dr. Florian Feist, Dr. Niklas Maximilian Bojanowski, Dr. Liang Yang and Samantha Catt who have taken the time to read and my manuscript or some part of it, and provided appreciated feedbacks and suggestions. Also, I express my gratitude to Dr. Florian Feist and Jan Hobich for the German translations proposed in this dissertation.

Many thanks to the technical staff, who makes our work easier. I would therefore like to thank the staff of INT, as well as Katharina Elies for her exemplary support of laboratory operations and duties. Also, I am grateful to Andreas Ganzbuhl who have shown great scientific and human abilities during his “Vertiefersarbeit” performed under my supervision.

A special thanks goes to AK Barner-Kowollik and AK Theato, who have been of amazing support during the day and in the evening.

Last but not least, I would like to thank my family and my friends (those who have been cited yet) for their crucial support outside the university.

ABBREVIATION TABLE

1D	One-dimensional
1PE	One-photon excitation
2D	Two-dimensional
2PE	Two-photon excitation
2Θ	Scattering angle
3D	Three-dimensional
9-BBN	9-Borabicyclo[3.3.1]nonane
ACN	Acetonitrile
ACQ	Aggregation caused quenching
AIE	Aggregation induced emission
AM	Additive manufacturing
aq	Aqueous solution
BHT	Butylated hydroxytoluene
BuA	Butylacrylate
BY1	Thioflavin T (Basic yellow 1)
CDLP	Continuous digital light processing
$CHCl_3$ / $CDCl_3$	Chloroform / deuterated chloroform
CLIP	Continuous liquid interface production
CNC	Computer numerical control
Col_h	Hexagonal columnar liquid crystal
Col_{ob}	Oblique columnar liquid crystal
Col_r	Rectangular columnar liquid crystal
Col_{tetr}	Tetragonal columnar liquid crystal
conc.	Concentrated
d	Scattering distance
dA	3,4,5-Tris((11-(acryloyloxy)undecyl)oxy)benzoic acid
dBzA	3,4,5-Tris((4-((11-(acryloyloxy)undecyl)oxy)benzyl)oxy)benzoic acid
dC12	3,4,5-Tris(dodecyloxy)benzoic acid
DCC	Dicyclohexylcarbodiimide
DCM	Dichloromethane
DCU	Dicyclohexylurea
DETC	7-Diethylamino-3-thenoylcoumarin
DLP	Digital-light processing
DMAP	4-Dimethylaminopyridine
DMD	Digital mirror device
DMF	Dimethylformamide
DMSO / DMSO-d_6	Dimethylsulfoxide / deuterated dimethylsulfoxide
DOSY	Diffusion-ordered spectroscopy
DSC	Differential scanning calorimetry
EDC	1-Ethyl-3-(3-dimethylaminopropyl)carbodiimide

EDMA	Ethyleneglycol dimethacrylate
EDX	Energy dispersive X-ray spectroscopy
ESI	Electron-spray ionisation
EtOAc	Ethyl acetate
EtOH	Ethanol
FDM	Fused deposition modelling
FTIR	Fourier transform infrared spectroscopy
H	Hysteresis
$H_{\|\|}$	Lyotropic hexagonal mesophase
H-bond	Hydrogen-bond
HEA	Hydroxyethyl acrylate
HOMO	Highest occupied molecular orbital
HRMS	High-resolution mass spectrometry
IC	Internal conversion
Ig369	Irgacure 369
Ig819	Irgacure 819
^{i}PrOH	Isopropan-2-ol
ISC	Inter-system crossing
LC	Liquid crystal / liquid crystalline
LUMO	Lowest unoccupied molecular orbital
M	2,4-Diamino-6-dodecylamino-1,3,5-triazine e
MALDI	Matrix-assisted laser desorption ionisation
MB	Methylene blue
MeOH	Methanol
M_n	Nominal mass
MO	Methylene orange
M_w	Molecular weight
NA	Numerical apperture
n-BuLi	n-Butyllithium
NLC	Nematic liquid crystal
NMR	Nuclear magnetic resonance
POM	Polarised optical microscopy
q	Scattering vector
r	Radius (used here to mention the radius of a discotic element of a hexagonal packing)
RAFT	Reversible addition-fragmentation chain transfer
RhB	Rhodamine B
S_0	Singlet ground state
S_1	Singlet excited state
SEM	Scanning electron microscopy
SLA	Stereolithography
T	2,4,6-Tris(1-(4-butoxyphenyl)-1H-1,2,3-triazol-4-yl)-1,3,5-triazine
T_1	Triplet excited state
TBIB	1,3,5-Tris(1H-benzo[d]imidazol-2-yl)benzene
TEM	Transmission electron microscopy
T_g	Glass transition temperature
THF	Tetrahydrofuran
TLC	Thin layer chromatography
TOF	Time-of-flight

TOF-SIMS	Time-of-flight secondary ion mass spectrometry
TPE	Tetraphenylethylene
UV-vis	Ultraviolet-visible light spectroscopy
VR	Vibrational relaxation
WAXS	Wide-angle X-Ray scattering
XRD	X-Ray diffraction
γ	Surface tension
Θ	Contact angle
λ	Wavelength
φ_S	Fraction of liquid-solid contact
$N(\mu, \sigma^2)$	Gaussian distribution (mean, standard deviation)
n	Director vector
Φ	Tilt angle

ABSTRACT

In recent decades, 3D printing has emerged as a promising manufacturing technique and has thus gained increasing research interest. Noticeably, the development of functional materials broadened the abilities of 3D printing technologies. Out of the large variety of 3D printing technologies, light-induced techniques , which rely on the curing or crosslinking of reactive molecules by light irradiation, are highly attractive. Taking advantage of photoinks being a formulation of molecular material precursors, light-triggered 3D printing techniques enjoy an unmatched freedom for the inclusion of functional components.

The 3D printing of porous materials allows for the fabrication of complex objects while retaining the unique properties of porous materials for absorption, adsorption, catalysis or affinity, among others. The shape-defined microfabrication of porous architectures is therefore desirable for many applications. Thanks to its microscale definition and its versatility, two-photon laser printing is a technique of a choice for the 3D prototyping of porous materials. In this work, I explore the use of this technology for the manufacturing of functional porous materials, within two different projects: i) the microprinting of porous structures based on columnar liquid crystals for selective adsorption, and ii) the micropatterning of amorphous porous polymeric compounds for the fabrication of multi-material structures.

In the first part of this dissertation, I focus on the fabrication of nanoporous microstructures via the manufacturing of columnar liquid crystalline photoresists by two-photon laser printing. The discotic liquid crystalline molecules contain nine terminal acrylate groups to support their crosslinking by light-triggered microprinting via free-radical polymerisation, which induces locking of the ordered liquid crystalline arrangement. By design of the discotic liquid crystalline molecule based on the hydrogen bonded self-assembly of three peripheral acids around a centre templating core, the crosslinked polymeric material can ultimately be given a nanoporosity by the chemical removal of the templating core. The pores thus have dimensions and arrangement intrinsic to the previously locked liquid crystalline phase. Owing to the high definition of the size and disposition of the nanopores, the crosslinked material is capable of a size-selective adsorption of small molecules. Furthermore, the

carboxylic acid moieties, which initially sustain the self-assembly of the peripheral acids with the templating core are deprotonated or protonated through simple chemical treatment. The so-obtained controlled polarisation of the nanopores allows for an additional charge-selectivity. In this work, I demonstrate the selective adsorptive properties of the printed structures using two small cationic dyes, methylene blue and thioflavin T, which successfully penetrate the printed structures. As well as using a big cationic dye, rhodamine B, and a small anionic dye, methylene orange, which cannot be adsorbed due to size and charge inadequacy, respectively.

In a second part, a superhydrophobic nanoporous material is applied to two-photon laser printing, for material-independent functionalisation. The initial nanoporous structures are manufactured by digital light processing. Their nanoporosity relies on a polymerisation-induced phase separation process, using 1-decanol as a porogen. The engendered porous printed objects exhibit superhydrophobic properties. By photografting of hydrophilic monomers, aided by two-photon laser patterning, hydrophilic patterns are fabricated in three dimensions, with high definition and design freedom. Discontinous dewetting of aqueous solutions or suspensions is then used to functionalise the structures in a material-independent manner. I first evidence the addition of hydroxyethyl moieties in the drawn patterns and visualise the achieved patterns quality by the deposition of rhodamine B as an easily traceable compound. After having proven its performance, I investigate the versatility of the method using polydopamine and polypyrrole. Then, I demonstrate that the method can also be used for the micropatterned deposition of nanoparticles using a suspension silica nanoparticles. Based on this result, I investigate the possibility to fabricate conductive structures via functionalisation with silver nanoparticles.

ZUSAMMENFASSUNG

In den zurückliegenden Jahrzenten hat sich der 3D Druck als vielversprechende Fertigungsmethode entwickelt und daher verstärktes Forschungsinteresse ausgelöst. Die Entwicklung funktionaler Materialien hat dabei die Möglichkeiten der 3D Drucktechnologie stark erweitert. Aus dem großen Fundus verschiedener 3D Drucktechnologien sind lichtinduzierte Methoden, die auf das Aushärten oder Quervernetzen von reaktiven Molekülen mittels Bestrahlung mit Licht basieren besonders attraktiv. Weil es sich bei den photochemisch aushärtbaren Tinten oft um Formulierungen aus molekularen Bausteinen handelt, gibt es nahezu unbegrenzte Möglichkeiten für den Zusatz funktionaler Komponenten.

Der 3D-Druck von porösen Materialien ermöglicht die Herstellung von komplexen Objekten unter Beibehaltung der durch die Porosität bedingten besonderen Eigenschaften ebendieser Materialien wie z.B. Absorptivität, Adsorptivität, katalytische Aktivität, Affinität und viel mehr. Die Fertigung von mikrostrukturierten porösen Architekturen erscheint daher als besonders attraktiv für verschiedenste Anwendungen. Das Zwei-Photonen-Laserdrucken ist aufgrund seiner Nano-Präzision bei gleichzeitiger Flexibilität das bevorzugte Verfahren um poröse 3D Prototypen zu generieren. In der vorliegenden Arbeit wird die Nutzung dieses Verfahrens im Rahmen zweier verschiedener Projekte untersucht: i) Das Zwei-Photonen-Laserdrucken poröser Strukturen basierend auf kolumnaren Flüssigkristallen zur selektiven Adsorption; ii) Die Mikrostrukturierung amorpher poröser Polymere für die Herstellung von heterogenen Oberflächen.

Im ersten Teil der vorliegenden Dissertation liegt der Fokus auf der Herstellung nanoporöser Mikrostrukturen mittels Zwei-Photonen-Laserdrucken beziehungsweise der Formulierung von kolumnaren Flüssigkristall-Fotolacken für diesen Zweck. Die scheibchenförmigen Flüssigkristallverbindungen enthalten neun terminale Acrylatgruppen die das Aushärten durch Licht beim Laserdrucken durch freie radikalische Polymerisation ermöglichen, und so die geordnete Flüssigkristallstruktur konservieren. Durch das Design der scheibchenförmigen Flüssigkristallverbindungen, das auf der

Wasserstoffbrückenbindung von drei peripheren Carbonsäuren um eine im Zentrum liegendes Templat basiert, ist es möglich das quervernetzte polymere Material in ein nanoporöses Material umzuwandeln, indem das im Zentrum liegende Templat anschließend entfernt wird. Die dabei gebildeten Poren spiegeln dabei die Dimensionen und Anordnung der zuvor konservierten Flüssigkristallphase wider. Durch die so erreichte Präzision hinsichtlich der Größenverteilung und Anordnung der Poren ist eine größenselektive Adsorption kleiner Moleküle durch das quervernetzte Material möglich. Außerdem ist durch die Carboxylatgruppen, die zunächst für die Selbstorganisation der peripheren Carbonsäuren um das im Zentrum liegendes Templat benötigt werden, eine Protonierung oder Deprotonierung möglich. Daraus ergibt sich die Möglichkeit die Polarisation der Poren zu kontrollieren und damit eine zusätzliche Ladungsselektivität zu realisieren. In der vorliegenden Arbeit werden die selektiven Adsorptionseigenschaften der gedruckten Objekte unter Beweis gestellt: zwei kleine kationische Farbstoffe, Methylenblau und Thioflavin T, können die in die Objekte eindringen während Rhodamin B aufgrund der Größe und Methylorange aufgrund positiven Ladung nicht adsorbiert werden.

Im zweiten Teil der Arbeit wird ein superhydrophobes nanoporöses Material mittels Zwei-Photonen-Laserdrucken für eine materialunabhängige Funktionalisierung modifiziert. Die nanoporösen Objekte werden zunächst mittels Digital Light Processing hergestellt. Ihre Nanoporösität wird durch polymerisationsinduzierte Phasenseparation unter Zuhilfenahme des porenbildenden Additivs 1-Decanol erzeugt. Die so fabrizierten porösen Objekte haben superhydrophobe Eigenschaften. Durch photochemisch induzierte Pfropfpolymerisation hydrophiler Monomere − realisiert durch Zwei-Photonen-Laserdrucken – können hydrophile 3-dimensionale Muster erzeugt werden. Diskontinuierliches Entnetzen wässriger Lösungen oder Suspensionen wird im Anschluss dazu genutzt die zuvor erzeugten Strukturen mit unterschiedlichsten Materialien zu funktionalisieren. Das Verfahren wird zunächst mithilfe der Adsorption des Farbstoffes Rhodamin B hinsichtlich der Qualität der erzeugten Muster evaluiert. Anschließend wird die Flexibilität des Verfahrens durch Funktionalisierung mit Polydopamin und Polypyrrol aus wässriger Lösung gezeigt. Sogar die mikrostrukturierte Abscheidung von Nanopartikeln aus einer Suspension von Silica-Nanopartikeln konnte gezeigt werden. Basierend auf den vorherigen Ergebnissen wurde zuletzt die Herstellung leitfähiger Strukturen mittels Funktionalisierung mit Silber-Nanopartikeln untersucht.

CONTENT

CHAPTER 1 | INTRODUCTION & THEORETICAL BACKGROUND ____ 1

3D printing ____ 2
Chemistry for light-triggered 3D printing ____ 5
Photoinitiators ____ 6
Chemistry for vat photopolymerisation ____ 9
Physics for light-triggered 3D printing ____ 13
Technologies for vat photopolymerisation 3D printing ____ 15
Techniques based on one-photon adsorption ____ 15
Two-photon 3D laser printing ____ 18

Functional materials for 3D printing ____ 21
Liquid crystalline materials ____ 21
The nematic mesophase ____ 23
Columnar liquid crystals ____ 26
Columnar mesophases and their characterisation ____ 27
Design of discotic mesogens ____ 33
Porous superhydrophobic materials ____ 36

CHAPTER 2 | AIMS ____ 41

CHAPTER 3 | TWO-PHOTON LASER PRINTING OF HEXAGONAL COLUMNAR LIQUID CRYSTALLINE MATERIALS ____ 43

Chemical synthesis and optimisation ____ 44
Synthesis of peripheral acid dA ____ 46
Synthesis of peripheral acid dBzA ____ 48
Synthesis of core TBIB ____ 52
Synthesis of core T ____ 52
Synthesis of core M ____ 53
Preparation of the H-bonded complexes ____ 53

Characterisation of H-bonded assemblies ____ 56

Formulation of a printable Col_h photoresist ____ 64

Characterisation of the Col_h properties ____ 66
1,3,5-Tris(1H-benzo[d]imidazol-2-yl) benzene (TBIB) assemblies ____ 67
Melamine and tris(triazolyl)triazine assemblies ____ 70
Alignment of the Col_h mesophases ____ 72

Microprinting of columnar LCs ____ 72

Core removal: towards ordered nanaporous materials ____ 79
Selective dye adsorption ____ 85

Screening of other designs ____ 89
Na:dA ____ 89
Assemblies using different core:dendric acid ratios ____ 90
Assemblies containing non-acrylated peripheral acids ____ 91
Covalent discotic mesogens ____ 92

CHAPTER 4 | **MICROPATTERNING OF AMORPHOUS POROUS MATERIALS** 97

DLP printing of superhydrophobic structures 99

Chemical considerations 101

Optimisation of the patterning process 103

Material-independent functionalisation by discontinuous dewetting 107

CHAPTER 5 | **CONCLUSION AND OUTLOOK** 113

CHAPTER 6 | **EXPERIMENTAL PART** 115

Materials and methods 115
General 115
POM 116
Two-photon laser printing 116
Microprinting of Col_h LCs 116
Sample preparation 116
Printing procedure 116
Micropatterning of superhydrophic porous materials 117
Sample preparation 117
Micropatterning of superhydrophobic structures 117
FTIR spectroscopy 117
FTIR of microstructures 117
FTIR of molecular species and polymeric films 118
Wide-angle X-Ray scattering 118
SEM imaging 118
Microprinted Col_h LCs 118
Micropatterned superhydrophobic structures 118
UV-vis spectroscopy 118
Fluorescence confocal microscopy 119
DLP 3D printing of superhydrophobic objects 119
Supercritical drying 119
Physical adsorption test of polyHEA on the DLP-printed porous structures 119
Material deposition 120
Digital microscopy of micropatterned structures 120
Confocal microscopy of micropatterned structures 120
Time-of-flight secondary ion mass spectrometry (TOF-SIMS) 120
Conductivity tests 121

Synthetic procedures 121
Core TBIB 121
Acid dA 122
Acid dBzA 123
Core M 128
Core T 128
Na:dA 130
TPE:dA_4 131
NO2:dA_3 132
dC12 133

Spectroscopic data 135
DOSY 155

BIBLIOGRAPHY 159

Chapter 1 INTRODUCTION & THEORETICAL

BACKGROUND

3D printing, or more generally "additive manufacturing (AM)" or "rapid prototyping", is a manufacturing concept that retained incredible attention in the past decades in various field such as bio- and tissue-engineering,[1-5] optics and photonics,[6-10] (micro)robotics,[11-15] microfluidics,[16] and many more.[17-20] To date, numerous 3D printing techniques are available and allow the manufacturing of metallic, composite or polymeric materials. In particular, light-triggered 3D printing techniques allow the fabrication of polymeric objects via the light-induced polymerisation of monomers contained in inks (photoresists). Thanks to their fundement on photoresists which are a formulation of reactive molecular spiecies, functional additives can be introduced to the printed materials in a relatively simple manner.[21] In this purpose, functional additives can be added to a printable photoresist, or chemically substituted with polymerisable moieties, which results in their covalent incorporation in the final polymeric material.[22]

The development of new functional materials for 3D printing openned new oportunities toward the further popularity of the technique. For example, the introduction of strengthening fibres,[23-29] carbon nanotubes[30-33] or cellulose nanocrystals[22, 34, 35] allowed the fabrication of objects of increased mechanical properties. The manipulation of glass transition temperature (T_g) allowed the fabrication of shape memory polymers.[36, 37] The use of porogens allowed the fabrication of porous superhydrophobic materials by polymerisation-induced phase separation.[38-40] And the printing of nematic liquid crystalline materials allowed the fabrication of stimuli responsive materials.[41, 42] Out of other, such photoresists demonstrated the potential of 3D printing for the manufacturing of high performance highly specific materials. In spite of the great efforts readily invested on the broadening of the variety of materials that can be fabricated using additive manufacturing technologies, the arise of the techniques is still young and a lot remains unexplored.[43]

In this chapter, I will introduce the main fields covered in the scope of this interdisciplinary dissertation and present the necessary theoretical background for the following. I will in particular present 3D printing generally and light-triggered 3D printing in detail, explore the field of liquid crystals and their current implication in 3D and 4D printing, and describe superhydrophobic materials and how they can be implemented to additive manufacturing.

3D printing

3D printing is a bottom-up computer-aided manufacturing technique in which a 3D design is reconstructed as a solid object from a stock material.[44] Material extrusion or, more precisely, fused deposition modelling (FDM) is, by far, the most popular 3D printing technique nowadays. The main reason for this popularity is its user-friendliness as well as its costs, which currently makes the technique accessible for in-house application.[45] FDM is based on the melting of a filament that is deposited at the desired location, and quickly cools down to regenerate a solid material, allowing the reconstruction of 3D objects.[46-48] In spite of the common first thought of 3D printing being based on FDM, it is important to note that it is only one of the numerous different techniques that have been developed over the years, as depicted in **Figure 1.1**. As I will later only focus on vat photopolymerisation techniques, and as a matter of the clarity of this chapter, I will not present all the techniques presented in **Figure 1.1**. For readers interested in further details, the following review articles can be consulted.[49, 50]

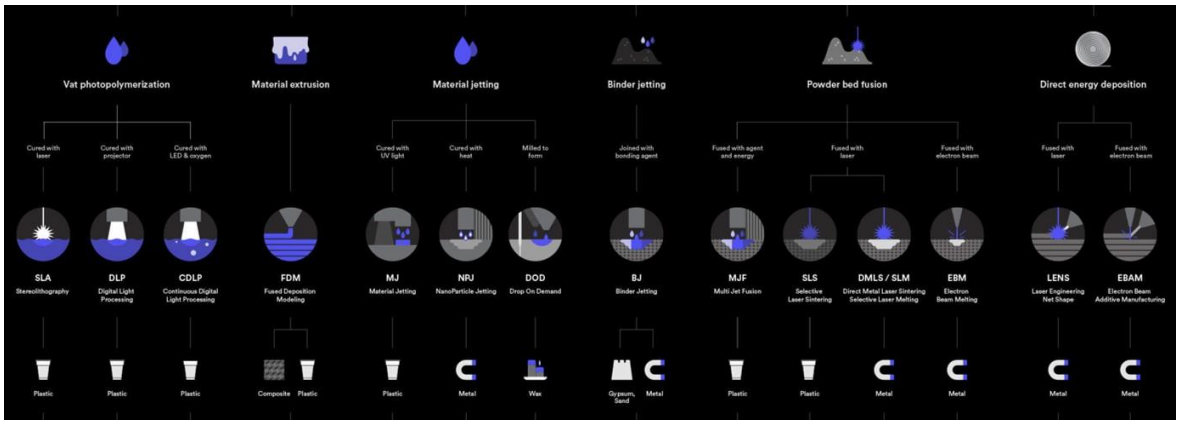

Figure 1.1. Schematic table of the main 3D printing technologies and of the materials that can be conventionally fabricated with each technique. Reproduced from HUBS 2022, accessed on the 4th of April 2022, <https://www.hubs.com/guides/3d-printing/>.

Additive manufacturing is especially versatile and user-friendly in the sense that printing paths can be easily computed by dedicated softwares ("computer-aided design") from a digital 3D shape of the user´s choice,[51, 52] and that a single printing instrument can be used to fabricate really diverse designs without the need of specific tooling. As a consequence, additive manufacturing is particularly well-adapted for prototyping, or for small scale production.[53, 54] Additionally, the fact that pieces are constructed through a bottom-up process allows a control of the geometry and architecture of the inner volume of the manufactured pieces. By the optimisation of the inner structural architectures of hollow parts, one can fabricate very light-weight objects of optimal mechanical properties for a given application.[55] Hollow structures can be used for material or weight saving, making 3D printing of great interest for fields where performance to weight ratio is of great importance, such as medicine[56, 57] or vehicle´s industry,[58-60] for example.

The bottom-up construction of 3D objects used in additive manufacturing comes with specific challenges and can be optimised by the development of adapted fabrication strategies. An attention should be put on the orientation of the part during printing, which can influence the post-processing of the parts, the amount of stock material used as well as the final performances of the parts.[61] First, an approach of fabrication along one-direction (slide by slide in some cases) individably comes with regions potentially floating over the course of the printing. In that regard, softwares automatically include supporting structures to allow the fabrication of the desired design. With an adaptation of the orientation of the part during printing, one can minimise the amount of supporting structures required, hence reducing the fabrication time and facilitating the post-processing of the piece. During post-processing, the piece is treated to have its mechanical properties enhanced (by heat or UV-curing, for example), the supporting structures are removed and the surfaces are manually smoothend. Secondly, it should be taken into account that the fabricated objects will have anisotropic mechanical properties. Indeed, a decreased sturdiness of the objects is observed across the links in-between the printing paths.[48, 62] An optimisation of the orientation of the piece during printing, with respect to the its expected usage and to the mechanical stresses it will endure when functioning or the use of strengthening additives is preferable.[63]

To put it in perspective with other manufacturing techniques, 3D printing can be compared to moulding and computer numerical control (CNC) machining, as representative of conventional manufacturing. Of the three methods, additive moulding is the best suited

technique for large scale manufacturing as it can rapidly produce pieces with homogeneous mechanical properties.[64, 65] However, it requires initial expenses for the building of moulds and facilities, hence requires an intensive primary optimisation of the piece´s shape. A useful comparison can be done in-between 3D printing and CNC machining, which nicely represents conventional manufacturing in the sense in which it uses methods such as drilling or routing. CNC machining is also a computer-aided technique, but conceptually opposite to 3D printing as it relies on material removal ("top-down" process). The top-down nature of CNC machining engenders material losses, however, unlike 3D printing, CNC has the advantage to produces objects of homogeneuous mechanical properties what can be beneficial for the fabrication of pieces enduring high stresses. Also, a big variety of different materials can theoretically be fabricated with the same CNC machine, even though each device is usually optimised for one type of material. The cost per part trends for all the three methods can be visualised as depicted in **Figure 1.2**.

Finally, the fabrication cost is usually deterministic toward a choice for a particular manufacturing technique. In **Figure 1.2**, it can be seen that the fabrication by 3D printing remains contained for a single part or for small amount of parts, however the cost per part is not significantly reduced by an upscaling of the production.[58] For CNC machining, it can be seen that the initial pricing is higher than for 3D printing but is rapidly reduced with the increasing scale of the production. This can be related to the facts that, upon upscaling, pieces can be smartly arranged to minimise material loss and that a recycling of the shavings can be setup. Finally, as mentioned in the entrance of this comparative part, moulding is specified for big-scale productions. Other considerations such as energy consumption, production time, etc. can be taken into account.[66]

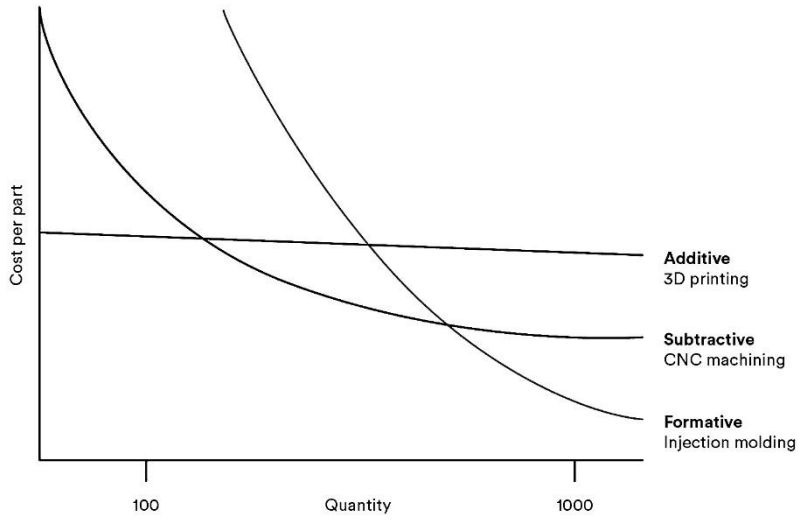

Figure 1.2. Schematic plot of the cost per part for manufacturing by 3D printing, injection molding and CNC machining. Adapted from HUBS 2022, accessed on the 4th of April 2022, <https://www.hubs.com/guides/3d-printing/>.

Chemistry for light-triggered 3D printing

As advanced before, the present thesis will be focussed on light-triggered additive manufacturing techniques, which are assembled under the general designation of "vat photopolymerisation" 3D printing. These processes utilise photo-triggered chemical reactions to modify a liquid ink ("photoresist") at a position being irradiated by light, which induces the formation of an isoluble solid phase. 3D models are then reconstructed through the sequencial printing of 2D slides, which spacing is denoted as "slicing distance", from an photoresist stored in a vat.[44] In some cases, the 2D slides are themselves produced by the printing of lines, which spacing is denoted as "hatching distance". Upon completion of the desired object, the residual unreacted photoresist can be washed away using a good solvent. The crosslinking of the photoresists used for vat photopolymerisation is supported by the use of reactive molecules which often represent the majority of the photoresist. Polymerisation reactions are the most common, but other strategies based on dimerisation reactions were also reported.[67-79] Finally, a post-processing by UV-irradiation can be used to increase the crosslinking density of the material, hence its mechanical properties.

The two main techniques representatives of vat photopolymerisation 3D printing are stereolithography (SLA), that was first described by Hull et al. in 1986,[80] and is acknowledged to be the initial 3D-printing technique. And digital light processing (DLP) which is conceptually similar to SLA and differs from the latter by the method used to

fabricate a 2D slide. Upon laser irradiation, a photoinitiator is used to convert the photonic energy into chemical energy. The reactive intermediates generated (radicals or acids) can be utilised for the polymerisation of vinyl containing monomers (acrylates, methacrylates, ethylenes, styrenes, etc.) by free-radical polymerisation or of epoxides by cationic ring-opening polymerisation. Also, other reactions such as thiol-ene coupling, photodimerisation or photo-induced reversible addition-fragmentation chain transfer (RAFT) polymerisation[81] have been successfully used for 3D printing purposes.

Typical formulations of inks (photoresists) for SLA and DLP consist in a photonitiator and a mxiture of monomers and crosslinker. The monomers and the crosslinker, which is a branched compound that carries several reactive groups, sustain the formation of a solid polymeric phase upon polymerisation. A photoinintiator is used to induce the polymerisation reaction under light-irradiation. Alternatively, solvent and additives can be used to adjust the viscosity of the ink, as well as the mechanical properties and functionality of the printed material.

I will later present the technical aspects of vat photopolymerisation techniques in more details. Before doing so, the following sections will be dedicated to describing the chemical and physical phenomena involved in vat photopolymerisation 3D printing.

Photoinitiators

The monomers used in vat photopolymerisation are in general not capable of a satisfactory light-induced self-initiation. Photoinitiators are therefore added to the formulation of the photoprintable photoresists and are responsible for light absorption and for the transformation of the irradiative energy into usable chemical energy, generating radicals or acidic species.[82] Although the photoinitiators only briefly take part in the polymerisation reaction, and represent a minor fraction of the structure of the final material, they can strongly influence its final properties and performances.[82, 83]

Radical photoinitiators are designed around an aryl acyl core that has the advantage to have a high extinction coefficient.[84] Radicals are generated by the photo-triggered scission of covalent bonds, that leads to the formation of one or several radicals via two main mechanisms, Norrish type I or Norrish type II. Norrish type I photoinitiators produce at least two radicals through the intramolecular cleavage of a covalent bond. This reactivity is observed for α-hydroxyketones[85, 86] (**Scheme 1.1**) and α-aminoketones,[87] where a cleavage

of the acylcarbonyl−C bond leads to the formation of two primary radicals; for diacylphosphanes[88, 89] where a potential cleavage of two acylcarbonyl−P bonds leads to four radicals; and for diacylgermanes[90-92] where a cleavage of the acylcarbonyl−Ge bonds leads again to potentially four radicals.

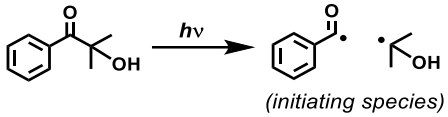

Scheme 1.1. Example of 2-Hydroxy-2-methylpropiophenone as a Norrish type I radical photoinitiator, and light-trigerred activation by Norrish type I reaction.

Examples of Norrish type II photoinitiators are benzophenones or thioxanones. In this case, photo-excitation does not lead to a homolytic bond cleavage. Instead, the excited photoinitiator undergoes an intermolecular excited state proton exchange with a co-initiator (e.g. amino compounds). Through the process, the benzophenone is reduced to the corresponding diphenylmethanol and one radical is formed on the α-position of the co-initiating amine (**Scheme 1.2**).[82, 93, 94]

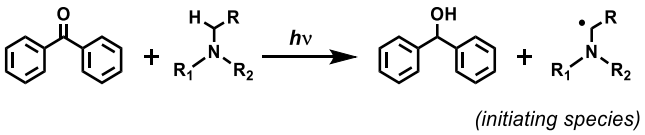

Scheme 1.2. Example of benzonephenone as a Norrish type II radical photoinitiator and light-trigerred activation by Norrish type II reaction.

A wide variety of photoinitiating species, having specific advantages, shortcomings and purposes are available for purchase today. Non-exhaustive lists of Norrish type I radical photoinitiators (**Figure 1.3**), as well as of Norrish type II photoinitiators and co-initiating species (**Figure 1.4**) are proposed below.

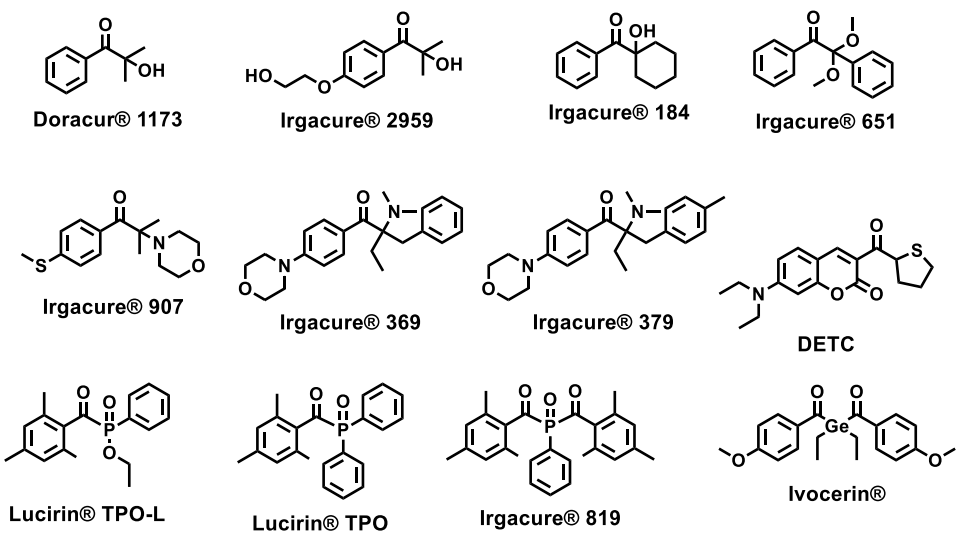

Figure 1.3. Example, chemical structure and commercial name of some Norrish type I photoinitiators.

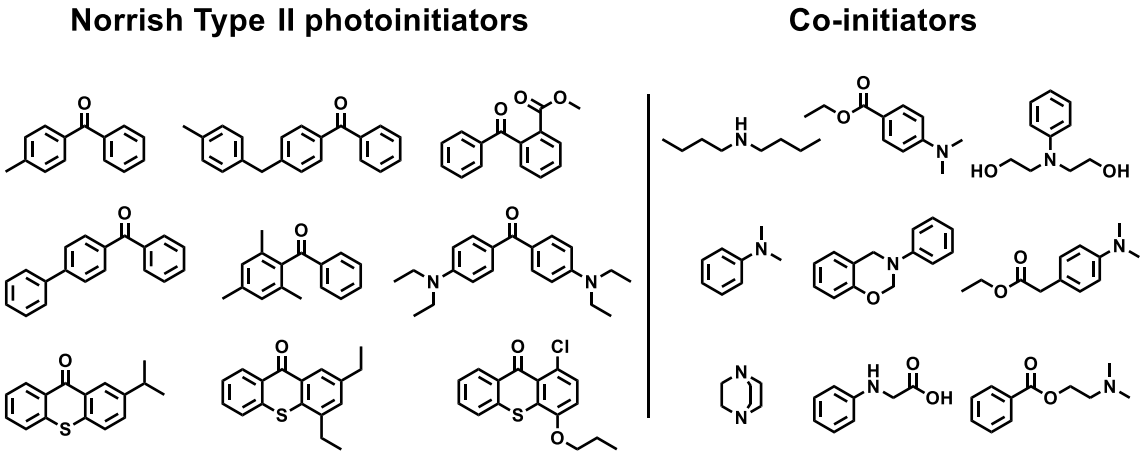

Figure 1.4. Example and chemical structures of some Norrish type II radical photoinitiators and co-initiators.

Cationic photointitiator have historically been based on the observation that aryldiazonium salts can generate an electrophilic BF_3 molecule via N_2 elimination.[95, 96] Nevertheless, their low temperature stability makes them poor cationic photoinitiators, as they can already react in the dark. A more optimised system relies on iodonium salts, which undergo a bond cleavage similar to that seen before for Norrish type I photoinitiators. The formed radicals can later react with a proton donor, generating a highly acidic metallic hydride, which can efficiently activate the monomers for cationic polymerisations reactions (**Scheme 1.3**).[97, 98]

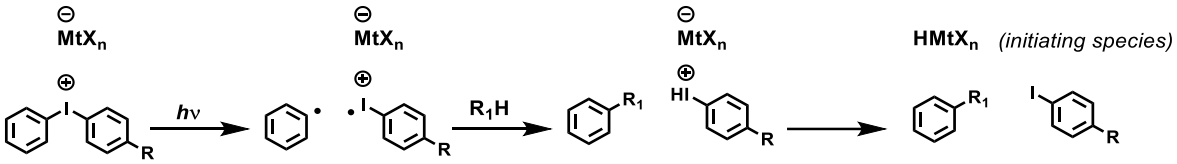

Scheme 1.3. Activation of a iodonium salt upon light-irradiation.

Some photoinitiators have been specifically designed for their use in two-photon polymerisation. Their photochemical reactivity is similar to that of the photoinitiators seen before. However, the alteration of the side groups of the photoinitiator can significantly increase their two-photon cross-section, thus their absorption in this regime.[99] In spite of the development of new photoinitiator being of great interest, and because I will, in my work, solely make use of the commercial photoinitiators presented before. I will not describe photonitiators optimised for two-photon processes in this dissertation.[50, 100, 101]

Chemistry for vat photopolymerisation

The free-radical polymerisation of molecules containing vinyl-groups is the most commonly used method for light-triggered 3D printing.[102] Out of the possible monomeric species, (meth)acrylates are prominent. Their popularity is noticeably justified by their high lability, that facilitate the formation of densely crosslinked polymeric materials. The free-radical polymerisation of acrylates proceeds by the propagation of a free radical, preferentially carried by the secondary carbon of the vinyl moiety, following a Markovnikov addition (**Scheme 1.4**). Despite this representation of a single chain growth being usually used, the complete understanding of the free-radical polymerisation of acrylates is not trivial and required consequent efforts over the years.[103] The free-radical polymerisation of acrylates depicts an increased probability of "backbiting" events to happen compared to other vinyl containing monomers. During "backbiting", a proton transfer (intramolecular or intermolecular) occurs from an α-position in the backbone to the propagating radical position, which transfers the free radical to a tertiary carbon of the backbone. Although the tertiary radicals are less labile than their secondary equivalent (which slows down the reaction at first), their likely occurrence engenders a high density of crosslinks by further propagation or recombination, which is of great interest for 3D printing purposes.[104] The chemical structures of well-known (meth)acrylate species used in this context are shown in **Figure 1.5**.[50]

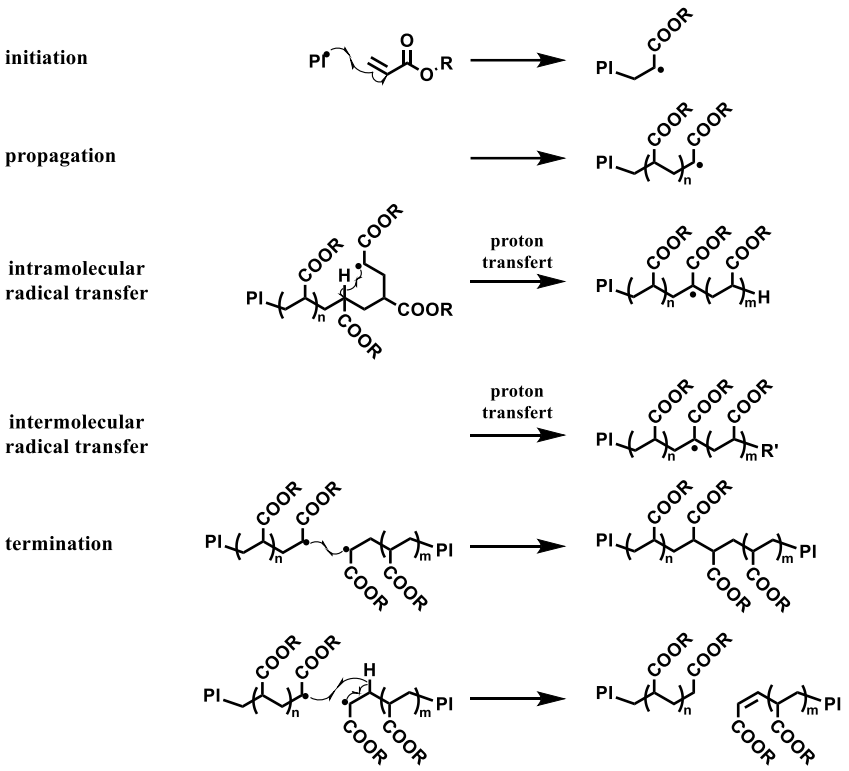

Scheme 1.4. Mechanism of the free-radical polymerisation of acrylates.

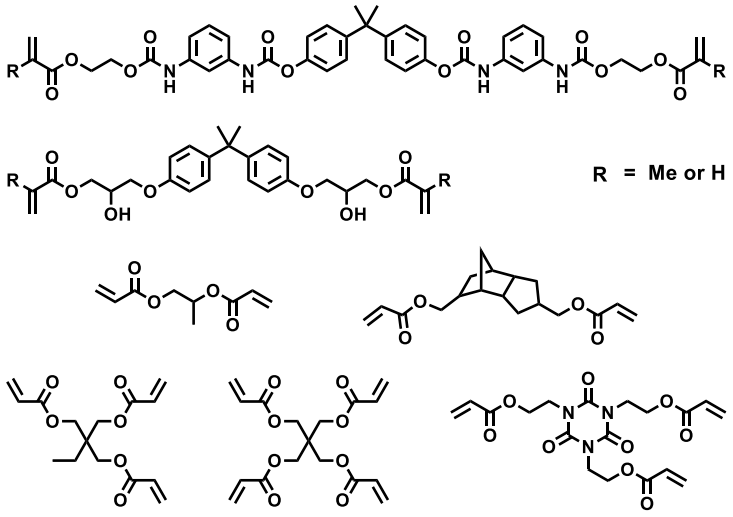

Figure 1.5. Example of (meth)acrylate containing compounds for 3D printing.[50]

A first main shortcoming of the free-radical polymerisation of (meth)acrylates for 3D printing is the shrinkage that it engenders.[105] Another important feature of the free-radical polymerisation of acrylates lies in the ability of oxygen to quench the reaction. Via the attachement of oxygen on the propagating radical, a peroxy radicals of relatively low reactivity is formed, which desables further propagation.[106] As will be seen later, this

reactivity is fundamental for techniques such as continuous liquid interface production (CLIP). For printing in oxygen-rich media, this quenching could be a drawback, in which case, other less oxygen-sensitive reactions would be preferred.

The thiol-ene(yne) polymerisation is an example of such a platform.[107] The thiol-ene(yne) polymerisation is a step-growth polymerisation reaction that involves two different compounds, a species that contains one or several thiol groups, and a compound having an insaturation such as alkenyls or alkynyls. The polymerisation is initiated by the proton transfer from the thiol to the radical initiating species, resulting in a thiolyl radical. The thiolyl radical thereafter attacks the insaturation, forming a secondary radical, similar to the radicals observed in the free-radical polymerisation of acrylates (**Scheme 1.5**).[108-110] The preferred propagation occurs via a proton exchange with an new thiol group. The thiol-ene free-radical polymerisation results in materials of low crosslinking density, which is, for example, of interest for the fabrication of hydrogels. Moreover, this system can be designed to be non-cytotoxic, making it relevant for biomedical applications.[5, 111-114] Nonetheless, the crosslinking density can be tuned, with formulations including branched compounds including several functional groups (**Figure 1.6**), or by using alkynes in place of alkenes. In the latter, a first coupling affords an alkene which can undergo the same reaction again.[108-112, 115-118] The thiol-ene polymerisation also shows a reduced oxygen sensitivity and lower polymerisation-caused shrinking when compared to the free-radical polymerisation of acrylates.

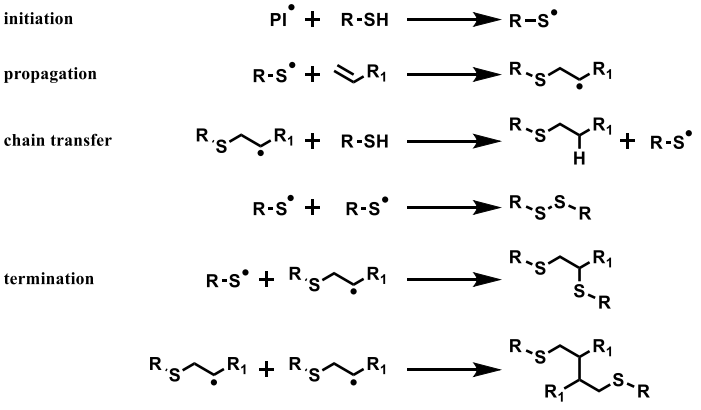

Scheme 1.5. Mechanism of the free-radical thiol-ene polymerisation.

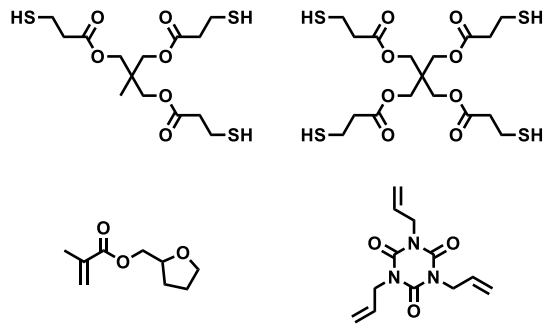

Figure 1.6. Structures of thiol-ene compounds in commercial inks.[50]

Recently, controlled polymerisation reactions, noticeably RAFT polymerisation (**Scheme 1.6**), were successfully implemented for 3D printing.[119-122] The use of RAFT for 3D printing allows a "living additive manufacturing" of polymeric materials. In their works, the authors took into account the ability to chemically alter the "parent network" obtained after the printing step. In contrast to free polymerisation reactions, where the parent network is said to be chemically "dead", RAFT-based 3D printing allows a chemical modification of the polymeric material after printing. Indeed, the presence of RAFT agents in the parent network allows a secondary polymerisation reactions to be peformed, leading to a "daughter network" that can contain several types of materials.

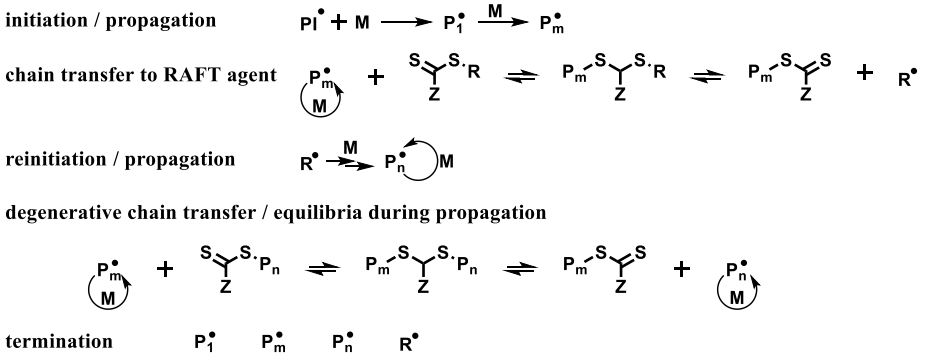

Scheme 1.6. Mechanism of RAFT polymerisation.

The cationic ring-opening polymerisation of epoxides in another important reactivity used for vat photopolymerisation 3D printing, with famous resists such as SU-8.[123, 124] The initiation of the cationic ring-opening polymerisation occurs by the attachment of an initiating acid to the ether, which activates the neighbouring carbons, with respect to the conventional reactivity of epoxides (**Scheme 1.7**). The propagation thereafter proceeds via a classical ring-opening polymerisation mechanism. Epoxides have several advantages over acrylates as the oxygen insensitivity of the cationic photopolymerisation, the lower shrinkage of the parts upon crosslinking or the greater strength of the final materials.[125-127]

However, the greater versatility and ease of use make acrylate preferable in many cases, for practical reasons.[128]

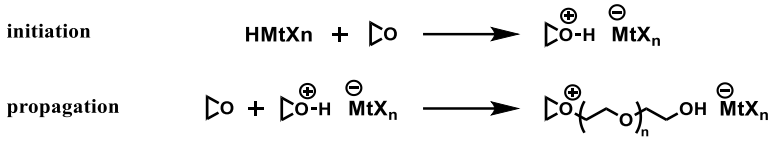

Scheme 1.7. Cationic ring-opening of epoxides.

Some photodimerisation reactions have the particularity to being self-induced, as the photodimerisation of coumarines (λ_{max} = 340 nm) for example. In this case , the coumarine group serves both as sensitizer and crosslinking moiety.[67-71] In other cases, a separated sentiziser can be used. The oxygen promoted dimerisation of amino acid residues have allowed the crosslinking and printing of proteins. In this case, the sensitization of oxygen by an additive dye (such as methylene blue or rhodamine B) can allow the photo-induced oxidation of tryptophan, histidine, tyrosine, cysteine and methionine. A coupling of the amino acid residues with their oxidised analogue can then occur via a condensation reaction.[72-79]

Physics for light-triggered 3D printing

Light-matter interaction is fundamental for light-triggered 3D printing techniques. On one hand, understanding the mechanisms by which molecules are photo-activated permits the designing of advanced photoinitiators. On the other hand, an understanding of how laser beams evolve in different media permits the optimisation of the methods and procedures for 3D printing.

As seen before, the light-harvesting properties of photoinitiator is supported by highly absorbing molecules built around aromatic moieties. Upon light-irradiation, valence electrons of the highest occupied molecular orbital (HOMO) are promoted into the lowest unoccupied molecular orbital (LUMO). While HOMOs are bonding molecular orbitals, LUMOs have an anti-bonding nature, leading to a decrease in bond order by one-photo excitation (1PE).[84] However, the so-generated energy can solely be exploited if the activated state of the light-harvester lives for a time long enough to allow it to undergo a chemical reaction, that would lead to stable species of higher energy. In that regard, the recombination of the electrons, regenerating a filled HOMO by radiative or non-radiative decay, is the main limiting factor. One does then describe the formation of photointiating species to occur from

a triplet excited state, for which recombinaison is disfavoured with respect to the multiplicity selection rule, hence increasing the lifetime of the excited state.[129] This sequence of phenomena is usually simplified and summarised in a Jablonski diagram that represents the overall energy levels of the ground state (S_0), the first singlet excited state (S_1), the second singlet excited state (S_2) and first triplet excited state (T_1) of the molecule, together with their associated vibrational levels. The transition phenomena in-between the states: absorption, vibrational relaxations (VR), internal conversion (IC), inter-system crossing (ISC), fluorescence and phosphorescence can then be simply visualised (**Figure 1.7**).

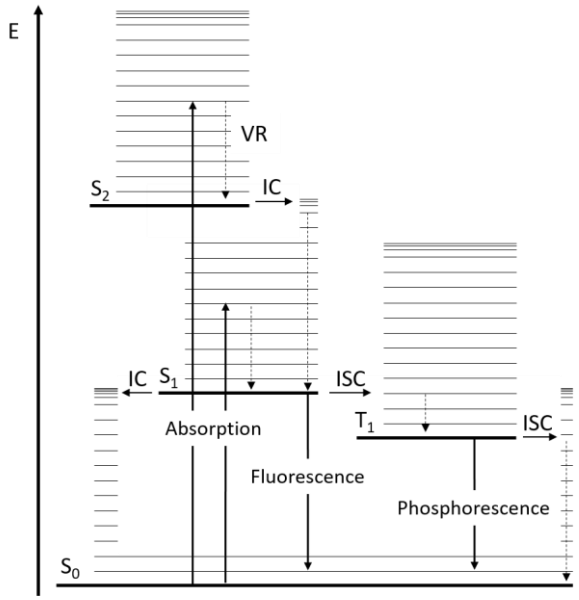

Figure 1.7. Example of Jablonski diagram. VR: vibrational relaxation; IC: internal conversion; ISC: inter-system crossing.

First theoretically described by Maria Goeppert-Mayer,[130] two-photon excitation (2PE) refers to the excitation of a molecule by the absorption of two distinct low-energy photons, through a virtual intermediate energy state. Due to this virtual state having no thermodynamic stability, it has a very short life-time in the femtosecond order which requires high light intensities. Practicallly, a focussed laser beam is used to generate a high light intensity at the focal point. This leads to the formation of a "voxel", contraction of "volume" and "pixel", that is the volume element in which the light intensity is high enough to allow 2PE to take place. In **Figure 1.8**, two examples of the indirect visualisation of 1PE and 2PE is shown for fluoresceine and fluorine 3.[131] The use of such high energies densities is however not possible if using continuous beam, as the heat at voxel could noticeably degrade the material being irradiated. To circumvent this, pulsed beams are used that allow

for a temperature management by relaxation within the resist. Considering the lifetime of the virtual intermediate state, pulsings in the femtosecond range are required. Two-photon laser printers are thus equiped with femtosecond pulsed IR lasers.

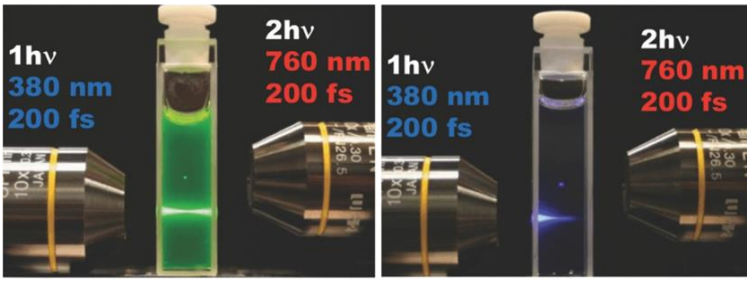

Figure 1.8. One-photon and two-photon excitation of fluorescein (left) and fluorine 3 (right). Reproduced from,[131] Copyright 2018, John Wiley & Sons.

For a focussed laser, the intensities along the *x*-, *y*- and *z*-directions follow Gaussian distributions. Given the corresponding standard deviations along *x* or *y*, σ_{xy}, and along z, σ_z, one can note the later as,

$$I_z \sim N(\mu_z, {\sigma_{xy}}^2)$$

$$I_{xy} \sim N(\mu_{xy}, {\sigma_z}^2)$$

where μ_i is the mean value along the direction i.

What can noticeably be observed practically, is a significantly bigger standard deviation along x and y than along z, leading to an ellipsoidal voxel.[132]

Technologies for vat photopolymerisation 3D printing

In the last parts, I described the fundamental phenomena involved in vat photopolymerisation techniques for the solidifaction of negative photoresists upon laser exposure. In this part, I will adress the technical aspects in more details in order to understand how instrumentations are equiped and what parameters can be adjusted for printing optimisation.

Techniques based on one-photon adsorption

SLA and DLP make use of continuous UV-vis laser light sources, and therefore operate based on one-photon excitation. An important factor for the successful operating of SLA and DLP relies in the irradiating energy that will be applied to the photoresist. The wavelength [nm] of the irradiating beam naturally has an effect on the latter, but remains technically

fixed for generic devices. Thereafter, the irrading energy will depend on the intensity [mW] of the laser beam as well as the printing speed (for SLA) or irradiation time (for DLP). When using a higher power and a longer exposure time, more energy is transferred to the resist thus an increased extent of polymerisation and crosslinking occurs, leading to a stronger material. On the other hand, high energies also generate a local temperature increase in the irradiated part of the photoresist which can result in a deterioration of the material.[133] A systematic screening of the printing parameters then allows the determination of the optimal printing parameters for a given photoresist. In parallel, a "curing depth" under the tested parameters is also determined, and should be considered during the construction of the printing jobs and noticeably when setting the slicing distance.[134]

When constructing the printing jobs the slide thickness naturally influences the surface smoothness as well as the time efficiency of the printing of a part. By the increasing of the slide thickness, a "staircase effect" is observed, limiting the surface smoothness of the final part. It also important to notice that the straight laser beam will deplete when impinging the photoresist, caused by refraction and absorption (**Figure 1.8**). Upon increasing the slide thickness, the depletion of the laser beam in the photoresist can lead to the formation of weak points or voids that can alter the mechanical properties of the final part.[63, 133]

SLA uses a scanning of the laser beam in the *xy*-plane to construct a slide of the material. After the completion of a slide, the layer of photoresist is renewed by the displacement of the supporting stage along the *z*-axis. As it is proposed in the patent from Hull et. al.,[80] several configurations of the printer can be used. In its easiest configuration, the stage can be fully immersed in the vat and the part can be progressively printed by lowering the stage in the vat. In this case, the light beam comes from the top of the vat and the photopolymerisation occurs at the surface of the photoresist. Though being technically simple, this design suffers major performances drawbacks. Most importantly, the size of the printable parts is limited by the size of the vat, which is a problem for the fabrication of big objects. Instead, modern SLAs are based on the third "upside-down" configuration proposed in the patent. In this configuration, the vat is equipped with a transparent window at its bottom, and the laser beam comes from the lower part of the instrument. The photopolymerisation hence occurs at the bottom of the vat rather that at the surface of the photoresist. The printed part is slowly pulled out of the vat, which allows the production of

parts of variable sizes with the same instruments, and limits the size of the vat, thus of the initial volume of photoresist necessary to fill it.[134]

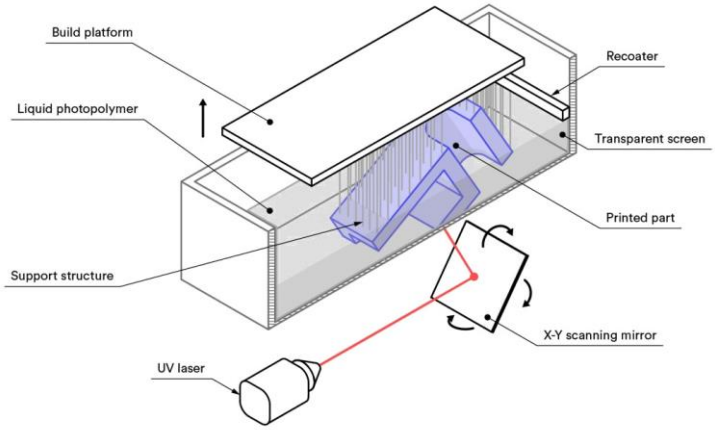

Figure 1.9. Schematic representation of a SLA printer. Adapted from HUBS 2022, accessed on the 12nd of Mai 2022, < https://www.hubs.com/knowledge-base/how-design-parts-sla-3d-printing/>.

In modern SLA, the most adapted way to achieve a fast and controlled targeting of pixels in the *xy*-plane, for the fabrication of a 2D slide, relies on a *xy*-scanning mirror or on galvanometer scanners. Galvanometer scanners are composed of two mirrors placed orthogonally one to another, and that can rotate along their axis. This setup allows the scanning of a stationery laser beam throughout any point of a *xy*-surface.[135]

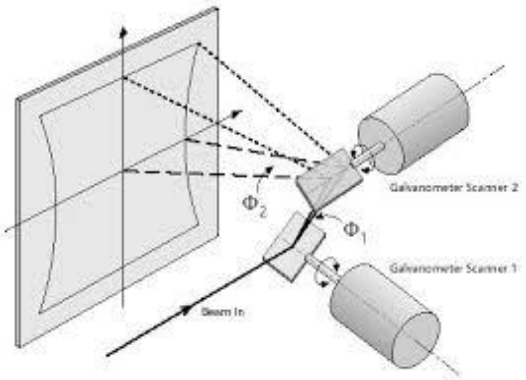

Figure 1.10. Schematic representation of a galvanometer scanner. Precision lasers scanning, 2022 accessed on the 4th of April 2022, <https://precisionlaserscanning.com>.

The light source and reflecting/scanning devices utilised is the main difference in-between SLA and DLP. As just seen, in SLA, one creates a slide pixel by pixel through the fast scanning of a punctual laser beam. Instead, DLP uses the irradiation of an entire slide at once from a stationery light source. This is achieved using a digital mirror device (DMD)

composed of an array of micromirrors which can independently be oriented in three positions: on, off or neutral (**Figure 1.11**). In this way, each micromirror corresponds to a pixel and enables the reconstruction of the targeted shape upon reflection of the light source.[136-138]

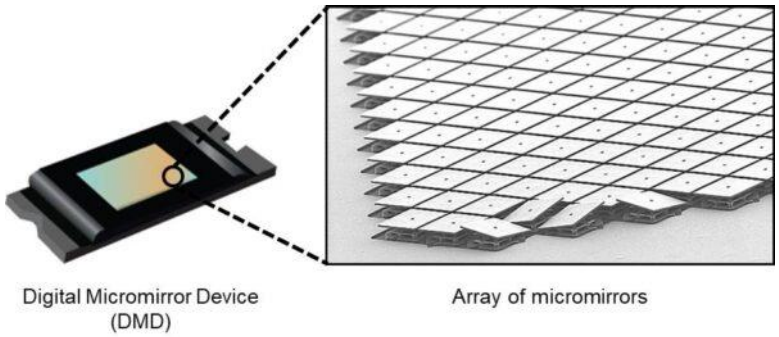

Figure 1.11. Picture and close-up view of a digital mirror device. Ibsen photonics 2022, accessed on the 4th of April 2022, <https://ibsen.com/resources/spectrometer-resources/dmd-spectrometers/>.

SLA and DLP are based on an iterative processes that fabricate parts slide by slide. This operating principle, as mentioned, leads to an anisotropic mechanical behaviour of the fabricated parts and also limits the speed of printing. Continuous liquid interface production (CLIP) (or continuous digital light processing (CDLP)) addresses this issue by proposing a strategy for the continuous printing of parts.[139, 140] The technology is based on the quenching of the free-radical polymerisation of acrylates by oxygen. In CLIP, the bottom window of the vat is designed to be permeable to oxygen, creating a gradient of oxygen concentration in the deep part of the photoresist. The photopolymerisation thus only takes place at a height at which the oxygen concentration becomes low enough to allow the proceeding of the free-radical polymerisation. In this way, a layer of non-solidified photoresist is constantly present and renewed at the bottom of the vat, allowing a continuous printing.

Two-photon 3D laser printing

Pioneered by Maruo in 1997,[141] two-photon 3D laser printing makes use of the two-photon excitation phenomenon to segregate the happening of photopolymerisation and crosslinking phenomena within the characteristic voxel of two-photon excitation. The technique is based on the idea that one can constructs 3D objects by the three-dimensional scanning of the voxel. Thanks to the reduced size of the voxel, a microscale fabrication of 3D objects and resolutions of about 100 nm can be achieved.[99, 142, 143] In the context of 3D printing, the resolution is given by the minimal spacing that allows the distinction of two

parallel single lines, based on this same system, the definition corresponds to the minimal achievable line width.

For 2PE based processes, the intensity I of the irradiating beam follows a normal distribution of mean μ and standard deviation σ^2.

$$I \sim N(\mu, \sigma^2)$$

Below a threshold intensity, the crosslinking density of the irradiated parts is not sufficient to obtain a solid and insoluble network. This minimal threshold will then be the minimal intensity for which printing can be achieved. The width of the intensity distribution at the threshold intensity corresponds to the voxel size, hence to the achievable definition. A second threshold corresponds to the overexposure of the photoresist (**Figure 1.12**). Above this threshold, undesired side reactions can occur and the photoresist is deteriorated. In the most extreme cases, the most volatile components of the photoresist can undergo a phase transition, resulting in the formation of bubbles and/or "explosions". Optimal printing parameters thus consist in a balance of crosslinking extend and thermal deterioration.[144]

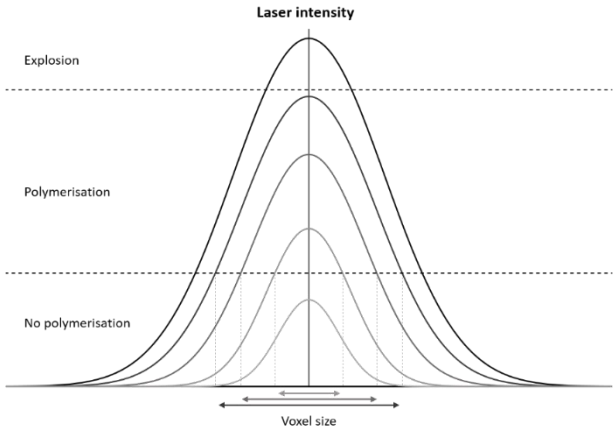

Figure 1.12. Representation of the intensity distribution for various laser powers. The two minimal and maximal thresholds as well as the voxel size for each laser power are shown.

The printing of two distinct lines in close proximity can be pictured using the two associated Gaussian curves of the intensities, and the effective irradiation dose should be given by the summed intensities of the neighbouring voxel positions. The susquent "proximity effect" can lead to two main issues. If the two distributions are far enough so that they are separated at the threshold intensity, the proximity effect can lead to a filling of the gap, hence to a reduced resolution (**Figure 1.13a**). In the case in which the proximity effect leads to a dramatically increased intensity in-between the closeby voxels, the second

threshold for the formation of bubbles and explosion can be reached, leading to a degradation of the photoresist (**Figure 1.13b**).[144, 145] The latter phenomena should be accounted for when setting the slicing and hatching distance used in the printing jobs and most often require them to be optimised.

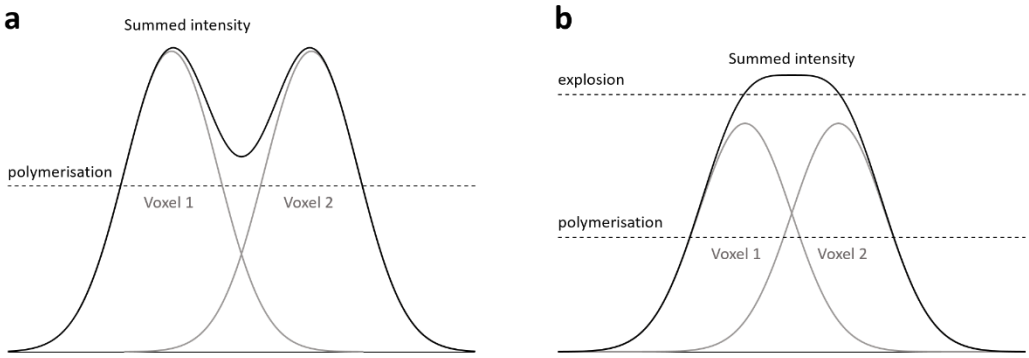

Figure 1.13. Representation of the proximity effect provoquing a) a loss of resolution and b) a degradation of the photoresist.

Two-photon 3D printers have progressively been made commercially available in the past decade which allowed an acceleration in the development of the technique. With respect to the size of the structures that are produced by the technique, a single drop of photoresist can used as stock material. Technically, the samples containing the photoresists can be mounted on a microscope stage that moves in *xy*-plane, and the objective is mounted on second stage that moves along the *z*-axis. Though such a setup allows the fabrication of 3D objects, the precision and velocity of the stage limits the quality of the achievable printing and the printing speed.[146] Instead, two-photon 3D laser printers use galvanometer scanners to achieve the *xy*-scanning of the voxel and piezoelectric elements for the scanning along the *z*-direction. In this case, the sample holder is primarily linked to the microscope stage by piezoelectric elements, enabling the holder to be very precisely and rapidly displaced along the *z*-axis.[146] Nevertheless, the available displacement amplitude of piezoelectric elements and the window reachable by galvonometer scanners have limitations that have to be considered for the printing of big objects. In this case, the targeted objects are split into smaller parts that can be fabricated separately.

One distinguishes two main operation methods for two-photon 3D laser printing. In "immersion-oil" configuration, the structures are printed on the glass substrate and in their intended *z*-orientation. The objective is then located across the substrate and is separated from the latter by oil. Immersion oil configuration is the easiest approach for two-photon 3D

laser printing but suffers the limitation that the maximal reachable structure height is dictated by the working distance of the objective used. This shortcoming can be addressed by using a "Dip-in" approach where the photoresist is included in-between the objective and the glass substrate. The Dip-in approach removes the barrier of height limitation and allows the printing of big structures.

At the end of the process, the printed objects can be isolated by the "development" of the remaining non-crosslinked photoresist, by solubilisation in a good solvent. The non-crosslinked photoresist is then washed out, while the insoluble crosslinked parts remain on the substrate. During development, capillary forces or miscelleneous external stresses may provoke a detachment of the structures from the substrate. In that regard, the glass substrates can be functionalised with reactive groups such as methacrylates that allow a covalent anchoring of the structures on the substrate.

Functional materials for 3D printing

Specific functionalities can be provided to the polymeric objects 3D printed by light-triggered techniques. This can be achieved by a smart formulation of the photoresists, either by embedding functional materials as additives or by using components that would generate a functionality during polymerisation. In our perspective review,[147] we have, for example, presented fibre reinforced photoresists,[23-29] photoresists including cellulose nanocrystals,[22, 34, 35] photoresists with embedded carbon nanotubes,[30-33] nematic liquid crystalline photoresists[148-153] or photoresists with embedded metal-organic frameworks.[154] Which allowed the printing of polymeric materials of increased material properties, as well as conductive, stimuli-responsive or gas absorptive polymeric materials. In this section, I will focus on the two classes of functional materials explored in the current dissertation, liquid crystalline and porous materials, with special emphasis on their use and potential in the field of 3D printing.

Liquid crystalline materials

The liquid crystalline (LC) state is a specific state of matter in which the molecules arrange in a systematic way, such as is the case for a crystalline solid, but in which the molecules enjoy a mobility that makes the LC state comparable to a liquid.[155] The first description of the LC state is currently reasonably unanimously attributed to Friedrich Reinitzer and his work published in 1888.[156] In the latter, the author was studying some

derivatives of cholesterol, and noticeably cholesteryl benzoate, when he observed the formation of a singular purple coloration upon slow cooling of an isotropic melt of the compound (described as "splendid" in the translation of the original work). The purple coloration later vanished upon further cooling, and a crystal state was observed. Upon heating from the crystaline state, the author observed the reciprocal behaviour; a first melting into a cloudy fluid material, followed by a clarification upon further heating. With the current understanding of LCs, these observations can easily be rationalised, I will dedicate the following part to present the current understanding of LCs.

Thermotropic LC materials are characterised by a double melting. At low temperatures, the so-designed "mesogens" (LC molecules) form a crystalline phase. Upon heating, a first transition is observed where the material gain fluidity, but where the mesogens remain constrained to an overall arrangement driven by weak intermolecular interactions (**Table 1.1**).[157] The study and understanding of the inner arrangement of the mesogens in this mesophase (LC phase) is the challenge the field of LC is addressing. Upon further heating from the LC state, the weak interactions that support the mesophase are disrupted and the material behaves as an amorphous fluid. The associated temperature to second melting is referred to as "clearing point" or "clearing temperature".

Table 1.1. Strength of important soft intermolecular interactions. Adapted from,[157] Copyright 2009, American Chemical Society.

Interaction	Strength [kJ mol^{-1}]
ion−ion	100−300
ion−dipole	20−200
dipole−dipole	5−50
hydrogen bonding	4−120
cation−π	5−80
π−π	0−50
Van der Waals	less than 5

Lyotropic LC form mesophases based on their concentration in a solvent. As for thermotropic LC, many systems were found to behave as lyotropic and a lot of efforts have been put into their understanding and manipulation.[158] The present part will however be focussed on thermotropic LC materials.

The nematic mesophase

Different level of mesophase organisation can be obtained from each individual type of thermotropic mesogens. The mesogens are usually classified with respect to their molecular shape; rod-shaped (calamitic), discotic, bent-shaped or cholesteric. The first important consideration is hence that mesogens rely on molecular structures of high stiffness for which their shape is clearly identified. The central mesogenic skeleton is thereafter substituted with fluid side chain providing the final mesogens with the necessary fluidity to prevent crystallation and to allow the formation of a LC mesophase.[159, 160]

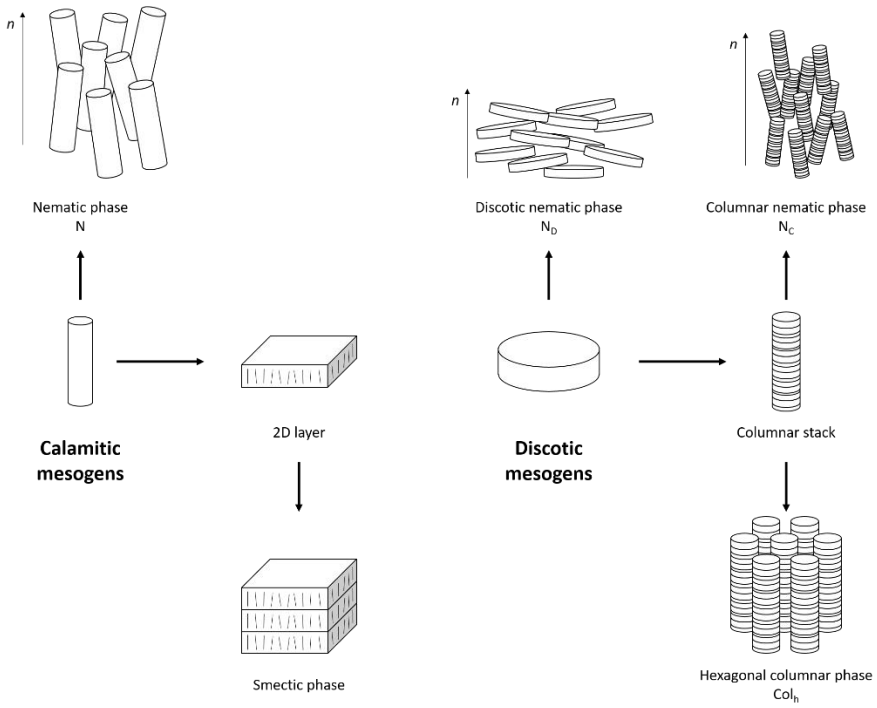

Figure 1.14. Representation of calamitic and discotic mesogens, together with their associated mesophases.

The nematic liquid crystalline (NLC) mesophase is the mesophase of lowest ordering. In the nematic phase, the mesogens are in average aligned with their axis of highest symmetry (main symmetry axis) parallel to a "director vector", *n*, that is defined as an attribute to the mesophase. Within a nematic phase, solely an averaged alignement of the mesogens along the director vector is observed, and no arrangement along the other spatial dimensions are observed.[161] The main advantage of the nematic phase resides in this relative simplicity and in its corresponding facilitated handling. Nematic LCs possess, for example, unique optical refraction properties that are currently used for display applications.[162] Using NLCs allows an access to the unique properties of LCs through a relatively simple alignment along a single

direction hence limits the complexity of the associated methods and processes. This supports the popularity of NLCs when compared to other LC materials. For practical reasons, mainly NLCs formed by calamitic mesogens are used, but nematic phases nonetheless also defined for discotic or bent-shaped mesogens.[163] In calamitic mesogens, the long symmetry axis contains covalent bonds, enabling the manipulation of the mesophase by the introduction of functional groups at this position. For example, the introduction of cyano groups having a strong dipole moment, is a conventional design and allows the alignment of the mesophase through the application of an external electric field.[164, 165]

In the field of the 3D printing of polymeric materials, the manufactured materials are solidified during the croslinking process. As a result, the arrangement of the mesophase will get locked to some extend, and the shape sensitivity of the fabricated materials toward phase transition can be exploited. When found in a nematic phase, the mesogens occupy a maximal length along the director vector and a minimal length across the director vector. If heated, the LC material will be provided the necessary mobility to arrange randomly, as a result, both a constriction along the initial director vector and an elongation across the initial director vector will be obtained. Importantly, the original nematic arrangement spontaneously re-establishes from the isotropic material, driven by forces applied by the matrix on the mesogens and by the formation of intermolecular interactions, which allows the repeated manifestation of the shape modification. This controlled anisotropic shape responsiveness is fundamental for the 3D printing of stimuli-responsive structures ("4D printing").[166, 167]

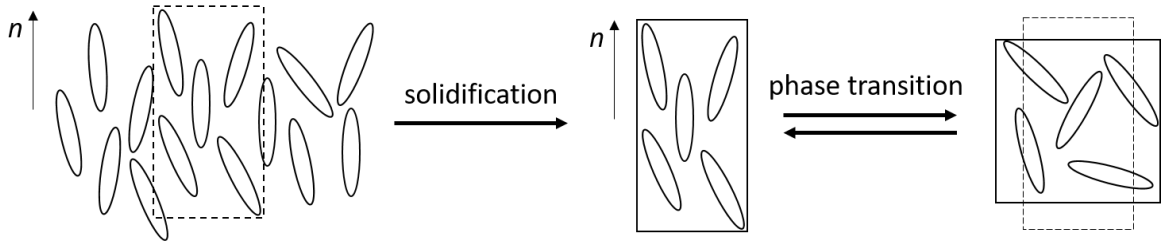

Figure 1.15. Representation of a nematic phase of calamitic mesogens (ellipses) and of the shape modification of a polymeric LC elastomer induced by phase transition.

Appart from the thermal disruption of the NLC phase, an similar response can be obtained if the arrangement is randomised by a shape modification of the mesogens. Noticeably, the light induced *Z/E*-isomerisation of azobenzene (λ_{max} = 330 nm) has been widely used. While the *Z*-azobenzene is calamitic and can be included in a NLC phase, the *E*-isomer creates

voids in the arrangement and forces a randomisation of the arrangement.[168] If the photoswitch is included within an elastomer, the *Z/E*-isomerisation induces the formation of loops and helps the randomisation further.[169]

The first step of 4D printing of NLCs is to obtain an aligned mesophase. For 3D printing techniques based on material deposition, it has been shown that an alignment can be achieved from the shearing force applied by the nozzle on the being-deposited molten material.[170-173] 3D printed structures of NLC elastomers were shown to be capable of applying a mechanical work onto weights upon phase transition.[170, 171] Also, NLC elastomers can be used to fabricate structures that bend upon exposure to an external stimulus when printed either on a flexible and inert substrate, or on a second layer of the LC polymer such as the respective alignments of the two layers are perpendicular to each other. The obtained bending can be used to prove the stimulus-responsiveness of a NLC material and used for the fabrication of functional structures, such as actuators.[170, 172]

The application of nematic LCs to SLA and DLP remained challenging for a long time. Indeed, due to the fluid nature of the photoresist for SLA and DLP, the alignement of the entire resist has to be maintained for the total duration of the printing task. However, considering the scale at which these techniques are operated, such an alignment of a large volume of the photoresist is not trivial. In their works Ullett et. al.[174, 175] and Tabrizi et. al.[176] made use of permanent magnets located around the vat to induce an alignment of a nematic mesophase. In both cases, the authors observed the successful locking of the nematic phase and printing. However, a miniature vat had as well as a consequent magnetic setup had to be used, which limits the achievable size of the printed structures. Later, Li et al.[177] achieved a shear-driven alignment of a nematic phase, applying a shearing force on the photoresist by the displacement of the photoresist tray.

Thanks to the smaller scale at which two-photon 3D laser printing is operated, the use and the control of nematic LCs and of their alignment is facilitated. Noticeably, the alignment can be triggered and controlled using electric fields,[164] polarised light[178] or surface segregation.[179-181] Wiersma and coworkers provided several examples of light-responsive 3D printed structures.[153, 182-186] In 2015,[187] the group fabricated a microscopic walker (**Figure 1.16**). The design was based on the printing of a light responsive polymeric block which elongates upon irradiation at 532 nm, and relaxes back to its original shape when the irradiation is stopped. In this case, the disruption of the nematic phase is caused by the light-

induced *Z/E*-isomerisation of the azobenzene photoswitch.[188-190] By adding a leg on each corner with a 45° angle, the microscopic walker can freely displace on a rough substrate upon repeated irradiation-dark circles. In 2017,[191] the group reported a design in which a 3D printed NLC pincer that can selectively fold and grab a presented object under light irradiation, with respect to the colour of the object presented. In this case, the folding is triggered by the local temperature increase resulting from the light absorption of the object presented. Other examples proved the incredible potential of two-photon 3D laser printed NLC elastomers for the fabrication of stimuli-responsive structures.[127, 150-152, 165, 168, 192-194]

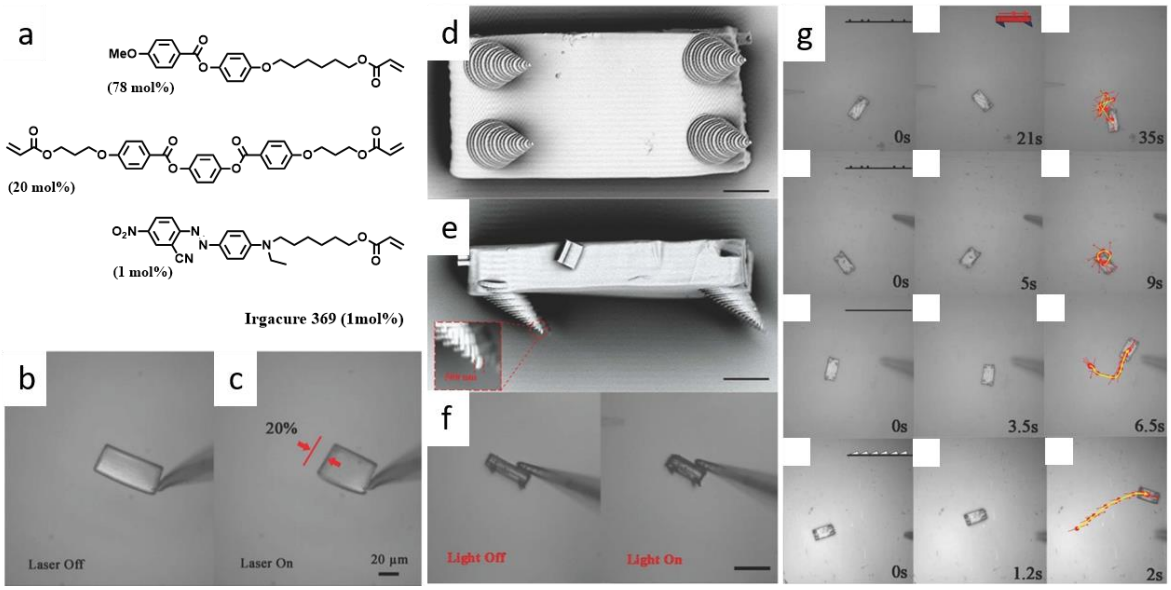

Figure 1.16. Microscopic walker fabricated by two-photon laser printing. a) Composition of the photoresist. b) Microscope image of the main block in the dark and c) under light-irradiation. Scanning electron microscopy of the microscopic walker with legs added in d) bottom view and e) side view. f) Microscope image of the microscopic walker in the dark and under light irradiation. g) Recorded displacement under pulsed light irradiation. Adapted from,[187] Copyright 2015, John Wiley & Sons.

Columnar liquid crystals

In 1977, Chandrasekhar et al.[195] pioneered modern research on columnar LCs. Knowledge prior to this work made use of the "graphitisation" of complex organic materials upon carbonisation at elevated temperatures.[196, 197] Indeed, graphite is known to be composed of two-dimensional sp^2 carbon sheets (graphene sheets), that are weakly bound together in the *z*-direction, by van der Waals interaction. Early investigations of columnar stacked molecules were based on this model directly, and used the pyrolysis of organic compounds at a temperature in the order of 500 °C to obtain graphite-like materials composed of polyaromatic hydrocarbon sheets of a molecular weight of about 1500 Da. The

particular graphite-like configuration of these materials can be studied by X-ray diffraction and lead to a specific birefringence of the materials.

In their work, Chandrasekhar et. al. studied the arrangement of benzene-hexa-[n]-alkanoates into a Col_h mesophase an evidenced the ability of relatively simple organic molecules to form columnar LCs under mild conditions, as the mesogens depicted a clearing point at about 86 °C, and the LC phase was formed from about 82 °C in the cooling step. With their approach for the design of discotic LCs mesogens, the authors paved the way toward a wide diversity of molecular structures for discotic LCs mesogens.

Columnar mesophases and their characterisation

Similar to the arrangement of calamitic mesogens, discotic mesogens can self-assemble into a "nematic discotic" phase, where the main symmetry axis of the discotic mesogens are in average aligned along a director vector. Also, thanks to their ability to self-assemble into columnar stacks, a second "nematic columnar" phase is the nematic arangement of columnar stacks of discotic mesogens (**Figure 1.17**). Nonetheless, nematic phases of discotic mesogens are rarely observed. [198]

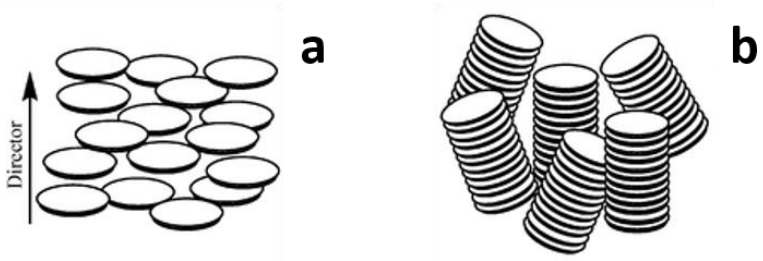

Figure 1.17. Nematic phases of discotic mesogens: a) nematic discotic and b) nematic columnar phases. Reproduced from,[198] Copyright 2010, the Royal Society of Chemistry.

More common columnar mesophases are engendered by the piling of discotic, conic or bent-shaped molecules into columns and by the arrangement of these columnar stacks into regular two-dimensional pavement. The most important patterns are hexagonal (Col_h), tetragonal (Col_{tetr}), oblique (Col_{ob}) and rectangular (Col_r) (**Figure 1.18**).[199] In a Col_h mesophase, the columns are arranged in a hexagonal pattern similar to a honeycomb pattern. In a Col_{tetr} mesophases, the columns draw a compact squared pavement. Finally, the Col_{ob} and Col_r consist in a squared and rectangular pavement, respectively, with an additional centre column. Of the latter, the Col_h mesophase is the most widely observed, in the

following, a general columnar mesophase appellation will thus refer to the Col_h mesophase. When applicable, other symmetries will be mentioned explicitely.

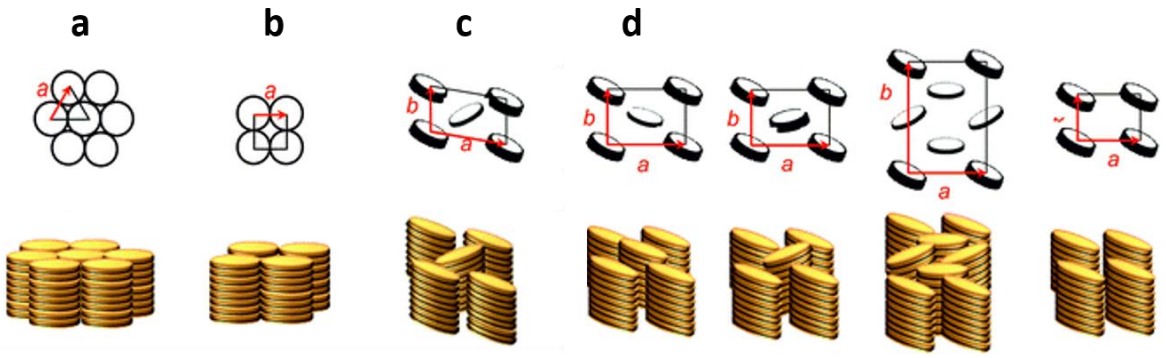

Figure 1.18. Examples of 2D pavements of columnar mesophases and their associated lattice parameters and 3D representation. The cross section of columns is drawn as circles; ellipses indicate a tilt of the mesogens. a) Hexagonal, b) tetragonal c) oblique and d) rectangular columnar mesophases. Adapted from,[199] Copyright 2011, the Royal Society of Chemistry.

In "randomly arranged" columnar mesophases, distinct liquid crystalline domains are formed and do not show a homogeneous long-range orientation. In aligned mesophases, a long-range alignement is obtained, the alignment is "planar" if the director vector of the mesophase is parallel to the substrate or "homeotropic" if the director vector is perpendicular to the substrate. A first improvement of the long-range alignment can be achieved by adjusting the cooling rate applied, which results in a widening of the domain size. Slower cooling rate, the mesogens are given more time to finely arrange with respect to each other, while faster cooling rates would force the formation of weak intermolecular interactions, restricting the mesogens´ mobility, hence their fine arrangement. A manipulation of the cooling rate may be sufficient to obtaining good long-range alignment. However, an external driving force for the alignment of the mesophase should be applied in most of the cases.[200]

A first approach consists in the tuning of the mesogen-substrate affinity. Toward a planar alignment, the side chain should have a strong affinity for the substrate while the inner core should be repulsed away from it (**Figure 1.19**a). If the inner core has a great affinity for the substrate while the side chains are repulsed away from it, a planar alignment is expected from the second layer of mesogens (**Figure 1.19**b). Finally a homeotropic alignment should be favoured by both the side chains and the inner core having a good affinity for the substrate, allowing them to spread on the surface and initiate the growing of columnar stacks (**Figure 1.19**c).[201]

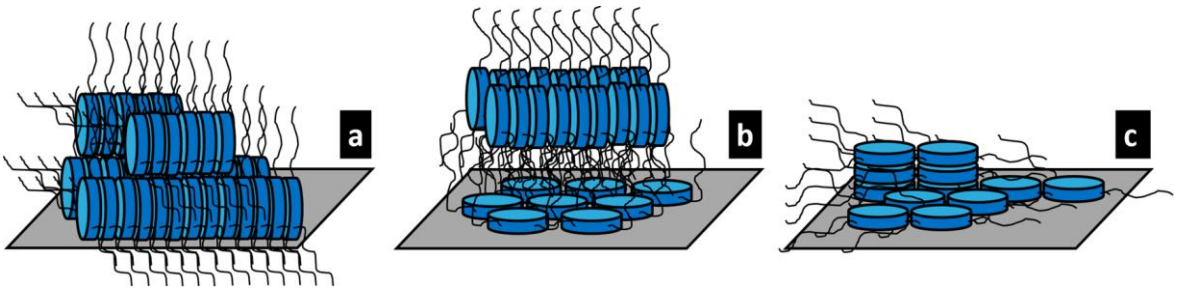

Figure 1.19. Representation of the alignment induced by a surface having a strong affinity for a) the side chains, b) the inner core and c) a similar affinity for the either the inner core and the side chains. Reproduced from,[201] Copyright 2018 American Chemical Society.

The application of an external magnetic field was shown to induce an alignment of the director vector perpendicular to the field. A stationary sample being exposed to a homogeneous magnetic field would hence be aligned within a plane normal to the field. In order to restrict the alignment further to a one-dimensional direction, a rotation of either the field or the sample along a secondary axis perpendicular to the field should be applied, inducing an alignment of the director vector along this secondary axis.[202] The alignment under an external magnetic field is pretty powerful, but requires advanced equipment and setups for the generation of a strong magnetic field, in the order of 5 T, as well as to generate the secondary rotation axis. Other alignement methodologies under an external electric fields, by surface patterning or by shearing are also possible but have not been as extensively reported.[203]

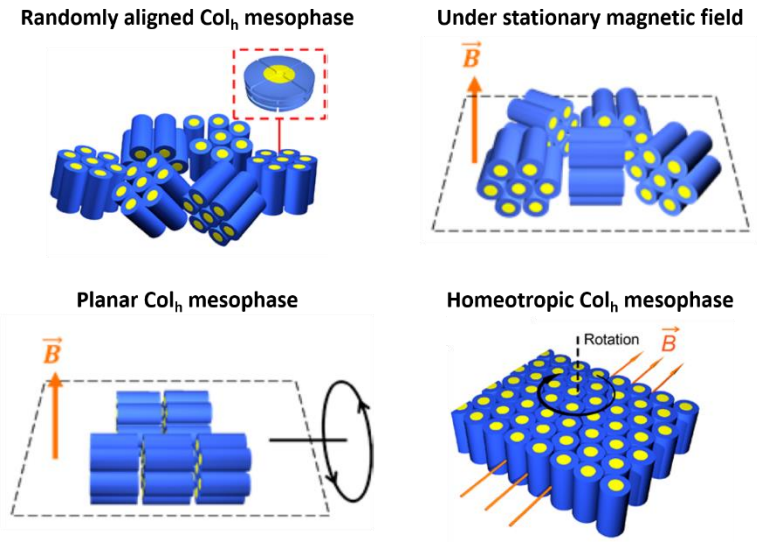

Figure 1.20. Representation of a randomly aligned Col_h and its alignment by the application of an external magnetic field and rotation toward planar or homeotropic alignment. Adapted from,[202] Copyright 2014 American Chemical Society.

The unique birefringence of columnar LCs allows a first instinct of the LC properties of the compound to be accessed by microscope imaging under crosspolarisers. By polarised optical microscopy (POM), conic fan-shaped or focal conic LC textures are in particular incative of the formation of a columnar mesophase (**Figure 1.21**). Other rarer features such as spherulitic textures or "straight line defects" are attributed to a columnar mesophase and a high degree of order, respectively.[204, 205] While the appearance of the mesophase by POM is indicative of the nature of the material, the domain size is related to the long-range ordering of the mesophase. For the analysis of thermotropic LCs, the samples are placed in a heating stage and POM allows a direct visualisation of the phase transitions. Nevertheless, POM analysis does not allow to complete characterisation of columnar LCs. To obtain a qualitative and quantitative determination of the mesophase, X-ray diffraction techniques should be used.

The expected POM of aligned columnar mesophases are particular as their appearance by POM depends on the angle at which they are observed. When imaged from a direction perpendicular to the director vector, a colourful and homogeneous appearance is expected. If imaged along the director vector, no LC texture should be observed, which is similar to the appearance of an isotropic phase.[202, 203, 206, 207] The interpretation of the results hence requires an advanced preliminary understanding of the LCs properties of the material.

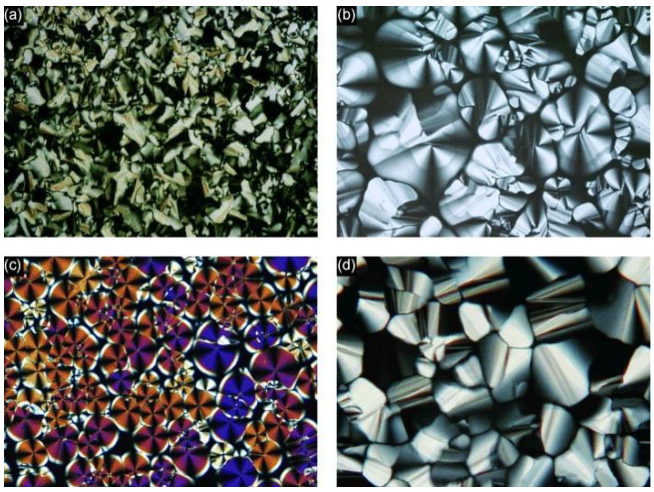

Figure 1.21. Example of LC textures characteristic of Col_h mesophases. a) Conic fan-shaped texture, b) focal conic texture, c) spherulitic texture with maltese crosses and d) straight line defects. Reproduced from,[205] Copyright 2007, John Wiley & Sons.

The XRD analysis of columnar mesophase, the reflections peaks always depict a certain broadness, indicative of the fluidity of the phase. As stated previously, the mesogens within

a LC phase enjoy some mobility, which results in an uncertainty in their spatial location, thus of the intermolecular spacings. On the other hand, crystalline phases lead to an observation of really sharp peaks that transcript their high ordering.

For Bragg´s planes with Miller indices h, k and l, a constructive interference will result in a signal depending on the scattering angle 2θ of the X-ray beam with respect to the Bragg´s law

$$n\lambda = 2d_{hkl}\, sin\left(\frac{2\theta}{2}\right) \qquad (1)$$

where d is the scattering distance and λ is the wavelength of the X-ray source source (for CuKα, λ = 1.5406 Å). To each distance can then be associated a scattering vector q by

$$q_{hkl} = \frac{2\pi}{d_{hkl}} \qquad (2)$$

And the value of the scattering vector can be expressed as a function of the scattering angle by

$$q_{hkl} = \frac{4\pi}{\lambda}\, sin\left(\frac{2\theta}{2}\right) \qquad (3)$$

Therefore, the wide-angle region of the spectrum will contain information about small features, while the small angle region will contain information about symmetry elements with wider spacing.

For columnar LCs, the wide-angle region contains a very broad reflection that corresponds to the corelation of the aliphatic chain as well as a sharper, yet broad, (001) reflection for the π-π stacking of the aromatic core. The broadness of the (001) reflection indicates a large irregularity of the spacing between the discotic mesogens along the director vector. The small-angle region shows the long-range two-dimensional arrangement of the columns; and are sharper, indicative of a regular pavement in the *xy*-plane. The small-angle reflections contain information about the symmetry of the pavement as well as about the spacing in-between the columns. An interpretattion of the small-angle reflection is achieve via the analysis of the relative distances of each signal, most often the scattering vectors are used in that purpose. For a Col_h mesophase, a $1{:}\sqrt{3}{:}\sqrt{4}{:}\sqrt{7}$ ratio of the q-values is expected with respect to the symmetry of the pavement (**Figure 1.22**). For other columnar meshophases, this ratio will warry, as for example for a Col_{tetr} mesophase, $1{:}\sqrt{2}{:}2{:}\sqrt{5}{:}\sqrt{8}{:}3$.

The indexing of the significantly rarer Col_{ob} and Col_r mesophases are not as simple due to the several lattice constants.[208]

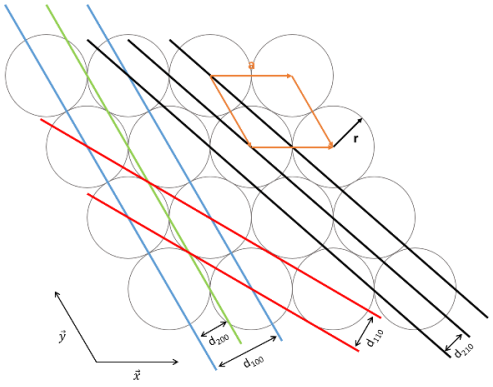

Figure 1.22. Representation of the hexagonal arrangement within a (001) slice of a Col_h mesophase.

For a hexagonal packing, the lattice constant a corresponds to the diameter of an elementary circular element within a (001) slide. The radius r of the circular elements of the the hexagonal arrangement corresponds to the diffraction d_{110}, and the diameter can be expressed as a function of d_{110}. In accordance to the relative distances for a hexagonal arrangement, d_{110} can be expressed as a function of d_{100}, hence

$$a = 2\,r = 2\,d_{110} = \frac{2}{\sqrt{3}}\,d_{100} \tag{4}$$

For a better approximation, a was calculated using the averaged $\overline{d_{100}}$ using the corresponding value of d_{100} from the respective distance d_i of each exploitable diffraction peak. The lattice constant a of a hexagonal packing can therefore be expressed as

$$a = \frac{2}{\sqrt{3}}\,\overline{d_{100}} = \frac{2}{\sqrt{3}}\left(\frac{d_{100} + \sqrt{3}\,d_{110} + \sqrt{4}\,d_{200} + \sqrt{7}\,d_{210} + \ \ldots}{n_{diffractions}}\right) \tag{5}$$

More generally, for a hexagonal arrangement, the distance d_{hk0} corresponding to the (hk0) reflection can be calculated as a function of the lattice constant a by[208]

$$\frac{1}{d_{hk0}^2} = \frac{4}{3}\left(\frac{h^2 + hk + k^2}{a^2}\right) \tag{6}$$

Hence,

$$\frac{1}{d_{100}^2} = \frac{4}{3a^2} \quad \rightarrow \quad a = \frac{2}{\sqrt{3}}d_{100} \tag{7}$$

and

$$d_{hk0}^2 = \frac{1}{h^2 + hk + k^2} d_{100}^2 \quad (8)$$

Randomly aligned columnar mesophases result in circular reflections, corresponding to the random orientation of the director vectors of the LCs domains. On the other hand, long-range alignment of the LCs domains is characterised by the observations of focal points in the 2D diffractogram. They are due to the coherence of the Bragg´s planes in aligned samples and their distribution is related to the symmetry of the sample at the orientation considered. If we consider a polymeric film of an aligned mesophase that is analysed by XRD in transmission. For a Col_h mesophase with a planar alignment, one observes a line alignment of the small-angle reflections, as well as a line alignment of the wide-angle reflection 90° appart. In the case of a homeotropic alignement, the small-angle reflection will have a hexagonal distribution that is caused equivalent Bragg´s planes. With respect to equation (6), it can be seen that several different Miller indices will yield the same distance value, for example, the $(1,0)$, $(0,1)$, $(\overline{1},0)$, $(0,\overline{1})$, $(\overline{1},1)$ and $(1,\overline{1})$ planes will yield the same distance value.

Design of discotic mesogens

A classical design of the aromatic core consists in an aromatic or polyaromatic core. Big polyaromatic molecules such as coronene for example, are known to form columnar crystalline phases.[209] For big polyaromatics, such an arrangement is favourable with respect to other arrangements such as herringbone packing[210] or sandwich herringbone packing of dimers,[211] that can be observed for benzene or pyrene, respectively. This preference it caused by the maximised π-π interractions and packing density. It is then natural to make use of such core for the design of discotic mesogen.[212-214] As mentioned previously, the rigid self-aggregating polyaromatic cores are substituted with fluid side chains to prevent the formation of a crystalline phase and increase the mobility of the discotic mesogens.[159] An example of a discotic mesogen is proposed in **Scheme 1.8**.[215]

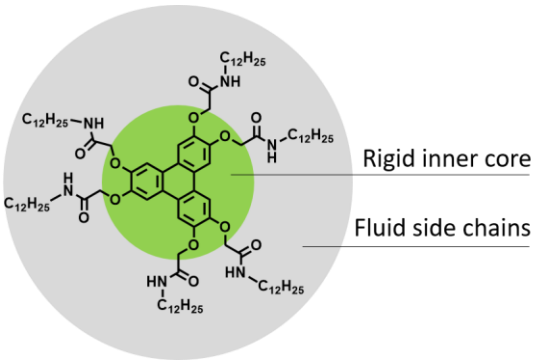

Scheme 1.8. Example structure of a discotic mesogen based on a triphenylene core.[215]

However, polyaromatic molecules are only one example of cores around which columnar mesogens can be built. Dendritic species received interest in the LC community and allowed the systematic study of the arrangement with respect to the core's size. As dendrimers are built by the successive addition of a defined group (each addition is denoted as a "generation"), the study of their arrangement helps a deep understanding of the aggregation process. The iterative addition of a specific motif by which dendrimers are synthesised is not without remembering biological processes. Their study is then additionally used for the understanding of the impact of the primary structure (with repect to the nomenclature used for proteins) on aggregation in natural systems.[157] In the context of LCs, it can be concluded that the arrangement in columnar mesophases will be favoured for compounds having only a few generations. For bigger dendrons, the molecular fluidity becomes prevalent and there are no longer likely to be found in a flat discotic configuration. Functional cores can be used, in which case, their functionality can be forwarded to the mesophase. For example, using discotic mesogens built around a crown-ether[216-218] or a porphyrin[219] core, or columnar LCs of metallomesogens.[220, 221]

Vinayakumara et. al.[222] used a dual donor-acceptor maleimide moiety to fabricate H-bonded discotic mesogens. The authors obtained the mesogen monomer via the Wittig reaction of gallaldehyde with triphenylphosphoranylidenyl succinimide and characterised the formation of a Col_h mesophase of H-bonded assemblies of three molecules. In the case in which a spacing phenyl ring is included, the molecule preferentially self-assemble into a dimeric assembly which behaves as a calamitic mesogen, forming a smectic mesophase.

In my work, I studied the making of nanoporous materials by using H-bonded discotic mesogens. It was shown that H-bonded multi-component discotic mesogens can effectively

being formed and that the resulting supramolecular assemblies behave as discotic mesogens.[223-226]

Pioneered by Lee et. al.,[227] terminal crosslinkable groups can be introduced on the aliphatic chains of H-bonded discotic mesogens that are built around template core. This allows a solidification of the material by the crosslinking of these groups which locks the LC arrangement and makes the obtained polymeric substance further exploitable as functional material. Noticeably, removing the centre core, provides the materials with a high porosity by the freeing of the volume previously occupied by the template core, resulting in the formation of pores. Previous studies on LC based based porous materials were consistently using lyotropic LCs of amphiphilic molecules.[228-232] Driven by their experience with thermotropic columnar LCs, the authors proposed H-bonded self-assembled discotic mesogens as an alternative pathway for the preparation of porous materials mimicking natural membranic channels. Such porous materials have potential application in recognition, separation, catalysis and synthesis of nanocomposites. Further studies have provided a deeper understanding of crosslinkable discotic mesogens, proposed various designs and investigated their practical utilisation.

From then, the works initially inspired by Lee at al., have widen the variety of possible designs of thermotropic self-assembled discotic mesogens for the fabrication of porous materials. Some systems were, for example, based on melamine derivative,[233-237] triazines,[238] 1,3,5-tris(1H-benzo[d]imidazol-2-yl) benzene,[239] chiral amines,[240] or triazoles.[241] Reversing the position of the donor and acceptor groups, similar assemblies can be designed around cores containing carboxylic acid moities and pyridine terminated peripheral molecules.[242-246]

Osuji and coworkers reported several nice example of the homeotropic alignement of Col_h mesophases and their further crosslinking into polymeric films. The group noticeably used systems using fatty acids as peripheral acids,[207] studied the tilt of the discotic mesogens within the homeotropic Col_h mesophase,[247] or utilised the porous homeotropic Col_h polymeric films as actual mebranes.[248] In many cases, the homeotropic alignment could be directly imaged by transmission electron microscopy (TEM).[202, 206, 207, 247] TEM results nicely demonstrates the high ordering and regularity of nanopores when based on a LC phase.

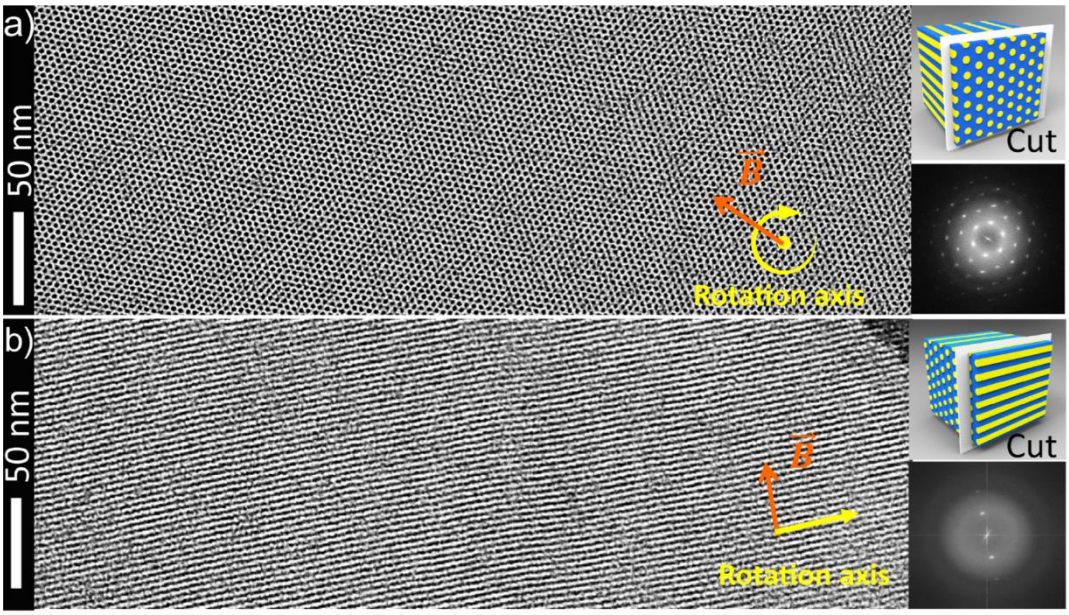

Figure 1.23. TEM images, schematic representation of the cut imaged and associated WAXS diffractograms of an aligned Col_h mesophase. The specimen was cut a) perpendicular or b) parallel to the secondary rotation axis. Reproduced from,[202] Copyright 2014 American Chemical Society.

Porous superhydrophobic materials

Superhydrophobic materials are defined by a high water repulsiveness and are characterised by contact angle, the contact angle of water being above 150°. For a droplet being deposited on a flat surface, the contact angle depends on the affinity of the solvent with the material the surface it is deposited on. Thus, it depends of the hydrophobicity of the material in the case of the deposition of a water droplet. The contact angle θ_w is determined at the triple point solid-liquid-vapour, and can be expressed as a function of the corersponding solid-vapour, γ_{SV}, solid-liquid, γ_{SL}, and liquid-vapour, γ_{LV}, surface tensions with respect to the Yound-Dupre equation.[249]

$$\cos\theta^Y = \frac{\gamma_{SV} - \gamma_{SL}}{\gamma_{LV}} \quad (9)$$

However, the contact angle is never practically greater than 125°−130° for flat surfaces. Superhydrophobicity can then only be accessed via rough surfaces. A droplet deposited on a rough hydrophobic surface wets the surface in two ways described by the Wenzel equation[250] and Cassie-Baxter equation (**Figure 1.24**).[251, 252] In the Wenzel state, the water fully contacts the rough surface and the contact angle evolves with respect to the ratio, r, of

the specific surface area (liquid-solid contact area) with the projected surface area (footprint of the droplet) by

$$\cos\theta = \mathrm{r}\cos\theta^{Y} \tag{10}$$

As a result, the contact angle of water with hydrophilic materials ($\theta^{Y} < 90°$) will decrease and that with hydrophobic materials ($\theta^{Y} > 90°$) will increase.

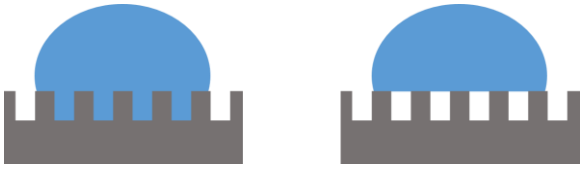

Figure 1.24. Schematic representation of a water droplet deposited on a rough surface in the Wenzel state (left) and Cassie-Baxter state (right).

In the Cassie-Baxter state, the droplet solely wets a fraction of the solid hydrophobic material while the remaining of the contact area is in contact with the vapour phase. In this state, the contact angle is expressed as

$$\cos\theta = \varphi_S\,(\cos\theta^{Y} + 1) - 1 \tag{11}$$

where φ_S is the fraction of the liquid-solid contact and $(1 - \varphi_S)$ the fraction of the liquid-vapour contact. The relationship of the contact angle in both the Wenzel state and Cassie-baxter states with respect to the Young-Dupre contact angle, as well as a representation of both state of the wetting of rough surfaces in shown in **Figure 1.25**.[253]

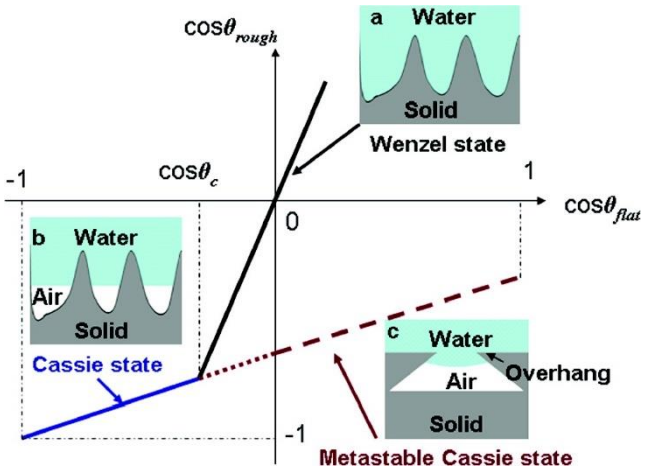

Figure 1.25. Relationship of $\cos\theta$ ($\cos\theta_{rough}$) with $\cos\theta^{Y}$ ($\cos\theta_{flat}$) in a a) Wenzel state, b) Cassie-Baxter state and c) metastable Cassie-Baxter state. In each case, a representation of the wetting is shown. Reproduced from,[253] Copyright 2007, American Chemical Society.

Appart from an increased static contact angle, superhydrophibic materials should be capable of low water retention. The dynamic contact angle is usually determined by the tilt-drop method. By tilting a surface of the rough hydrophobic solid material with a deposited water droplet, one can determine an hysteresis factor H, indicative of the force necessary to remove the droplet from the surface, by

$$H_w = \theta_{A,w} - \theta_{R,w} \quad (12)$$

where θ_A is the advanced contact angle and θ_R the receding contact angle. θ_A and θ_R are determined at the sliding angle (or tilting angle) Φ at which the droplet flows or rolls away. For a Wenzel state, H and Φ are high ,while those for a Cassie-Baxter state are very low (< 10°). Superhydrophobic materials can then be defined as materials with a high contact angle (θ > 150°) as well as a low tilt angle.[254]

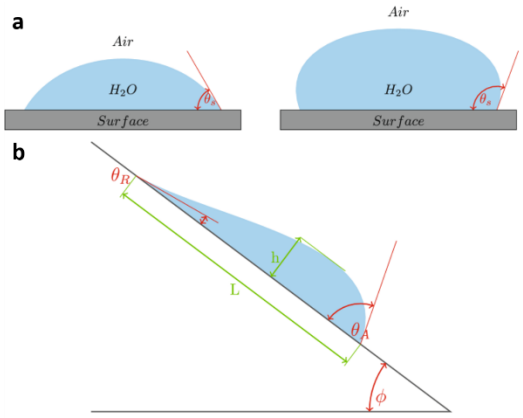

Figure 1.26. Representation of a) the static contact angle θ_s for a hydrophilic (left) and a hydrophobic (right) surface. And b) of the advanced contact angle θ_A and the receding contact angle θ_R upon tilting the surface with an angle Φ. Reproduced from,[255] Copyright 2021, Springer Nature.

Originally inspired by bio mimicking of lotus leaves, superhydrophobic materials can be obtained by the fabrication of materials with a high specific surface area.[256, 257] Their high water repellency provides supehydrophobic suface with self-cleaning,[258] low friction,[259] anti-corrosion,[260] anti-icing,[261] or anti-biofouling[261] properties.[262] Surfaces depicting a high specific surface area can be prepared by numerous ways including photolithgraphy,[263, 264] templating, plasma treatment and more.[265] Noticeably, porous materials and aerogels are good examples of materials with a high specific area.[38, 266-268]

In their work, Dong et. al.[39, 40] proposed a specific DLP ink formulation which contains a hydrophobic acrylate monomer (butyl acrylate, BuA, 30 wt%), a methacrylated crosslinker

(ethylene glycol dimethacrylate, EDMA, 20 wt%), a photoinitiator (Ig819, 2 wt% with respect to BuA+EDMA) and a porogen (1-decanol, 50 wt%). Upon photopolymerisation, a phase separation occurs with the porogen diffusing out of the polymeric phase, what engenders a biphasic system comparable to a porous material. Due to the rather fragile polymeric scaffold and the capillary forces applied to it by the solvent during a conventional drying, the retention of the porosity cannot be sustained this way. Therefore, specific cryo-drying procedure is used in which the polymeric matrix is frozen and solidified at low temperature, prior to solvent removal. With this procedure, the authors obtained a highly porous material which exhibited superhydrophocity, as was confirmed by contact angle tests. Moreover, as the superhydrophobicity arised from the porosity of the material, it was not only provided to the external surfaces, but to the entire bulk of the printed objects. Contact angle experiments for polymeric objects fabricated from photoresists including or excluding a porogen showed contact angles of 155° and 74°, respectively, evidencing the prominent importance of porosity for the superhydrophobicity of the 3D printed objects.

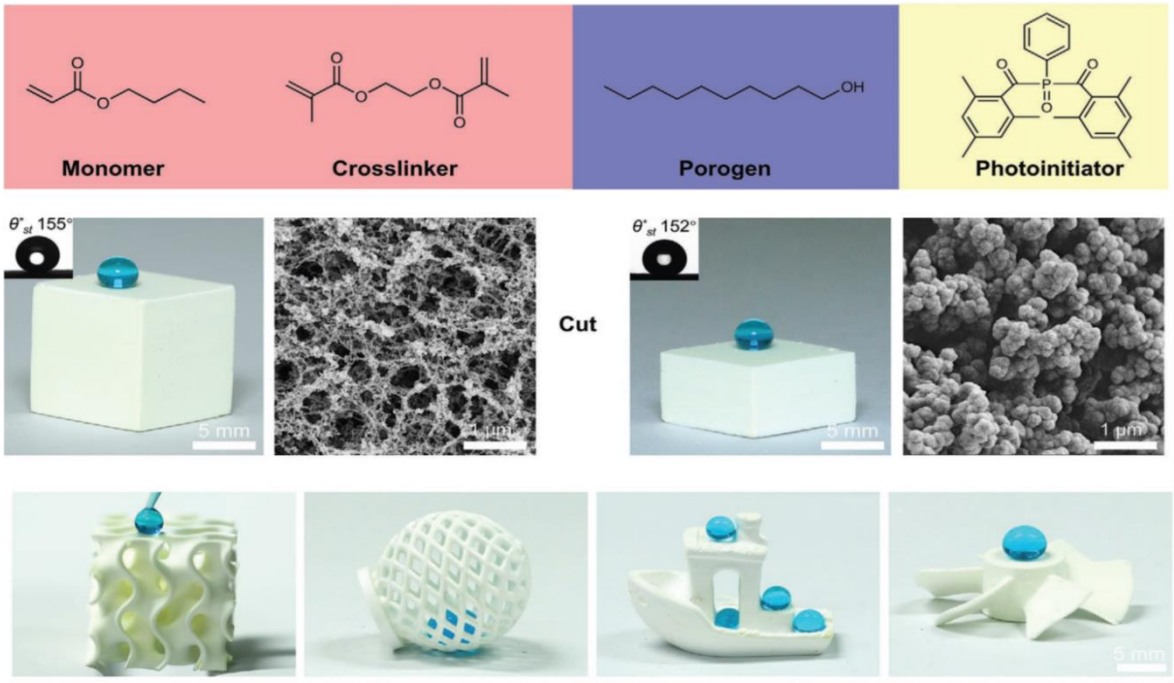

Figure 1.27. Composition of the ink propsed by Dong et. al. toward porous superhydrophilic polymeric object. Evidencing of the bulk porosity, hence superhydrophobicty for a DLP printed cube. Example of DLP 3D printed superhydrophobic objects with complex geometries. Reproduced from,[40] Copyright 2021, John Wiley & Sons.

Chapter 2 AIMS

In this dissertation, the use of two photon 3D laser printing as a versatile tool for the creation as well as the post-modification of porous materials is proposed. The main goal is to enlarge the span of functional porous materials which can be treated using the additive manufacturing technique, and hopefully serve specific purposes for future manufacturing challenges.

As already mentioned in the previous section, porous materials play an important role in different areas such as catalysis, filtration, separation, or molecular recognition. In the first part (chapter 3), I exploit the use of two-photon laser printing for the manufacturing of porous microstructures. Therefore, I made use of columnar hexagonal liquid crystals (Col_h LCs), which have unique structural advantages and functional abilities. To date, some works presented the use of Col_h polymeric materials based on self-assembled discotic mesogens, as selective adsorber or selective membranes for purification purposes. Nonetheless, and despite the established procedures for the making of such materials by photocrosslinking, the shaped-defined processing of Col_h LCs was not described until date. The main goal of this dissertation is to develop a new approach allowing for the creation of well-defined and highly ordered porous microstructures based on Col_h LCs, by employing two-photon laser printing.

The fabrication of multi-material objects is of tremendous importance to access complex functional devices. However, such fabrication remains highly challenging, and utilised strategies often remain material-specific. The second main goal of the current thesis (chapter 4) is the development of a versatile strategy for the functionalisation of porous materials with high resolution and in three dimensions, by combining the advantages of two-photon laser printing and discontinuous dewetting. In particular, the fabrication of superhydrobic porous structures, that can be post-functionalised with a hydrophilic monomer to exhibit patterned discontinuous water affinity, is selected as a promising approach.

Chapter 3 TWO-PHOTON LASER PRINTING OF HEXAGONAL COLUMNAR LIQUID CRYSTALLINE MATERIALS

In this chapter, I will focus on the design and fabrication of highly ordered nanoporous materials based on Col_h LCs. For this purpose, I synthesised a library of different mesogenic self-assemblies. These generally consisted on the H-bonded assemblage of three gallic acid derivatives around a central templating core. A determination of the LC behaviour of the discotic mesogens, by POM, as well as a precise characterisition of the Col_h arrangement, by WAXS, prior to the porosity generating step was critical. The nanoporosity being engendered by the removal of the centre cores of the assemblies via H-bond breakage, a precise determination of the Col_h arrangement directly influenced the dimension and arrangement of the nanopores of the final polymeric species, hence of their final performances. Thus I selected the most promising compounds, based on POM and WAXS results, for further investigation for two-photon laser printing. In addition to allowing the formation of a porous material, a design based on the H-bonding helps to circumvent a competitive light absorption from the core with respect to the photoinitiator. Typical extended polyaromatic cores or conjugated π-systems were rejected as the absorption of the laser energy by polyaromatic mesogens could lead to undesired side-reactions and would significantly complicate the microprinting of the LCs materials or make it impossible.

Finally, porous microstructures were prepared by the removal of the templating cores via H-bonds breakage and the selective adsorption of small dyes molecules by the porous microstructures was successfully demonstrated.

In the first part of this chapter, I will present our work on 3:1 H-bonded assemblies. The synthetic pathways and synthesis optimisation of the building blocks will be discussed.

Then I will present our work on the characterisation and optimisation of the formation of H-bonded assemblies with the desired 3:1 ratio of the peripheral acids and core as well as the corresponding investigation on the LC properties of the H-bonded assemblies. Once characterised, the LC mesophases will be printed by two-photon laser printing and the corresponding nanoporous polymeric materials tested for their chemical adsorptive capabilities using traceable dye molecules (**Figure 3.1**).

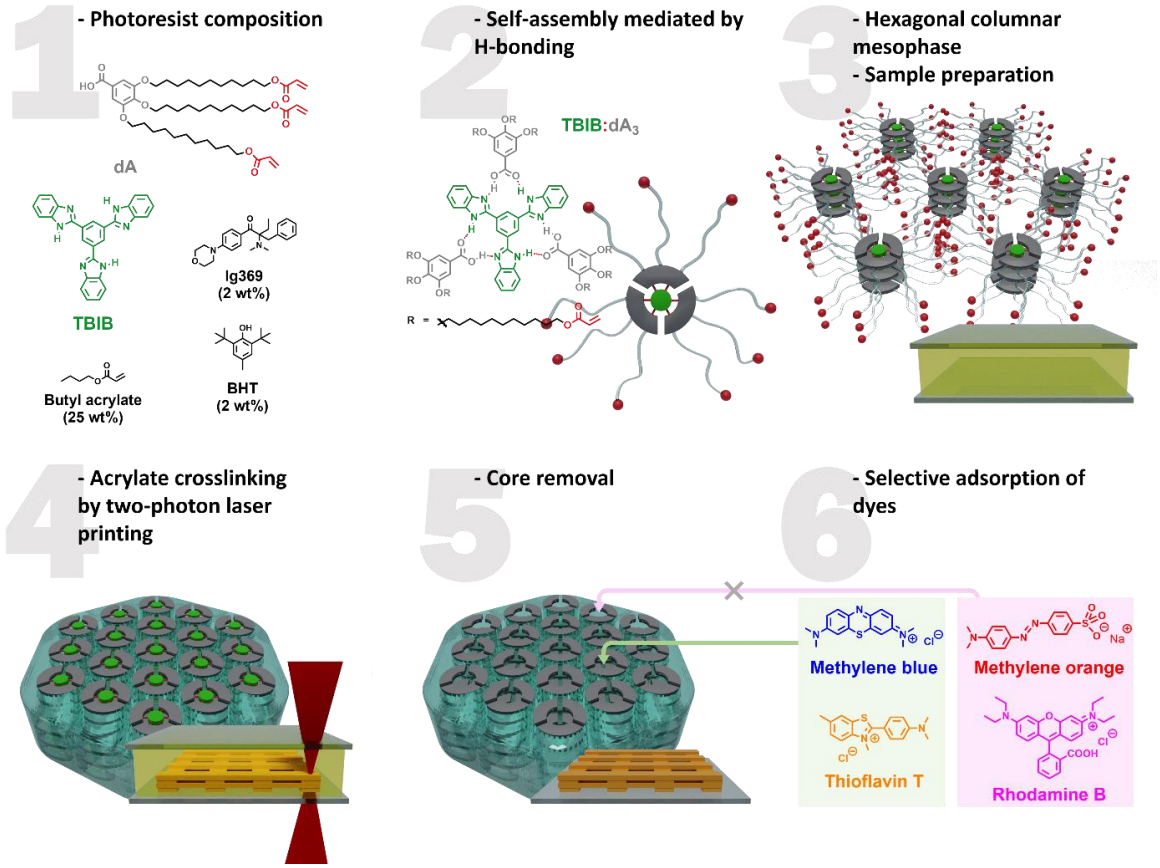

Figure 3.1. Overview of the project described in this chapter. **(1)** Chemical structures of the building blocks (**dA** and **TBIB**) and additives (Ig369, BHT and butyl acrylate) used in the system. **(2)** Chemical structure and schematic representation of the H-bonded assembly **TBIB:dA$_3$** **(3)** Formation of a hexagonal columnar mesophase. **(4)** Two-photon laser printing via photocrosslinking of the terminal acrylate groups. Upon crosslinking, the arrangement of the Col$_h$ mesophase is locked. **(5)** Removal of the core from the developed microstructures upon H-bonding breakage, with a retention of the Col$_h$ arrangement. **(6)** The effective size and polarisation of the pores allow for selective adsorption of chemical species.

Chemical synthesis and optimisation

In order to be able to study the material behaviour of the target structures, the synthesis of the building blocks, adapted from literature were optimised for yield, reproducibility and simplicity. It should be noted that all the syntheses detailed in the following were performed

under yellow light to avoid an undesired preliminary photopolymerisation of the light-sensitive species.

I investigated three different cores, based on 1,3,5-tris(1H-benzo[d]imidazol-2-yl)benzene (**TBIB**), tris(triazolyl)triazine (**T**) and melamine (**M**). **TBIB** was not functionalised, **T** and **M** were included with aliphatic chains for better solubility, to prevent crystallisation and favour molecular mobility. Those cores were chosen for their flatness, rigidity and their ability to form several H-bonds when in contact with carboxylic acid moieties. Two different peripheral acids based on gallic acid were synthesized, **dA** and **dBzA**, where **dBzA** contains additional benzyl spacers. The respective chemical structures of the building blocks are shown in **Figure 3.2**. The two cores were designed with undecyl aliphatic side chains to allow a LC behaviour of the molecules, to which terminal acrylate polymerisable groups were added. The introduction of a high number of polymerisable groups enables the locking of the LC arrangement by photocrosslinking without the aid of a secondary crosslinker. Moreover, a high number of polymerisable groups is essential for the fabrication of polymeric microstructures by two-photon laser printing.

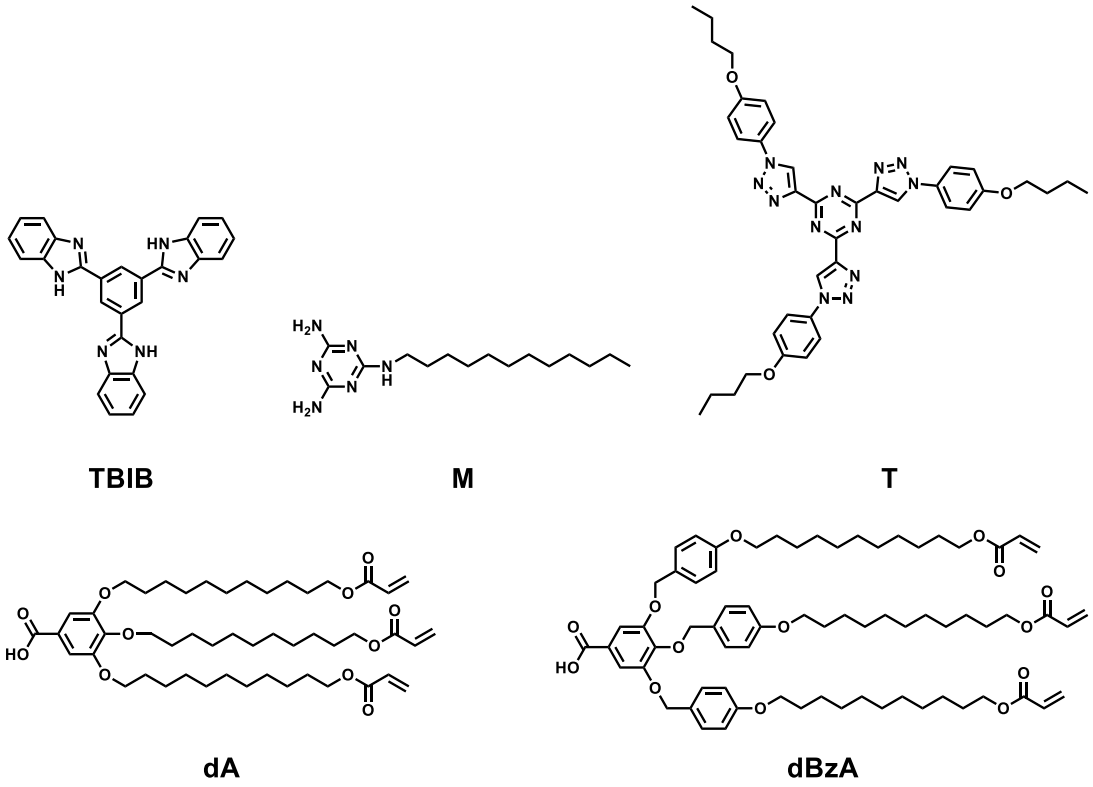

Figure 3.2. Chemical structures of the bulding blocks used in the scope of this project. The three templating cores **TBIB**, **T** and **M**, and the two pheripheral acids **dA** and **dBzA**.

Synthesis of peripheral acid dA

dA was afforded in a three-step synthesis with an overall 62 % yield. Ethylgallate was first substitute with three 1-oxyundecyl side chains using 11-bromoundecan-1-ol to afford ethyl 3,4,5-tris((11-hydroxyundecyl)oxy)benzoate (**1**). The ethyl protection of **1** was removed under basic conditions using NaOH, leading to 3,4,5-tris((11-hydroxyundecyl)oxy)benzoic acid (**2**). Finally, **2** was decorated with terminal acrylate groups by nucleophilic substitution with acryloyl chloride in basic conditions. The synthetic route is summarised in **Scheme 3.1** and the detailed synthetic procedure are available in chapter 6.

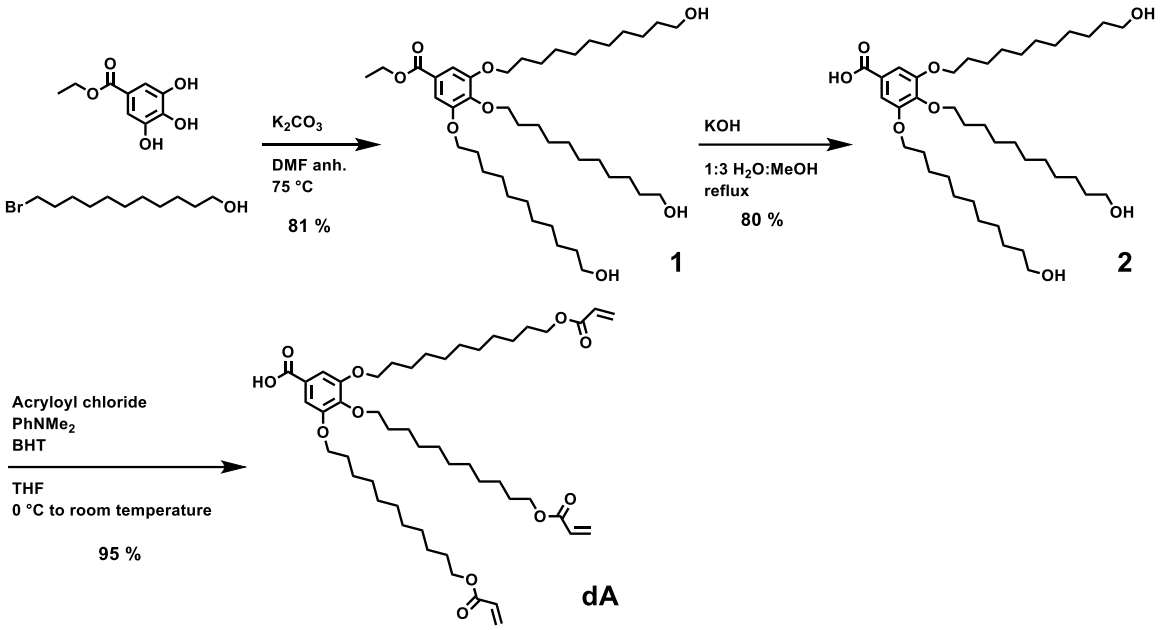

Scheme 3.1. Synthetic route for **dA**.

The addition of 11-bromoundecan-1-ol on ethylgallate was performed in anhydrous DMF and afforded **1** in good yields (81 %). To facilitate the synthetic step, it has been attempted to perform the substitution in anhydrous THF using methyl gallate in place of ethyl gallate.[269] Unfortunately, no conversion was observed for the latter. The catalytic effect of DMF was determined to be primordial for the addition reaction to be efficient. Despite its high boiling point, DMF can be completely removed under high vacuum and by co-evaporation with water. The crude **1** was used for further removal of the ethyl protective group of the carboxylic acid moiety. This synthetic step toward **2** worked with good (80 %) yields without the need of further optimisation.

The decoration of **2** with acrylate groups was carefully investigated. The synthesis of **dA** has been reported with excellent yields by performing the reaction in 1,4-dioxane at 60 °C for 1 h, using *N,N'*-dimethylaniline as a base.[248] Unfortunately, all my efforts in this direction resulted in a crosslinked material, which was attributed to thermal polymerisation. Procedures at room temperature, with an addition of acryloyl chloride at 0 °C, have therefore been favoured. In further optimisation, I focussed on the determination of a good solvent/base mixture. In particular, triethylamine/DCM and *N,N'*-dimethylaniline/THF[270] mixtures were attempted. In spite of triethylamine/DCM being very popular for the decoration of terminal alcohols with acrylate groups, using acryloyl chloride. I found that these conditions (30 % yield after purification) were significantly outperformed by the *N,N'*-dimethylaniline/THF mixture (82 % yield after purification). Moreover, the performance of the reaction using *N,N'*-dimethylaniline and THF had little sensitivity to ambient oxygen and moist. Considering this observation, the procedure can further be simplified eliminating the need to work under a N_2 atmosphere. The addition of acryloyl chloride at 0 °C was observed to be primordial for an efficient conversion. The addition being exothermal, the addition of acryloyl chloride at room temperature led to minor pre-polymerisation that can significantly alter the performances of the materials using the so-synthesised compounds.

The purification of the obtained acrylate-functionalised compound **dA** was initially performed by flash silica gel column chromatography. However, major loss of material was observed using this purification technique as the yield for the purification was solely in the range of 30 %. This was attributed to the strong interaction of the acrylate groups with the silica stationary phase. Even though it would be possible to minimise this effect by using other stationary phases such as basic alumina or triethylamine-deactivated silica, I determined that a simple recrystallisation from EtOH or EtOAc afforded satisfactorily pure products with remarkably reduced material loss (final yield of 95 %, at best). To avoid primary crosslinking and considering the efficiency of the purification method, I found that the use of a slight excess of the solvent when compared to theoretically perfect recrystallisation was preferable. This adaption allowed to reduce the heating needed to get the crude **dA** in solution, and favoured purity over higher yields. Using this procedure, I reproducibly obtained high purity **dA** in good yields. When stored, **dA** was shown to undergo pre-polymerisation over time, even when storred at 4 °C. To circumvent this issue, and regarding the ease of the optimised procedure, I preferred the synthesis of small batches

that were directly used for further application. Being more inert and easily stored at room temperature, **2** can be prepared in bigger scales and used progressively.

Synthesis of peripheral acid dBzA

Another targeted acrylated compound consisted in a structure similar to that of **dA**, featuring additional aromatic moieties without leading to an extending of the aromatic core. This adaptation was meant to favour the columnar stacking of the resulting mesogens by increasing the number of intermolecular interactions. Therefore, benzyl spacers were introduced between the central gallic acid moiety and the aliphatic spacers. The resulting peripheral acid building block will be denoted as "**dBzA**".

dBzA was synthesised through a seven-step synthesis with an overall yield of 24 % (**Scheme 3.2**). 10-Undecen-1-ol was converted to 1-bromo-10-undecene (**3**) by Appel reaction. Methyl 4-hydroxybenzoate was substituted with **3** resulting in methyl 4-(10-undecenyloxy)benzoate (**4**). **4** was then reduced to 10- undecenyl-1-oxybenzyl alcohol (**4**) using lithium aluminium hydride, and then to 1-(chloromethyl)-4-(undec-10-en-1-yloxy)benzene (**5**) using thionyl chloride. **5** was used for the three-fold substitution of ethyl gallate toward ethyl 3,4,5-tris((4-(undec-10-en-1-yloxy)benzyl)oxy)benzoate (**6**). The double bonds of **6** were then oxidised to a terminal alcohol using 9-BBN. This step also allowed the removal of the ethyl protection of the benzoic acid, affording 3,4,5-tris((4-((11-hydroxyundecyl)oxy)benzyl)oxy)benzoic acid (**7**). **7** was finally decorated with acrylate groups to obtain **dBzA**.

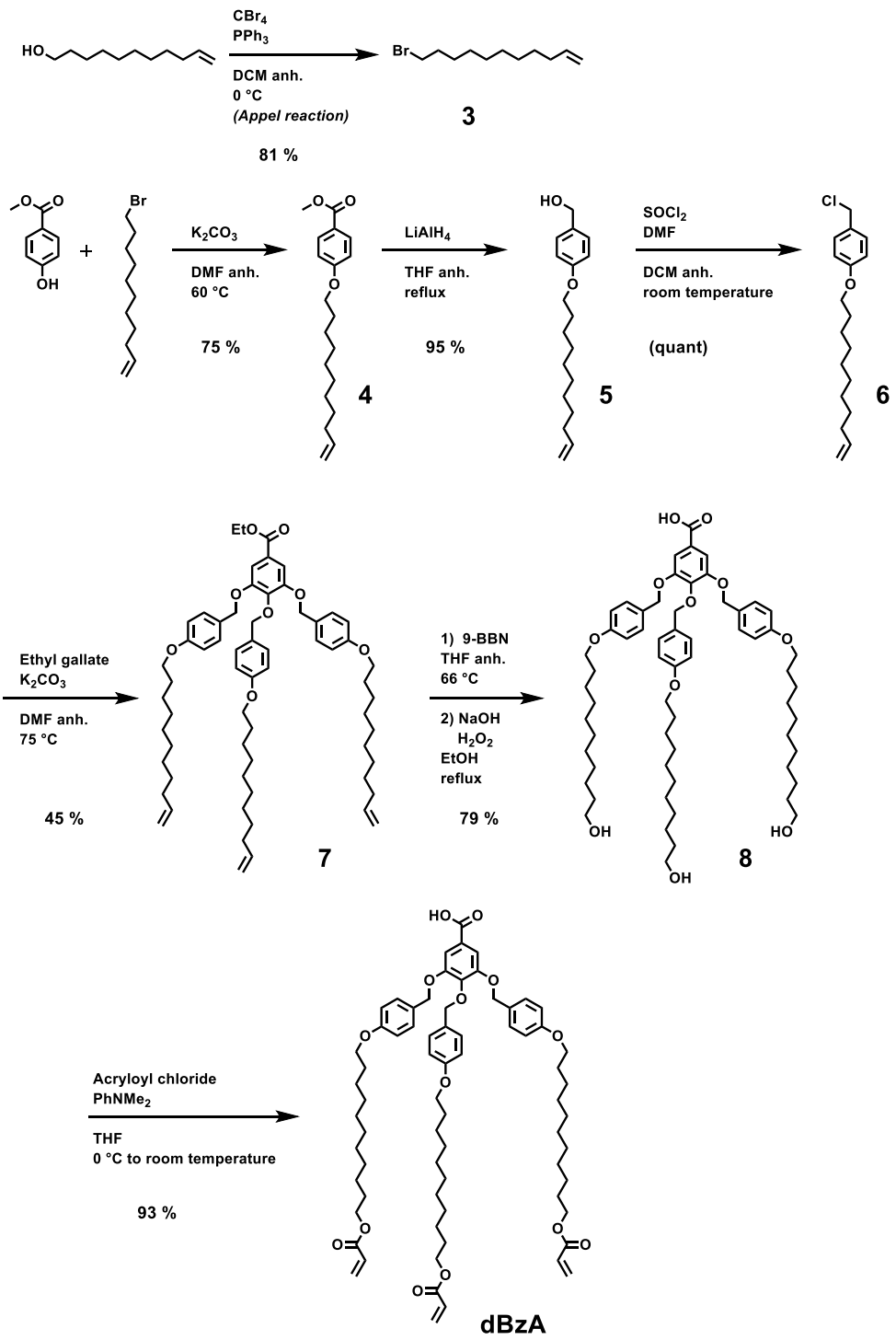

Scheme 3.2. Synthetic route for **dBzA**.

The formation of **3** from 10-undecene-1-ol by Appel reaction was performed using reported procedures and did not require further optimisation. A purification by flash column chromatography was necessary and afforded **3** in quantitative yields. In spite of its excellent conversion, the Appel reaction is not very mass-efficient and create a stoichiometric amount of organic phosphine oxides.

The addition of **3** on methyl 4-hydroxybenzoate toward **4** was attempted in various solvents. Noticeably, reaction in acetone or acetonitrile did not allow yields greater than 41 % after purification. Based on the previous synthesis of **1**, the reaction was performed in DMF, improving the yield to 75 %.

The reported procedures of the reduction of **3** to **4** were performed overnight. With such a reaction time, yields not greater than 14 % were obtained. An excessive reaction time resulted in product degradation, the synthetic step was easily adjusted by greatly reducing the reaction time. Following the reaction conversion over time by ^{1}H-NMR, I evidenced that a quasi-complete conversion was achieved after 1 h, and that degradation was indeed beeing observable after 3 h. Based on this result, a reaction time of 1.5 h was chosen, which afforded **4** in 95 % yield.

The chlorination of **5** to form **6** was performed according to reported procedures. Suspecting **6** to be fairly unstable and considering that all the side-products of the reaction are volatile, I did not attempt any purification. The crude product was used for further synthesis without purification. In order to obtain a brominated compound in place of the chlorinated **6**, it was also attempted to use the Appel reaction presented before. However, I could not isolate the pure corresponding compound, most likely due to the instability of the brominated compound and its possible decomposition on the stationary phase.

As mentioned, the three-fold addition of **6** on ethyl gallate was the most challenging step of the synthesis of **dBzA**. The main parameter for optimisation was the stoichiometry of the addition of **6**, in that regard, a significant excess of **6** had to be used. By TLC, one can observe that an input of 3.3 equivalents of **6** results in significant one-fold and two-fold addition. The use of at least 3.5 equivalents of **6** favoured the three-fold addition of **6** on ethyl gallate, thus increasing the overall yield and facilitating the isolation of **7**. To improve the efficiency of the reaction, 1.5 equivalents of potassium iodide was used as iodide source for in-situ halogen exchange. When both increasing the stoichiometric loading of **6** and using KI (1.5 eq.), the yield toward **7** was significantly increased from 7 % yield to 45 % yield. Even though a larger excess of **6** can be seen as contradiction of the previous efforts to obtain the latter, it was not found to be worth trying to save starting material during this step. Regarding the aim to study the materials formed from **dBzA**, I accepted the 45 % yield obtained (that is in the range of the yields reported in literature[271]) and did not optimise this step further. Nevertheless, in this synthetic step lies the most potential for future

improvement of the overall yield of **dBzA**. An alternative could lie in the a Finkelstein reaction of **6** towards the corresponding bromide or iodide, prior to its addition on ethylgallate.

An oxidation preceded by a hydroboration was chosen to force the formation of primary alcohols. As widely known, thanks to the anti-Markovnikov addition of boron on alkenes, this procedure greatly favours an enantiopure product. The subsequent oxidation allows the cleavage of both the boron-oxygen bonds and the ethyl ester, yielding terminal alcohols and a carboxylic acid, respectively. The simultaneous oxidation of the terminal alkenes into primary alcohols and deprotection of the carboxylic acid group was performed according to a previously reported procedure.[271] The proposed procedure worked well, and the single adaption of the procedure consisted in an increase of the borane equivalents from 4.5 eq to 6 eq.

The procedure for the decoration of **8** with acrylate groups forming **dBzA** was performed in accordance to the optimisation described earlier for the synthesis of **dA**. For the synthesis of **dBzA**, a procedure in THF, and using *N,N'*-dimethylaniline as a base was again shown to perform in a satisfactory manner.

As mentioned before, the chosen system relies on the self-assembly of the peripheral acids around templating centre cores. We designed two peripheral acids containing aromatic moieties that can extend the effective rigid core of the corresponding discotic mesogens after self-assembly, hence take part in the aggregation of the mesogens while not resulting in a species containing highly absorptive, extended π-systems. I presented **dA** that contained a single phenyl unit as aromatic part, and **dBzA** that includes three additional benzyl spacers near the aromatic core. I will now focus on the inner templating cores of the targetted assemblies. The templating cores were chose to have a rigid flat structure, including aromatic moieties to support the aimed π-π stacking of the assemblies. As well as to have conveniently located hydrogen donating and accepting spots to support the H-bonding driven self-assembly of the targeted mesogens. In that regard, I chose two structures built around a rigid triazine skeleton and one that relies on a tri(imidazolyl)benzene.

Synthesis of core TBIB

TBIB was synthesised by condensation reaction of trismesic acid with *o*-diaminobenzene in hot polyphosphoric acid. The purification of **TBIB** appeared to be challenging in the sense that specific instrumentation was required. Using conventional lab equipment, I could not satisfactorily reproduce the purification by sublimation at 400 °C proposed in literature.[248, 272] However, the use of high purity building blocks is of tremendous importance for the well behaving of the H-bonded assemblies as LC mesogens. Thankfully, the group of Prof. Chinedum Osuji (the University of Pennsylvania, Philadelphia, PA, USA), agreed to provide the core, purified using their instrumentation.

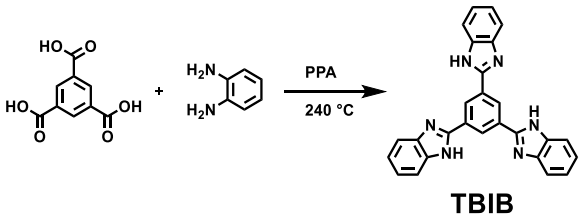

TBIB

Scheme 3.3. Snythetic route for **TBIB**.

Synthesis of core T

The core **T** was prepared in three main steps with an overall yield of 18 % (**Scheme 3.4**). The synthesis is based on the combination of an azide, 1-azido-4-butoxybenzene (**9**), and a tris-alkyne, 2,4,6-tris((trimethylsilyl)ethynyl)-1,3,5-triazine (**10**), by Click chemistry. **9** was prepared by diazotation of 4-butoxyaniline followed by reaction with sodium azide. **10** was prepared from trimethylsilylacetylene and trichlorotriazine. Trimethylsilylacetylene was first converted to ((trimethylsilyl)ethynyl)zinc(II) chloride which enables its cross-coupling on trichlorotriazine using $Pd(Ph_3)_4$ as catalyst. A second approach based on the direct nucleophilic addition of (trimethylsilyl)ethynyl lithium on trichlorotriazine did not afford **9.** The copper-catalysed alkyne-azide cycloaddition[273] ("Click reaction" as initially proposed by Sharpless and coworkers[274]) of **9** and **10** was performed according to literature and afforded **T** in 39 % yield. No further optimisation was performed.

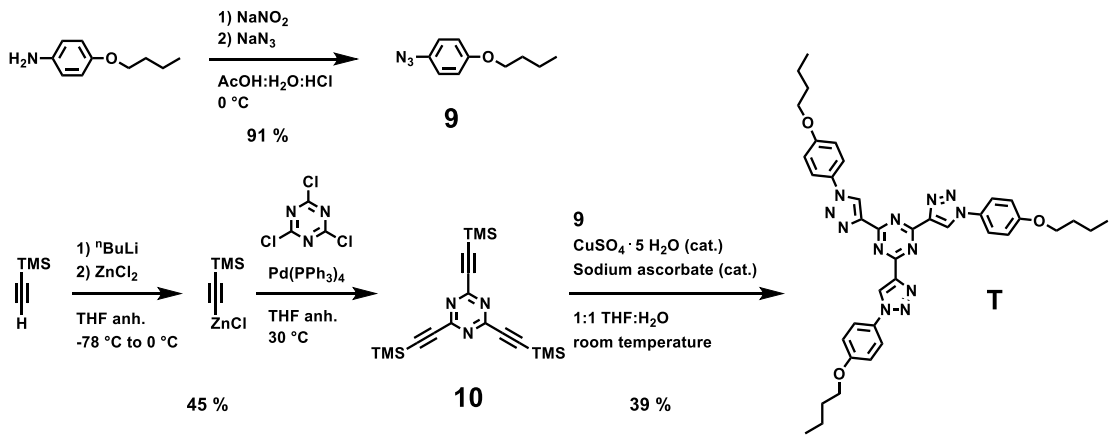

Scheme 3.4. Snythetical route for **T**.

Synthesis of core M

Core M was synthesised by the addition of dodecylamine on 2-Chloro-4,6-diamino-1,3,5-triazine. The reaction was performed in 1,4-dioxane using sodium hydrogenocarbonate as base, according to a literature procedure.[236] The reaction performed well and **M** was afforded in good yield (86 %) without further optimisation.

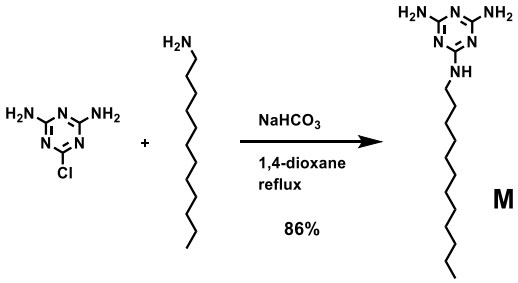

Scheme 3.5. Synthetic route for **M**.

Preparation of the H-bonded complexes

In this dissertation, I will note $\mathbf{X_x{:}Y_y}$ the assembly of y peripheral acids **Y** around x inner cores **X**. Even though most of this chapter will focus on H-bonded assemblies, this notation will similarly be used to identify a covalent or ionic interaction when presenting other designs that were also investigated in the scope of this project.

Once the separated building blocks had been successfully synthesised and characterised, the H-bonded assemblies were formed by mixing the corresponding core and acid with a 1:3.1 ratio in a $CHCl_3$:MeOH (1:0.07 v/v) and DCM for **TBIB**-assemblies and **M**- and **T**-assemblies, respectively. The assemblies consist in an inner template core which is surrounded by three peripheral acrylated acids. The entire assembly is supported by the

formation of six hydrogen bonds. In this thesis, I will be considering the following H-bonded assemblies: **TBIB:dA$_3$**, **M:dA$_3$**, **T:dA$_3$**, **TBIB:dBzA$_3$**, **M:dBzA$_3$** and **T:dBzA$_3$**. The chemical structures of the assemblies are shown in **Figure 3.3**.

For the preparation of the H-bonded discotic mesogens, the use of building blocks of high purity is essential to sustain the behaviour of the engendered complexes and materials. Hence, I made sure to only use chemicals of high purity and filter any intermediate solutions during the preparation of the assemblies. A slight excess of the peripheral acid was used to favour the formation of 3:1 assemblies and therefore improve the final LC properties of the materials. **TBIB** having a low solubility in $CHCl_3$, MeOH was used to bring the core in solution while maintaining the concentration of the solution as high as possible. Also, the least amount of MeOH was used to prevent the negative effect of the protic solvent on the formation of the structural H-bonds. The anhydrous solutions were left in the dark overnight to allow for the formation of the assemblies and prevent any light-caused preliminary crosslinking. The solutions of the assemblies were then drop-casted onto a clean microscope slide under a flux of N_2 and dried under high vacuum for 3 days. A detailed procedure is described in chapter 6. Maintaining anhydrous conditions greatly helps the gathering of good-quality Col_h LC materials, as moisture could alter the formation of the H-bonding framework. A preliminary procedure for the formation of the H-bonded assemblies by slow evaporation under vigorous stirring was attempted for the formation **M**- and **T**-assemblies, for which a clear and concentrated solution in DCM can be obtained. However, better results were obtained when using the procedure under anhydrous conditions motivated my choice to focus on this method. Drying under high vacuum for more than 3 days resulted in significant crosslinking of the LC material. This can be related to the lack of oxygen, which influence on the quenching of free-radical polymerisation is also manifested in the presence of a radical scavenger.[275]

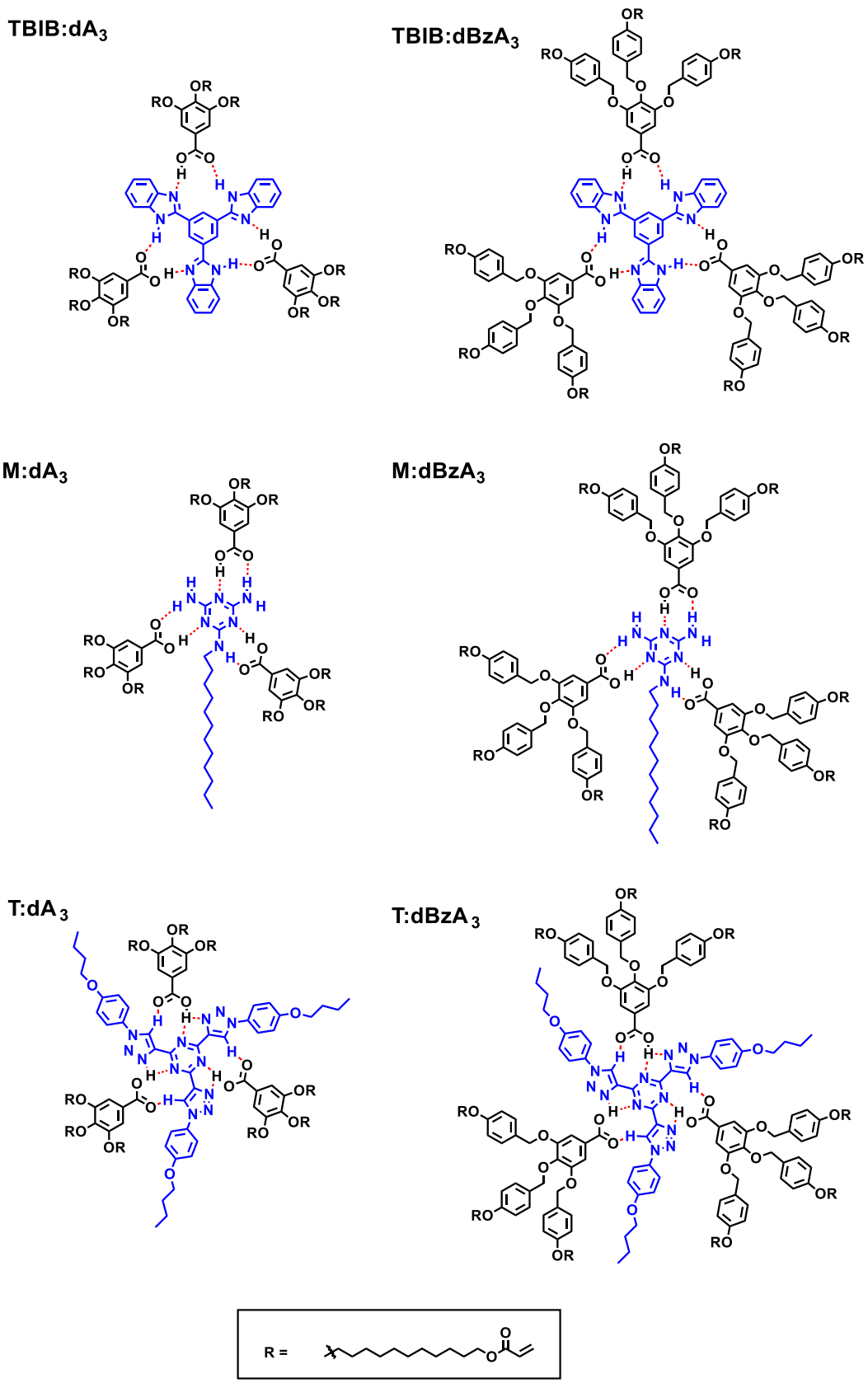

Figure 3.3. Chemical structures of **TBIB:dA$_3$**, **M:dA$_3$**, **T:dA$_3$**, **TBIB:dBzA$_3$**, **M:dBzA$_3$** and **T:dBzA$_3$**. The peripheral acids are shown in black, the templating cores in blue and the H-bonds with red dashed bonds.

Characterisation of H-bonded assemblies

The formation of the assemblies can be followed and evidenced by NMR and FTIR spectroscopy techniques. By ^{1}H-NMR, a shifting of the signals of the dendron's protons in close proximity to the H-bonded site was observed. For **TBIB:dA$_3$** only the spectra of **dA** and **TBIB:dA$_3$** could have been compared due to the poor solubility of **TBIB** in $CDCl_3$. For **M**- and **T**-assemblies, the shift of the signals from the protons of the cores are the main indicator of the intermolecular interactions. Although ^{1}H-NMR supports the effective formation of assemblies, the change in chemical shift, generally in the order of ±0.1 ppm, can be subjected to discussion in the absence of a calibration additive such as tetramethylsilane.

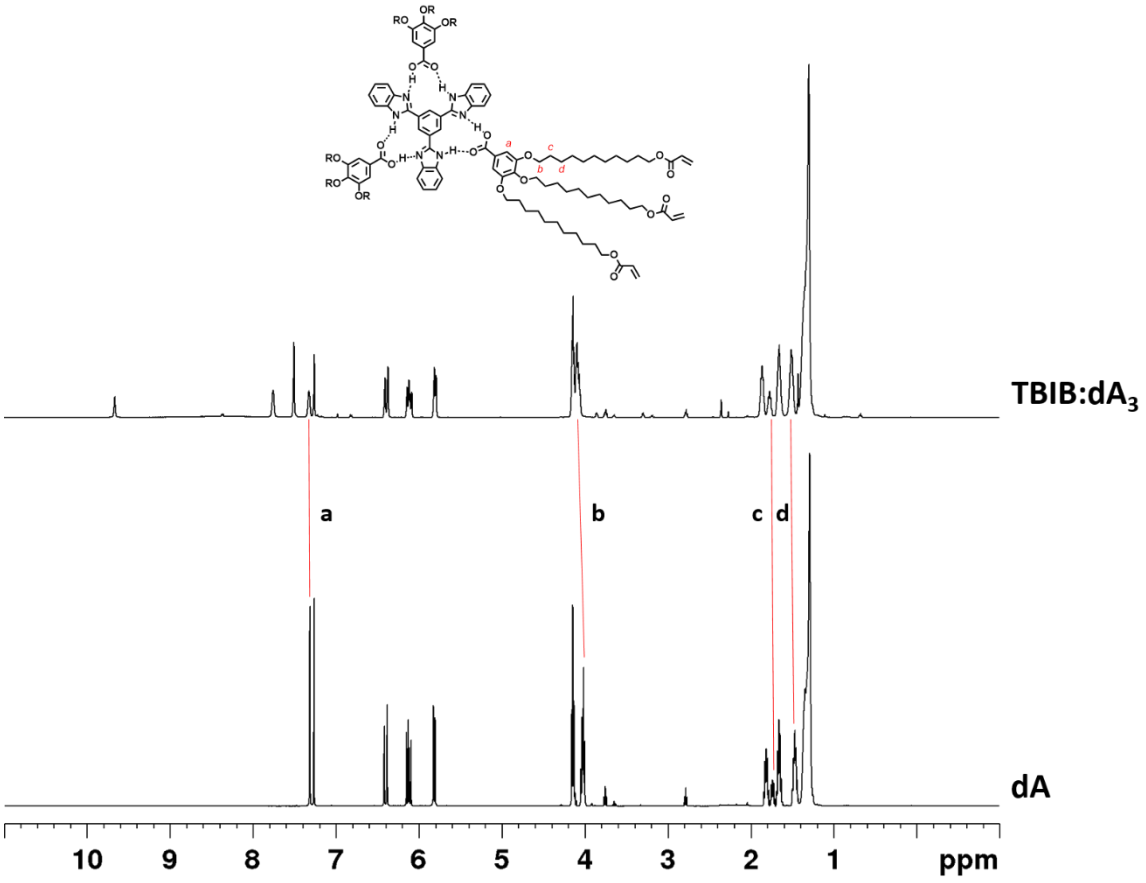

Figure 3.4. ^{1}H-NMR of **dA** (bottom) and **TBIB:dA$_3$** (top). Upon self-assembly, the peaks from the protons in close proximity to the H-bonds are shifted. The shifts are here highlighted by red lines.

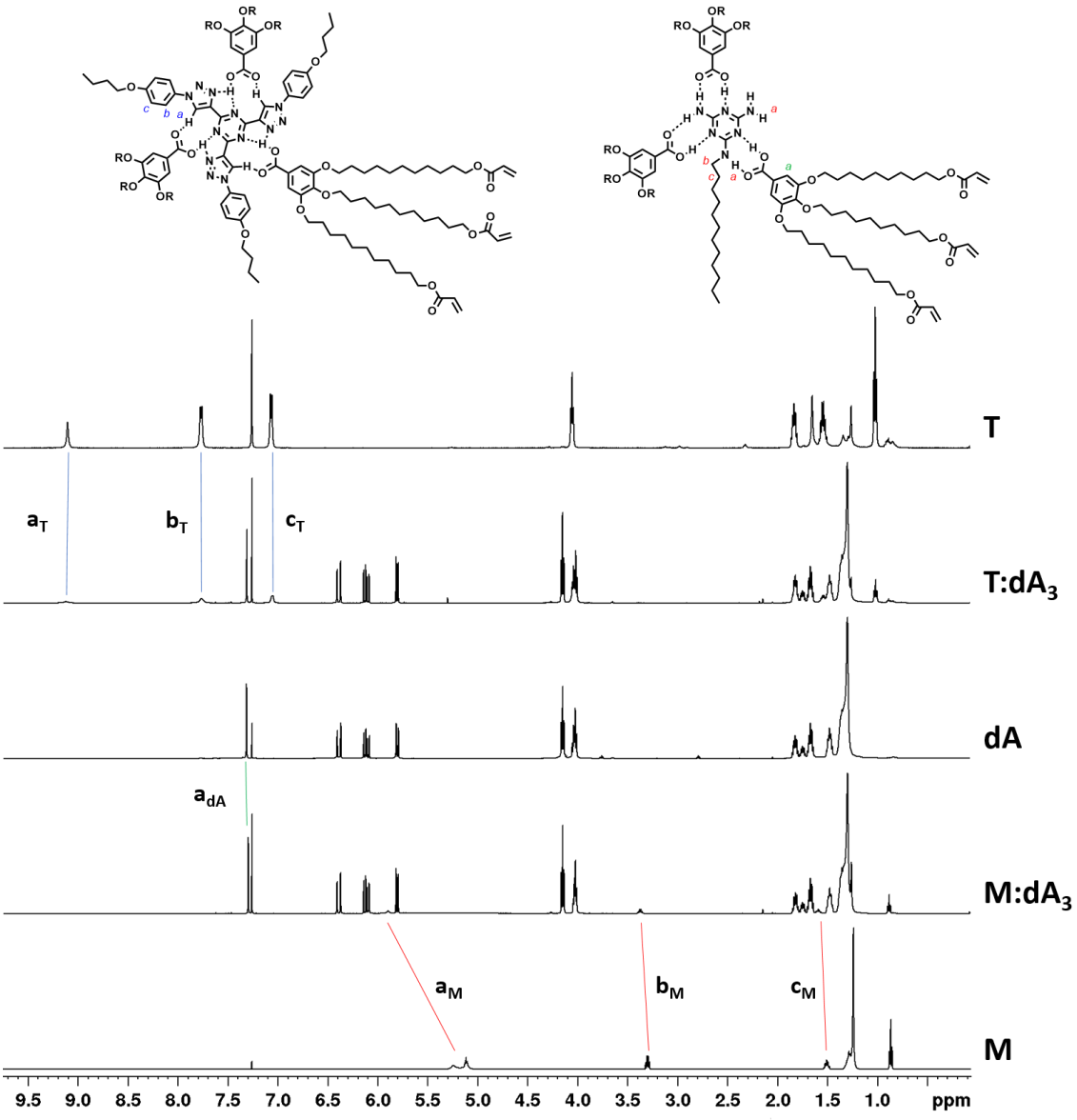

Figure 3.5. ^{1}H-NMR of **dA**, **M** and **T** as well as the corresponding H-bonded assemblies, **M:dA$_3$** and **T:dA$_3$**. Upon self-assembly, the peaks from the protons in close proximity to the H-bonds are shifted. The shifts are here highlighted by red lines.

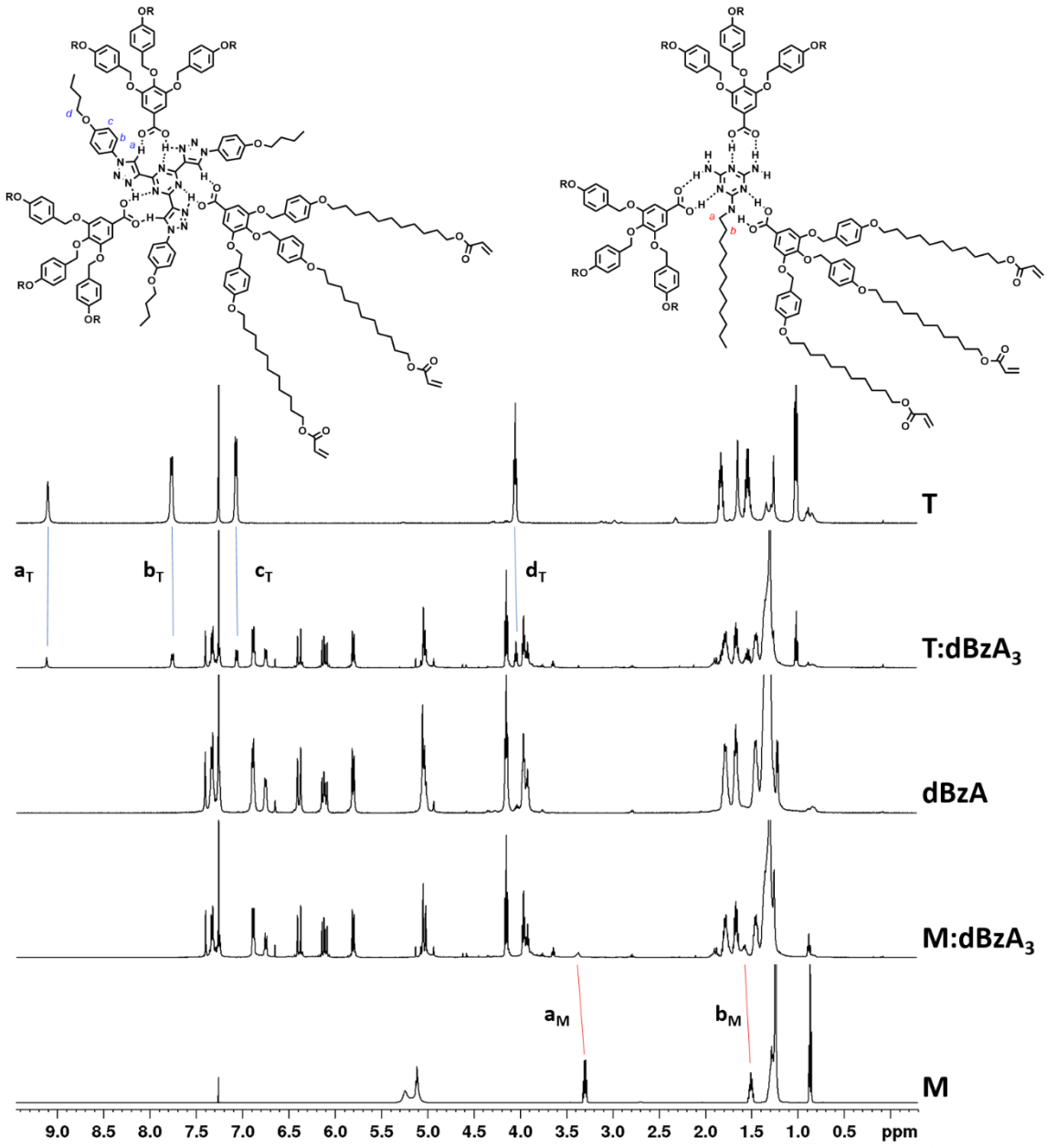

Figure 3.6. ^{1}H-NMR of **dBzA**, **M** and **T** as well as the corresponding H-bonded assemblies, **M:dBzA$_3$** and **T:dBzA$_3$**. Upon self-assembly, the peaks from the protons in close proximity to the H-bonds are shifted. The shifts are here highlighted by red lines.

In addition, I attempted to detect the formation of the H-bonded assembly of **T:dA$_3$**, **M:dBzA$_3$** and **T:dBzA$_3$** by diffusion ordered spectroscopy (DOSY)[276] using solutions of the assemblies in $CDCl_3$. DOSY is a pseudo 2D NMR technique that allows the differentiation of chemical compounds based on their diffusion (which is related to their size). Although DOSY is usually most suited to large molecules which shape can be approximated as a sphere (e.g. proteins), one can obtain informative results for smaller

molecules as well. For spherical species, the Stokes-Einstein equation can be used to relate the measured diffusion coefficient to an actual size of the molecule by

$$D = \frac{k_B T}{6\pi\eta r} \tag{13}$$

where D is the diffusion coefficient, k_B the Boltzmann constant, T the temperature, η the viscosity of the medium and r the radius of the spherical molecule.

In the context of this project, I aimed to detect the change in size induced by the formation of H-bonded complexes. Indeed, although the diffusion coefficient measured can be directly used to approximate the size of the assemblies, the variation of the diffusion coefficients for the assemblies compared to the pure compounds would be indicative of the formation of bigger species. Moreover, upon the formation of assemblies, the proton signals of both the core and peripheral acids are expected to have an associated diffusion coefficient that is identical for all signals, which indicates that both species diffuse at the same speed, so most likely together. The results did not a have a precision that could undoubtedly support the formation of assemblies. I observed a difference in the diffusion coefficients for the assemblies with respect to that of **dA**, **dBzA**, **M** or **T** (associated diffusion coefficient are given in **Table 3.1**). However, the diffusion coefficients for all proton signals within the assemblies could not be assigned to a single diffusion coefficient. Moreover, the diffusion coefficient of the assemblies were in same case greater than the diffusion coefficient of the corresponding peripheral acids. These results can be attributed to a decomposition of the assemblies when dissolved in a moist solvent at low concentration. Overall, DOSY did not appear to be adapted for the analysis of the formation of self-assemblies in this case. DOSY spectra are shown in chapter 6.

Table 3.1. Diffusion coefficients of the H-bonded assemblies, **dA**, **dBzA**, **M** and **T**.

Compound	Diffusion coefficient [$m^2\ s^{-1}$]
Assemblies	$3.75 \cdot 10^{-10}$
dA	$3.50 \cdot 10^{-10}$
dBzA	$3.00 \cdot 10^{-10}$
M	$7.00 \cdot 10^{-10}$
T	$4.25 \cdot 10^{-10}$

Following the H-bonding process was more informative when monitored by FTIR. FTIR is a common way to follow the formation of H-bonds.[277] Indeed, upon the formation of hydrogen bonds, the chemical environment in its surrounding can be significantly altered. The strength of H-bonds can be approximated to 4–120 kJ mol^{-1}, which is a considerably large range. Effectively, the strength of hydrogen bonds is strongly affected by the acidity of the proton donor as well as the basicity of the acceptor and can have various forms. While weak H-bonds are mostly of electrostatic nature, stronger H-bonds can induce a sharing of the hydrogen atom in-between the donor and the acceptor sites.[277] Although more noticeable for stronger interaction, the variation in bond strength and effective atomic weight can be detected by FTIR.

By FTIR, the formation of **TBIB:dA$_3$** induced a shift of the C=O stretch bands (1679 cm^{-1} to 1673 cm^{-1}; 1272 cm^{-1} to 1265 cm^{-1}) and of the O–H bend band (1333 cm^{-1} to 1325 cm^{-1}) from the benzoic acid moiety of **dA**. The C=O stretch band at 1729 cm^{-1} corresponds to the acrylate moiety and was unchanged in the process. An ionic-like N^+–H band at 3254 cm^{-1} corresponding to the H-bonding of the **TBIB** supported the assembly of **TBIB:dA$_3$** further (**Figure 3.7**).[201]

Similar studies were carried out for the other assemblies. The FTIR analysis of the formation of **TBIB:dBzA$_3$** (**Figure 3.8**), **M**-assemblies (**Figure 3.9** and **Figure 3.10**) and **T**-assemblies (**Figure 3.11** and **Figure 3.12**) are shown thereafter. In these results, the main vibration bands described before can again be used to support the formation of the 3:1 assemblies. The main bands are noticeably the C=O stretch band at about 1680 cm^{-1} as well as the O–H bend band at around 1330 cm^{-1}.

The formation of **TBIB:dBzA$_3$** is evidenced by the appearance of an ionic-like N^+–H band at 3244 cm^{-1}, similar to what was observed for **TBIB:dA$_3$**. Also, a clear shift of the C=O stretch band from 1683 cm^{-1} to 1677 cm^{-1} and of the O–H bend band from 1331 cm^{-1} to 1326 cm^{-1} further supports the effective self-assembly of the building blocks.

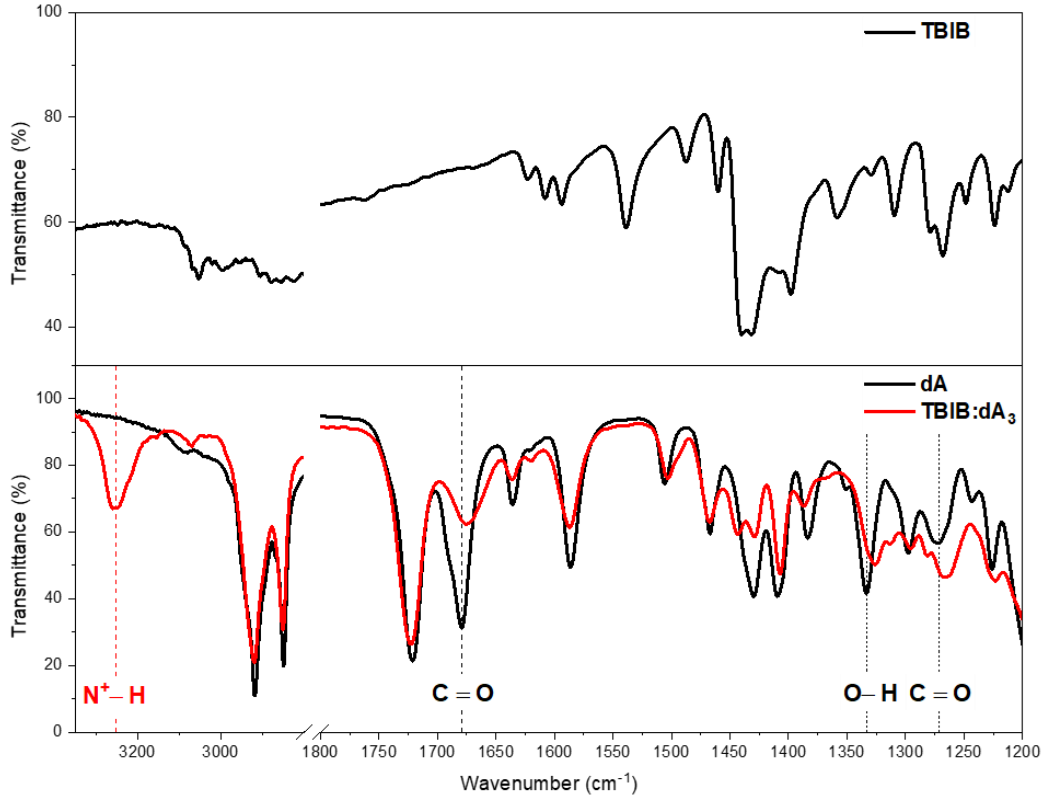

Figure 3.7. FTIR spectra of the centre core **TBIB**, the peripheral acid **dA** and of H-bonded assembly **TBIB:dA$_3$**.

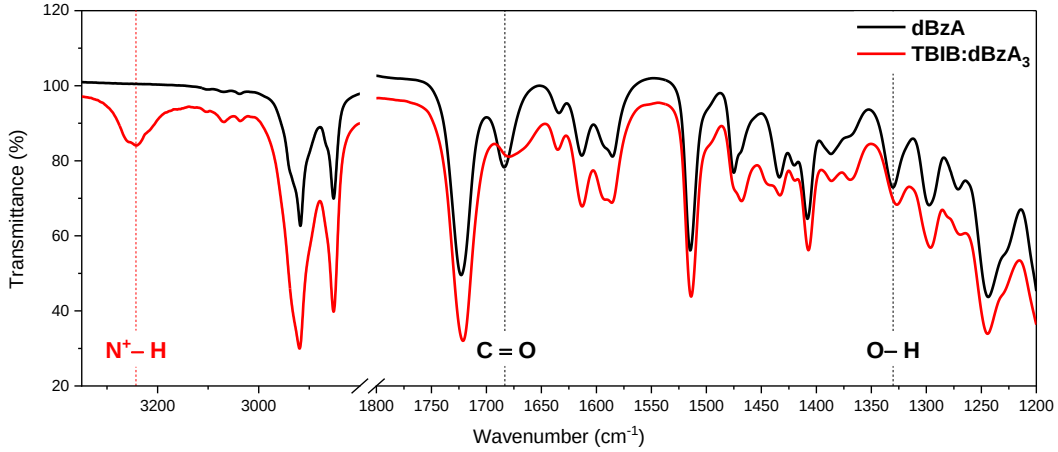

Figure 3.8. FTIR spectra of peripheral acid **dBzA** and of H-bonded assembly **TBIB:dBzA$_3$**.

In the FTIR study for the formation of **M:dA$_3$**, the shifts of the characteristic bands are less pronounced than the observation for **TBIB:dA$_3$**. The C=O stretch bands were shifted from 1679 cm^{-1} to 1682 cm^{-1} and from 1272 cm^{-1} to 1269 cm^{-1}, whilst the bending band of the O–H bond was shifted from 1333 cm^{-1} to 1332 cm^{-1}. Although these results indicate the formation of new interactions, it can be argued that they are not sufficiently conclusive. The FTIR analysis of the formation of **M:dBzA$_3$** were more conclusive than the previous for **M:dA$_3$**. The C=O stretch band was shifted from 1683 cm^{-1} to 1677 cm^{-1}. In spite a lowered intensity cannot be fully indicative of the formation of a H-bond, the fact that this vibration band almost disappeared can be highlighted. The O–H bend band was shifted from 1331 cm^{-1} to 1327 cm^{-1}. In the case of **M:dBzA$_3$**, the results supported the formation of a H-bonded assembly.

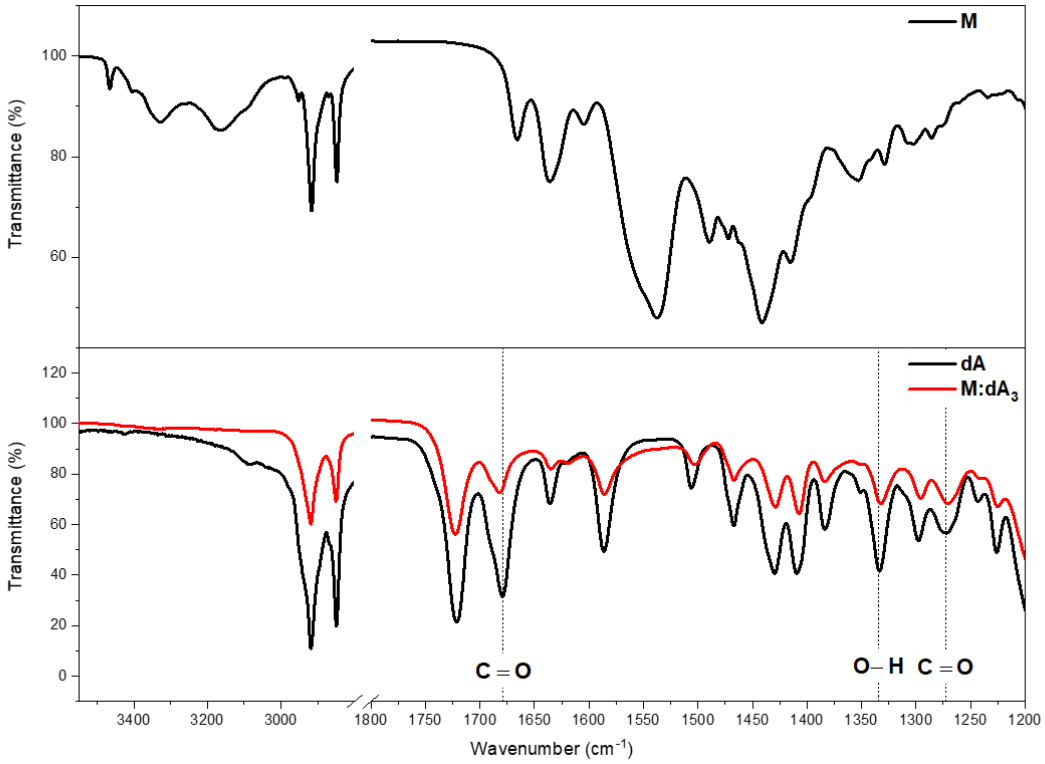

Figure 3.9. FTIR analysis of the formation of **M:dA$_3$**.

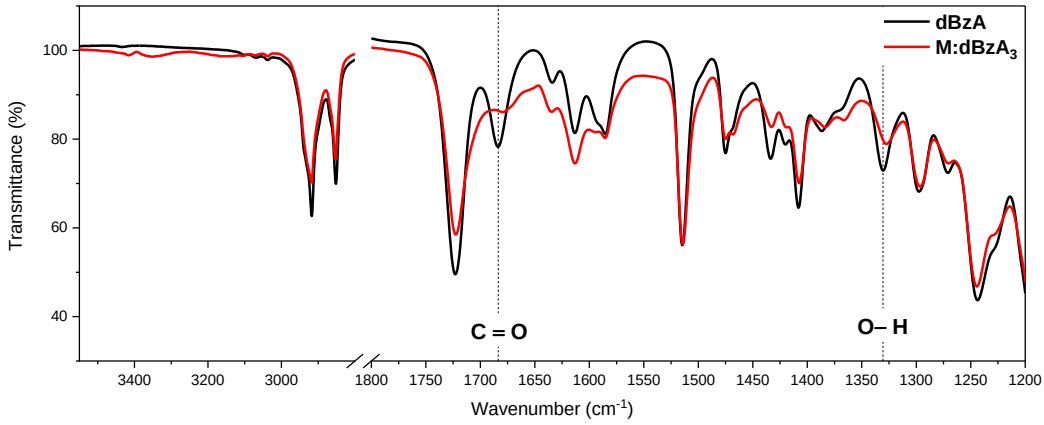

Figure 3.10. FTIR analysis of the formation of **M:dBzA$_3$**.

The same analysis of **T:dA$_3$** and **T:dBzA$_3$** (**Figure 3.11** and **Figure 3.12**) led to conclusions identical to those proposed for **M:dA$_3$** and **M:dBzA$_3$**. Thus, the effective assembly of **T:dA$_3$** is indicated by the FTIR study, but can be subjected to discussion. On the hand, the effective assembly of **T:dBzA$_3$** was evidenced with certainty. An overview of the main shifts of vibration bands observed is proposed in **Table 3.2**.

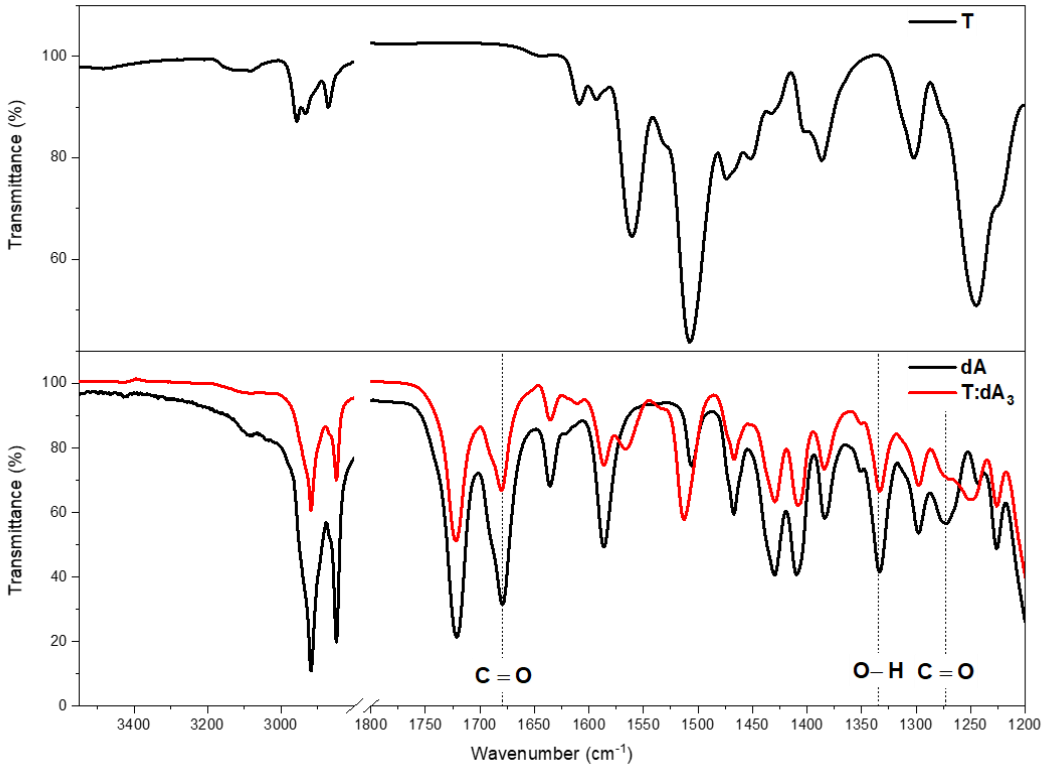

Figure 3.11. FTIR analysis of the formation of **T:dA$_3$**.

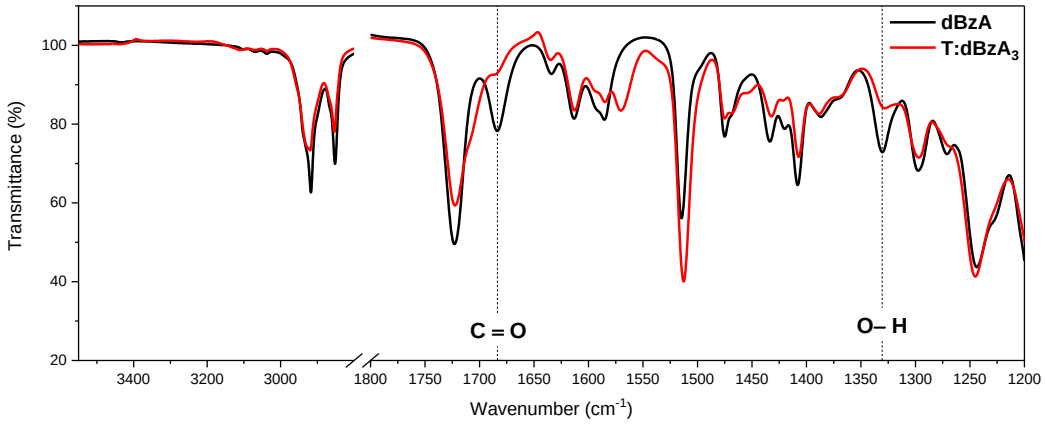

Figure 3.12. FTIR analysis of the formation of **T:dBzA$_3$**.

Table 3.2. Assignement and wavenumber value of the main IR vibration bands for the peripheral acids **dA** and **dBzA** as well as for their corresponding **TBIB**-, **M**- and **T**-assemblies.

Vibration band	C=O stretch	O–H bend	C=O stretch	N^+–H stretch
dA	1679	1333	1272	–
dBzA	1683	1331	–	–
TBIB:dA$_3$	1673	1325	1265	3254
TBIB:dBzA$_3$	1677	1326	–	3244
M:dA$_3$	1682	1332	1269	–
M:dBzA$_3$	1677	1327	–	–
T:dA$_3$	1681	1333	1272	–
T:dBzA$_3$	1684	1327	–	–

all wavenumbers are given in cm^{-1}

Formulation of a printable Col$_h$ photoresist

The transfer of the H-bonded assemblies to microprinting requires the formulation of a convenient photoresist. Thanks to the design of the Col$_h$ mesogens, photocrosslinkable groups were already included in sufficient amount, thus the addition of a crosslinker was not necessary. For two-photon laser printing, a relatively high loading of the photoinitiator (generally around 2 wt% for Irgacure photoinitors) should be used. A radical scavenger was used to prevent the photoresist to be prematurely crosslinked to a problematic extend during thermal treatment and storing; as well as to widen the window of usable laser-powers and writing speeds. In particular, I used Irgacure 369 (Ig369) (2 wt%) as a photoinitiator and BHT (2 wt%) as a radical scavenger. To ensure for an accurate and homogeneous loading

of the two additives, they were introduced in the material during the initial step of the mixing of the building blocks.

I tested Ig819, Ig369 and DETC as potential photoinitiators, each of which resulted in satisfactory crosslinking of the material. DETC was not as well dispersed in the material than the Irgacure photoinitiators, due on its tendency to aggregate in microcrystalline domains. Ig369 and Ig819 performed similarly well for inducing crosslinking under UV-irradiation. However, Ig369 was determined a bigger window of laser powers, and noticeably allowed the use of a lower laser power. The more promising performances of Ig369 for two-photon irradiation-induced crosslinking motivated my choice to focus on it. In regard to the radical scavenger, BHT gave by far the best results. Thanks to the two isobutyl substituents of the hydroxytoluene core, BHT has a solubility in organic solvents that is superior to other hydroxytoluene-based radical scavengers. Also, BHT provides a good stability to the photoresist, while not interfering with the photoinitiator. Unlike other scavenging species such as (2,2,6,6-Tetramethylpiperidin-1-yl)oxyl (TEMPO), BHT permits high and variable loadings without critically altering the printing of the photoresist.

POM analyses exhibited **TBIB**-assemblies having a clearing point of about 170 °C. This temperature regime is problematic in the sense that acrylate groups are known to be thermally crosslinked at a similar temperature. As a matter of the LC arrangement of the discotic mesogens, a preliminary crosslinking decreased the mesogens mobility and thus altered the quality of the mesophase, or even locked the isotropic phase. Regarding the printing process, the phenomenon affected the reproducibility of the printing and made the development of the printed samples challenging or impossible. For these reasons, it was highly desirable to retain the mesogens non-crosslinked over the thermal formation of the Col_h mesophase. Therefore, 25 wt% of butylacrylate (BuA) were incorporated to the formulation of the photoresists based on **TBIB**-assemblies in order to lower their clearing point.[78] In this way, the clearing point of the photoresist decreased from 170 °C to about 100 °C, which made them usable for further investigation.

M- and **T**-assemblies were found to have clearing temperatures that were not problematic in regard of the thermal crosslinking of the acrylate functionalities. Clearing points of 48 °C, 53 °C, 59 °C and 52 °C were found for **M:dA$_3$**, **T:dA$_3$**, **M:dBzA$_3$** and **T:dBzA$_3$**, respectively. These temperature regimes allowed the eased thermal

manipulation, printing and development of the photoresists without the aid of a supplementary additive.

Characterisation of the Col_h properties

As stated previously, the size and arrangement control of the the porosity which is aimed in this project relies entirely on the structure of the Col_h mesophase. Hence, the effective formation of a mesophase, as well as its detailed characterisation, were fundamental initial steps for the success of the concept developed in this chapter. Also, a detailed understanding of the system helped for a better reproducibility in the sample preparation, as well as an easier and faster troubleshooting.

The thermal properties of the photoresists were determined by POM. By slowly cooling the LCs material from the isotropic state, the formation of mesophases was directly imaged. POM analyses were performed by confining a sample of the LC photoresist in-between two glass slides. Upon melting, the sandwich was pressed to ensure the formation of a homogeneous film of a thickness defined by aluminium spacers. The functionalisation of the glass slides was adapted to the intended use of the sample. Specifically, non-functionalised glass was used for the fabrication of macroscopic films by UV-irradiation (390−395 nm, 900 mW). This facilitated the separation of the sample after crosslinking, allowing the isolation of free-standing films for associated characterisation. For microprinting experiments, a functionalisation with methacrylates was used, as will be seen later.

The characterisation of the thermal properties by differential scanning calorimetry (DSC) unfortunately remained unfruitful, and a correlation with the POM finding for the formation of mesophases could not be established. Most likely due the slowliness of the formation of mesophases and the low associated heat release. Therefore, the thermal phase transitions of the LC photoresists were determined based on POM results.[278]

POM is powerful to get a fast and reasonably reliable indication of the LC phase. However, a full characterisation of the mesophase can only be claimed with the support of consistent WAXS analysis. Powder X-ray diffraction provides further information about the mesophase and its dimensions. Information about the liquid crystalline nature and about the arrangement can be extracted from the 1D projection of the diffractogram.

1,3,5-Tris(1H-benzo[d]imidazol-2-yl) benzene (TBIB) assemblies

The POM analysis of **TBIB**-assemblies depicted the formation of conic fan-shaped LC textures upon cooling from the isotropic sate, indicative of the mesogenic behaviour of those assembliesn (**Figure 3.13**). A Col_h mesophase was formed from 100 °C when using a cooling rate of -1 °C min^{-1}. By using a cooling rate of -0.2 °C min^{-1}, the mesophase was formed from 95 °C. The Col_h mesophase forming at a lower temperature when using a slower cooling rate was not unexpected. Slow cooling rate would provide the system a threshold thermal energy for a longer time. Faster cooling rates forced the phase transition within clusters, transition that quickly propagates through the entire material. This observation is also in agreement with long-range ordering being favoured by slower cooling rates.[206] The formation of a clear and homogeneous isotropic melt was a challenging step for the preparation of Col_h mesophases, and persistent domains could eventually be observed. The procedure used here allowed for great reproducibility and material economy, but could be subjected to further improvement. Further optimisation of the viscosity of the photoresists could allow a deposition by spin-coating which would improve the homogeneous deposition of the substrates further.

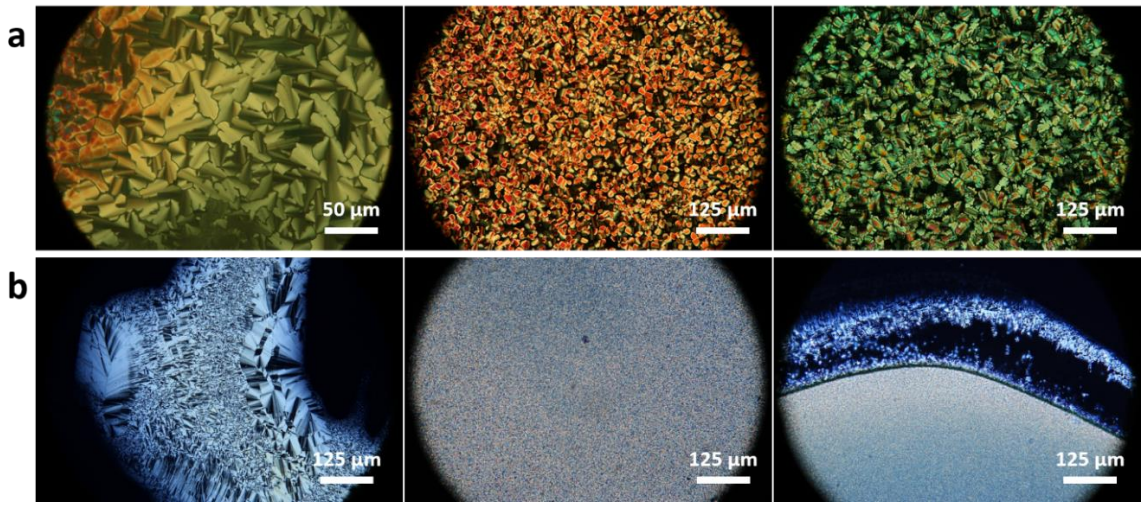

Figure 3.13. POM images of LC textures obtained with photoresists based on a) **TBIB:dA$_3$** and b) **TBIB:dBzA$_3$**. a) Conic fan shaped LC textures were observed for 4−16 µm thick samples. b) Conic fan-shaped LC textures were observed for regions solely "wetted" by the resists; for 4−16 µm thick regions, small domains were imaged.

WAXS data provided a more detailed characterisation of the Col_h mesophase and of its dimensions. For a photoresist based on **TBIB:dA$_3$**, the material was analysed as a non-crosslinked fluid photoresist; as a crosslinked polymeric LC film after UV-irradiation; and

as a crosslinked LC film after chemical manipulation (as will be described later). A characterisation of the material by WAXS at each step allowed to prove the retention of the Col_h arrangement throughout the fabrication.

First, I analysed the non-crosslinked photoresist by trapping a sample of the photoresist between two polyacrylamide foils using a specific gel sample holder. The corresponding WAXS data (**Figure 3.14**) showed a pattern of the small-angle reflections which supports the formation of a Col_h mesophase. A hexagonal arrangement was evidenced by sharp reflections at q^*, $\sqrt{3}\,q^*$, $\sqrt{4}\,q^*$ and $\sqrt{7}\,q^*$, corresponding to the (100), (110), (200) and (210) reflections. For the non-crosslinked photoresist, a lattice constant a = 3.96 nm was calculated, which is in accordance with previous results.[201, 248] In the wide-angle region, one can observe a broad (001) reflection for the π-π stacking of the aromatic cores, d_{001} = 0.35 nm, and a reflection from the liquid-like correlations of the aliphatic chains, $d_{aliphatic}$ = 0.45 nm. As expected for a columnar liquid crystal, the broadness of these wide-angle reflections indicates the irregular spacing of the mesogens in the *z*-directions and the fluidity of the inter-columnar medium. The photoresist was analysed as obtained after the incorporation of the BuA additive and prior to any thermal treatment; the not perfectly smooth aspect of the wide-angle reflections can be attributed to a minor amount of crystalline domains in the photoresist.

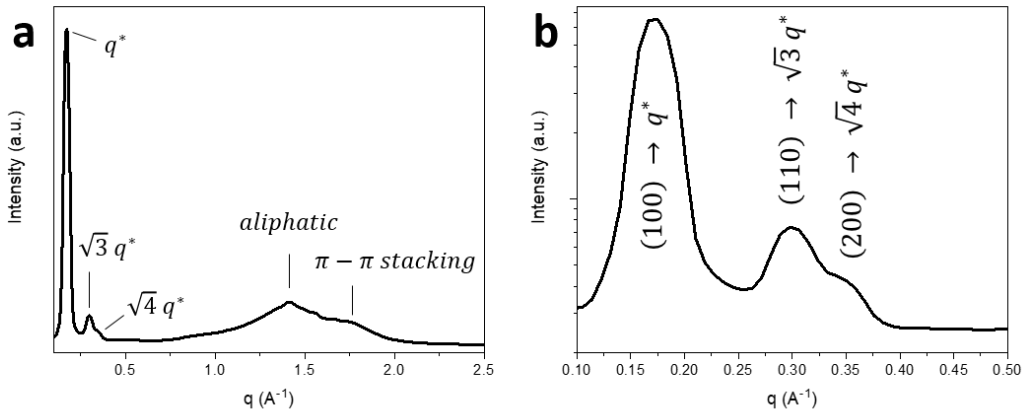

Figure 3.14. 1D projection of the WAXS data for a non-crosslinked photoresist based on **TBIB:dA$_3$**. a) Complete range spectrum and b) small-angle region of the spectrum. For the zoom in the small-angle region, the intensity is given in logarithmic scale for better visualisation.

An important step is the ability to crosslink the Col_h photoresist into a polymeric material, whilst not altering the Col_h arrangement. In this work, I will discuss two

crosslinking methods based either on 1PE or on 2PE. By UV-irradiation, 16 µm thick macroscopic polymer film were fabricated from a layer of the Col_h photoresist. This method was readily reported several times and was here used as a control. The retention of the Col_h arrangement in polymeric films was determined by POM and WAXS. Thereafter, microprinting by two-photon laser printing allowed the crosslinking of the photoresist with spatial control.

It was critical for further functional properties that the crosslinking of the LC photoresist is non-destructive with respect to the LC arrangement. For microstructures, POM allowed us to observe the conservation of the LC textures through printing. Especially, conic-shaped LC textures with big domain size were observed for 20 µm thick microprinted structures. As mentioned in chapter 1, columnar mesophases can be aligned by surface affinity. The observation of the best LC textures in the close proximity of the glass substrate was attributed to this affinity effect.

WAXS data showed the Col_h arrangement to be conserved over crosslinking for films of a photoresist based on **TBIB:dA$_3$**. By the WAXS analysis of free-standing films, I observed again a ratio of the q-values in the small-angle region corresponding to a hexagonal pavement, as well as broad reflections for the distances along the director vector (**Figure 3.15a**). For crosslinked films, I calculated an inter-columnar spacing of a = 4.02 nm, thus very similar to the arrangement before crosslinking. The scale of the microprinted structures does unfortunately not allow their analysis by WAXS. Therefore, I assumed that the microprinted structures should exhibit similar behaviour than films made of strictly identical photoresists.

In the case of the self-assemblies employing the bigger **dBzA** peripheral acid, **TBIB:dBzA$_3$**, the WAXS analysis of a photocrosslinked film revealed a more poorly defined mesophase. The increased broadness of the (100) reflection is indicative of a significantly more irregular two-dimensional arrangement. Also, it shadowed the (110), (200) and (210) reflections in the small-angle regions. Although shoulders can be observed and could be attributed to the (110) and (200) reflections, the inconsistency of the q-values did not allow a proper characterisation of the mesophase (**Figure 3.15b**).

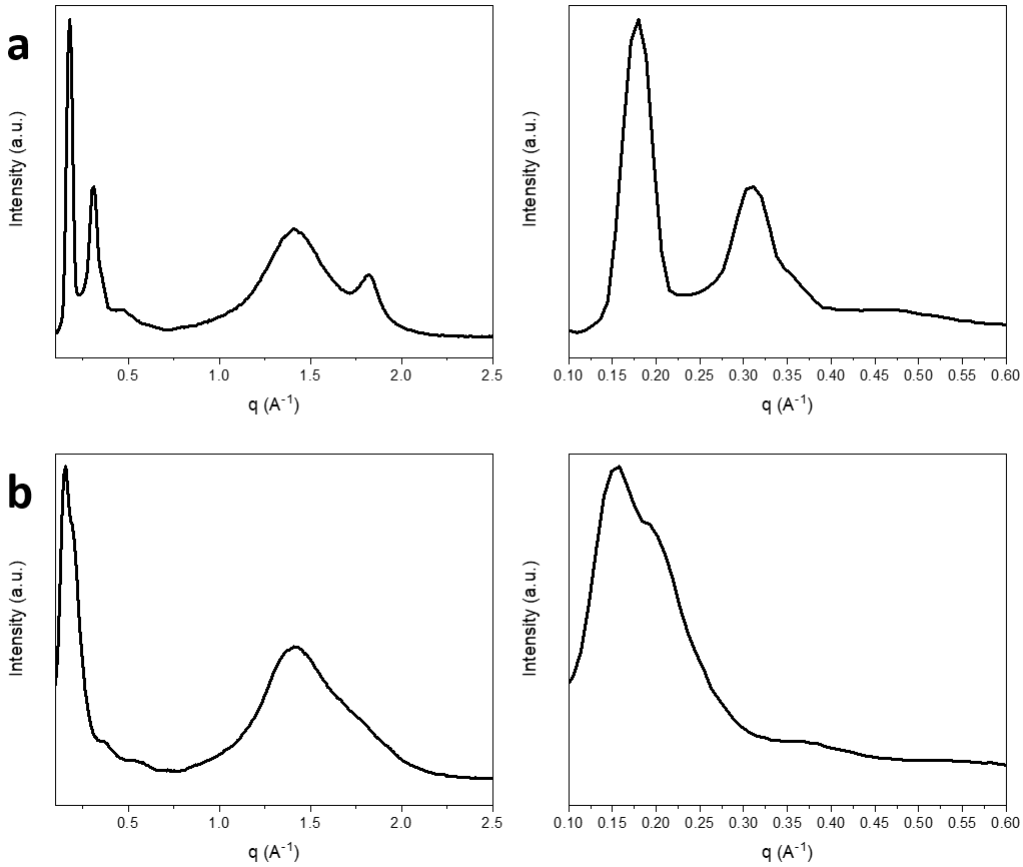

Figure 3.15. 1D projection of WAXS data for polymeric films of photoresists based on a) **TBIB:dA$_3$** and b) **TBIB:dBzA$_3$**. The entire spectrum (left) and zoom in the small-angle region is depicted for both.

Melamine and tris(triazolyl)triazine assemblies

The POM analyses of **M:dBzA$_3$** and **T:dBzA$_3$** showed the formation of small birefringent domains. When compared to the behaviour of the building blocks alone which assembled in crystalline needles, this result indicates a LC behaviour of the discotic assembly. On the other hand, the small size of the domains did not correspond to the formation of a high quality Col$_h$ mesophase. The WAXS data for crosslinked films of **M:dBzA$_3$** displayed a very prominent (100) reflection, and reflections of much lower intensities which could be assigned to the (110) and (220) reflections. However, the overall roughness of the spectrum indicated the presence of microcrystalline domains. **T:dBzA$_3$** depicted similar features than the previously described **TBIB:dBzA$_3$**. That is, the broadness of the (100) reflection mostly hided the signals for the (110) (200) and (210) reflections by superposition.

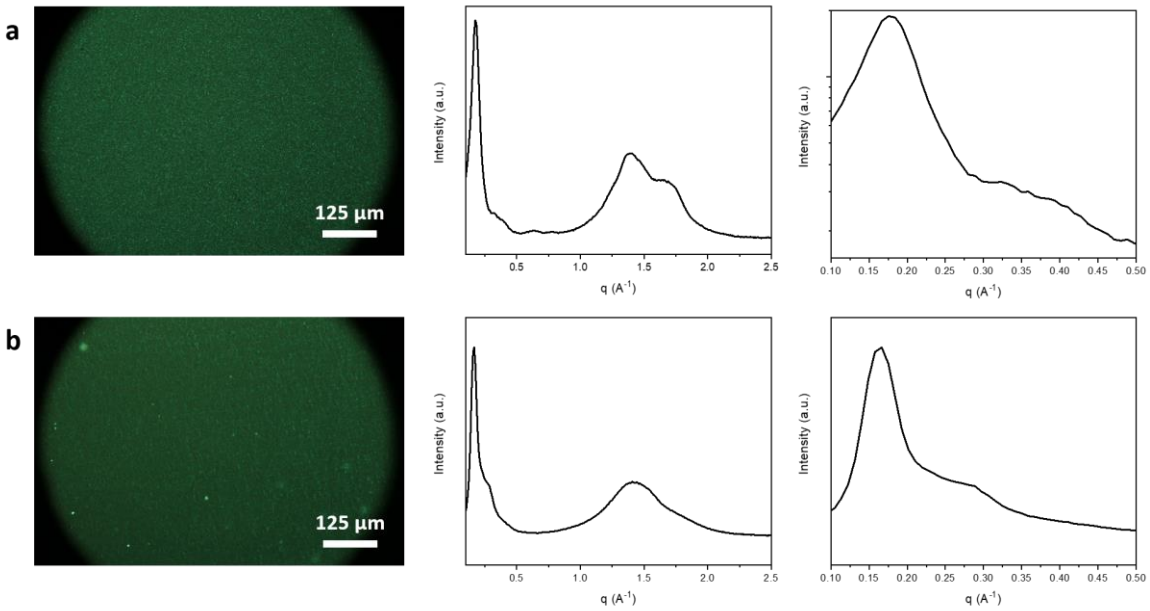

Figure 3.16. POM and 1D projection of WAXS data for a) **M:dBzA$_3$** and b) **T:dBzA$_3$**.

The POM analyses of **M:dA$_3$** and **T:dA$_3$** resulted in the observation of needle-shaped domains. This finding is indicative of a significant crystallisation of the photoresist. This observation was later confirmed by WAXS data (**Figure 3.17**).

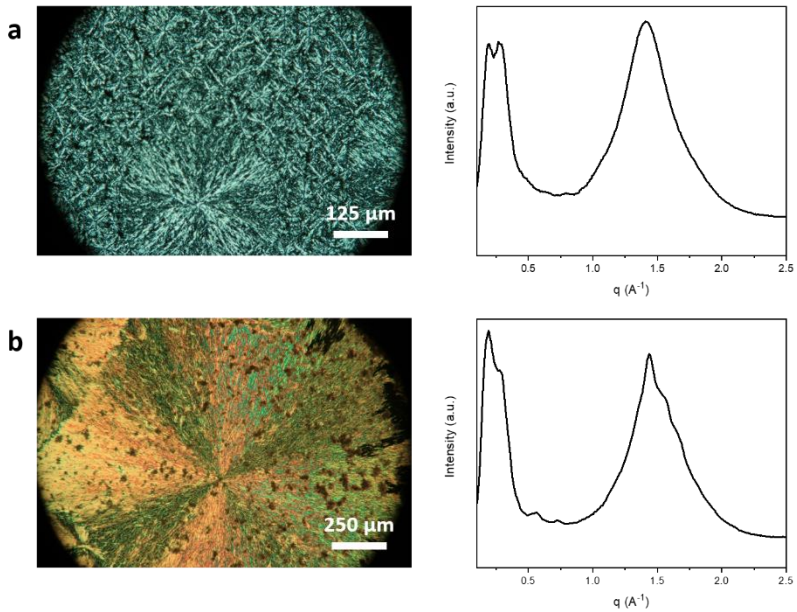

Figure 3.17. POM and 1D projection of WAXS data for a) **M:dA$_3$** and b) **T:dA$_3$**.

Alignment of the Col_h mesophases

As presented in chapter 1, surface affinity is a common technique for the alignment of columnar LC mesophases. Within this work, I tested various substrate functionalisation. Functionalisation by silanisation allowed the preparation of methacrylate-, amino- and octadecyl-functionalised glass substrates, using 3-(trimethoxysilyl)propyl methacrylate, (3-Aminopropyl)triethoxy silane and trichloro(octadecyl) silane, respectively. Also, the coating of glass substrates with polyviynyl alcohol (PVA) or polystyrene sulfonate (PSS) by spin-coating allowed the fabrication of alcohol-functionalised and highly polar sulfonated substrates. Finally, using a polydimethylsiloxane (PDMS) block in place of one of the glass substrate was also attempted.[206] Nonetheless, none of the attempts toward a long-range homeotropic alignment of the mesophases was successful.

Also, an alignment using an electric field was pursued. Electric fields with an intensity of 15 V, 30 V and 60 V either parallel or perpendicular to the substrates were tested. Such as for an alignement by surface affinity, no clear differentiation of the LC textures could have been observed by POM, and the corresponding WAXS characterisations did unfortunately not show any evidence of long-range alignment. Therefore, the printing was carried out using polydomain Col_h samples, which, with respect to the previously shown WAXS data, have an ordering that can readily provide the corresopnding porous materials with substantial adsorptive properties.

Microprinting of columnar LCs

The characterised Col_h photoresists were investigated for their printability by two-photon microprinting. In order to have a reproducible platform for potential further investigation, the microprinting experiments were performed using a commercially available two-photon laser printing instrument (Photonics Professional GT, Nanoscribe GmbH). I focussed on the study of **TBIB:dA$_3$** due to the better LC behaviour described previously. Sandwich cells of the photoresists were prepared with at least one of the glass slides functionalised with methacrylate groups to ensure the good adhesion of the microprinted structures on the substrate and to avoid their desorption during development or further manipulation. The thickness of the sandwich cells was set to 64 µm (four 16 µm spacers) in order to have the opportunity to explore various structure heights and facilitate the development of the microprinted samples. I observed some limitation of the printing of

the Col_h photoresists caused by their birefringence and translucency. To limit this negative effect, I used an 25x magnification objective with a numerical aperture of NA = 0.8. The use of this objective allowed to prevent diffraction-caused shortcomings, while using a 63x, NA = 1.4 objective could result in the formation of several foci. On the other hand, using a 25x magnification objective limited the possible achievable definition as it engenders a voxel of a bigger size with respect to a 63x objective. Additionally, the printing was performed in oil-immersion configuration in order to lessen the path length of the laser beam in the Col_h photoresist (**Figure 3.18**).

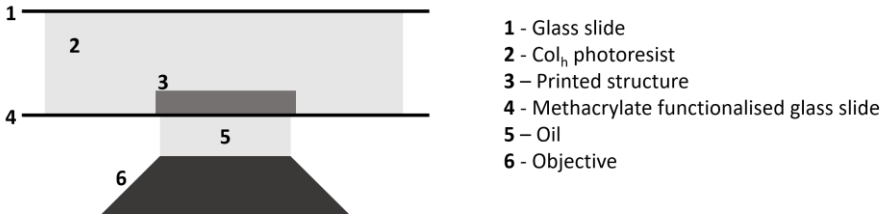

Figure 3.18. Schematic representation of the setup used for the two-photo laser microprinting of Col_h photoresists.

With these adaptations, I could extend the height threshold up to about 30 µm. Above this threshold, the definition and the quality of the printing was observed to be decreased (**Figure 3.19**). The interface finding was performed manually by adjusting the position of the microscope stage in the *z*-direction. A focal point which was initially attributed to the exact position of the interface, was later determined to be systematically located about 8 µm below the interface, by SEM analysis. The systemic nature of the offset allowed the application of a correction in the printing programme directly, and the observed focal point was still used as practical reference.

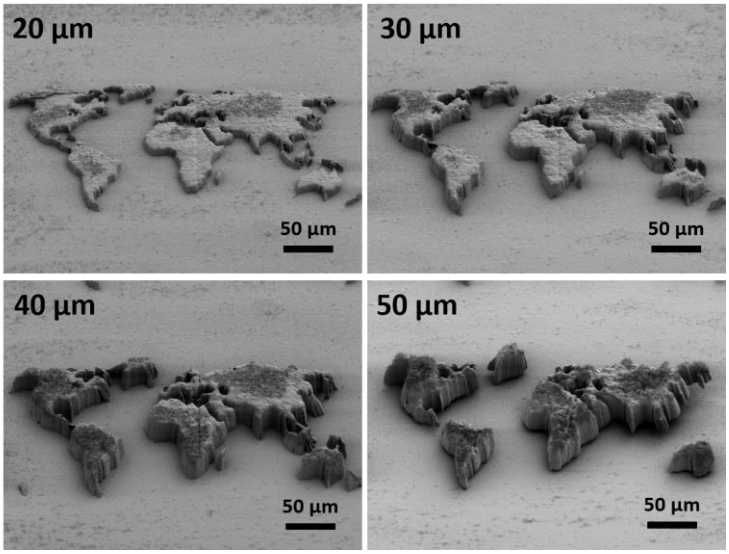

Figure 3.19. SEM images (45° sample mount) of world map structures with a height of 20 µm, 30 µm, 40 µm and 50 µm. The structures were fabricated by two-photon laser printing using a photoresist based on **TBIB:dA$_3$**.

I optimised the printing parameters based on relatively high scanning speeds of 20 mm s^{-1} and 25 mm s^{-1} to show the ability of the Col_h photoresists to be fabricated into large structures with contained printing times, what could facilitate their use for the fabrication of elaborated microdevices. The optimisation was done by printing 100 × 100 × 20 $µm^3$ cuboid microstructures at variable laser powers for each scanning speed. It can be argued that an optimisation based on the printing of single lines instead of microstructures can be imployed. However, the microstructures could here not be observed during printing, but were solely visualised after the development of the samples. Also, the optimisation geometries were chosen to reproducibly adhere to the substrate and be retained through development. Here, the thickness of the test blocks provides an additional certainty for the photoresists to be effectively treated even with a reference *z*-position below the substrate-photoresist interface.

In each case, I retained the lowest possible laser power which resulted in a sufficient crosslinking to ensure the shape integrity of the microprinted structures. A laser power of 20 mW and 25 mW was optimal when using a printing speed of 20 mm s^{-1} and 25 mm s^{-1}, respectively. Lower intensities resulted in soft structures which were often deteriorated during development. Too high intensities lead to local degradations of the Col_h mesophase or of the global resist by overexposure or microexplosion (**Figure 3.20**).

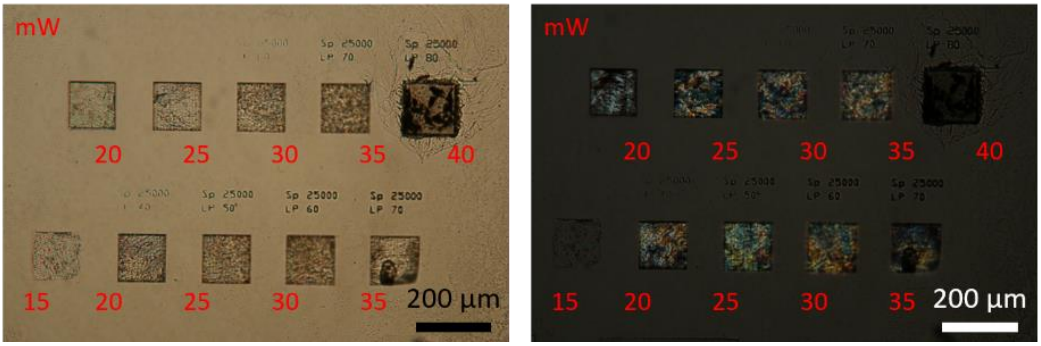

Figure 3.20. An example of power sweep for **TBIB:dA$_3$** using a constant scanning speed of 25 mm s^{-1}. Optical images without (left) and with (right) cross polarisers. The laser power used for each cuboic structure is given in mW and shown in red.

The development of the printed structures was performed by submerging the cell in a adequate solvent ($CHCl_3$:MeOH for **TBIB**-assemblies) to dissolve the surplus of non-crosslinked photoresist. After the complete removal of the unreacted photoresist, the cell can easily be open and the printed structures were further washed in the same solvent system. This mild development method preserved the printed structures from mechanical stresses that could destroy them, favouring the isolation of good quality structures. Alternatively, the sandwich cell could be open manually and the slide carrying the structures washed alone. Although being more time-effective, this method led to increased likeliness of the desorption or breakage of the microprinted structures.

After optimisation with the aid of simple cuboid structures, the photoresists were tested for their ability to be processed into more complex "2.5D" geometries (a map of the world, a hexagon with hole and a representation of the inner circle in Karlsruhe). These models were designed to be right-prisms, but to contain more challenging features in the *xy*-plane compared to simple blocks. Based on the SEM imaging of the printed structures, I determined that 2.5D structures can be printed with great definition, smooth and straight surfaces, sharp edges and low-shrinkage (**Figure 3.21**).

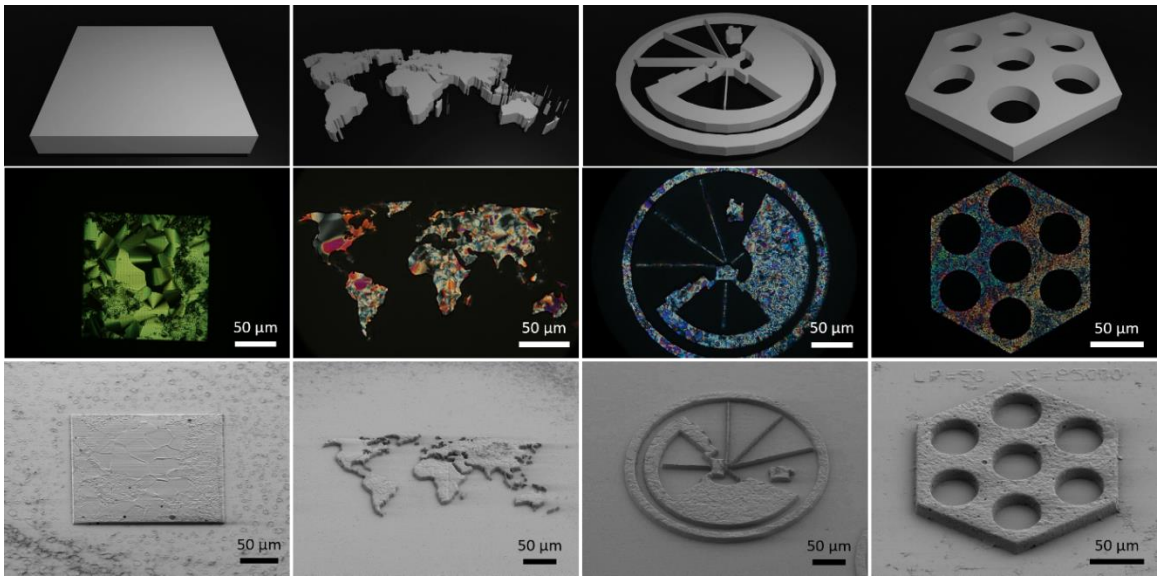

Figure 3.21. Example of 2.5D geometries fabricated by two-photon laser printing of a photoresist based on **TBIB:dA$_3$**. For each structure, a model (top), a microscope image (middle) and a SEM image (bottom) are shown.

Due to the height limitation discussed before, the design of suitable geometries including 3D feature such as void or overhanging parts was not trivial. Indeed, the birefringence of the Col$_h$ photoresists and the use of a 25x magnification objective led to a fairly large apparent voxel size. Thus, a significant proximity effect was observed in the *z*-direction. Optimal designs would then consist of geometries not bigger than 30 µm in height and with a relatively large footprint to favour adhesion to the substrate. Also, interesting and conveniently sized features should be included in both the *xy*-plane and the *z*-direction. As such designs, I proposed a structure based on two intricated verticed cubes, a cubic pilling of rods and of the 3D representation of the logo of our group.

From the SEM imaging of microstructures fabricated by two-photon laser printing (**Figure 3.22** to **Figure 3.24**), the following conclusions can be formulated. For the example of the structure based on intricate cubes, the thin suspended parts on the edge of the structure suffer from mechanical instability, hence often collapsed. This can be attributed to an undersizing of the thickness of the suspended part. For the cubic pilling of rods, in was observed that the void in-between the layers were not big enough, thus two neighbouring layers were often merged. The 3D representation of the logo of our group did show the ability to create hollow parts in a printed volume, as can be seen by observing the definition of the letters in the corresponding cylinders. However, the top cylinders were often found to be linked to the substrate and the expected void beneath them not freed. A

successful inclusion of 3D features would thus require an optimisation of the design of the initial model, design in which the respective size of the empty and hanging parts are correctly balanced to allow the emptying of the void and the mechanical integrity of the hanging part. With the height constraint that I observed, this remained challenging and I could unfortunately not propose any perfect example to confirm the reasoning. Nevertheless, we are pretty confident, with the apparent performance of the Col_h photoresists toward printing, that 3D structures can be accessed. Which could be achieved either by the smart design of the printing structures, or by the optimisation of the LC photoresist. Aligned Col_h materials with a long-range correlation were shown to have an increased transparency,[202, 240] which would enable the printing of thicker structures and thus offer more freedom for 3D designs.

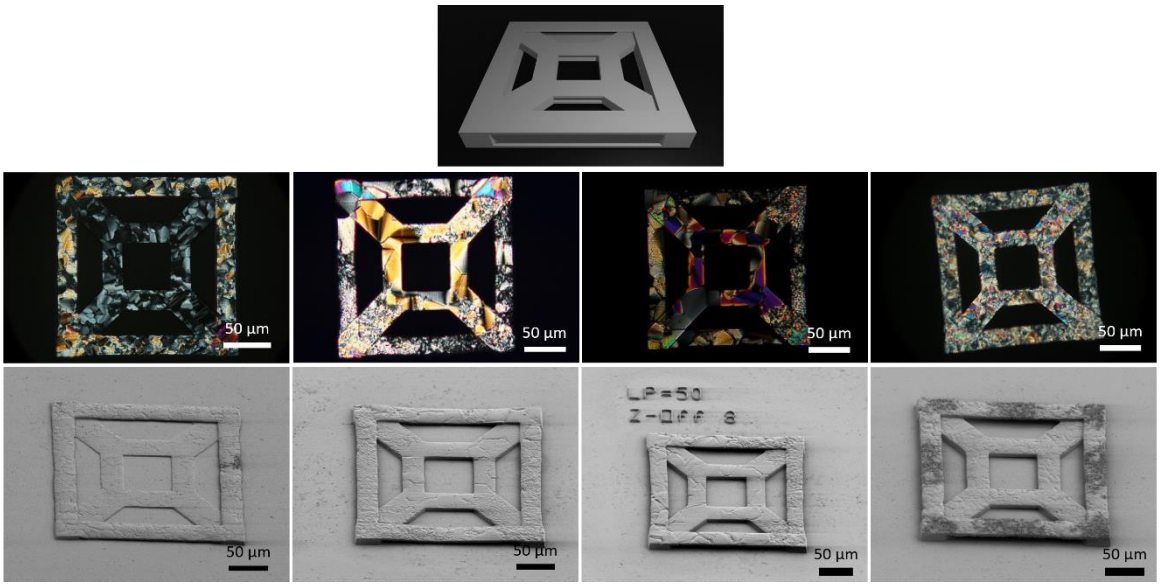

Figure 3.22. Examples of a structure based on two intricated cubes fabricated by two-photon laser printing of a photoresist based on **TBIB:dA$_3$**. A model of the printed geometry in shown on top. For each structure, a microscope image (middle) and a SEM image using a 45° sample mount (bottom) are shown.

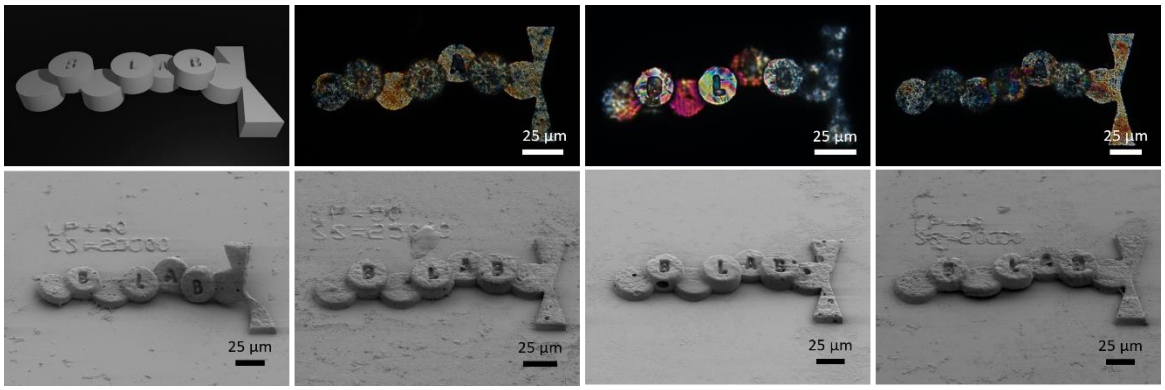

Figure 3.23. Examples of the logo of Blasco lab fabricated by two-photon laser printing of a photoresist based on **TBIB:dA$_3$**. A model of the printed geometry in shown on the top left. For the three structures on the right, a microscope image (middle) and a SEM image using a 45° sample mount (bottom) are shown.

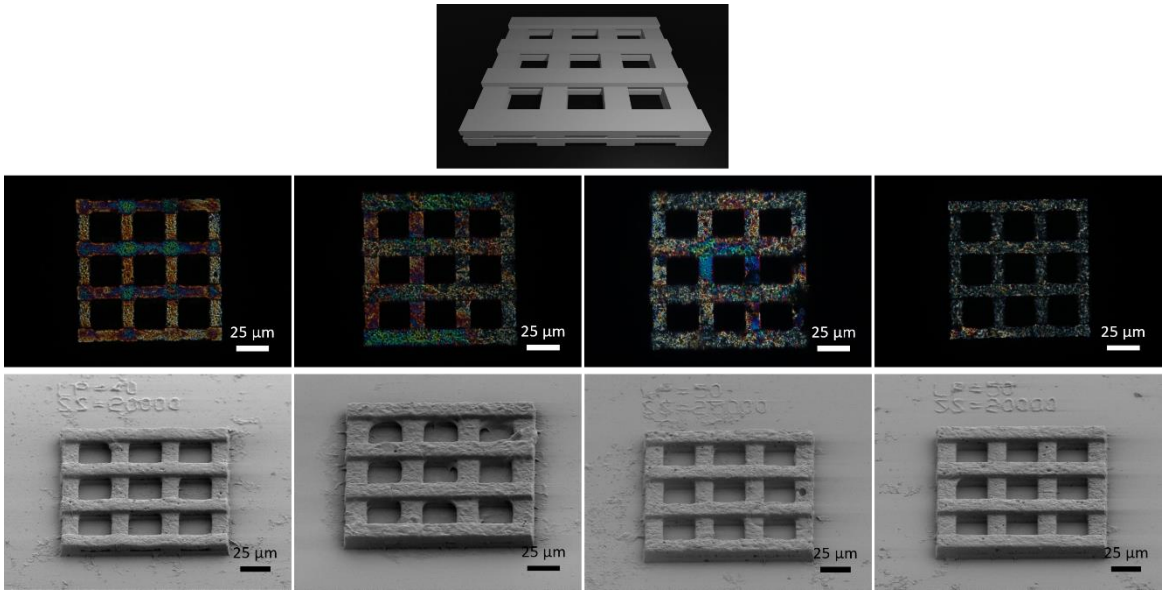

Figure 3.24. Examples of a cubic pilling of rods fabricated by two-photon laser printing of a photoresist based on **TBIB:dA$_3$**. A model of the printed geometry in shown on top. For each structure, a microscope image (middle) and a SEM image using a 45° sample mount (bottom) are shown.

The POM imaging of the printed structures showed a retention of the LC textures of **TBIB:dA$_3$**, as depicted in **Figure 3.21** to **Figure 3.24**. This supported the previous observation for UV-crosslinked polymeric films that the Col_h arrangement is unaltered by the crosslinking of the photoresist during the printing procedure and gets simultaneously locked. Some additional examples are shown by **Figure 3.25**.

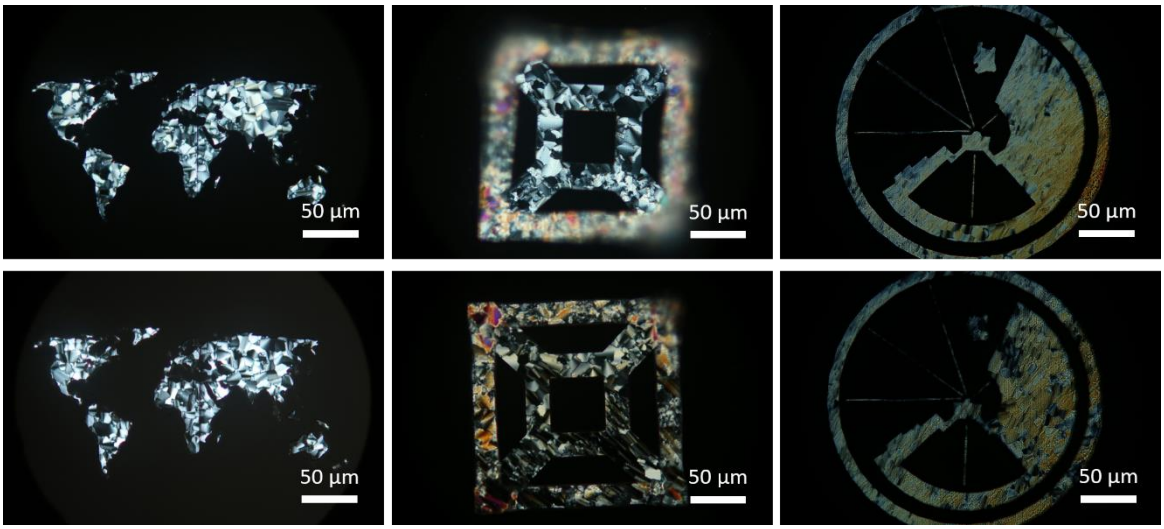

Figure 3.25. POM of microstructures fabricated by two-photon laser printing using a LC photoresist based on **TBIB:dA$_3$**.

Core removal: towards ordered nanaporous materials

The mesogens being designed as H-bonded assemblies, the templating cores can be removed by the breakage of the H-bonds via chemical treatment with 0.1 wt% NaOH in DMSO. Upon core removal, pores are created by the freeing of the central volume of the columnar stacks. Thanks to the Col$_h$ arrangement and its locking during crosslinking, the such created pores have a distribution precisely defined by the arrangement of the mesophase and a size defined by the core used.[234, 279] This size definition permits a size selectivity of the material. The porous material are expected to remain impermeable to molecules bigger than the core that was just removed, while smaller molecules can penetrate the pores. For **TBIB**, **M** and **T** cores, the resulting pores size was reported to be in the range of 0.5 nm to 1.5 nm, **M** being the smallest and **T** the largest.[201, 279]

For **TBIB:dA$_3$**, the retention of the Col$_h$ arrangement upon core removal was studied by WAXS. The WAXS data of 16 µm thick films were compared before and after core removal. I confirmed the conservation of the LC arrangement by the observation of the key reflections presented before. Also, the WAXS data indicated the conservation of the scale of the arrangement. As depicted by **Figure 3.26**, the lattice constant was calculated to be a = 3.96 nm after core removal, which was consistent with that of the photoresist a = 3.96 nm as well as that of the polymeric film before core removal, a = 4.02 nm. The main reflections in the small-angle region, their associated q-values and distances for the **TBIB:dA$_3$** photoresist, as well as for the crosslinked films (before and after core removal)

are listed in **Table 3.3**. Based on these results, I evidenced that photocrosslinking locked the LC mesophase and that the locking of the arrangement by the polymeric matrice allowed, in a second time, the removal of the templating core without the loss of the Col_h arrangement.

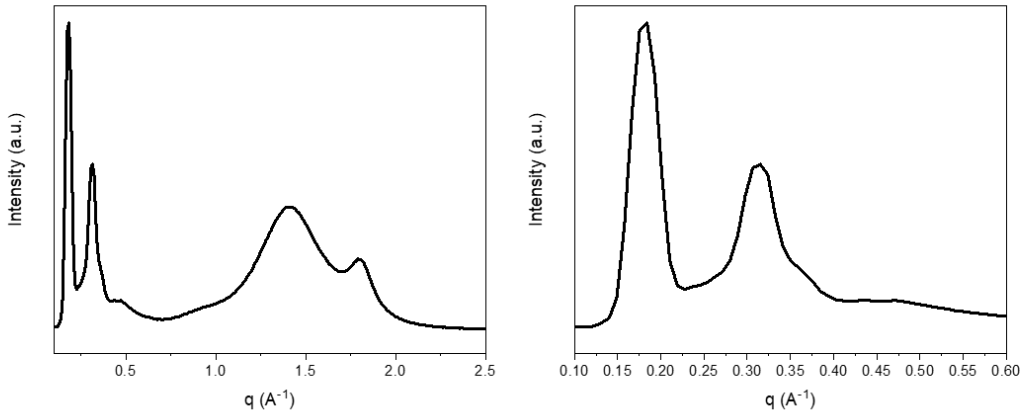

Figure 3.26. 1D projection of the WAXS data for a polymeric film of a photoresist based on **TBIB:dA$_3$** after core removal in 0.1 wt% NaOH in DMSO.

Table 3.3. Details of the small-angle reflection for the **TBIB:dA$_3$** photoresist, for a crosslinked of for a crosslinked film after core removal.

Photoresist		Cross-linked film		After core removal			
q (Å^{-1})	d(nm)	q (Å^{-1})	d(nm)	q (Å^{-1})	d (nm)	Ratio	Assignment
0.184	3.41	0.180	3.49	0.184	3.41	1	(100)
0.315	1.99	0.311	2.02	0.315	1.99	$\sqrt{3}$	(110)
0.367	1.71	0.364	1.73	0.367	1.71	$\sqrt{4}$	(200)
		0.480	1.31	0.480	1.31	$\sqrt{7}$	(210)
a = 3.96 nm		**a = 4.02 nm**		**a = 3.96 nm**			

With the previous WAXS findings, I showed that the Col_h arrangement remained unaltered over the entire fabrication, and thus should allow for a size selective adsorption. Nevertheless, the removal of the templating core not only frees the central volume of the columns, leading to a porous material. Additionally, the process of removing the templating core engenders the carboxylic acid moieties of the peripheral acids **dA** to be located at the boundaries of the pores. Thanks to acido-basic reactivity of these moieties, the polarisation of the pores could be tuned. After core removal in basic conditions, the pores are surrounded with anionic carboxylate moieties and can be neutralised by the protonation of the carboxylate moieties toward the corresponding carboxylic acid, **Figure 3.27**. The effective

charge of the pores being tunable in this way is the fundament for a charge selectivity of the nanoporous Col_h polymeric materials. The pores surrounded by carboxylate groups are most adapted for the adsorption of cationic molecules, while protonation of the groups modifies the affinity of the materials for the adsorption of neutral molecules.[279] Considering the previously presented size selectivity, we can further refine the selectivity abilities of nanoporous Col_h materials. With negatively charged pores, the material will only be permeable to small cationic molecules. After protonation, the porous material will be permeable to small neutral molecules. In order to draw conclusions about the adsorptive properties of the LC polymeric species, it is necessary to control the removal of the cores as well as the chemical manipulation of the affinity of the pores.

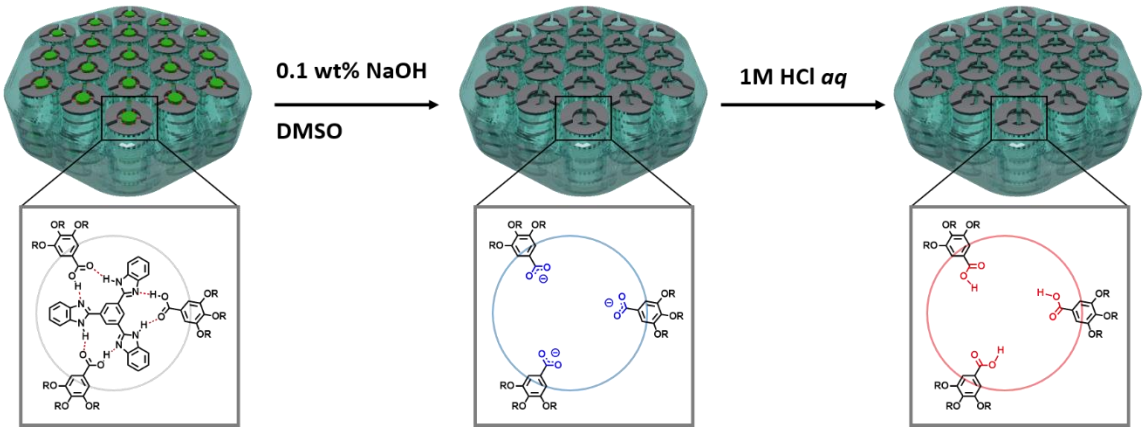

Figure 3.27. Representation of the core removal from **TBIB:dA$_3$**. For each, a representation of the polarity of the pores is shown.

Identically to FTIR being a powerful technique to follow the formation of H-bonds, their breakage in a basic medium, and protonation in a protic acidic medium can also be evidenced by this technique. Upon **TBIB** removal from **TBIB:dA$_3$**, as well as deprotonation of the carboxylic acid of the assemblies forming carboxylates, I observed the splitting of the C=O stretch band at 1679 cm^{-1} into a C=O asymmetric stretch band at 1565 cm^{-1} and a C=O symmetric stretch band at 1376 cm^{-1}. The loss of the N^+–H vibration band at 3254 cm^{-1} indicates the complete removal of the **TBIB** core. For **TBIB:dA$_3$**, such a study was performed both for microstructures and polymeric films and the corresponding spectra are shown by **Figure 3.28a** and **Figure 3.28b**, respectively.

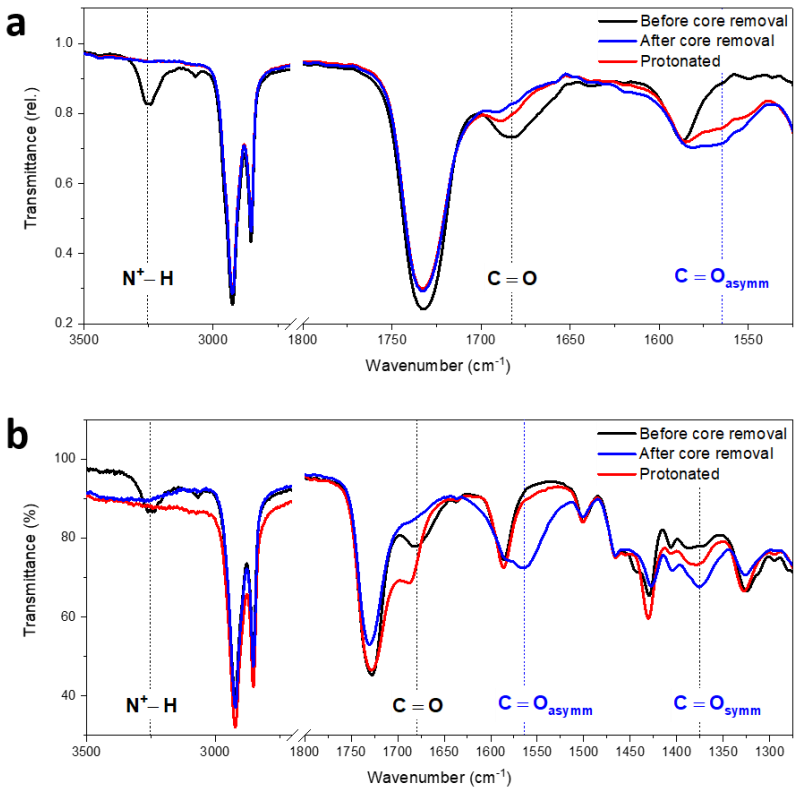

Figure 3.28. FTIR study of the removal of the templating core from a crosslinked LC photoresist based on **TBIB:dA$_3$**. a) Study of a $150 \times 150 \times 10$ µm^3 cuboid structure fabricated by two-photon laser printing and, b) study of a polymeric film fabricated by UV-irradiation.

Similar FTIR studies of the core removal from polymeric films were performed on **M**- and **T**-assemblies. For those, such as for the FTIR study of the formation of the assemblies, the N^+–H band, specific of **TBIB**, could not be used to prove the successful removal of the templating cores. Similarly to what was shown for **TBIB:dA$_3$**, the removal of the templating core from the LC polymeric films induced a split of the carboxylic acid of the peripheral acids into a symmetric and an asymmetric vibration band (**Figure 3.29**), the symmetric vibration band was more pronounced for **dA** than for **dBzA**. Although those results have room for improvement, they showed our ability to remove the templating core in 0.1 wt% NaOH in DMSO, and to later protonate the carboxylate moieties in 1 M HCl *aq*.

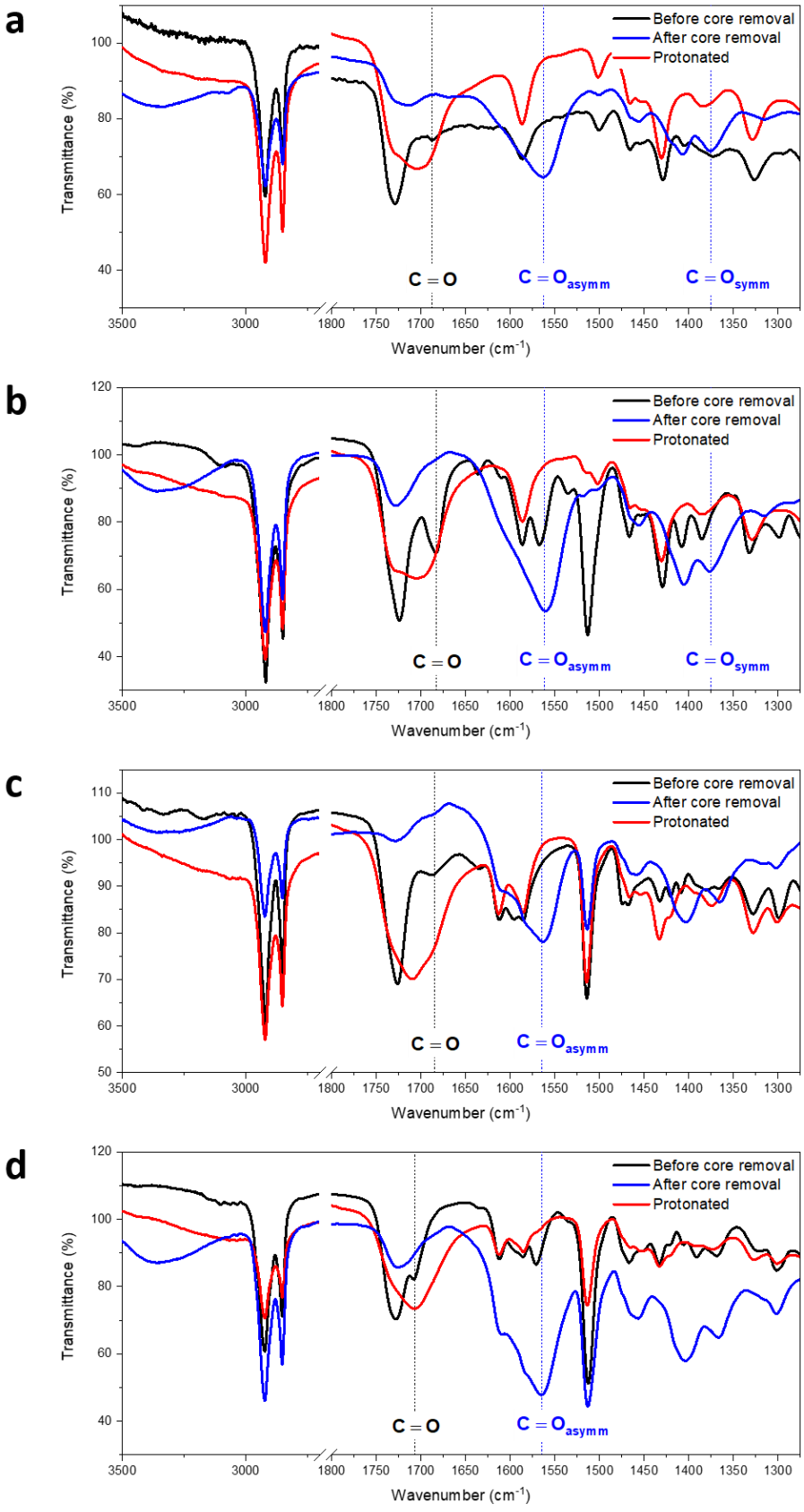

Figure 3.29. FTIR study of the removal of the templating core from a crosslinked film of a LC photoresist based on a) **M:dA$_3$**, b) **T:dA$_3$**, c) **M:dBzA$_3$** and d) **T:dBzA$_3$**.

In the examples shown in **Figure 3.29**, a deterioration of the films was observed, by the disappearing C=O vibration band for the acrylate at 1729 cm^{-1}. In this case, the films were exposed to the DMSO solution overnight. Due to their scale difference, I observed that either the microstructures or macroscopic polymer films had very different sensitivity toward the exposure to 0.1 wt% NaOH in DMSO. By recording the evolution of the FTIR spectrum of **TBIB:dA$_3$** over time for either of the forms of the crosslinked photoresist, this sensitivity difference can be visualised. The microstructures were found to be altered for exposure time of an hour, with the necessary exposure time for complete core removal ranging from 3 to 10 minutes. For an exposure time of one hour, one can see the disappearing C=O vibration band for the polyacrylate matrix at 1729 cm^{-1}. On the other hand, the films fabricated by UV-irradiation required exposures of several hours to show complete core removal (**Figure 3.30**), and degradation was observed after about 9 h. In both cases, the polymeric material was stable to an exposure to 1 M HCl *aq* for several hours.

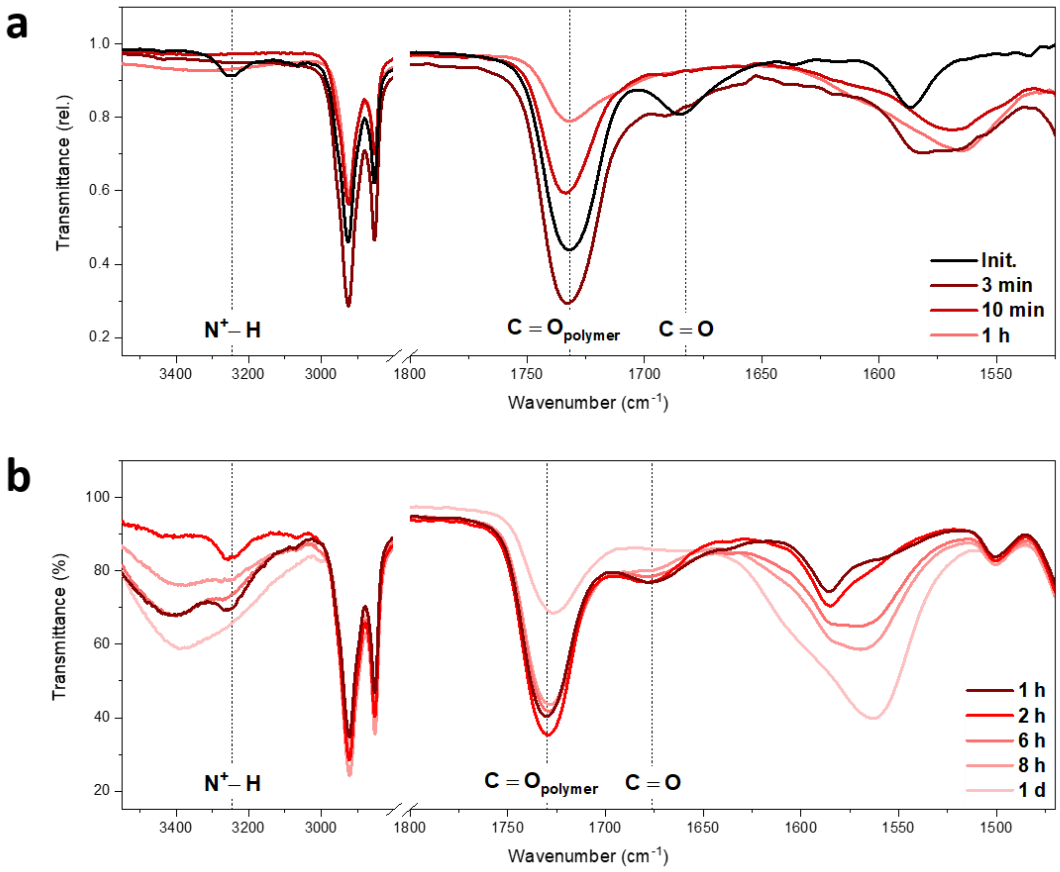

Figure 3.30. FTIR spectrum over time for a) a mictructure and b) a crosslinked film of a photoresist based on **TBIB:dA$_3$** under core removal with 0.1 wt% NaOH in DMSO.

Selective dye adsorption

In the previous paragraphs, I demonstrated that discotic mesogens can be fabricated by the H-bonding driven self-assembly of peripheral acids carrying terminal acrylate groups around a centre templating core and that the so-obtained discotic mesogens form a Col_h mesophase through an adapted thermal treatment. Thereafter, I showed that these compounds can be microprinted by two-photon laser printing with a retention of the LC arrangement and that the templating cores can be removed by chemical treatment, whilst mainting the initial ordering of the mesophase. As a last step, the nanoporous materials were tested as functional polymeric materials for the selective adsorption of molecules. Again, these tests will be focussed on polymeric materials based on **TBIB:dA$_3$**.

The nanoporous Col_h substances with benzoate moieties at the boundaries of the pores are expected to have a selectivity for small cationic molecules. I tested the selectivity of microprinted structure using four easily traceable water-soluble ionic dyes. I considered two small cationic dyes, methylene blue (**MB**) and thioflavin T (**BY1**). As expected, the adsorption of **MB** and **BY1** in microstructures was confirmed by a strong blue and yellow coloration of the microstructures after dye adsorption (**Figure 3.32**). Moreover, fluorescence confocal microscopy of a microstructure with **MB** adsorbed evidenced the homogeneous penetration of the dye within the bulk of the microstructures. To test the selectivity of the adsorption, I considered rhodamine B (**RhB**) as a big cationic molecule and methylene orange (**MO**) as a small anionic molecule. In spite of its adequate charge, the adsorption of **RhB** was negated by its large size. Contrarily, the size of **MO** was adequate for its adsorption but its penetration was prevented by its negative charge.

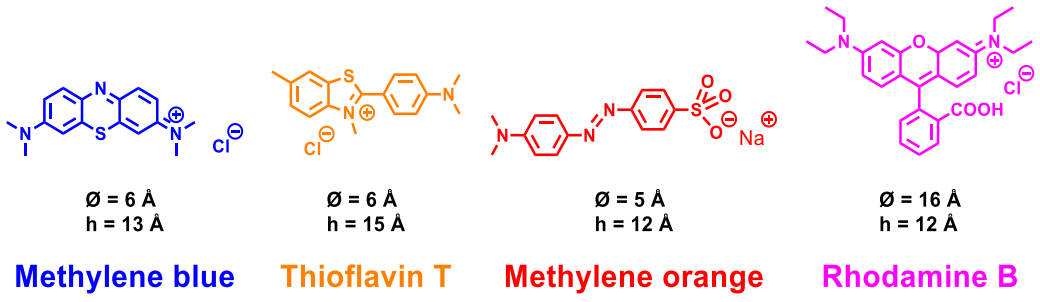

Figure 3.31. Chemical structures of methylene blue (**MB**), thioflavin T (**BY1**), methylene orange (**MO**) and rhodamine B (**RhB**). The size of each dye is proposed considering a cylindrical shape of diameter Ø and height h.[279, 280]

The exposure of nanoporous Col_h microstructures to aqueous solutions of **MO** and **RhB** only led to a small colouration of the microstructures, that can be attributed to the deposition of dye molecules at the surface of the microstructures (**Figure 3.32**). The confocal fluorescence microscopy study of structures exposed to **RhB** unexpectedly showed a fluorescence that could not be attributed to the residual fluorescence of the photoinitiator. With the current state of the investigation it remains unclear whether a minor diffusion of the dye solution could lead to shortcoming when going to small structures or if the observation could be attributed to a bad quality of the samples analysed. Similar experiments for the detection of **BY1** and **MO** were not possible as the two dyes do not have any usable fluorescence at the available excitation wavelengths.

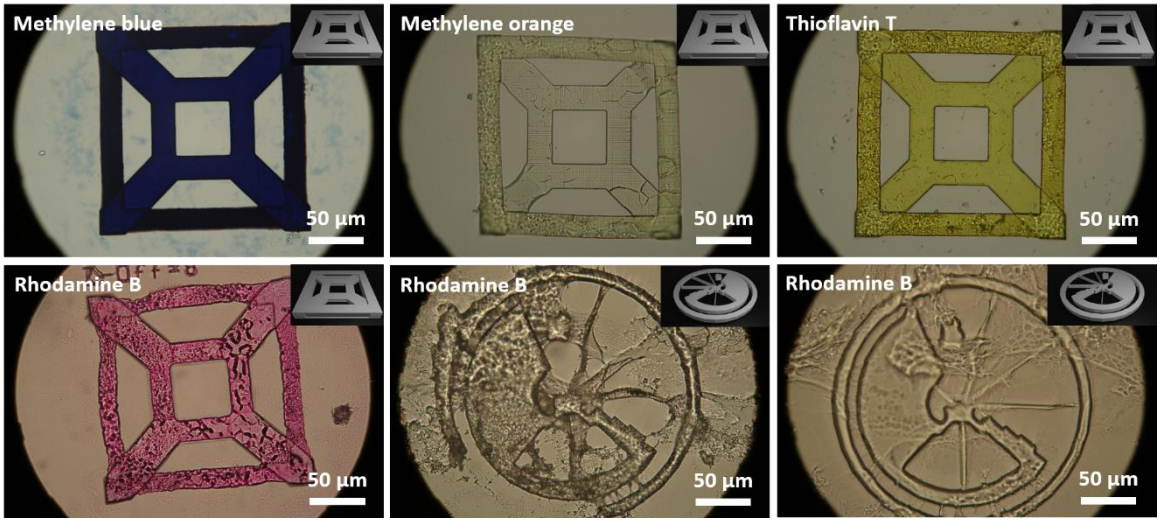

Figure 3.32. Optical microscopy images of microstructures after core removal and exposure to a solution of **MB**, **BY1**, **MO** and **RhB**. The model of the printed structures is shown in the top right corner of the images.

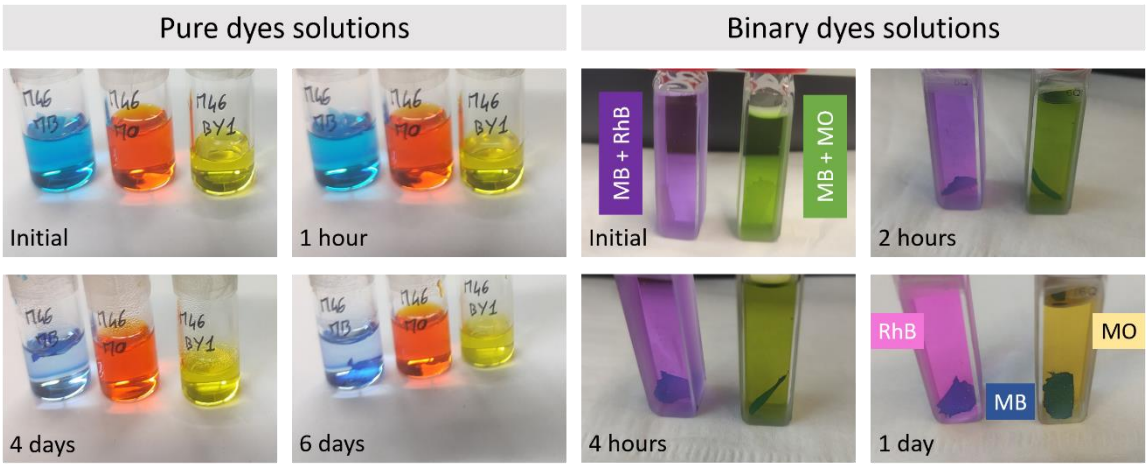

Figure 3.33. Photographs over time for the selective adsorption of dyes in polymeric films of a photoresist based on **TBIB:dA$_3$** for pure solutions of **MB**, **MO** and **BY1**, and for binary mixtures (**MB + RhB** and **MB + MO**).

A precise study of the adsorption process was carried out by UV-vis spectroscopy using macroscopic crosslinked films. The Col_h films with core removed were immersed in aqueous solutions of the dyes and the UV-vis absorption was followed over time. A first observation that can be made is the visual colour change of the dye solutions over time (**Figure 3.33**), which indicated the expected selectivity. By UV-vis (**Figure 3.34**), I showed that **MB** and **BY1** were adsorbed over time, as can be concluded from the decreasing absorption of the dye solutions. On the other hand, the absorption of the **MO** and **RhB** solutions did not decrease over time, indicating that the dyes remained in solution. The UV-vis analysis of pure dye solutions thus supported the expected selectivity of the nanoporous films for the absorption of small cationic molecules. The adsorption selectivity was further tested by exposing the films to binary **MB + RhB** and **MB + MO** solutions. For a binary **MB + RhB** solution, a clear size selectivity was concluded from the decreasing intensity of the **MB** absorption bands and from the stationary intensity of the **RhB** absorption band. Surprisingly, I could not obtain similar results for a **MB + MO** binary mixture. In this case, a clear decrease of the **MO** absorption band was observed. The same result was obtained when using indentical concentrations of **MB** and **MO** and carefully controlling the integrity of the polymeric matrix by FTIR, prior to adsorption analysis. It is not clear from which phenomenon this decrease arised, considering that the dye solution were not buffered, pH-dependent shortcomings can be envisaged as potential explanation.

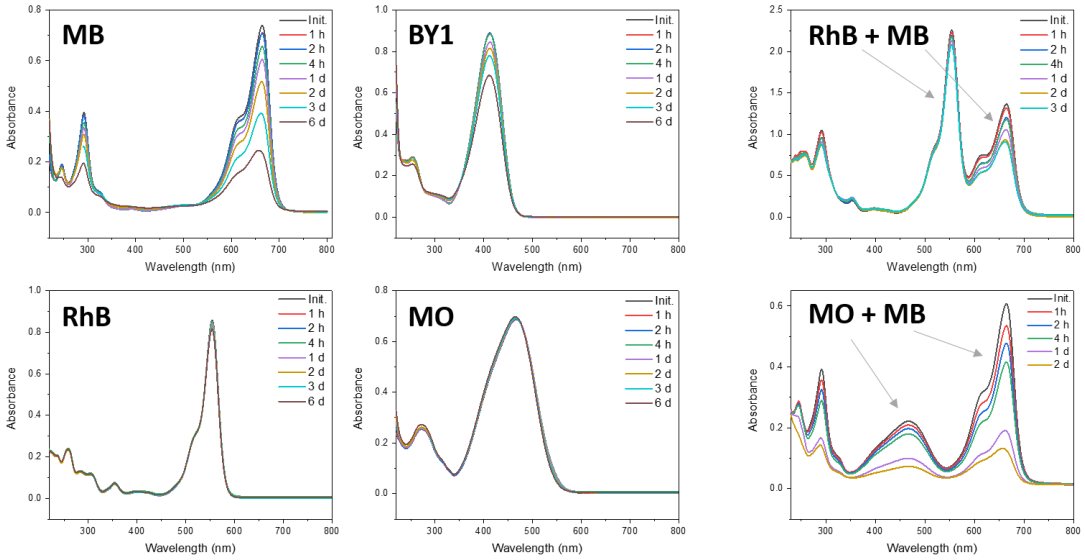

Figure 3.34. UV-vis study of the adsorption of methylene blue (**MB**), thioflavin T (**BY1**), rhodamine B (**RhB**) and methylene orange (**MO**) within the pores engendered by the removal of the **TBIB** templating core from a crosslinked film of **TBIB:dA$_3$**.

WAXS analysis of macroscopic films with **MB** or **BY1** adsorbed demonstrated the conservation of the Col$_h$ ordering, providing the last evidence of the stability of the arrangement throughout the entire fabrication, development, core removal and dye adsorption process (**Figure 3.35**).

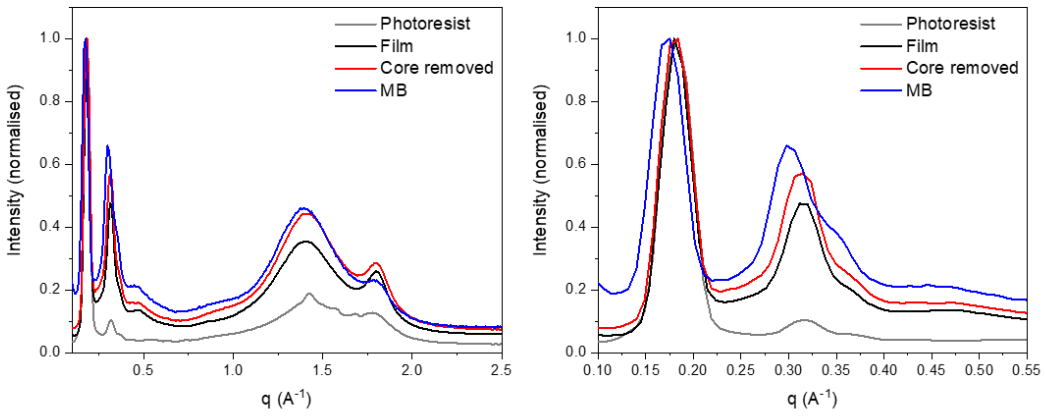

Figure 3.35. 1D projection of the WAXS data for **TBIB:dA$_3$** at each step presented in this chapter: as a non-crosslinked photoresist; as a crosslinked polymeric film before and after core removal as well as after the adsorption of **MB**.

Screening of other designs

Additional designs of Col_h mesogens have been studied. With these examples, I aimed to explore systems of greater simplicity or of different functionality. First, the sodium benzoate analogue of **dA**, **Na:dA** (**Figure 3.36**) was previously reported to self-assemble in a Col_h mesophase.[202] Secondly, using the same **M** and **dA** building blocks than presented previously, a change in the ratio used for the construction of a H-bonded assembly may lead to large structural changes. By using a ratio of 1:1 peripheral acid:core, I aimed to obtain H-bonded self-assemblies of six cores with six peripheral acids (**Figure 3.37**).

Also, I attempted to synthesise two different covalent discotic mesogens. Both molecules were prepared by the addition of **dA** groups on a central molecule by Steglich esterification. A three-fold esterification on 2,4,6-trinitrobenzene-1,3,5-triol led to a discotic mesogen with a high electron density concentrated on the central core, which was expected to have good LC properties (**Scheme 3.6**). And a four-fold esterification on tetrakis(4-hydroxyphenyl)ethylene afforded a photopolymerisable mesogen with a tetraphenylethylene (**TPE**) core (**Figure 3.39**). **TPE** is a rare example of an aggregation-induced fluorophore, by using this core, I aimed to investigate the potential Col_h behaviour of such mesogen as well as the opportunity of fabricating strongly fluorescent structures upon crosslinking.

Na:dA

Na:dA has the advantage to not require any pre-assembly step when compared to H-bonded discotic systems. The system consisting of a single component was aimed to be a more simple alternative to the complex H-bonded assemblies presented beforehand. **Na:dA** was previously reported to self-assemble as a thermotropic Col_h mesophase, or as a lyotropic hexagonal LC phase ($H_{||}$) when formulated with butylacrylate (8 wt%) and water (3 wt%).[202] In this work, I solely investigated the thermotropic LC properties of **Na:dA**.

Na:dA was synthesised by the simple deprotonation of **dA** with NaOH, the synthetic procedure and characterisation are available in chapter 6. Within the scope of this work, **Na:dA** was determined a clearing point of 58 °C by POM, what is quite lower than the expected value of 65 °C. Upon cooling, POM imaging unfortunately resulted in the observation of needles, syndromic of a crystalline phase.

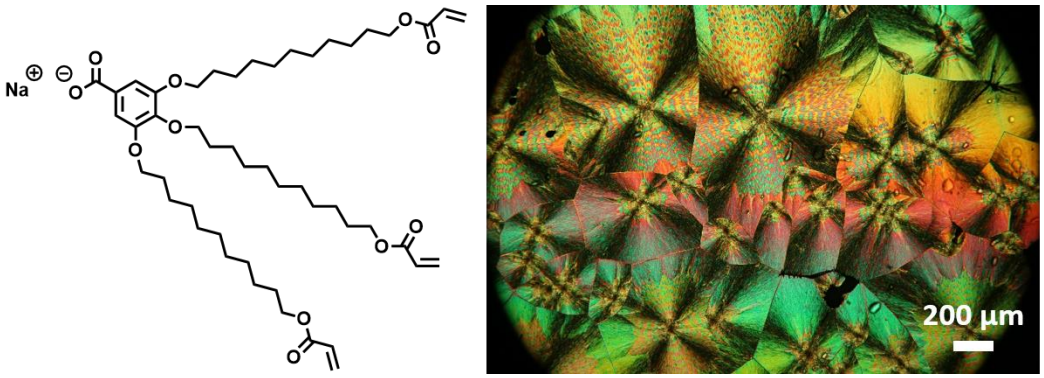

Figure 3.36. Chemical structure of **Na:dA** and POM image at room temperature after thermal treatment.

Assemblies using different core:dendric acid ratios

By modifying the peripheral acid:core ratio of the H-bonded assemblies from 3:1 to 1:1, I expected the formation of larger discotic H-bonded assemblies containing six cores and six acids.[281] In such a complex, six cores self-assemble by H-bonding to form a much larger core. For melamine cores, six emplacements remain free for the H-bonding of six carboxylic acid moieties. With this approach, I aimed to show the versatility of designs based on H-bonded assemblies by evidencing that a minor modification of the preparation procedure used before can lead to nanoporous materials with very different pores´ size. From exploratory POM screenings, a clearing point of 60 °C was observed for **M_6:dA_6**. The phase transition upon cooling showed the formation of needle-like structures, symptomatic of crystalline phases.[282] The WAXS data of **M_6:dA_6** indicated several close reflections in the small-angle region as well as a distribution of the like-liquid aliphatic correlation indicative of a fluidity to an extent. However, the q-values ratio of the measured reflection could not be attributed to a configuration in particular. Also, the q-values obtained did not correspond to an inter-columnar spacing in the order of the expected value of a = 7.58 nm, reported by Feringán et. al.[281] but were rather much smaller.

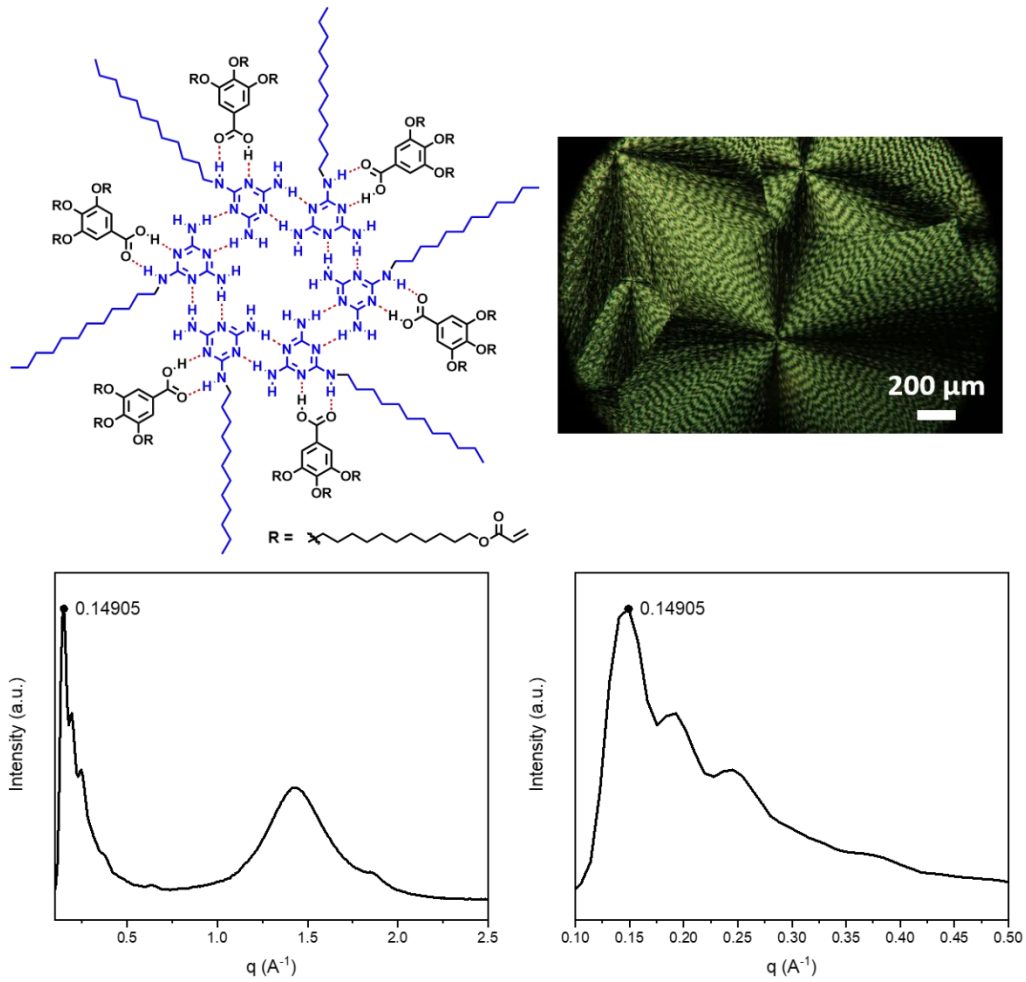

Figure 3.37. Chemical structure of **M_6:dA_6** and relevant characterisations. A POM image at room temperature after thermal treatment. WAXS data of a crosslinked film and zoom in the small-angle region of the spectrum.

Assemblies containing non-acrylated peripheral acids

A discotic molecule surrounded by simple aliphatic chains is by far the most reported design. This system offers a perfect platform for the exploration of the main **TBIB:dA_3** system detailed in this chapter. By removing the acrylate groups, the LC material becomes easier to handle as it is largely more chemically inert. I started by synthesising the corresponding dendritic acid 3,4,5-tris(dodecyloxy)benzoic acid (**dC12**) by simple three-fold addition of 1-bromoundecane to ethyl gallate and removal of the ethyl protection under basic condition. Assemblies using **dC12** were then prepared in the same way than their **dA** counterparts. **TBIB:$dC12_3$** showed a clearing point of about 240 °C and a transition to a LC phase at 205 °C. Upon transition to the mesophase, LC textures that can be assigned to a Col_h mesophase homeotropicallly aligned could be observed (**Figure 3.38**).[201] However,

in the lack of corresponding WAXS data, this assumption could not be confirmed. Effectively, **TBIB:dC12$_3$** was majorly used to interpret the POM results for other systems.

Instead, I investigated the possibility of using a combination of both the acrylated dendritic acid **dA** and the purely aliphatic dendritic acid **dC12**. In this way, one can understand whether the addition of inert peripheral acids could limit the effect of pre-polymerisation on **TBIB:dA$_3$** analogues. An increased control on the reactivity of the Col$_h$ photoresist could provide more freedom upon the thermal manipulation of the substances thus leading to their handling.

I prepared two assemblies using **dA**:**dC12** ratios of 1:2 (**TBIB:dC12$_2$dA**) and 1:1 (**TBIB:dC12$_{1.5}$dA$_{1.5}$**). However, POM analysis showed that the **dC12** content used were not sufficient to strongly modify the Col$_h$ behaviour of the assemblies containing the two different dendritic acids (**Figure 3.38**). Moreover, crosslinking tests by UV-irradiation evidenced the low performances of those compounds as photoresists. This last observation in particular made them badly adapted for our aim of processing Col$_h$ LCs by light-triggered 3D printing.

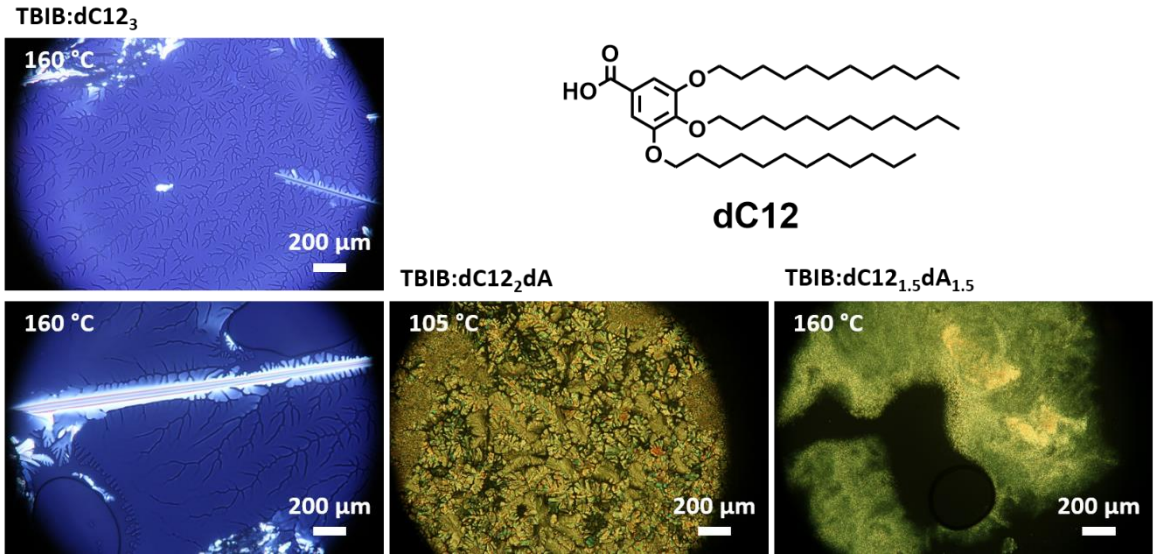

Figure 3.38. Chemical structure of **dC12** and POM analysis of **TBIB:dC12$_3$**, **TBIB:dC12$_2$dA** and **TBIB:dC12$_{1.5}$dA$_{1.5}$**.

Covalent discotic mesogens

Furthermore, I tested two different designs of fully covalent discotic molecules. A first one was based on a 2,4,6-trinitrobenzene-1,3,5-triol core. Through the three-fold attachment of **dA** groups on this core by Steglich esterification, I obtained a large, fully

covalent discotic mesogen. However, I could again not evidence any satisfying Col_h behaviour of the compound.

Using a highly polar inner core was expected to favour the formation of Col_h by phase segregation. **NO2:dA$_3$** (**Scheme 3.6**) was synthesised by the esterification of 2,4,6-trinitrobenzene-1,3,5-triol and **dA**. Initially attempted using dicyclohexylcarbodiimide (DCC), it was fast observed that a clean separation of the pure **NO2:dA$_3$** and dicyclohexylurea (DCU) was challenging. This was addressed by using 1-ethyl-3-(3-dimethylaminopropyl)carbodiimide (EDC) in place of DCC. In this case, the pure **NO2:dA$_3$** was isolated after flash column chromatography, in 41 % yield. The detailed synthetic procedure and characterisation is described in chapter 6. The discotic mesogen was further analysed for its LC properties by DSC, **Figure 6.1**. Unfortunately, no obvious clearing and mesophase formation could have been observed in this manner. Initially envisaged as a simplified platform for the study of the microprinting of columnar LC by two-photon laser printing, the investigation on **NO2:dA$_3$** were abandoned based on the DSC results.

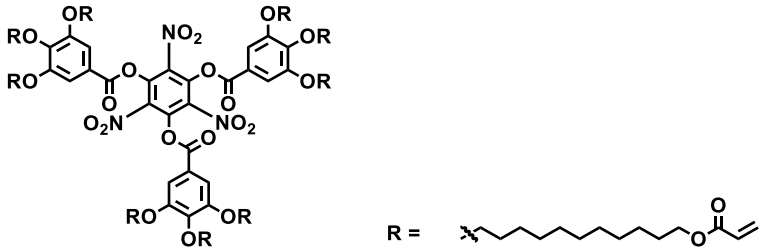

Scheme 3.6. Chemical structure of **NO2:dA$_3$**.

A second design was based on a TPE inner core. TPE is a fluorophore that has the particularity to improve its fluorescence yield upon aggregation, or more generally by the restriction of its molecular vibration. Such a fluorophore is designated as “aggregation-induced emission” (AIE)[283-285] in opposition to the “aggregation caused quenching” (ACQ) observed for most of other fluorophores.[284-288] The behaviour of fluorophores exhibiting AIE is mostly influenced by their properties in solution and the pathways that are then available for non-radiative decays. In the case of TPE, the rotation of the phenyl moieties offers a very efficient pathway for energy dissipation that quenches their fluorescence. When in solid state, the aggregation of the fluorophores restricts the rotation of the phenyl groups, making fluorescence a most profitable decaying pathway.[288-290] In the solid state, conventional luminophores experience an ACG due to the strong overlap of their π-

systems. These interactions strongly influence the energetic configuration of the luminophores when found in aggregates, by energy transfer or modification of energetic levels by conjugation. Unlike such fluorophores, the inter-molecular interactions in-between the TPE molecules of an aggregate are quite insignificant, making the luminophore fairly insensitive to the later effect. In spite of these low inter-molecular interactions, Schultz et. al.[291] reported that an adapted mesogen design based on **TPE** could preferentially arrange into columnar LC.

In this part, I aimed to see if a design containing terminal acrylate groups would behave similarly. And, moreover, whether this rare class of material could be transposed to 3D printing. Exploratory UV-vis measurements demonstrated that **TPE:dA$_4$** only possessed a weak absorption at 390−395 nm, which theoretically allows its use for two-photon laser printing at 780 nm. A clearing point was observed at 39 °C by POM and no birefringence could be observed upon cooling. Also, WAXS data did not provide any strong evidence of the formation of an ordered phase. Based on the previous results, it can be concluded that **TPE:dA$_4$** most likely remained amorphous. No further investigation was performed on the compound. **TPE:dA$_4$** was designed to be an improved compound, when compared to the compounds synthesised by Andreas Ganzbuhl (KIT) in his work. **TPE:A** and **TPE:A$_2$** consisted in a TPE core substituted with one and two undecyl aliphatic side chains carrying terminal acrylate group, respectively. The POM study of **TPE:A** and **TPE:A$_2$** highlighted the formation of crystalline needles, also, these compounds suffered from their low acrylate contents during crosslinking under UV-irradition or microprinting. More precisely, **TPE:A** could not be crosslinked by UV-irradition, and attempts of the printing of **TPE:A$_2$** remained unfruitful. Details about **TPE:A** and **TPE:A$_2$** can be found in the dedicated report.

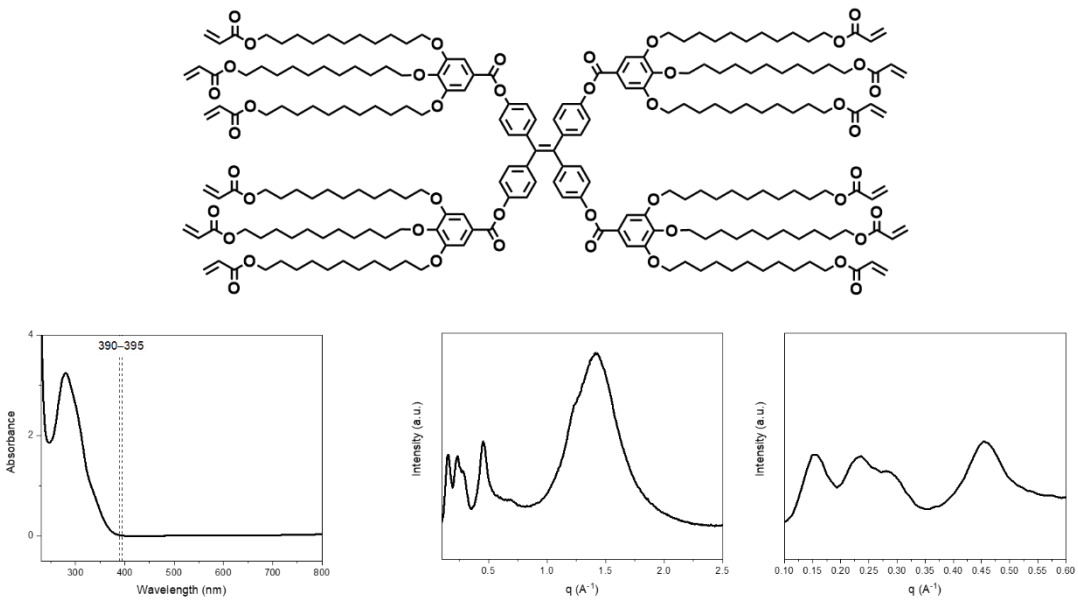

Figure 3.39. Chemical structure of **TPE:dA$_4$** and associated analysis. From left to right, UV-vis absorption spectrum with a highlight of the 390−395 nm region, WAXS dat for a crosslinked film, and a zoom in the small-angle region.

Chapter 4 MICROPATTERNING OF AMORPHOUS POROUS MATERIALS

The micrometer sized fabrication of functional multimaterial objects is a key point for the fabrication of complex multifunctional devices or architechtures, but remains a difficult challenge. To date, traditional lithography is the most advanced technique for the fabrication of multi-material devices with micro- to nano-scale definition.[292] However, lithography relies on the use of photomasks, each photomask being usable for a single design.[293] The use of additive manufacturing techniques, such as vat photopolymerisation techniques, thus become handy in the sense that geometries can easily be adapted on the spot. Two-photon laser printing has readily proven its potential for the fabrication of multimaterial objects.[294] Nevertheless, a multi-step fabrication of functional photoresists remains a time-consuming,[295] and challenging process as advanced optimisation may be required at each step, what greatly limits the material versatility of the strategy.[119, 296-298]

Discontinuous dewetting is a powerful and versatile method for the patterned surface deposition of functional material.[299-301] The method relies on the utilisation of surfaces having considerable affinity difference, hence confining the solution on the regions of greatest affinity. Upon solvent evaporation, the solute will thus be selectively deposited on these area. Thanks to its simplicity, scalability and versatility, discontinuous dewetting has been applied for the fabrication of optical waveguides,[302] flexible electronics[303] or devices for miniaturised biological screenings.[304]

In this chapter, I will detail our work on the two-photon laser micropatterning of DLP printed superhydrophilic porous objects, by the photografting of hydrophilic hydroethyl acrylate groups. The creation of hydrophilic patterns on the superhydrophobic matrices allow the site-specific deposition of aqueous solution/supensions on the hydrophilic regions (by discontinuous wetting). The micro-scale definition and the design freedom provided by two-photon lithography allows the drawing of a theoretically endless variety of pattern

shapes in a three-dimensional manner. Once cryo-dried, the objects with a patterned discontinuous polarity were tested for material deposition by discontinuous dewetting. The method was first tested and optimised by the deposition of an easily traceable rhodamine B (**RhB**) dye. Once the methology has been established, we investigated the versatility of the method for the site-specific and material-independent deposition of functional compounds (**Figure 4.1**).

This project was carried out in collaboration with the group of Prof. Pavel A. Levkin (Institute of Biological and Chemical Systems – Functional Molecular Systems (IBCS-FMS), Karlsruhe Institute of Technology (KIT)). They provided their experience with the handling and the printing of superhydrophobic porous materials by DLP, as well as their experience with discontinuous dewetting. My main contribution was development of the micropatterning protocols as well as the characterisation of the funtionalised structures.

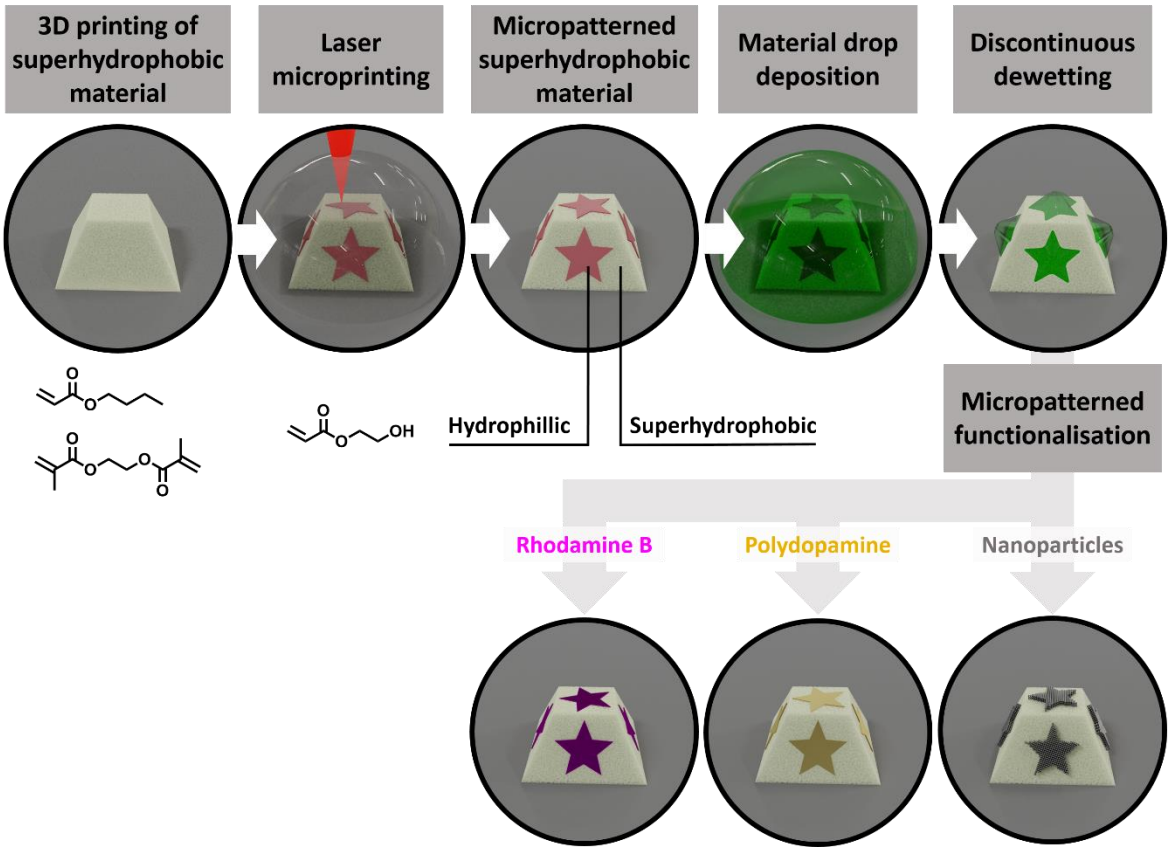

Figure 4.1. Overview of the project described in this chapter. Superhydrophobic truncated pyramids are produced by DLP. A 3D micropatterning is then achieved by two-photon laser printing using hydroxyethyl acrylate, leading to a discontinuous hydrophilic-superhydrophobic object. The micropatterned objects can be functionalised by the discontinuous dewetting of aqueous solutions/suspensions, in a material-independent manner.

DLP printing of superhydrophobic structures

Despite the 3D printing of the material of interest is a known process, the geometries and scale of the DLP printed objects were adapted within the scope of this project to enable their subsequent patterning by two-photon laser printing. Due to technical constraints related to the working distance of the objective used for the patterning step (25x, NA = 0.8; working distance = 380 µm), structures of more than about 250 µm in height could not safely be worked with, considering that the Dip-in printing mode was used. Practically, as the *z*-position was adjusted with respect to the photoresist-glass interface, it was necessary that the DLP structures could be located in-between the substrate and the objective, with minimal risk to get in contact with the objective. Additionally, we aimed to study the three-dimensional patterning of the DLP structures, to do so we considered truncated pyramid structures. By not having fully vertical side faces, the truncated pyramid geometry allowed to study the 3D patterning of DLP printed objects as it circumvented the shadowing effect that could be observed for simple right-prisms. The height constraint and targeted geometry required a specific use of DLP.

Conventional DLP printing of truncated pyramids of the desired dimensions was challenging regarding the resolution of the technique. The targeted geometry was a truncated pyramid with dimensions of 400 µm × 400 µm at the base, 200 µm × 200 µm at the top at 200 µm in height. Screening trials demonstrated some instabilities at this scale due to (i) the height of each slide, and to (ii) the required extremely precise setting of the holding stage along the *z*-axis. The height of each individual stage lead to a staircase-like appearance of the side faces.[305] This was considered a minor issue as, as will be detailed in the following part, comfortable error margins were used during the patterning step. As a matter of fact, large volume around the theoretical surface location were scanned to ensure the effective scanning of the entire surface, taking its roughness into account. Unless major shadowing effect, caused the opacity of the material, a different effective appearance of the side faces should only have little effect on the efficiency and quality of the micropatterning by two-photon laser printing. More problematically, the DLP system showed inconsistency in the location of the first slide along the *z*-axis, leading to weakly attached objects of uncontrolled height.

For the printing of small structures, we observed that the initial position of the stage could have a dramatic effect on the printed objects. Two main cases can be differenced, in a the

first one, a significant part of the structures was not printed, limiting our investigation for the three-dimensional patterning of the super-hydrophobic objects. On the other hand, the structures can be attached to the surface by the photocrosslinking of the ink in-between the first slide and the supporting stage, with a conic-shaped attachment link (shape caused by depletion of the UV-beam within the ink). This lead to the structures being dramatically higher than expected, which was crippling in the context of our project. Also, this lead to a greatly reduced anchoring surface area of the objects on the supporting substrate and thus to their likely detachment. Some example of such printed structures are shown in **Figure 4.2**.

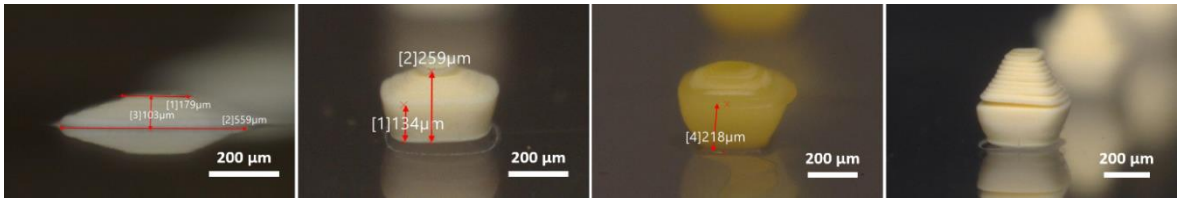

Figure 4.2. Optical microscopy images of truncated pyramids printed by conventional DLP methodologies.

Instead, the truncated pyramid geometries were constructed by making direct use of the depletion of the light beam in the ink. The glass substrate was placed at the bottom of the vat and the truncated pyramid were constructed through a single irradiation. Thanks to the depletion of the beam, the obtained objects contained angled side faces. The decreasing energy of the beam throughout impinging the polymerised photoresists leads to a sudden stop of the crosslinking events due to effective light intensity dropping below the crosslinking threshold. As a result, the printed truncated pyramids contaned a reasonably flat top surface. Apart from allowing for reproducible fabrication of a determined geometry (**Figure 4.3**), this special procedure induces a noticeable reduction of the printing time (2 min), as no stage movements are required.

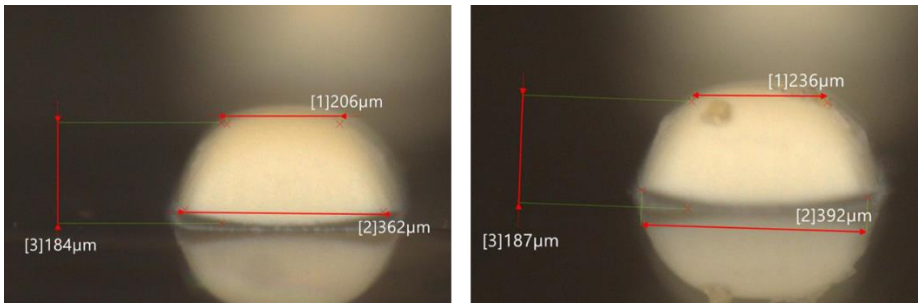

Figure 4.3. Optical microscopy images of truncated pyramids printed by DLP using the depletion-assisted approach.

Chemical considerations

DLP does generally not lead to a fully crosslinked polymeric material, but often leaves a good part of the reactive groups unreacted. A common approach for the improvement of the material properties of DLP-printed objects resides in a post-processing UV-curing of the fabricated objects that increases the crosslinking density and provides the printed parts with better mechanical properties.[306] In the present work, we instead used this feature as an opportunity for the photografting of a hydrophilic photo-reactive species during the patterning step.

The patterning is achieved via two-photon laser printing by scanning a volume that corresponds to a right-prism based on the desired pattern, and making use of a mixture of hydroxyethyl acrylate and Ig369 (2 wt%) as photoresist. The photo-induced polymerisation was theorised to lead to the attachment of hydrophilic HEA moieties on the superhydrophobic object by free-radical polymerisation. A pathway in which a preliminary oligomerisation of HEA occurs prior to its attachment can be argued. Within the scope of this project, we mainly explored the practical aspect of the fabrication process and did not deeply explore the chemical mechanisms involved. Hence, we are currently incapable of providing the reader with strong evidences supporting our hypothesis in that regard. Nonetheless, an alternative pathway in which oligomers are grafted on the superhydrophobic objects remains unlikely to significantly alter the quality of the patterning and the aimed reversal of the wettability of the patterned areas.

Even though we did not study the grafting mechanism in fine detail, some observations went in the sense of our theoretical model. First, FTIR analysis of the DLP printed material showed the effective presence of a C=C stretch band at 1635 cm^{-1} corresponding to the vinyl moieties of the (meth)acrylate groups (**Figure 4.4**). Also, it was observed that protecting the DLP printed structures from ambient light exposure resulted in much more reliable grafting, which suggests the importance of the photoreactive groups of the DLP objects.

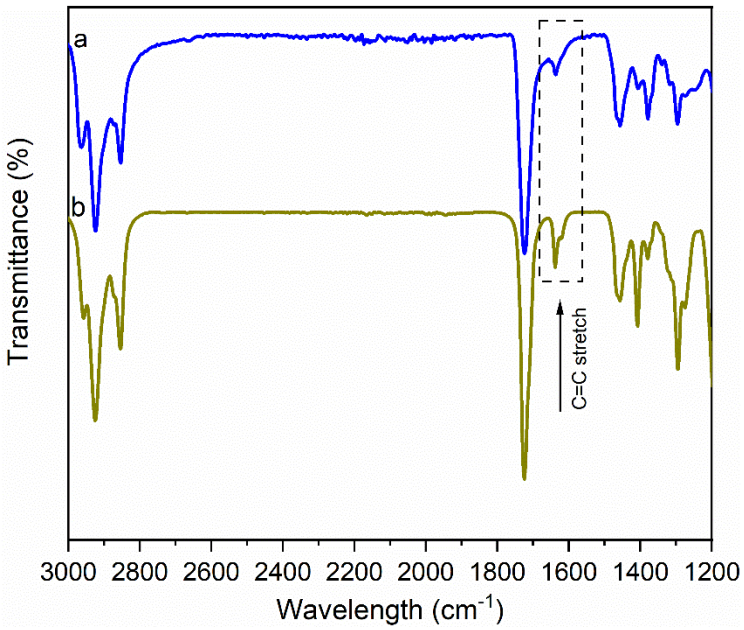

Figure 4.4. FTIR spectra of (a)the DLP-printed object and (b) the ink solution used for DLP printing.

Then, the photographting of hydroxylethyl methacrylate in place of hydroxyethyl acrylate did not result in any patterning. This indicates the necessity of using a monomer with a relatively high reactivity to obtain a patterning. Time-of-flight secondary ion mass spectrometry (TOF-SIMS) also indicates a high concentrations of $CH_3CH_2O^-$ fragment on the patterned regions, supporting that the affinity difference between the patterned and non-patterned regions was effectively a consequence of the high concentration of hydroxyethyl moieties in the patterned region. By TOF-SIMS, the signals of C_2OH^- (m/z = 41.01 Th) and $C_2H_3O_2^-$ (m/z = 59.03 Th) fragments from HEA for example, as well as PO_2^- (m/z = 62.98 Th) and PO_3^- (m/z = 78.95 Th) fragments from the Ig819 photoinitiator were recorded. Finally, the finding of the hydroxyethyl groups at the end of the fabrication process indicates their strong adhesion to the DLP printed objects, considering the numerous expositions to good solvent throughout the fabrication process. Effectively, the micropatterned objects were stored in acetone prior to their cryo-drying in supercritical CO_2. Based on these observation, a physical adhesion of the hydroethyl moieties on the DLP printed objects in reasonably unlikely.

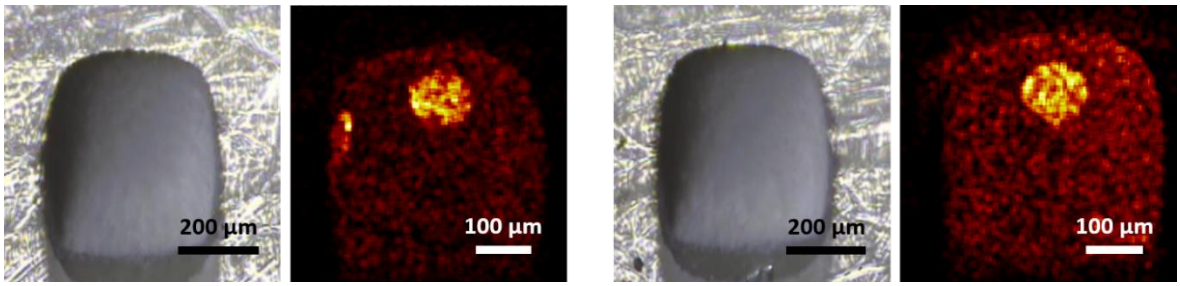

Figure 4.5. Two examples of the TOF-SIMS analysis of the photografting of HEA on the superhydrophobic structures. For both, microscope image of the patterned truncated pyramid analysed (left) and sum of the signals for C_2OH^- (m/z = 41.01 Th), $C_2H_3O_2^-$ (m/z = 59.03 Th), PO_2^- (m/z = 62.98 Th) and PO_3^- (m/z = 78.95 Th).

Optimisation of the patterning process

First, the optimisation was focused on the generation of a well-adapted 3D file and its convenient placing on the existing DLP structures. Due to the rough texture of the truncated pyramids as well as their observed swelling in the HEA resist used for patterning step, we chose to use comfortable margins to avoid issues related to geometry factors. Also, the determination of the *z*-position of the top surface of the truncated pyramid (polymer-photoresist interface) could only be determined with a low precision. Instead, we decided to use the resist-glass interface as a basis for the *z*-position. By scanning cylinder of a 150 µm diameter and 100 µm height at various positions around the theoretical height of the top surface, we observed that a 60/40 location (µm below/µm above) of the cylinder with respect to the theoretical *z*-position of the top surface was optimal for the reproducibility of the patterning. The patterning of the side faces was achieved using geometries where the targeted pattern was drawn as a 100 µm tall right-prism based on this pattern that was angled to be perpendicular to the theoretical side face. In the scope of this project, no shortcoming related to this procedure was observed and thus did not require systematic optimisation.

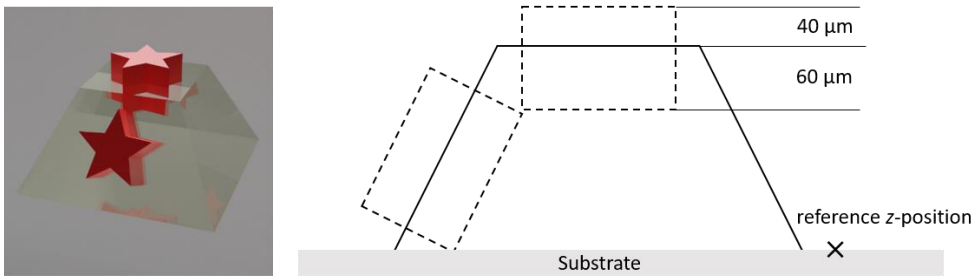

Figure 4.6. 3D and schematic representation of the volume scanned for the micropatterning of truncated pyramids. Left: the volumes scanned for the drawing of star-shaped patterns are shown in red, the truncated pyramid with its theoretical dimensions is shown as a yellowish glass. Right: Side-view cut of the volumes scanned. The truncated pyramid is represented on a substrate and the utilised reference interface is indicated with a cross. For clarity, the HEA-based photoresist is not displayed.

As previously mentioned, the nanoporosity of the DLP printed truncated pyramids are fundamental for their superhydrophobicity. In order to have patterned structures with later optimal behaviour toward discontinuous dewetting, the integrity of the nanoporosity is primordial. An overexposure of the DLP structures during the patterning process degraded their texture, hence leaded to a decreased patterning definition. A loss of porosity in the close periphery of the pattern induced a heat-triggered decreased water repulsiveness, which results in a "shadowing" upon functionalisation. On the other hand, an insufficient exposure lead to inconsistency of the patterning caused by sparse photografting. Therefore, a good balance had to be found, for which a qualitative and reproducible patterning can be achieved with minimal or no degradation of the texture of the DLP structures. Patterning parameters were investigated by screening variable values of scanning speed and laser power for the patterning by two-photon laser printing. The patterning quality was judged via the deposition of **RhB** on the patterns by discontinuous dewetting and the imaging of the patterns by optical microscopy. Optical microscopy can already demonstrate some altering of the material at high laser power, where bubbles (resulting from a local melting of the DLP structures during patterning) can be observed, noticeably on the side patterns. In particular, we used scanning speeds of 2 mm s^{-1}, 5 mm s^{-1}, 10 mm s^{-1}, 20 mm s^{-1} and 40 mm s^{-1} at a constant 35 mW laser power (**Figure 4.7**). Also, laser powers ranging from 5 mW to 50 mW with 5 mW increments at a constant scanning speed of 10 mm s^{-1} were screened (**Figure 4.8**). By minimising laser power and maximising scanning speed, we concluded that optimal patterning was obtained using a scanning speed of 10 mm s^{-1} and a laser power of 35 mW.

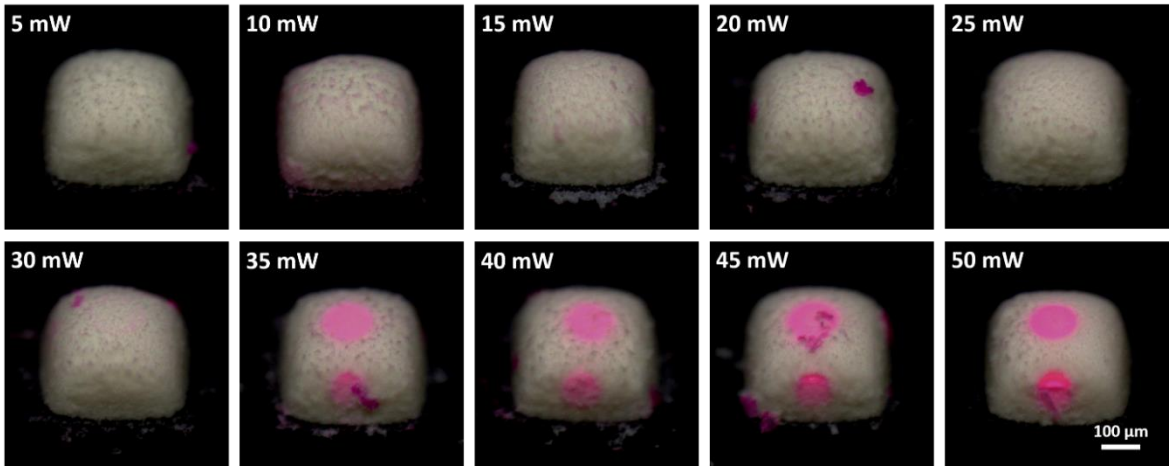

Figure 4.7. Patterning using a constant scanning speed of 10 mm s^{-1} at various laser powers.

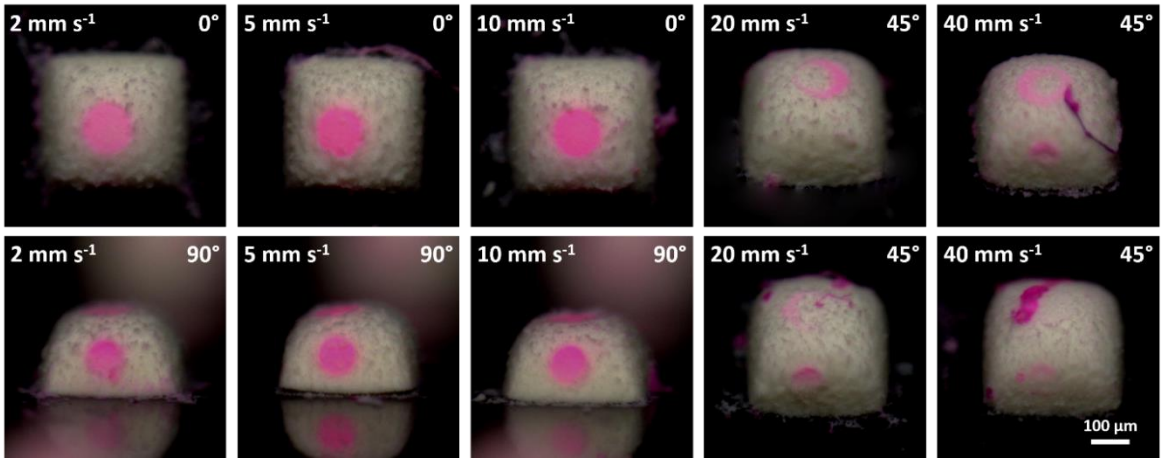

Figure 4.8. Patterning using a constant laser power of 35 mW at various scanning speeds.

The integrity of the texture can be more finely visualised by SEM. In the examples shown in **Figure 4.9**, one can see that the texture of the porous superhydrophobic structures was successfully retained. Upon exposure to an aqueous medium, a collapse of the material was observed and cuvette-like patterns were created (these can also be observed in the previous microscope images of **Figure 4.7** and **Figure 4.8**). This effect was attributed to the aggregation of the hydrophobic polymer upon wetting as well as to the capillary forces upon solvent evaporation. The altering of the texture upon exposure to an aqueous medium was not considered as problematic in the scope of this project. Moreover, the observation of this collapse confirms the complete wetting of the hydrophilic patterns upon exposure to aqueous solutions.

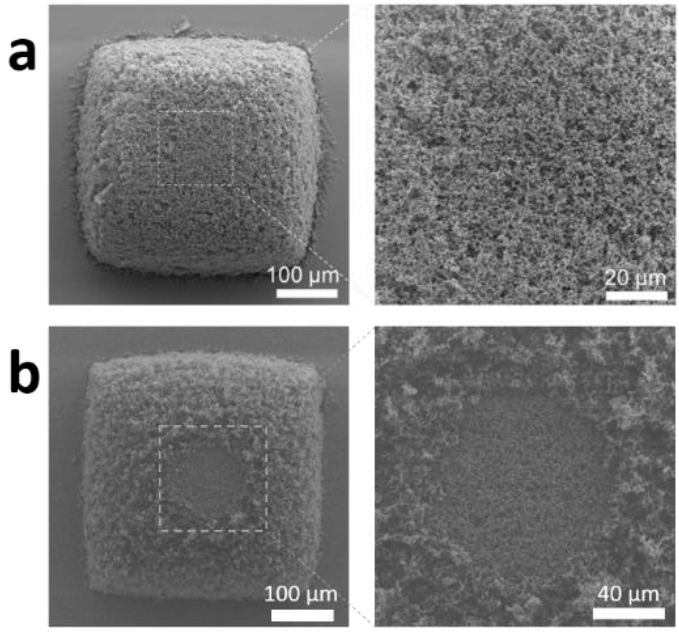

Figure 4.9. SEM image of a micropatterned structure (a) before and (b) after exposure to an aqueous solution of rhodamine B. In each case, a zoom in the pattern (right) is shown.

Pattern geometries were then designed to include features of increasingly challenging complexity. By going to a triangular shape, three sharp angles are included. In this step, the patterning method by discontinuous wettability was put to test as triangular patterns could not be a result of natural wetting and solvent evaporation, but required the segregation of the droplet on a pattern of corresponding shape. A star was designed to include more sharp angles and thinner features. A spiral contained further smaller features though no sharp angles. Text demonstrated that unlinked areas are similarly patterned without merging. Finally, an empty square showed that unlinked non-functionalised areas can be obtained. By visualisation using a **RhB** solution for the site-specific functionalisation of the super-hydrophobic objects, we were promisingly not able to evidence limitations of the method.

Similarly, we investigated the freedom in design of the patterning of the side face of the truncated pyramids. Good results were obtained for circular, triangular and star-shaped patterns. On the other hand, a spiral-shaped pattern showed the limitation in the patterned deposition of **RhB** on the sides of the structure.

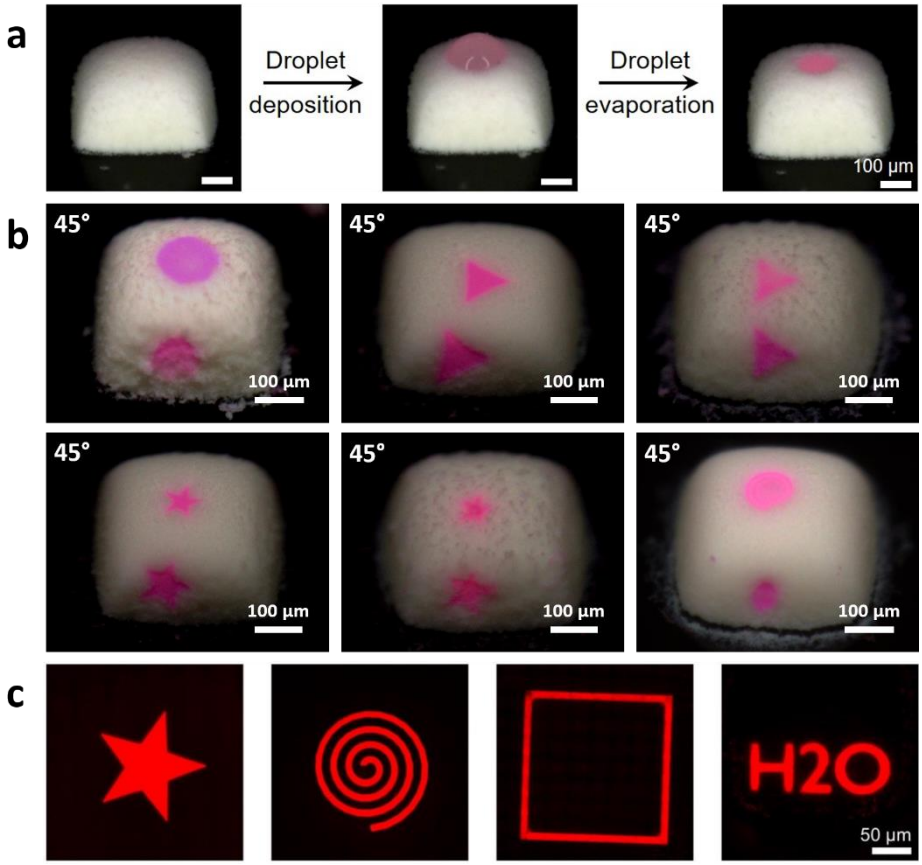

Figure 4.10. Micropatterned deposition of **RhB**. a) Microscpe images of the discontinuous dewetting of a solution of **RhB**. b) Microscope images of superhydrophobic truncated pyramids functionalized with **RhB** on the top and sides surfaces, using patterns shaped as a circle, triangle, star and spiral. c) Fluorescence microscopy images of top patterns, shaped as star, spiral, square and "H2O" text.

Material-independent functionalisation by discontinuous dewetting

The proposed two-step fabrication procedure presented herein was tested for its versatility. As just seen, we first explored the functionalisation of increasingly complex patterns with rhodamine B, from a simple circle to a triangle, a star, a spiral, an empty square or text. In a second step, we tested the deposition of various materials by discontinuous dewetting. We tested the deposition of polydopamine, the deposition of $FeCl_3$, followed by the site-specific $FeCl_3$-aided polymerisation of pyrrole, the deposition of silica nanoparticles as well as the deposition and sintering of silver nanoparticles toward conductive patterns.

Well-established techniques were readily reported to be capable of a two-dimensional patterned functionalisation of horizontal surfaces. However, only a few enabled the patterned functionalisation of three-dimensional objects. For example, electron-beam lithography,[307]

two-photon laser printing[308] and dip-pen lithography[309] were shown to be capable of the task. However, the chemistry and the procedures involved in the functionalisation have to be adapted and optimised specifically for each individual functional group added.[307-309] Those approaches would thus require big development efforts whenever the targeted functionality is modified. In contrast, our approach is not based on specific chemistry but is instead based on a general phenomenon which should theoretically only constrained by the ability of getting an aqueous solution or suspension of the targeted functional material.

Polydopamine is a substrate-independent surface coating that is widely used for its biocompatibility, anti-fouling, conductivity or catalytic activity.[310-312] We achieved the micropatterned deposition of polydopamine by immersing the micropatterned pyramids in a polydopamine tris-buffer (pH = 8.5) for 1 h. Thanks to its dark colour, the polydopamine patterns could be identified by optical microscopy. An elemental mapping of the polydopamine-coated pyramids was also achieved by TOF-SIMS which confirmed the successful micropatterning of polydopamine. In the obtained images, we could identify some polydopamine residues on the superhydrophobic surfaces. This can be attributed to the highly adhesive property of the coating agent.[313, 314] We would suggest that this could be improved by using a perfluorinated methacrylate in place of n-butylmethacrylate in the formulation of the DLP ink. However, we did not do any investigation of this other formulation in the scope of this project.

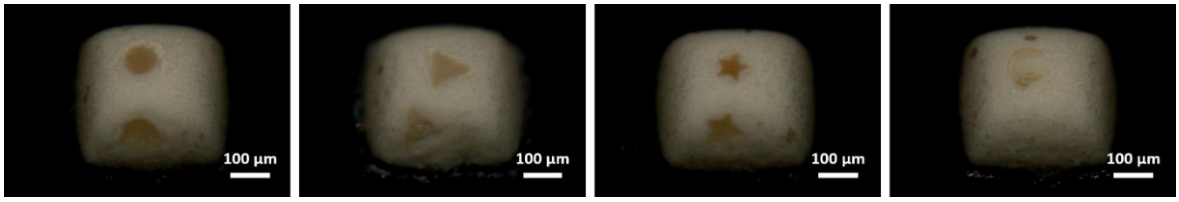

Figure 4.11. From left to right, circle, triangle, star and spiral micropatterns functionalized with polydopamine.

Secondly, we showed the possibility for elementary chemical reaction to occur on the patterns. In that regard, $FeCl_3$ was first micropatterned and the $FeCl_3$-functionalised structures were incubated in pyrrole vapour for 30 min, what leaded to the site-specific polymerisation of the later, both on the top and side faces of the pyramids.[315, 316] This example demonstrates the potential to performs simple chemical reactions directly on the patterns. Polypyrrole is known to be an organic conductive material. We therefore tested simple electrical circuit for conductivity. 10 µm thick line were drawn through the entire

block and two larger squares were added on the side of the pyramid as contacting electrodes. Unfortunately, no clear conductivity could have been measured, which highlight the need of an optimisation of the system. To access conductive patterns, we chose to focus on the optimisation of the geometry and the measurement procedure, eliminating shortcomings from the conductivity of the deposited material as much as possible. Therefore, we instead considered the deposition of silver nanoparticles followed by sintering (150 °C, 30 min). Prior to working with silver nanoparticles, we began by studying the deposition of nanoparticles, using silica nanoparticles.

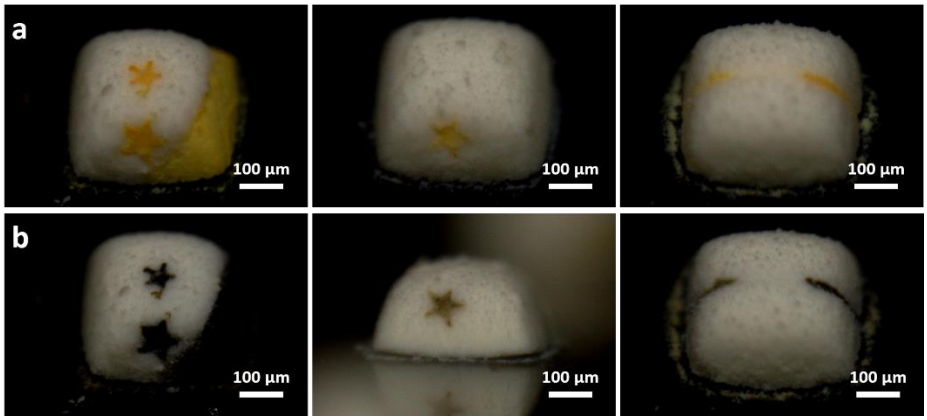

Figure 4.12. Microscope images of micropatterned structures a) functionalised with $FeCl_3$ and b) after exposure to pyrrole vapour.

The precise patterning of nanoparticles can be essential for fundamental research or for practical application in sensing, catalysis, advanced optics or organic electronics,[317-320] however remains challenging, on 2D and 3D surfaces.[304] Our investigations on silica nanoparticles showed results for their patterned deposition that were beyond expectations. Effectively, not only were good fidelity patterns obtained. But, we additionally observed, by SEM imaging, an arranged pilling of the nanoparticles.

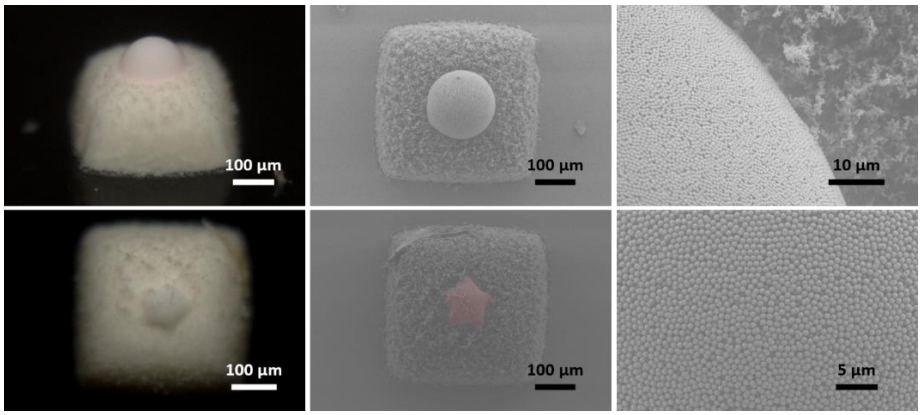

Figure 4.13. Microscope images and SEM images of micropatterned silica nanoparticles. A fake colouring of the bottom left SEM image was used to highlight the star-patterned deposition of silica nanoparticles.

Having demonstrated the patterning of nanoparticles, we went further with our aim of constructing conductive patterns. Preliminary tests showed that the effective conductivity of silver nanoparticles when deposited on the superhydrophobic substrate had an associated resistance of 40 to 50 $\Omega\ m^{-1}$ upon the deposition of 5 layers of the nanoparticles (a single layer did not lead to any measurable conductivity). Similar patterns as before (10 µm line with electrodes on the side) were first investigated. Those evidenced major issues related to the design and measurement procedures. Upon contacting, the thin conductive line was repeatedely broken forfeiting the measurement of any conductivity. The issue was addressed by thickening the conductive line to 150 µm, as well as by using a flexible thin gold wire in the prolongation of the contacting needle in order to limit the breakage of the pyramids upon contacting. We observed that the deposition of a single layer of the nanoparticles followed by sintering did not yield evident conductivity, similar the observations in the test experiments. Nonetheless, the direct deposition of additional layers led to a severe loss in patterning definition, in spite of significantly increasing the conductivity. By sintering the patterns after each deposition step, we could obtain conductive patterns deposited with 5 layers of silver, with great definition and design fidelity, as was demonstrated by optical microscopy and energy dispersive X-ray spectroscopy (EDX). The conductivity measurement of the so-produced silver patterns showed a conductivity with an associated resistance of 350 Ω. This finding showed the ability of the site-defined functionalisation method developed in our work to generate 3D conductive patterns on complex 3D objects.

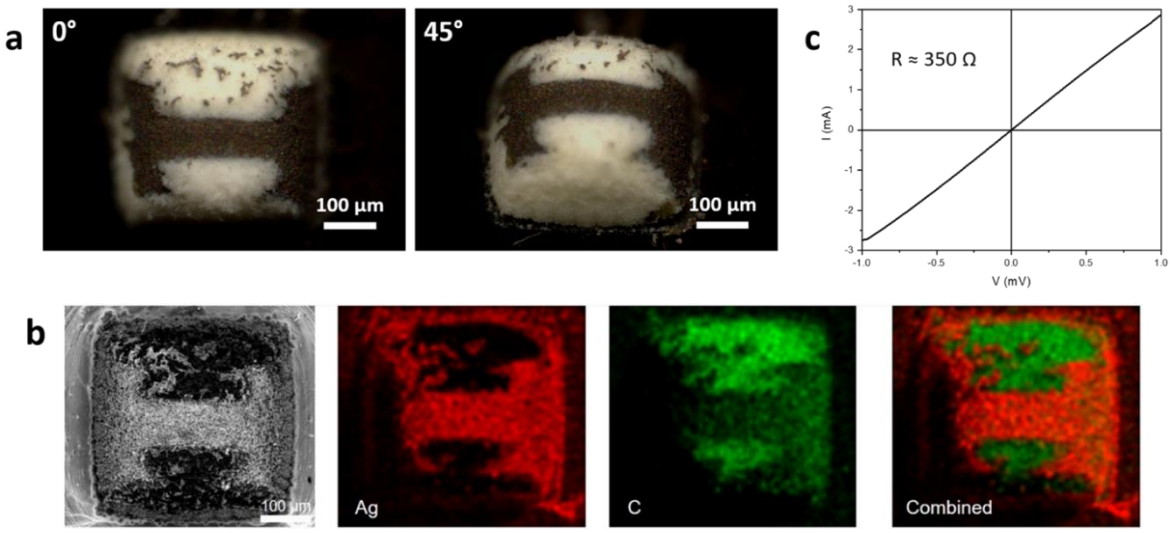

Figure 4.14. a) Microscopic images of Ag nanoparticles micropatterned onto superhydrophobic structures. b) SEM-EDX images of the Ag patterns showing the distribution of Ag. c) I-V curve for a pattern (150 µm line width, 300 µm line length) functionalised with 5 layers of Ag nanoparticles with sintering at 150 °C between each sintering and associated resistance.

Chapter 5 CONCLUSION AND OUTLOOK

The use of two-photon laser printing allowed the creation of two different types of porous materials based on either LCs photoresist (chapter 3) or amorphous materials (chapter 4), evidencing the versatility and potential of the approach.

In the first project detailed, I demonstrated the first example of the microprinting of crosslinkable Col_h LC photoresist, and proved the functional abilities of the structures fabricated by two-photon printing. The utilised LC photoresists were characterised in detail by POM and XRD. The characterised photoresists were then photocrosslinked by two methods. UV-irradiation afforded polymeric films which can be used as reference. The same photoresists were also fabricated by two-photon laser printing and 2.5D structures were printed with great definition, smooth surfaces and low shrinkage. The printing of structures of increasing height showed a limitation of about 30 µm, threshold above which significant loss in surface quality was observed. The limitation in structure´s height was attributed to the transluscency and diffractive properties of the LC photoresists. These factors together with the limited workable space and proximity effect in the *z*-direction made the inclusion of 3D features challenging in the context of my work. Highly nanoporous microstructures were engendered by the chemical treatment and core removal from the printed structures, and allowed for the size and charge selective adsorption of dyes. During the entire fabrication, the retention of LC arrangement was proven by POM and XRD. Future studies focussing on the printing of more transparent aligned mesophases may enlarge the printable span of the LC photoresists, and open more opportunities for the manufacturing of Col_h LCs into complex functional 3D structures.

In the second project, I developed a new approach for the fabrication of multi-material object by a two-step fabrication involving DLP and two-photon laser printing. In particular, porous superhydrophobic DLP-printed objects were post-functionalised with hydrophilic groups in a three-dimensional and shaped-defined manner, during a patterning step by two-photon laser printing. The photografting of hydroxyethyl acrylate on the porous polymeric

material was proven by TOF-SIMS and FTIR. The fabricated object of highly defined discontinuous water affinity could then be functionalised by the site-specific wetting of aqueous solutions/suspensions. The material-independency of the method was proven using rhodamine B, polydopamine, polypyrrole, sillica nanoparticles and silver nanoparticles. Within the scope of this investigation, I did not identify significant limitations in the versatility of the method, with respect to pattern design or material nature. The measured conductivity of patterned circuits functionalised with silver nanoparticles (associated resistence of 350 Ω) demonstrated the potency of the method for the fabrication of functional elements such electrical circuit. With respect to these results, I am confident that the method could be used as a simple and reliable platform for the fabrication of multimaterial devices in the future, for functional puposes or for the manipulation of biochemical species, for example.

Chapter 6 EXPERIMENTAL PART

Materials and methods

All the chemicals were purchased from conventional suppliers (Sigma Aldrich, TCI Europe, Thermo Fisher Scientific or ABCR) and used without further purification. Anhydrous solvents were purchased from Thermo Fisher Scientific. All procedures using anhydrous conditions were performed under an inert N_2 atmosphere using conventional Schlenk line techniques. All syntheses were performed under yellow light and BHT was used as a radical scavenger during the addition of acrylates functions. For these reactions, BHT was added again after the filtration of the dried organic extract and solvent evaporation was performed at 33 °C. During the recrystallization of **dA** and **dBzA** the heat exposure of the compound was limited to its minimum.

General

^{1}H-NMR and ^{13}C-NMR experiments were performed using a Bruker Ultrashield plus-500 spectrometer (^{1}H: 500 MHz, ^{13}C: 125.8 MHz). Chemical shifts are reported in part per million (ppm) and calibrated to the solvent as internal standard. DOSY data were obtained on a Bruker AM 400 (400 MHz). Chemical shifts are expressed in parts per million (ppm) and calibrated with respect to D_2O as internal standard. DOSY experiments were performed at 298 K using a LED-bipolar gradient paired with 2 spoil gradients (ledbpgp2s), with 16 incremental steps in the gradient strength, ramped from 2 % to 98 % of the maximum gradient strength. 8 scans were recorded per increment step. The gradient pulse length δ (p30) and diffusion delay Δ (d20) were specifically optimised in each case. The spectra were calibrated and phased using TopSpin. The pseudo-2D DOSY plots were computed using Bruker Dynamic Center, fitting the intensity decay as $I(g) = I_0 \exp\left(-D\ g^2\ \gamma^2\ \delta^2\ (\Delta - \frac{\delta}{3})\right)$.

ESI-TOF mass spectrometric data were obtained using a Bruker Daltonics micrOTOF-Q II.

POM

POM was performed using a Leica DMLM HC L35P equipped with an Instec HCS302 heating stage coupled to an Instec mK2000 temperature controller.

Two-photon laser printing

Two-photon laser printing was performed using a Photonic Professional GT instrument (Nanoscribe GmBH), using a 25×/NA = 0.8 objective lens (Zeiss LCI Plan-Neofluar 25×/0.8), using a laser with a central wavelength of 780 nm.

Microprinting of Col_h LCs

Sample preparation

A sample of the Col_h photoresist was sandwiched in between two glass slides, using a methacrylate functionalization for the glass slide receiving the printed structures. Prior to printing, the Col_h material was formed by controlled temperature processing using a heating stage, the thickness of the Col_h material was controlled using 4 layers of 16 µm aluminum foil as spacer.

Printing procedure

The microprinting was performed in oil-immersion mode using galvanometer scanners in the *xy*-plane and using a piezoelectric element in the *z*-direction. The printing jobs were constructed using a hatching distance of 0.3 µm and a slicing distance of 0.5 µm. If necessary, the printing jobs were split using 250 × 250 × 50 μm^3 rectangular domains. The focal point was manually set at the interface of the photoresist and the glass substrate before each job. The microprinting was achieved using a scanning speed of 25 mm s^{-1} and a laser power of 25 mW, or a scanning speed of 20 mm s^{-1} and a laser power of 20 mW. After microprinting, the microstructures were isolated by development of the sandwich cell in a $CHCl_3$:MeOH mixture.

The printing jobs were computed using DeScribe, and from .stl files constructed using Blender.

Micropatterning of superhydrophic porous materials

Sample preparation

The superhydrophobic truncated pyramids were stored wet in acetone after DLP printing, to avoid their collapse caused by drying. For micropatterning, the structures were taken out of acetone and rapidly topped with the patterning mixture, hydroxyethyl acrylate (98 wt%) and Ig819 (2 wt%).

Micropatterning of superhydrophobic structures

The micropatterning was performed in Dip-in mode, using galvanometer scanners in the *xy*-plane and objective translation along the *z*-axis. The focal point was manually set at photoresist-glass substrate interface prior to any lateral stage translation. The volumes for patterning were scanned with a scanning speed of 10 mm s^{-1} and a laser power of 35 mW. The scanned volumes were constructed with a hatching distance of 0.5 µm and a slicing distance of 1 µm. If relevant, the volumes were split using 250 × 250 × 100 $µm^3$ rectangular domains. The scanned volumes were constructed with the *xy*-origin along their centre-of-mass, and aligned on the truncated pyramid manually. A semi-automatic alignment of the scanned volumes on the truncated pyramids, using a preliminary manual coordinate spotting, was used for the conductive patterns. The scanned volumes for the surfaces parallel to the glass substrate were constructed as 100 µm tall right prisms of the patterns, located at 60 µm and 40 µm below and above the theoretical *z*-location of the surface. The scanned volumes for angled surfaces were constructed as 100 µm tall right prism of the patterns, and angled according to the theoretical angle of the surfaces.

FTIR spectroscopy

FTIR of microstructures

Infrared spectra of the microstructures were taken using an IR microscope (Bruker Hyperion 1000) coupled to a FTIR spectrometer (Bruker Tensor 27) using non-polarised light of a thermal light source. Atmospheric (water vapor and CO_2) absorption was suppressed by purging the whole beam path with dry air. The microstructures were located by means of white light microscopy, and were placed in the center of a circular aperture with a diameter of 105 µm. All spectra were taken in transmittance geometry with a resolution of 4 cm^{-1} and 100 scans. Relative transmittance spectra were calculated by normalizing the

measurements to the transmittance of the bare substrate at a position next to the microstructures.

FTIR of molecular species and polymeric films

FTIR were measured using ATR (iS50 FT-IF, Nicolet). The spectra were measured in a region of 4000 cm^{-1} to 400 cm^{-1} with a resolution of 4 cm^{-1} and 20 scans.

Wide-angle X-Ray scattering

Wide-angle X-ray scattering (WAXS) experiments were performed using a Xeuss 2.0 Q-Xoom (Xenocs SA, Grenoble, France) instrument, equipped with a Genix3D Cu ULC (ultra low divergence) micro focus source of Cu-Kα with an energy of 8.04 keV and a wavelength of 1.5406 Å, and a Pilatus3 R 300K detector (Dectris Ltd., Baden, Switzerland). The non-crosslinked photoresist was placed in a gel-holder, packed between two polyimide foils with a sample thickness of 0.5 mm. Crosslinked films were measured without substrate. The 2D scattering patterns were obtained using a sample to detector distance of 80 mm, resulting in a range of accessible scattering vector (q) from 0.10 to 3.85 $Å^{-1}$. We used an azimuthal integration of the scattering patterns to obtain 1D plots of the intensity I(q) versus q with $q=4\pi\sin(2\theta/2)/\lambda$, where 2θ is the scattering angle and λ is the wavelength of the Cu-Kα source. The measurement time was set to 1800 s and 600 s for the non-crosslinked photoresists and the crosslinked films, respectively.

SEM imaging

Microprinted Col_h LCs

The samples, sputter-coated with a 5 nm gold layer, were imaged using a Zeiss Leo 1530 scanning electron microscope operating at 2.0 kV. For volumes visualization, 45° tilted pin mounts were used.

Micropatterned superhydrophobic structures

The samples were sputter-coated with a 10 nm gold layer, and imaged using a Zeiss Leo 1530 scanning electron microscope operating at 5.0 kV.

UV-vis spectroscopy

UV-vis spectra were recorded on an Agilent Cary 5000 UV-Vis-NIR spectrophotometer.

Fluorescence confocal microscopy

Fluorescent *z*-stacks of 3D microstructures were carried out on a LSM 980 (Carl Zeiss, Germany) operating in the AiryScan SR-4Y mode. The images were taken using a 20x/0.8 objective. A 639 nm diode laser was used for excitation, and the emission at 670─720 nm was collected.

DLP 3D printing of superhydrophobic objects

The inks used for DLP 3D printing consisted of 30 wt% butyl acrylate as the monomer, 20 wt% ethylene glycol dimethacrylate (EDMA) as the crosslinker, 50 wt% 1-decanol as porogen, and 2 wt% Ig819 as photoinitiator. All components were mixed in an amber vial and sonicated (Elmasonic S 30H, 37 kHz, 80 W) for 30 min to obtain a homogenous ink solution.

The superhydrophobic 3D structures were printed using a commercial desktop DLP printer (Miicraft Prime 110) equipped with a LED projector (385 nm) with an intensity of 1.0 mW cm^{-2} at the vat, and a *xy*-resolution of 40 μm. After printing, the 3D-printed objects were immersed in acetone for 24 h to remove the porogen and the unreacted monomers.

Supercritical drying

The patterned objects were first immersed in acetone for 24 h. After complete solvent exchange, the structures were dried by CO_2 supercritical drying to avoid the collapse of the nanoporous structures.[39] Briefly, the patterned objects immersed in acetone were transferred to the chamber of the Leica EM CPD030 supercritical apparatus. Acetone was replaced by liquid CO_2 by repeatedly flushing with liquid CO_2. The chamber temperature and pressure were then increased to 35 °C and 90 bar to maintain the CO_2 in supercritical conditions. Finally, the chamber pressure was gradually decreased to atmospheric pressure to release the gaseous CO_2. The entire supercritical drying process took about 40 min.

Physical adsorption test of polyHEA on the DLP-printed porous structures

To clarify whether the polyHEA patterns on the surface are either due to covalent binding or physical adsorption of polyHEA, the DLP-printed porous structures were immersed into a 10 wt% polyHEA ($M_n = 3.2 \cdot 10^4$ g mol^{-1}, $M_w = 1.4 \cdot 10^5$ g mol^{-1}, analysed by gel

permeation chromatography using dimethylacetamide) in EtOH for 24 h. The structures were then treated with respect to the supercritical drying procedure presented before.

Material deposition

For the deposition of rhodamine B, silica nanoparticles and silver nanoparticles, the aqueous material solutions were first prepared as follows: 0.5 g L^{-1} **RhB** solution was obtained by dissolving **RhB** in water, 1 wt% silica nanoparticle suspension was prepared by diluting a commercial silica dispersion (5 wt% in water, d = 900 nm) with water, and 2 wt% silver nanoparticle suspension was prepared by diluting a commercial silver ink (30 wt% in ethylene glycol) with water. Using a pipette, a droplet (3 µL) of the solution was used to cover the micropatterned 3D structures and then pooled away. Due to the effect of discontinuous wetting, a daughter droplet was left on the hydrophilic patterns, while the unmodified regions were not wetted. Upon evaporation of the daughter droplet, the functional solute remained deposited on the wetted area. For silver nanoparticles, a further annealing step was performed at 150 °C for 30 min. For the deposition of polydopamine, the micropatterned 3D structures were immersed in a 2 g L^{-1} solution of 3-hydroxytyramine in tris-buffer (10 mM, pH = 8.5) for 1 h.

Digital microscopy of micropatterned structures

Digital microscope images of the samples were obtained by a Keyence BZ 9000. The images were taken at several angles.

Confocal microscopy of micropatterned structures

Confocal microscope images of the samples patterned with fluorescent dyes (Rhodamine B) were taken using a Zeiss LSM 800 instrument. The top surface of the samples was imaged. Due the highly porous nature of the 3D printed objects, they were not transparent enough to record 3D *z*-stack images.

Time-of-flight secondary ion mass spectrometry (TOF-SIMS)

TOF-SIMS was performed on a TOF.SIMS5 instrument (ION-TOF GmbH, Münster, Germany) equipped with a Bi cluster primary ion source and a reflectron type time-of-flight analyser. UHV base pressure was $< 2 \cdot 10^{-9}$ mbar. For good mass and lateral resolution, the Bi source was operated in "delayed extraction" mode providing unbunched Bi_3^+ primary ion pulses at 25 keV energy. Delayed extraction mode further reduced topography artefacts and

charging effects. Nevertheless, an electron flood gun still had to be used to compensate sample charging. The primary ion beam was scanned across a 500 × 500 µm^2 surface area, and 128 × 128 or 256 × 256 data points were recorded. Spectra were calibrated with respect to the omnipresent OH^-, C_2^-, C_2H^-, C_3^-, and C_3H^- peaks. Based on these datasets the chemical assignments for characteristic fragments were determined.

Conductivity tests

The electrode patterns were contacted by source measurement unit (SMU) needles prolonged with a thin gold wire. I-V curves from -1 V to 1 V were recorded using an Agilent 4156C parameter analyser. The resistance is extracted from the slope of the I-V curves and is computed on Origin.

Synthetic procedures

Core TBIB

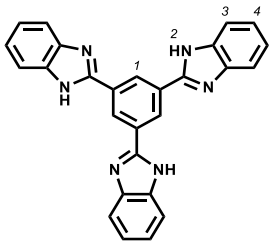

The **TBIB** core was synthesised according to a previously reported procedure.[272] o-Phenylenediamine (4.20 g, 20 mmol) and 25 mL of hot polyphosphoric acid were combined and stirred at 180 °C until a homogeneous solution was obtained. 1,3,5-Benzenetricarboxylic acid (6.49 g, 60 mmol) was added to the mixture, and the reaction was stirred at 240 °C overnight. The resultant dark blue melt was poured into 400 mL of cold water and neutralised with 5 M NaOH *aq* to pH ≈ 14. The crude product obtained by filtration was fully dried and further purified three times by sublimation at 400 °C at reduced pressure (1 mbar). ^{1}H NMR (500 MHz, DMSO-d_6): δ = 13.42 (s, 3H, Hb), 9.15 (s, 3H, Ha), 7.65 (m, 6H, Hc), 7.28 (m, 6H, Hd). ^{13}C-NMR (125.8 MHz, DMSO-d_6): δ = 150.4, 143.8, 135.4, 131.9, 125.5, 123.0, 122.0, 119.0, 111.8. HRMS, ESI, (m/z) $[M-H]^+$ calcd for $C_{27}H_{18}N_6$: 427.1672, found: 427.1644.

Acid dA

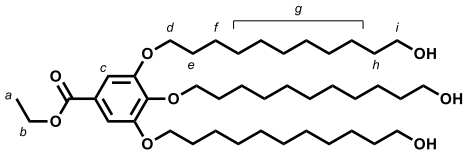

Ethyl 3,4,5-tris((11-hydroxyundecyl)oxy)benzoate (1): 1 was synthesised according to reported procedure.[321] Ethyl gallate (2.00 g, 10.1 mmol) and K_2CO_3 (14.00 g, 101 mmol, 10.0 eq) were suspended in anhydrous DMF (60 mL) under a N_2 atmosphere. The suspension was stirred vigorously at 75 °C for 30 min. 11-Bromoundecan-1-ol (7.60 g, 30.3 mmol, 3.0 eq) was slowly added at 75 °C, and the reaction mixture was stirred at 75 °C overnight. After the completion has been evidenced by TLC (1:1 EtOAc:DCM), the reaction mixture was filtered, evaporated and dried under reduced pressure, co-evaporation with water was used to remove the residual DMF. The residue was then taken in water and extracted in EtOAc (4 times, 350 mL total). The combined organic layers were dried over $MgSO_4$, filtered, evaporated and dried under reduced pressure. The crude product (4.35 g, 8.18 mmol, 81 % yield) was obtained as a colourless powder and used for further synthesis without purification. ^{1}H-NMR (500 MHz, $CDCl_3$): δ = 7.24 (s, 2H, Hc), 4.34 (m, 2H, Hb), 4.00 (m, 6H, Hd), 3.63 (m, 6H, Hi), 1.84−1.69 (m, 6H, He), 1.59−1.42 (m, 12H, Hf, Hh), 1.29 (m, 45H, Ha, Hg). ^{13}C-NMR (125.8 MHz, $CDCl_3$): δ = 166.6, 152.9, 142.4, 125.2, 108.1, 73.6, 69.3, 63.1, 61.1, 32.9, 30.4, 29.7, 29.7, 29.7, 29.6, 29.5, 29.4, 26.2, 25.9, 14.5.

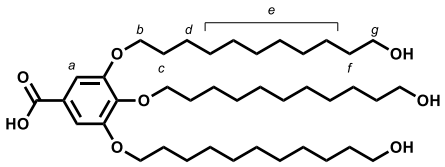

3,4,5-tris((11-hydroxyundecyl)oxy)benzoic acid (2): 2 was synthesised according to reported procedure.[321] **1** (4.35 g, 8.18 mmol) was dissolved in a solution of KOH (2.80 g, 49.7 mmol, 8.1 eq) in 3:1 MeOH:H_2O (80 mL) and the reaction mixture was refluxed overnight. After being cooled down, the reaction mixture was neutralised with 3 M HCl *aq* and extracted in EtOAc. The combined organic layers were dried over $MgSO_4$, filtered, evaporated and dried under reduced pressure. Recrystallisation from EtOAc afforded the pure **2** as a white powder (3.32 g, 4.88 mmol, 80 % yield). ^{1}H-NMR (500 MHz, $CDCl_3$): δ = 7.31 (s, 2H, Ha), 4.03 (m, 6H, Hb), 3.65 (m, 6H, Hg), 1.84−1.69 (m, 6H, Hc), 1.59−1.42

(m, 12H, Hd, Hf), 1.29 (m, 36H, He). ^{13}C-NMR (125.8 MHz, $CDCl_3$): δ = 170.4, 152.9, 143.1, 124.1, 108.7, 73.6, 69.3, 63.2, 32.8, 30.4, 29.8, 29.8, 29.7, 29.7, 29.6, 29.5, 29.4, 29.3, 26.1, 25.9.

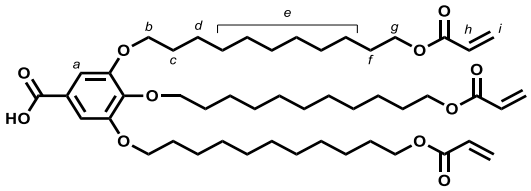

3,4,5-tris((11-(acryloyloxy)undecyl)oxy)benzoic acid (dA): The synthesis of **dA** was adapted from reported procedures.[270] A solution of **2** (500 mg, 0.74 mmol) and BHT (head of spatula) in THF (10 mL) was treated with *N,N´*-dimethylaniline (292 mg, 0.3 mL, 2.42 mmol, 3.3 eq) at room temperature and stirred at room temperature for 30 min. The mixture was then cooled down to 0 °C and treated with acryloyl chloride (220 mg, 0.2 mL, 2.42 mmol, 3.3 eq). The reaction mixture was then stirred at room temperature overnight. 5-6 drops of MeOH were added and the mixture was stirred at room temperature for 30 min. It was then topped with 1 M HCl *aq.* (15 mL) and extracted in EtOAc (4 times, 150 mL total). The combined organic layers were dried over $MgSO_4$, filtered, evoparated and dried under reduced pressure. The crude product was purified by recrystallisation from EtOH to afford the pure **dA** as a white powder (509 mg, 0.60 mmol, 82 % yield). ^{1}H-NMR (500 MHz, $CDCl_3$): δ = 7.31 (s, 2H, Ha), 6.41−6.38 (m, 3H, Hi), 6.14−6.09 (m, 3H, Hh), 5.82−5.80 (m, 3H, Hi), 4.15 (t, J = 6.7 Hz, 6H, Hg), 4.03 (m, 6H, Hb), 1.85−1.70 (m, 6H, Hc), 1.70−1.43 (m, 12H, Hd, Hf), 1.40−1.25 (m, 36H, He). ^{13}C-NMR (125.8 MHz, $CDCl_3$): δ = 166.5, 153.0, 143.2, 130.6, 128.8, 108.7, 73.6, 69.3, 64.9, 30.4, 29.8, 29.7, 29.7, 29.6, 29.5, 29.4, 29.4, 28.7, 26.2, 26.1. HRMS, ESI, (m/z) $[M-Na]^+$ calcd for $C_{49}H_{78}O_{11}$: 865.5436, found: 865.5362.

Acid dBzA

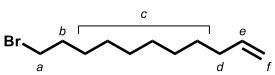

1-Bromo-10-undecene (3): 3 was synthesised according to reported procedure.[322] A solution of 10-undecen-1-ol (15.00 g, 88.08 mmol) in DCM (250 mL) was treated with CBr_4 (32.10 g, 96.89 mmol, 1.1 eq) and PPh_3 (25.40 g, 96.89 mmol, 1.1 eq) at 0 °C and stirred at

0 °C for 2 h. The reaction was quenched with H_2O and extracted with DCM (3 times, 800 mL total). The combined organic layers were dried over $MgSO_4$, filtered, evaporated and dried under reduced pressure. The crude residue was purified by flash column chromatography (DCM) to afford the pure product as colourless oil in quantitative yield. ^{1}H-NMR (500 MHz, $CDCl_3$): δ = 5.81 (m, 1H, He), 5.02−4.90 (m, 2H, Hf), 3.40 (t, J = 6.8 Hz, 2H, Ha), 2.04 (m, 2H, Hd), 1.85 (m, 2H, Hb), 1.47−1.24 (m, 12H, Hc). ^{13}C-NMR (125.8 SMHz, $CDCl_3$): δ = 139.3, 114.3, 34.2, 33.9, 33.0, 29.5, 29.2, 29.0, 28.9, 28.3.

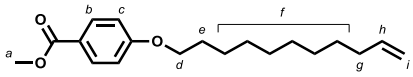

Methyl 4-(10-undecenyloxy)benzoate (4): 4 was synthesised according to reported procedure.[323] Methyl 4-hydroxybenzoate (6.63 g, 43.56 mmol) and K_2CO_3 (6.63 g, 56.63 mmol, 1.3 eq) were suspended in anhydrous DMF (240 mL) and the reaction mixture was stirred at 75 °C for 30 min. **3** (15.00 g, 45.74 mmol, 1.05 eq) was added at 75 °C and the mixture was stirred at 75 °C for 1 day. The reaction mixture was then filtered, evaporated and dried under reduced pressure. The residue was taken in DCM and washed with 1 M HCl *aq* (200 mL), H_2O (3 times) and brine. The organic layer was dried over $MgSO_4$, filtered, evaporated and dried under reduced pressure. The crude material was purified by flash column chromatography (1:4 n-hex:DCM) to afford pure **4** (11.65 g, 38.25 mmol, 88 % yield) as a white powder. ^{1}H-NMR (500 MHz, $CDCl_3$): δ = 7.97 (m, 2H, Hb), 6.90 (m, 2H, Hc), 5.81 (m, 1H, Hh), 5.01−4.92 (m, 2H, Hi), 4.00 (t, J = 6.6 Hz, 2H, Hd), 3.88 (s, 3H, Ha), 2.04 (m, 2H, Hg), 1.79 (m, 2H, He), 1.49−1.26 (m, 12H, Hf). ^{13}C-NMR (125.8 MHz, $CDCl_3$): δ = 167.1, 163.1, 139.3, 131.7, 122.4, 114.2, 68.3, 52.0, 33.9, 29.6, 29.5, 29.5, 29.2, 29.0, 26.1. HRMS, ESI, (m/z) $[M-Na]^+$ calcd for $C_{19}H_{28}O_3$: 327.1931, found: 327.1914.

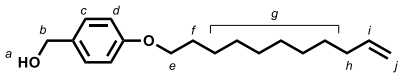

10- Undecenyl-1-oxybenzyl alcohol (5): 5 was synthesised according to reported procedure.[271] A solution of **4** (4.97 g, 16.32 mmol) in anhydrous THF (20 mL) was added to a refluxing solution of 2.4 M $LiAlH_4$ in THF (12.24 mL, 29.38 mmol, 1.8 eq). The reaction mixture was refluxed for 1.5 h. Moist THF was added to quench the remaining hydride. The

reaction mixture was acidified with 3 M HCl *aq* and dried under reduced pressure. The residue was dissolved in Et_2O (300 mL), dried over $MgSO_4$, filtered, evaporated and dried under reduced pressure. The crude product was recrystallised from n-hexane to afford the pure **5** (4.29 g, 15.52 mmol, 95 % yield) as a white solid. ^{1}H-NMR (500 MHz, DMSO-d_6): δ = 7.20 (m, 2H, Hc), 6.85 (m, 2H, Hd), 5.79 (m, 1H, Hi), 5.01 (t, J = 5.7 Hz, 1H, Ha), 5.01−4.91 (m, 2H, Hj), 4.40 (d, J = 5.6 Hz, 2H, Hb), 3.92 (t, J = 6.5 Hz, 2H, He), 2.01 (m, 2H, Hh), 1.68 (m, 2H, Hf), 1.47−1.25 (m, 12H, Hg). ^{13}C-NMR (125.8 MHz, DMSO-d_6): δ = 157.6, 138.8, 134.4, 127.9, 114.0, 114.0, 67.3, 62.6, 33.2, 29.0, 28.8, 28.7, 28.7, 28.5, 28.3, 25.5.

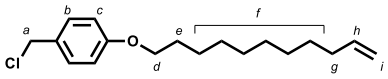

1-(Chloromethyl)-4-(undec-10-en-1-yloxy)benzene (6): 6 was synthesised according to reported procedure.[271] To a solution of **5** (6.00 g, 21.71 mmol) and anhydrous DMF (1.6 mL) in anhydrous DCM (65 mL) was slowly added $SOCl_2$ (2.2 mL, 3.60 g, 30.4 mmol, 1.4 eq) under a N_2 atmosphere, and the reaction mixture was stirred at room temperature for 2 h. After the complete conversion was evidenced by TLC (DCM), the mixture was evaporated and dried under reduced pressure. The pure **6** was obtained in quantative yield as a pale orange oil and used for further syntheses without additional purification. ^{1}H-NMR (500 MHz, DMSO-d6): δ = 7.33 (m, 2H, Hb), 6.89 (m, 2H, Hc), 5.78 (m, 1H, Hh), 4.99−4.89 (m, 2H, Hi), 4.70 (s, 2H, Ha), 3.93 (t, J = 6.5 Hz, 2H, Hd), 1.99 (m, 2H, Hg), 1.68 (m, 2H, He), 1.41−1.24 (m, 12H, Hf). ^{13}C-NMR (125.8 MHz, $CDCl_3$): δ = 159.4, 139.3, 130.1, 129.6, 114.8, 114.3, 68.2, 46.2, 33.9, 29.6, 29.5, 29.5, 29.3, 29.2, 29.0, 26.1.

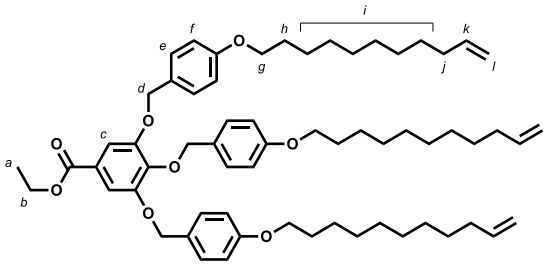

Ethyl 3,4,5-tris((4-(undec-10-en-1-yloxy)benzyl)oxy)benzoate (7): 7 was synthesised according to reported procedure.[271] A suspension of ethyl gallate (1.15 g, 5.81 mmol),

K_2CO_3 (7.23 g, 52.3 mmol, 9.0 eq) and KI (1.45 g, 8.7 mmol, 1.5 eq) were suspended in anhydrous DMF (120 mL) and the mixture was stirred at 60 °C for 30 min. To the mixture was added a degassed solution of **6** (6.00 g, 2.35 mmol, 3.5 eq) in anhydrous DMF (20 mL). The resulting reaction mixture was stirred at 60 °C overnight. The reaction mixture was cooled down to room temperature and poured in ice-water (700 mL). The aqueous phase was extracted with Et_2O (5 times, 700 mL total). The combined organic layers were washed with 1 M HCl *aq* (1 time), H_2O (2 times) and brine (1 time), dried over $MgSO_4$, filtered, evaporated and dried under reduced pressure. The crude product was purified by flash column chromatography (30 vol% n-hex in DCM) and further recrystallisition from isopropanol to afford the pure **7** (2.55 g, 2.62 mmol, 45 % yield) as a white powder. ^{1}H-NMR (500 MHz, $CDCl_3$): δ = 7.36 (s, 2H, Hc), 7.34−7.23 (m, 6H, Hf), 6.90−6.74 (m, 6H, He), 5.81 (m, 3H, Hk), 5.14−5.00 (s, 6H, Hd), 5.00−4.91 (m, 6H; Hl), 4.34 (q, J = 7.1 Hz, 2H, Hb), 3.98−3.90 (m, 6H, Hg), 2.04 (m, 6H, Hj), 1.77 (m, 6H, Hh), 1.38 (t, J = 7.1 Hz, 3H; Ha), 1.49−1.25 (m, 36H; Hi). ^{13}C-NMR (125.8 MHz, $CDCl_3$): δ = 166.4, 161.0, 159.2, 152.8, 142.6, 139.4, 130.4, 129.4, 128.8, 125.5, 114.7, 114.6, 114.3, 109.4, 74.8, 71.3, 68.2, 65.7, 61.2, 34.0, 29.7, 29.6, 29.5, 29.4, 29.3, 29.1, 26.2, 14.5. HRMS, ESI, (m/z) $[M-Na]^+$ calcd for $C_{63}H_{88}O_8$: 995.6371, found: 995.6663.

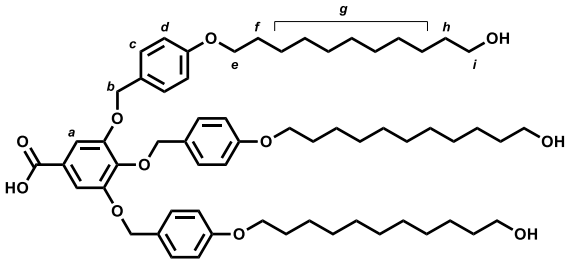

3,4,5-Tris((4-((11-hydroxyundecyl)oxy)benzyl)oxy)benzoic acid (8): 8 was synthesised according to reported procedure.[271] **7** (2.24 g, 2.3 mmol) in anhydrous THF (10 mL) was slowly added to a 0.5 M solution of 9-BBN in THF (27.6 mL, 13.8 mmol, 6.0 eq) at 66 °C and the mixture was stirred at 66 °C for 1.5 h. After complete conversion was evidenced by TLC (DCM), the reaction mixture was cooled down to room temperature. Anhydrous EtOH (10 mL), degassed 6 M NaOH *aq* (23 mL) and degassed 30 % H_2O_2 (46 mL) were slowly added in this order. The reaction mixture was refluxed for 1.5 h. The mixture was evaporated and dried under reduced pressure. The residue was taken in H_2O, and the solution was acidified with 3 M HCl *aq* and the aqueous phase was extracted with

DCM (4 times, 600 mL total). The combined organic layers were washed with brine, dried over $MgSO_4$, filtered, evaporated and dried under reduced pressure. The crude material was purified by precipitation in n-hexane from THF to afford the pure **8** (1.72 g, 1.72 mmol, 75 % yield) as a white powder. ^{1}H-NMR (500 MHz, $CDCl_3$): δ = 7.39 (s, 2H, Ha), 7.35─7.24 (m, 6H, Hc), 6.90─6.74 (m, 6H, Hd), 5.05 (m, 6H, Hb), 3.98─3.90 (m, 6H, He), 3.64 (t, J=6.5 Hz, 6H, Hi), 1.77 (m, 6H, Hf), 1.56 (m, 6H, Hf), 1.49─1.25 (m, 36H, Hg). ^{13}C-NMR (125.8 MHz, $CDCl_3$): δ = 169.9, 159.2, 152.8, 143.1, 130.4, 129.8, 129.4, 128.8, 128.6, 114.6, 114.2, 109.8, 74.8, 71.2, 68.2, 63.2, 36.4, 32.9, 29.7, 29.7, 29.5, 29.5, 29.4, 26.2, 25.9. HRMS, ESI, (m/z) $[M─Na]^+$ calcd for $C_{61}H_{90}O_{11}$: 1021.6375, found: 1021.6608.

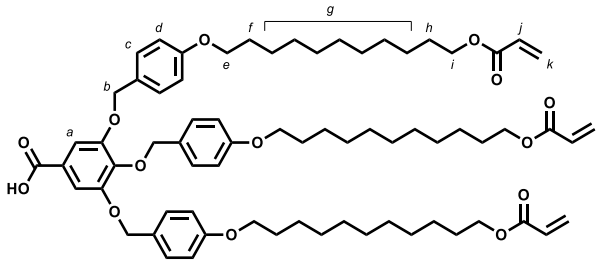

3,4,5-tris((4-((11-(acryloyloxy)undecyl)oxy)benzyl)oxy)benzoic acid (dBzA): dBzA was synthesized by adapting reported procedure.[270] A solution of **8** (500 mg, 0.5 mmol) and BHT (head of spatula) in THF (5 mL) was treated with *N*,*N*´-dimethylaniline (0.21 mL, 1.65 mmol, 3.3 eq) and the solution was stirred at room temperature for 30 min. Acryloyl chloride (149 mg, 0.13 mL, 1.63 mmol, 3.3 eq) was added to the reaction mixture at 0 °C, and the reaction mixture was stirred at room temperature overnight. After completion, a few drops of MeOH were added and the reaction mixture was stirred for 30 min. 1.5 M HCl *aq* (15 mL) were added and the reaction mixture was extracted with EtOAc (4 times, 100 mL total). The combined organic layers were dried over $MgSO_4$, filtered, evaporated and dried under reduced pressure. The crude product was purified by recrystallisation from EtOH to afford pure **dBzA** (539 mg, 0.46 mmol, 85 % yield) as a white solid. ^{1}H-NMR (500 MHz, $CDCl_3$): δ = 7.41 (s, 2H, Ha), 77.35─7.24 (m, 6H, Hc), 6.90─6.74 (m, 6H, Hd), 6.39 (m, 3H, Hk), 6.15─6.09 (m, 3H, Hj), 5.81 (m, 3H, Hk), 5.05 (m, 6H, Hb), 4.15 (m, 6H, Hi), 3.98─3.90 (m, 6H, He), 1.78 (m, 6H, Hf), 1.66 (m, 6H, Hh), 1.49─1.25 (m, 36H, Hg). ^{13}C-NMR (125.8 MHz, $CDCl_3$): δ = 170.3, 166.5, 159.2, 152.8, 143.3, 130.6, 130.4, 129.4,

128.8, 114.6, 114.2, 109.9, 74.8, 71.2, 68.2, 64.9, 29.7, 29.6, 29.5, 29.4, 29.4, 28.7, 26.2, 26.0. HRMS, ESI, (m/z) $[M-Na]^+$ calcd for $C_{70}H_{96}O_{14}$: 11183.6692, found: 1183.6798.

Core M

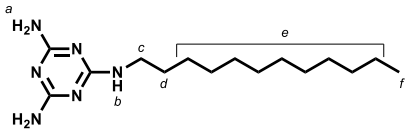

2,4-diamino-6-dodecylamino-1,3,5-triazine (M): M was synthesised according to reported procedure.[236] 2-Chloro-4,6-diamino-1,3,5-triazine (2.00 g, 13.74 mmol), dodecylamine (3.06 g, 16.49 mmol, 1.2 eq) and $NaHCO_3$ (1.38 g, 16.49 mmol, 1.2 eq) were dissolved in anhydrous 1,4-dioxane (75 mL) and the reaction mixture was refluxed under a N_2 atmosphere for 6 h. After being cooled down to room temperature, the reaction mixture was poured in H_2O (150 mL). The aqueous suspension was filtered and the precipitate was washed with H_2O. The crude material was purified by flash column chromatography (10:1 DCM:MeOH) to afford the pure **M** (3.47 g, 11.79 mmol, 86 % yield) as a white solid. ^{1}H-NMR (500 MHz, $CDCl_3$): δ = 5.24−5.11 (m, 5H; Ha, Hb), 3.30 (dt, J_{HNH}=5.9 Hz, J_{HCH}=7.0Hz, 2H; Hc), 1.51 (q, J=7.1 Hz, 2H; Hd), 1.34−1.18 (m, 18H; He), 0.87 (t, J=6.9Hz, 3H; Hf). ^{13}C-NMR (125.8 MHz, $CDCl_3$): δ = 166.8, 40.8, 32.0, 29.9, 29.8, 29.8, 29.7, 29.7, 29.5, 29.5, 27.0, 22.8, 14.2. HRMS, ESI, (m/z) $[M-H]^+$ calcd for $C_{15}H_{30}N_6$: 295.2605, found: 295.2469.

Core T

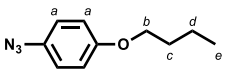

1-azido-4-butoxybenzene (9): 9 was synthesised according to reported procedure.[223] A solution of $NaNO_3$ (440 mg, 6.76 mmol, 1.1 eq) in H_2O (2.5 mL) was slowly added to a solution of 4-butoxyaniline (1.00 g, 6.05 mmol) in a mixture of H_2O (16 mL), acetic acid (36 mL) and HCl *conc.* (3.2 mL) at 0 °C. The reaction mixture was stirred at 0 °C for 5 min, and a solution of NaN_3 (488 mg, 7.08 mmol, 1.2 eq) in H_2O (2.5 mL) was slowly added at 0 °C. The reaction mixture was further stirred at 0 °C for 2 h. Upon total conversion was evidenced by TLC (DCM), the mixture was extracted in DCM (3 times, 200 mL total). The combined organic layers were washed with 10 % NaOH *aq* (100 mL), dried over $MgSO_4$, filtered, evaporated and dried under reduced pressure. The pure **9** (1.05 g, 5.50 mmol, 91 %

yield) was afforded as an orange oil. ^{1}H-NMR (500 MHz, $CDCl_3$): δ = 6.96−6.86 (m, 4H, Ha), 3.94 (t, J = 6.5 Hz, 2H, Hb), 1.76 (quint, J = 7 Hz, 2H, Hc), 1.49 (h, J = 7.5 Hz, 2H, H4), 0.98 (t, J = 7.4 Hz, 3H, He). ^{13}C-NMR (125.8 MHz, $CDCl_3$): δ = 156.7, 132.2, 120.1, 115.8, 68.2, 31.4, 19.3, 14.0.

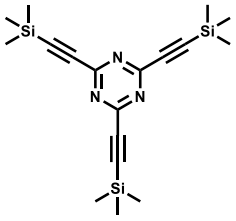

2,4,6-tris((trimethylsilyl)ethynyl)-1,3,5-triazine (10): 10 was synthesised according to reported procedures.[324, 325] A mixture of 1.6 M n-BuLi in n-hexane (7 mL, 11.2 mmol, 5.5 eq) in anhydrous THF (10 mL) was slowly added to a solution of ethynyltrimethylsilane (1.00 g, 10.18 mmol, 5.0 eq) in anhydrous THF (15 mL) at -78 °C. The reaction mixture was stirred at room temperature for 5 min. A solution of $ZnCl_2$ (1.53 g, 11.2 mmol, 5.5 eq) in anhydrous THF (10 mL) was added to the mixture at -78 °C and the reaction mixture was stirred at room temperature for 3 h. The reaction mixture was evaporated and dried under reduced pressure, and the residue was dissolve in anhydrous THF (20 mL). The solution was added to a solution of trichlorotriazine (375 mg, 2.04 mmol) and $Pd(PPh_3)_4$ (116 mg, 0.1 mmol, 5 mol%) in anhydrous THF. After being stirred at 30 °C for 3 h, the reaction mixture was topped with 1 M HCl *aq* (20 mL) and extracted in Et_2O. The combined organic layers were dried over $MgSO_4$, filtered, evaporated and dried under reduced pressure. The dark residue was washed with MeOH to afford **10** (84 mg, 0.23 mmol) as a light brown powder. Further crystallisation from the concentrated MeOH phase afforded an additional 250 mg (0.68 mmol) of **4** (45 % yield in total). ^{1}H-NMR (500 MHz, $CDCl_3$): δ = 0.27 (s, 27H). ^{13}C-NMR (125.8 MHz, $CDCl_3$): δ = 159.8, 102.4, 100.1, -0.7.

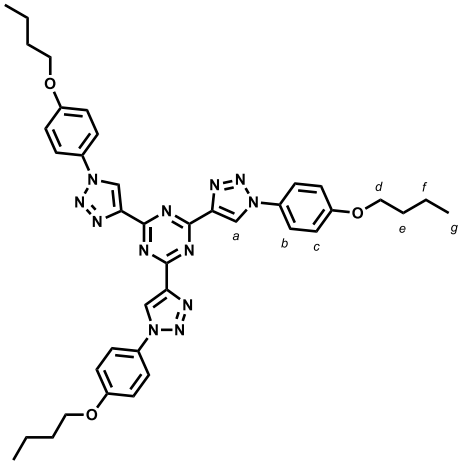

2,4,6-tris(1-(4-butoxyphenyl)-1H-1,2,3-triazol-4-yl)-1,3,5-triazine (T): T was synthesised according to reported procedure.[223] A degassed solution of tetrabutylammonium fluoride (2.55 g, 9.74 mmol, 4.0 eq) in THF (12 mL) was added to a solution of **9** (1.54 g, 8.03 mmol, 3.3 eq), **10** (900 mg, 2.43 mmol), $CuSO_4 \cdot 5\ H_2O$ (78 mg, 0.49 mmol, 20 mol%) and sodium ascorbate (192 mg, 0.97 mmol, 40 mol%) in degassed 1:1 THF:H_2O (40 mL), and the reaction mixture was stirred at room temperature for 1 day. The reaction mixture was topped with additional H_2O and extracted in DCM (4 times, 500 mL total). The combined organic layers were dried over $MgSO_4$, filtered, evaporated and dried under reduced pressure. The residue was purified by flash column chromatography (DCM to 20 vol% EtOAc in DCM). Further recrystallisation from EtOH afforded the pure **T** (692 mg, 0.95 mmol, 39 % yield) as a white powder. ^{1}H-NMR (500 MHz, $CDCl_3$): δ = 9.10 (s, 3H, Ha), 7.76 (d, J = 8.2 Hz, 6H, Hb), 7.07 (d, J = 8.4 , 6H, Hc), 4.04 (t, J = 6.4 Hz, 6H, Hd), 1.82 (m, 6H, He), 1.53 (m, 6H, Hf), 1.01 (t, J = 7.4 Hz, 9H, Hg). ^{13}C-NMR (125.8 MHz, $CDCl_3$): δ = 166.9, 160.1, 145.9, 129.9, 126.0, 122.4, 115.6, 68.4, 31.3, 19.4, 14.0.

Na:dA

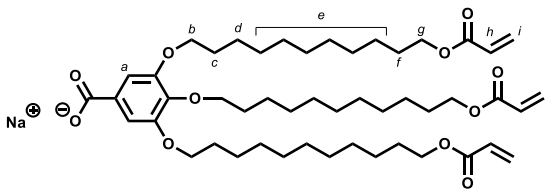

Sodium 3,4,5-tris(11'-acryloyloxyundecyloxy)benzoate (Na:dA): Na:dA was synthesised by adapting reported procedures.[202, 321] A solution of **dA** (200 mg, 0.24 mmol) and BHT (head of spatula) in THF (30 mL) was treated with a 2 M NaOH *aq* (0.13 mL, 0.26 mmol, 1.1 eq) and stirred at room temperature for 20 min. the reaction mixture was then

dried under reduced pressure and the residue was taken in Et_2O, filtered evaporated and dried. The residue was taken in acetone, filtered evaporated and dried under reduced pressure to afford the pure **Na:dA** (204 mg, 0.24 mmol) in quantitative yield. ^{1}H-NMR (500 MHz, $CDCl_3$): δ = 7.28 (s, 2H, Ha), 6.41−6.37 (m, 3H, Hi), 6.14−6.08 (m, 3H, Hh), 5.82−5.79 (m, 3H, Hi), 4.14 (t, J = 6.7 Hz, 6H, Hg), 4.00 (m, 6H, Hb), 1.82−1.70 (m, 6H, Hc), 1.68−1.41 (m, 12H, Hd, Hf), 1.38−1.24 (m, 36H, He). ^{13}C-NMR (125.8 MHz, $CDCl_3$): δ = 166.6, 152.9, 130.6, 128.8, 108.6, 73.6, 69.2, 64.9, 30.5, 29.8, 29.7, 29.7, 29.6, 29.5, 29.4, 29.4, 28.7, 26.2, 26.1.

TPE:dA$_4$

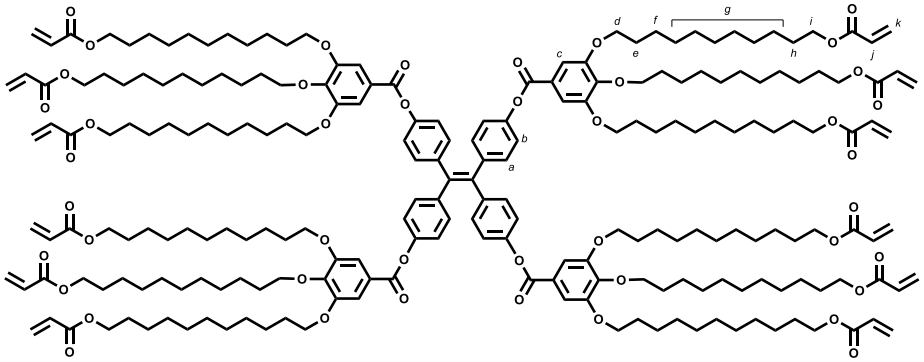

TPE:dA$_4$: TPE:dA$_4$ was prepared using reaction conditions for the Steglich esterification from reported procedures.[291, 326] Dicyclohexylcarbodiimide (DCC) (169 mg, 0.82 mmol, 6.0 eq) was added at 0 °C to a solution of **dA** (500 mg, 0.60 mmol, 4.5 eq) in anhydrous DCM (10 mL). After the mixture was stirred at 0 °C for 10 min, a suspension of tetrakis(4-hydroxyphenyl)ethylene (53 mg, 0.13 mmol) and 4-dimethylaminopyridine (DMAP) (32 mg, 0.26 mmol, 2.0 eq) in anhydrous DCM (5 mL) was added at 0 °C. The reaction mixture was stirred at room temperature for 7 d and at 35 °C for 1 d. The mixture was filtered over a pad of Celite and the organic phase was washed with 1 M HCl *aq* (2 times) and water, dried over $MgSO_4$, filtered, evaporated and dried under reduced pressure. The crude product was purified by flash column chromatography (3:1 to 2:1 n-hex:EtOAc) and further recrystallised from EtOH to afford **TPE:dA$_4$** (125 mg, 0.034 mmol, 26 % yield) as a pasty white solid. ^{1}H-NMR (500 MHz, $CDCl_3$): δ = 7.37 (s, 8H, Hc), 7.14 (d, J = 8.6 Hz, 8H, Hb), 7.00 (d, J = 8.6 Hz, 8H, Ha), 6.42 6.36 (m, 12H, Hk), 6.15 6.07 (m, 12H, Hj), 5.83 5.78 (m, 12H, Hk), 4.14 (t, J = 6.7 Hz, 24H, Hd), 4.03 (m, 24H, Hi), 1.85

1.71 (m, 24H, He), 1.66 (m, 24H, Hh), 1.47 (m, 24H, Hf), 1.40 1.22 (m, 144H, Hg). ^{13}C-NMR (125.8 MHz, $CDCl_3$): δ = 166.3, 164.9, 152.9, 149.7, 143.0, 140.9, 132.5, 130.4, 128.6, 123.9, 121.3, 108.5, 73.6, 69.2, 64.7, 30.36, 29.7, 29.6, 29.6, 29.5, 29.4, 29.3, 29.3, 29.3, 28.6, 26.1, 26.0. HRMS, MALDI, (m/z) $[M-H]^+$ calcd for $C_{222}H_{324}O_{44}$ 3695.319, found 3695.179.

NO2:dA$_3$

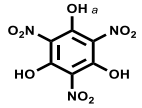

2,4,6-trinitrobenzene-1,3,5-triol (**11**): **11** was synthesised according to a reported procedure.[327] KNO_3 (3.20 g, 32.00 mmol, 4.0 eq) was slowly added to concentrated H_2SO_4 (30 mL) at 5 °C so that the temperature did not rise above 10 °C and the mixture was stirred at 5 °C for 15 min. Phloroglucin (1.00 g, 8.00 mmol) was slowly added at 5 °C so that the temperature did not rise above 10 °C, and the reaction mixture was stirred in an ice-bath for 15 min and at room temperature for 30 min. The reaction mixture was poured on ice (100 g) and the whole was stirred gently until the ice melted. The resulting precipitate was filtered and washed with a cold 1 M HCl *aq* solution to afford the pure **11** (1.50 g, 5.70 mmol, 71 % yield) as a bright yellow powder. ^{1}H-NMR (500 MHz, DMSO-d_6): δ = 8.89 (s, 3H, Ha). ^{13}C-NMR (125.8 MHz, DMSO-d_6): δ = 153.9, 122.0. HRMS, ESI, (m/z) $[M-H]^-$ calcd for $C_6H_3N_3O_9$: 259.9797, found: 260.0126.

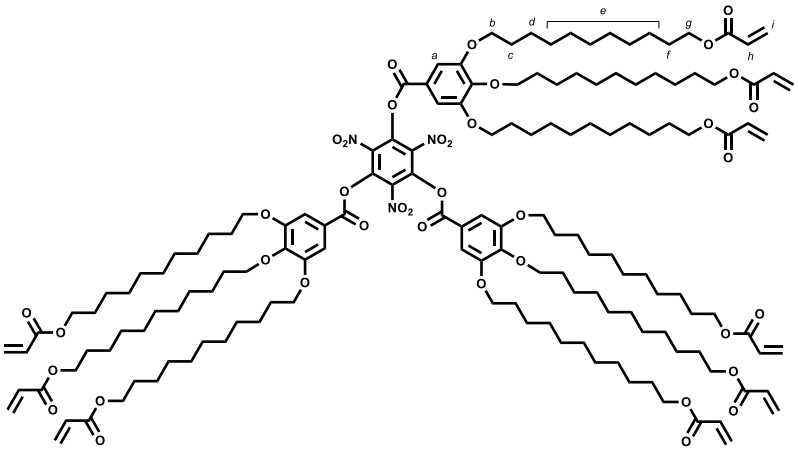

NO2:dA$_3$: A solution of **dA** (500 mg, 0.60 mmol, 3.4 eq) in THF (10 mL) was treated with 1-ethyl-3-(3-dimethylaminopropyl)carbodiimide (EDC) (126 mg, 0.81 mmol, 4.5 eq)

at 0 °C and stirred at 0 °C for 10 min. The reaction mixture was treated with a suspension of **11** (76 mg, 0.18 mmol) and DMAP (33 mg, 0.27 mmol, 1.5 eq) in THF (5 mL) at 0 °C and stirred at room temperature for 4 days. The reaction mixture was evaporated and dried under reduced pressure and the residue was taken in DCM. The organic phase was washed with 1 M HCl *aq*, $NaHCO_3$ *aq* and brine, dried over $MgSO_4$, filtered, evaporated and dried under reduced pressure. The crude product was purified by flash column chromatography (1:2 to 1:1 EtOAc:n-hex) to afford the pure **NO2:dA$_3$** (200 mg, 0.07 mmol, 41 % yield) as a white powder. ^{1}H-NMR (500 MHz, $CDCl_3$): δ = 7.30 (s, 6H, Ha), 6.41−6.36 (m, 9H, Hi), 6.14−6.07 (m, 9H, Hh), 5.82−5.80 (m, 9H, Hi), 4.13 (m, 18H, Hg), 4.03 (m, 18H, Hb), 1.84−1.71 (m, 18H, Hc), 1.69−1.42 (m, 36H, Hd, Hf), 1.40−1.25 (m, 108H, He). ^{13}C-NMR (125.8 MHz, $CDCl_3$): δ = 166.6, 153.0, 130.6, 128.8, 108.7, 73.6, 69.3, 64.9, 30.4, 29.8, 29.7, 29.7, 29.6, 29.4, 29.4, 29.3, 28.7, 26.0, 26.0.

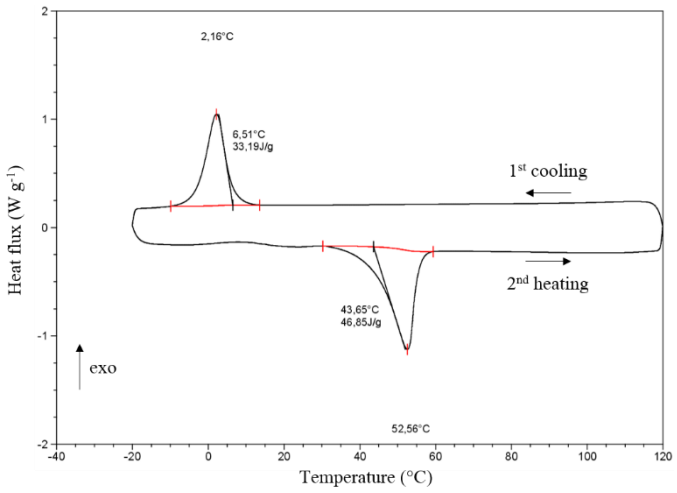

Figure 6.1. DSC analysis of **NO2:dA$_3$**.

dC12

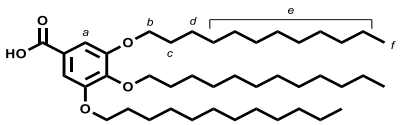

3,4,5-tris(dodecyloxy)benzoic acid (**dC12**): **dC12** was synthesised by adapting reported procedures. [321] A solution of ethyl gallate (1.00 g, 5.05 mmol) and K_2CO_3 (7.00 g, 50.46 mmol, 10.0 eq) in anhydrous DMF (40 mL) was stirred at room temperature for 20 min and treated with bromo-1-dodecane (4.10 g, 16.65 mmol, 3.3 eq). The reaction mixture was stirred at 75 °C for 1 day, filtered hot, evaporated and dried under reduced

pressure. The residue was taken in DCM and the organic phase was washed with 1 M HCl *aq*, water and brine. The organic phase was dried over $MgSO_4$, filtered, evaporated and dried under reduced pressure. The crude product was purified by flash column chromatography (4:1 DCM:n-hexane) to afford the ethyl protected **EtdC12**.

EtdC12 was dissolved in 3:1 THF:EtOH (340 mL) and added to 10 M NaOH *aq* (34 mL) and the mixture was refluxed for 6 h. The reaction mixture was then neutralised with HCl *conc.*. The mixture was concentrated under reduced pressure and stored at -20 °C overnight. The precipated was filtered and washed with cold water to afford the pure **dC12** as a white solid (2.5 g, 3.7 mmol, 73 % yield). ^{1}H-NMR (500 MHz, $CDCl_3$): δ = 7.32 (s, 2H, Ha), 4.02 (m, 6H, Hb), 1.80 (m, 6H, Hc), 1.48 (m, 6H, Hd), 1.26 (m, 48H, He), 0.88 (t, J = 6.9 Hz, 3H, Hf). ^{13}C-NMR (128.5 MHz, $CDCl_3$): δ = 171.6, 152.9, 143.1, 123.6, 108.5, 73.6, 69.2, 32.0, 30.3, 29.8, 29.7, 29.7, 29.7, 29.4, 29.3, 26.0, 22.7, 14.1.

Spectroscopic data

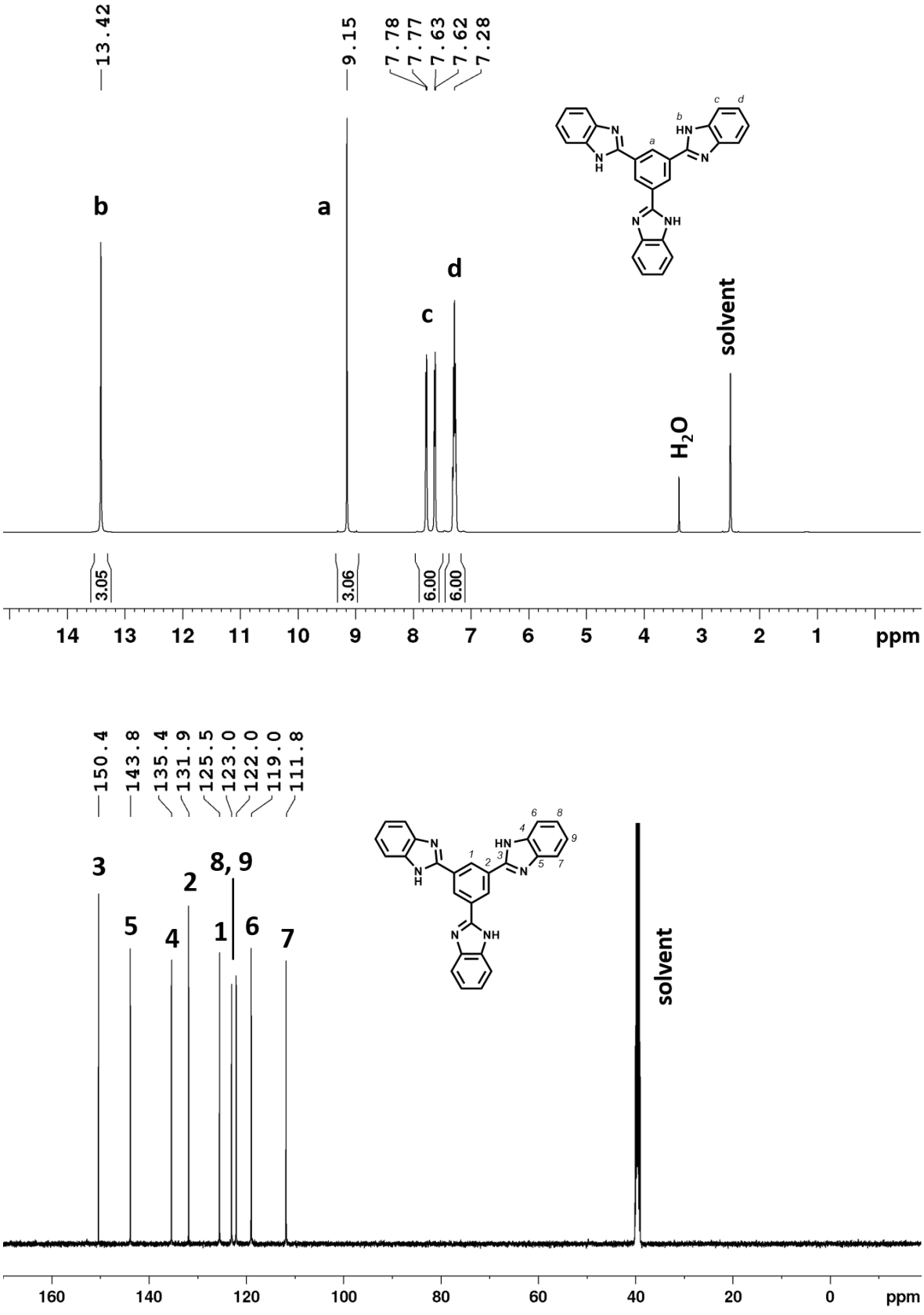

Figure 6.2. ^{1}H and ^{13}C-NMR of **TBIB** in DMSO-d_6.

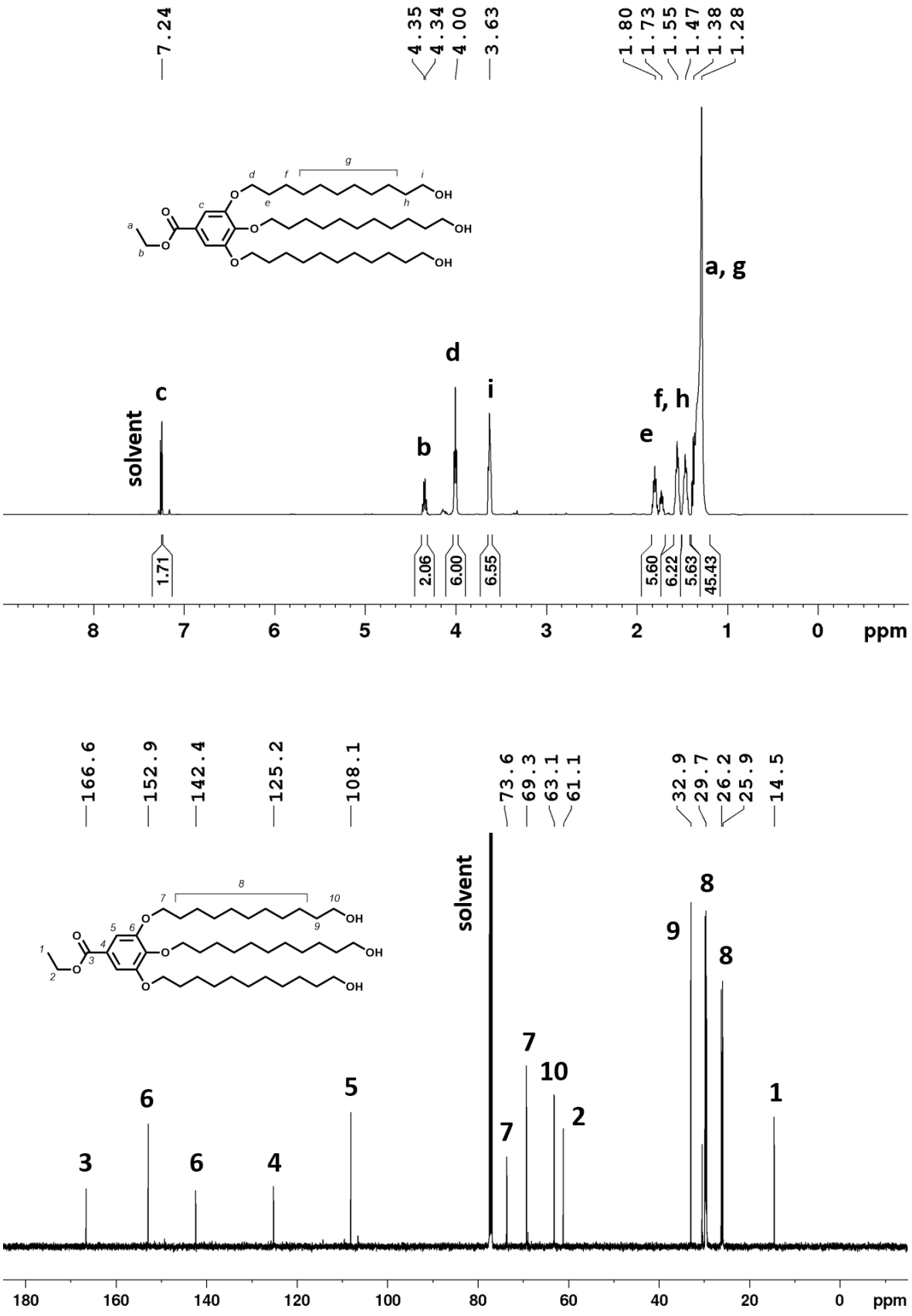

Figure 6.3. ^{1}H and ^{13}C-NMR of **1** in $CDCl_3$.

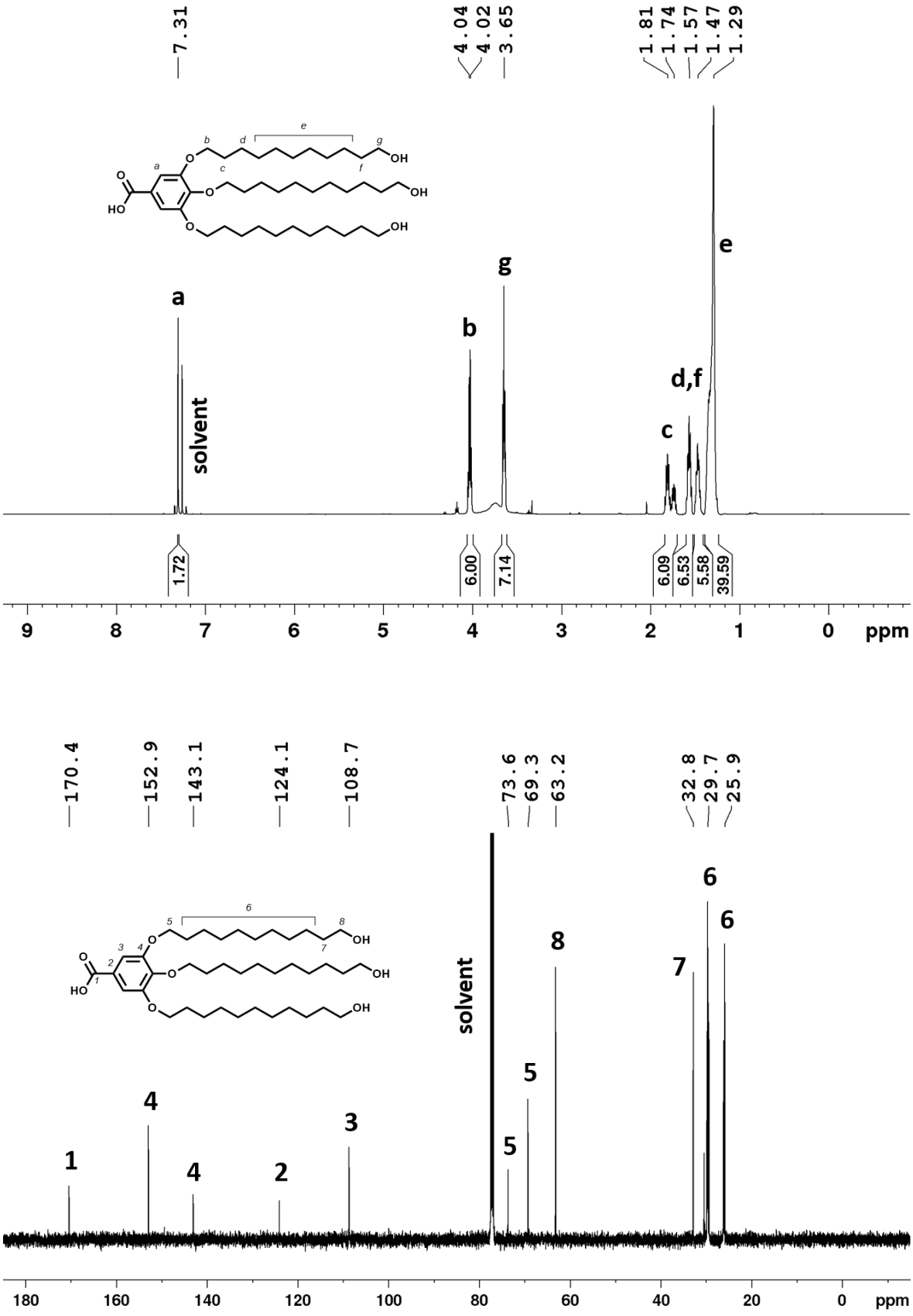

Figure 6.4. ^{1}H and ^{13}C-NMR of **2** in $CDCl_3$.

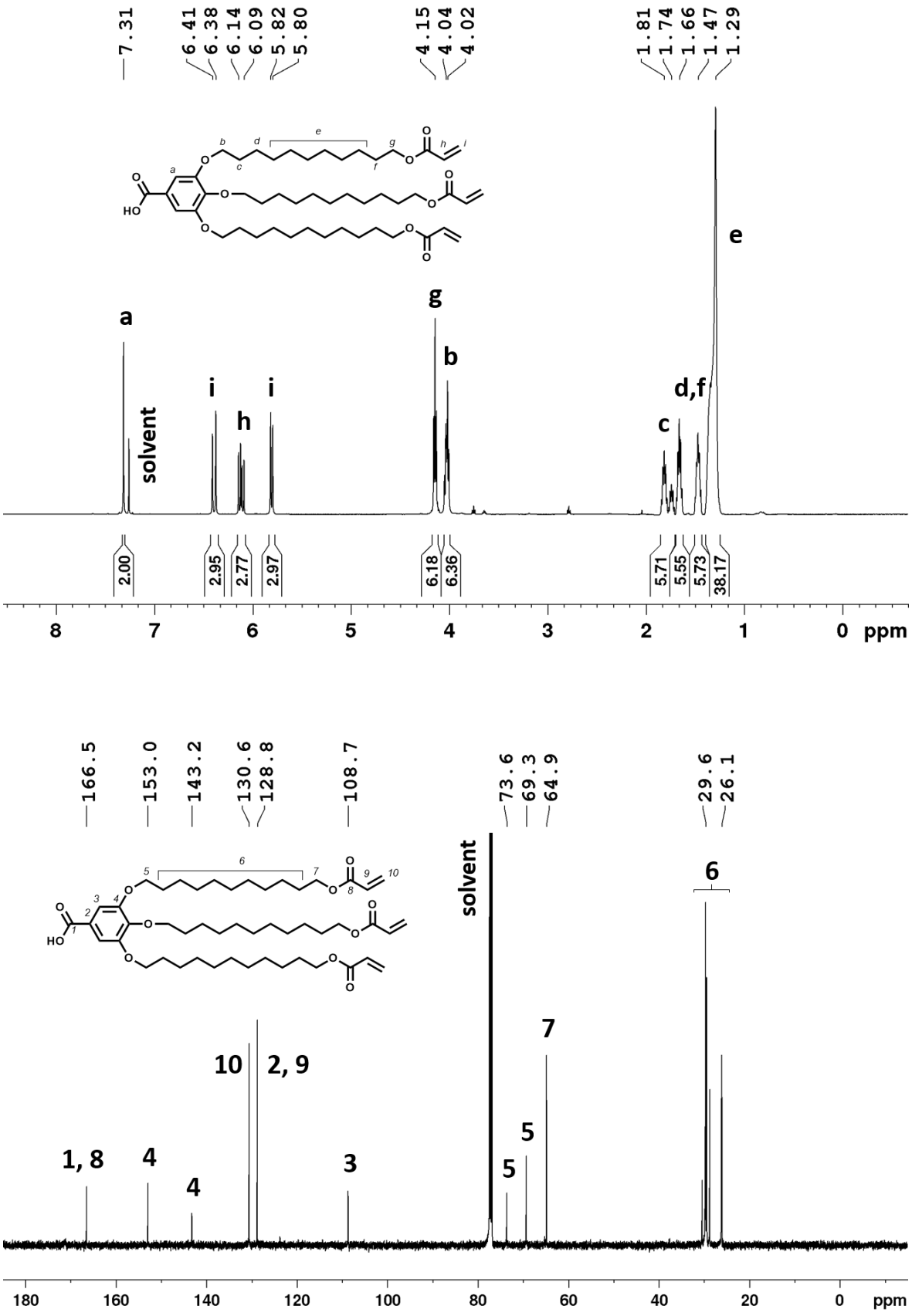

Figure 6.5. ^{1}H and ^{13}C-NMR of **dA** in $CDCl_3$.

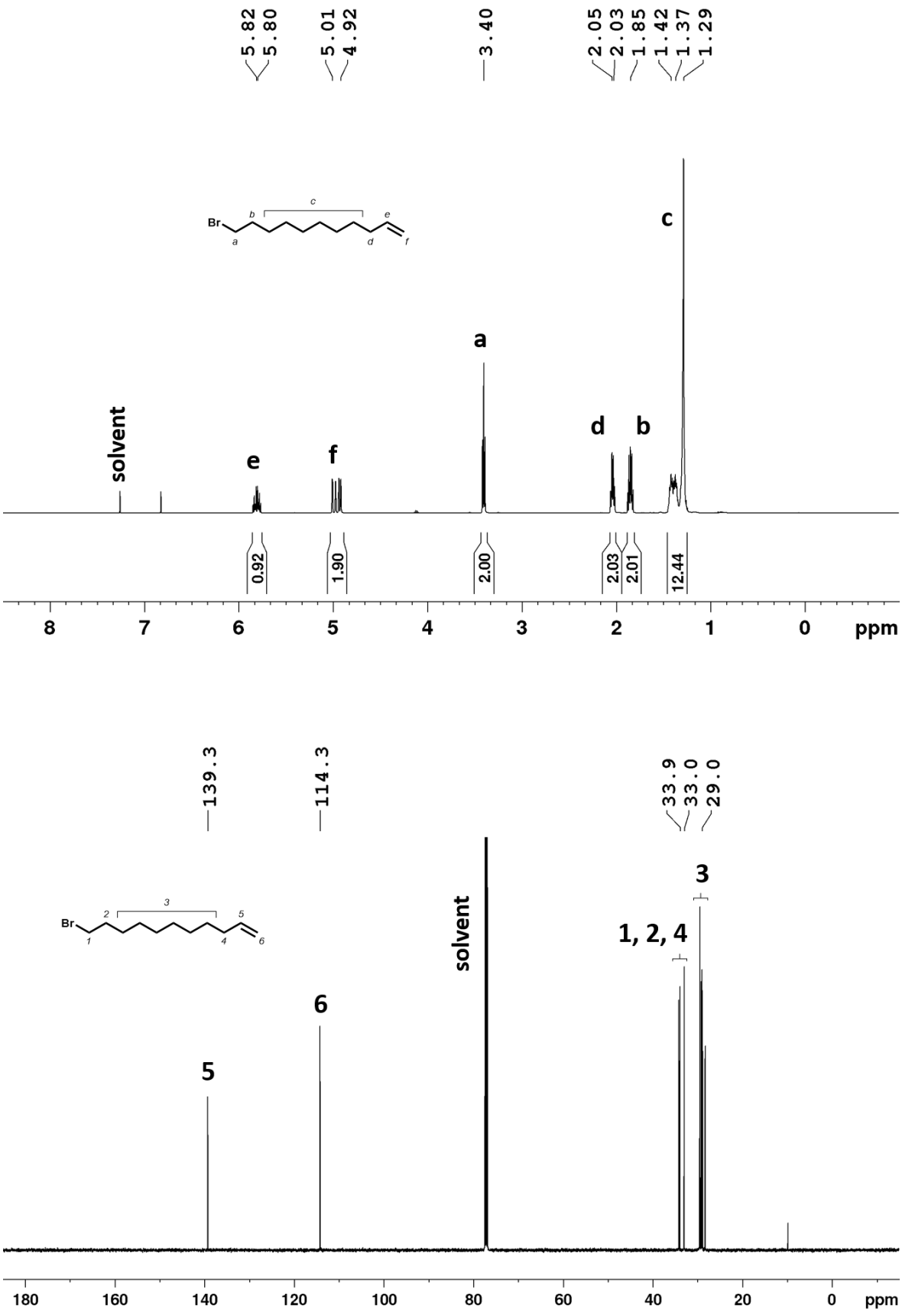

Figure 6.6. ^{1}H and ^{13}C-NMR of **3** in $CDCl_3$.

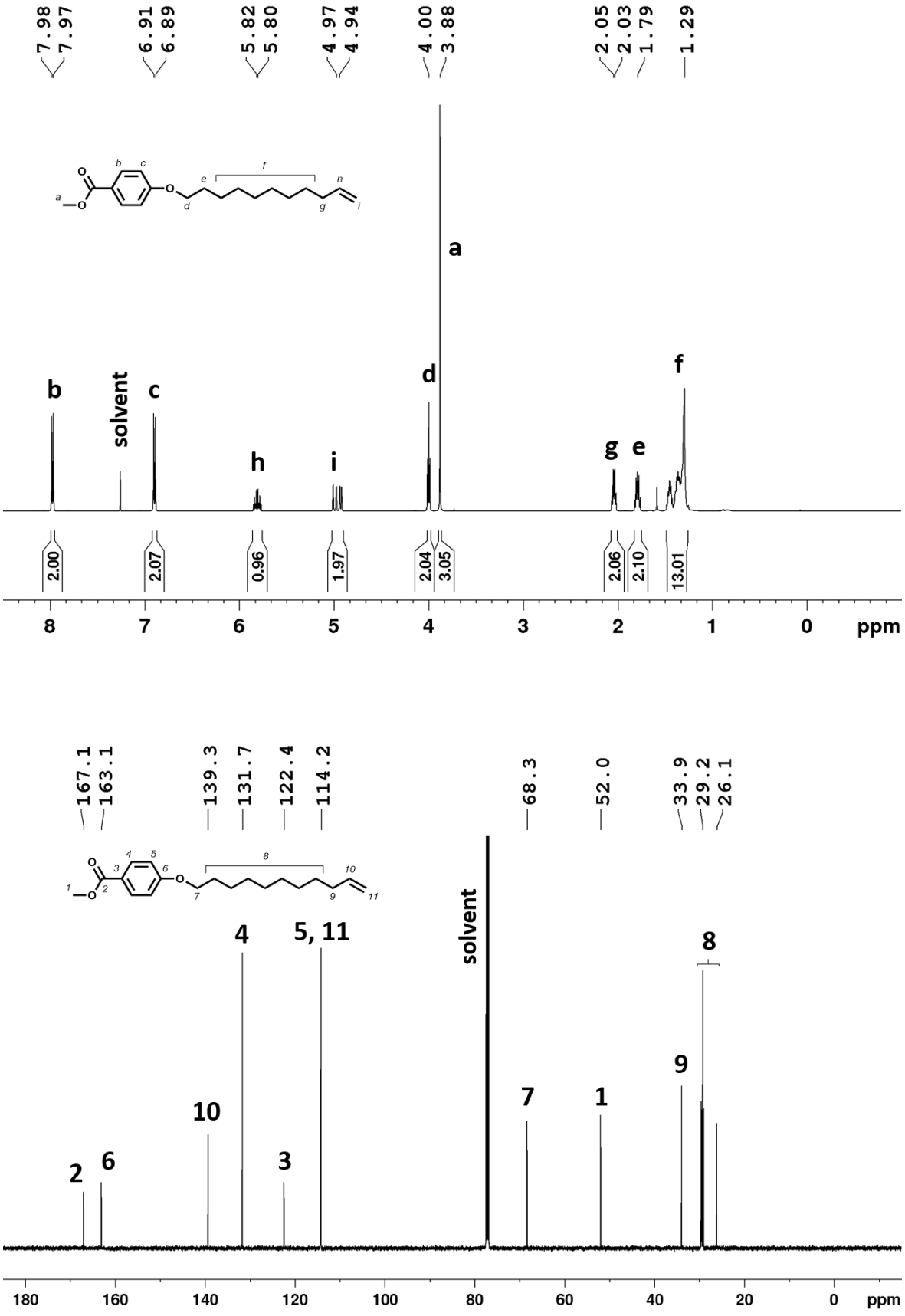

Figure 6.7. ^{1}H and ^{13}C-NMR of **4** in $CDCl_3$.

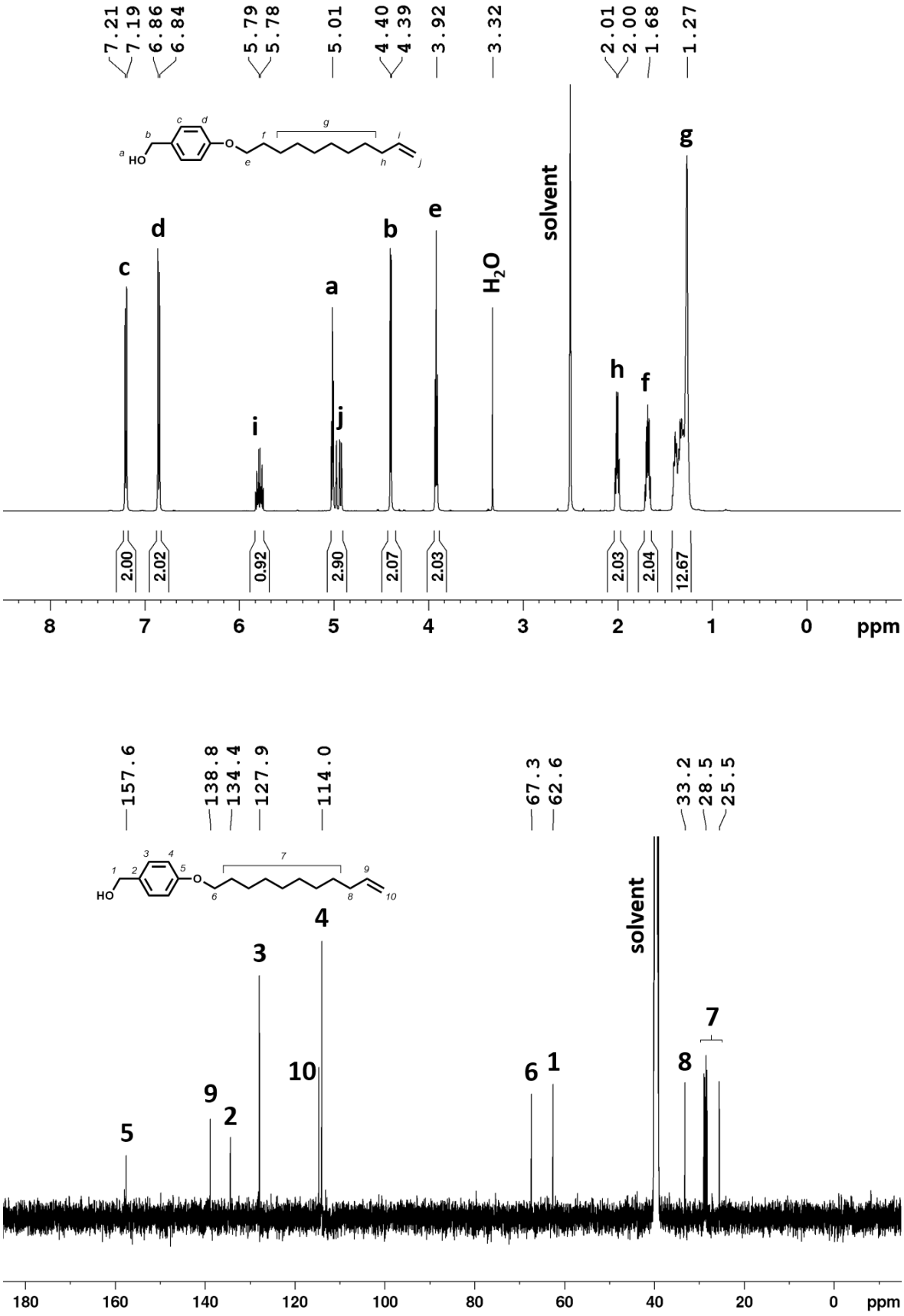

Figure 6.8. ^{1}H and ^{13}C-NMR of **5** in DMSO-d_6.

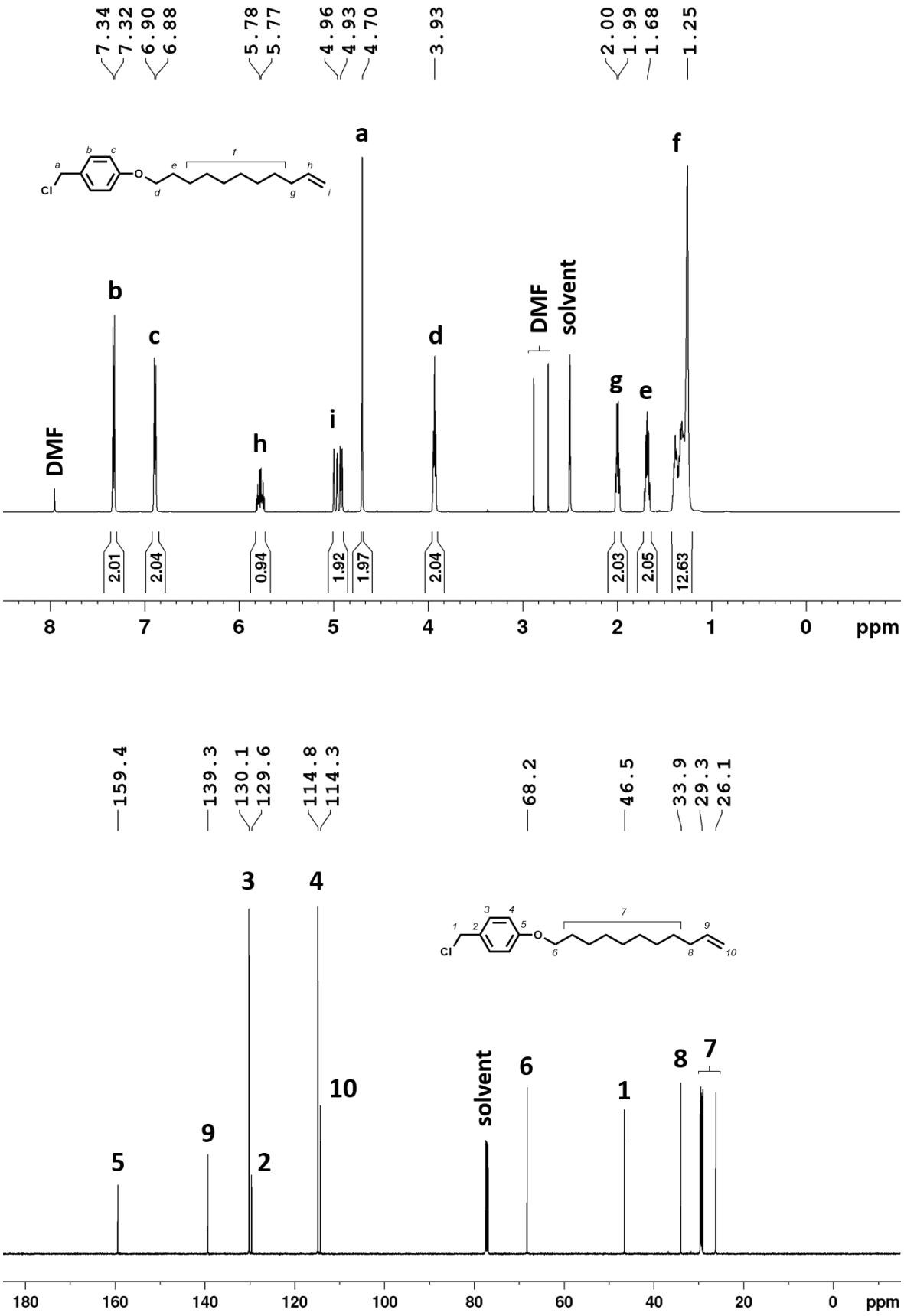

Figure 6.9. ^{1}H-NMR of **6** in DMSO-d_6 and ^{13}C-NMR of **6** in $CDCl_3$.

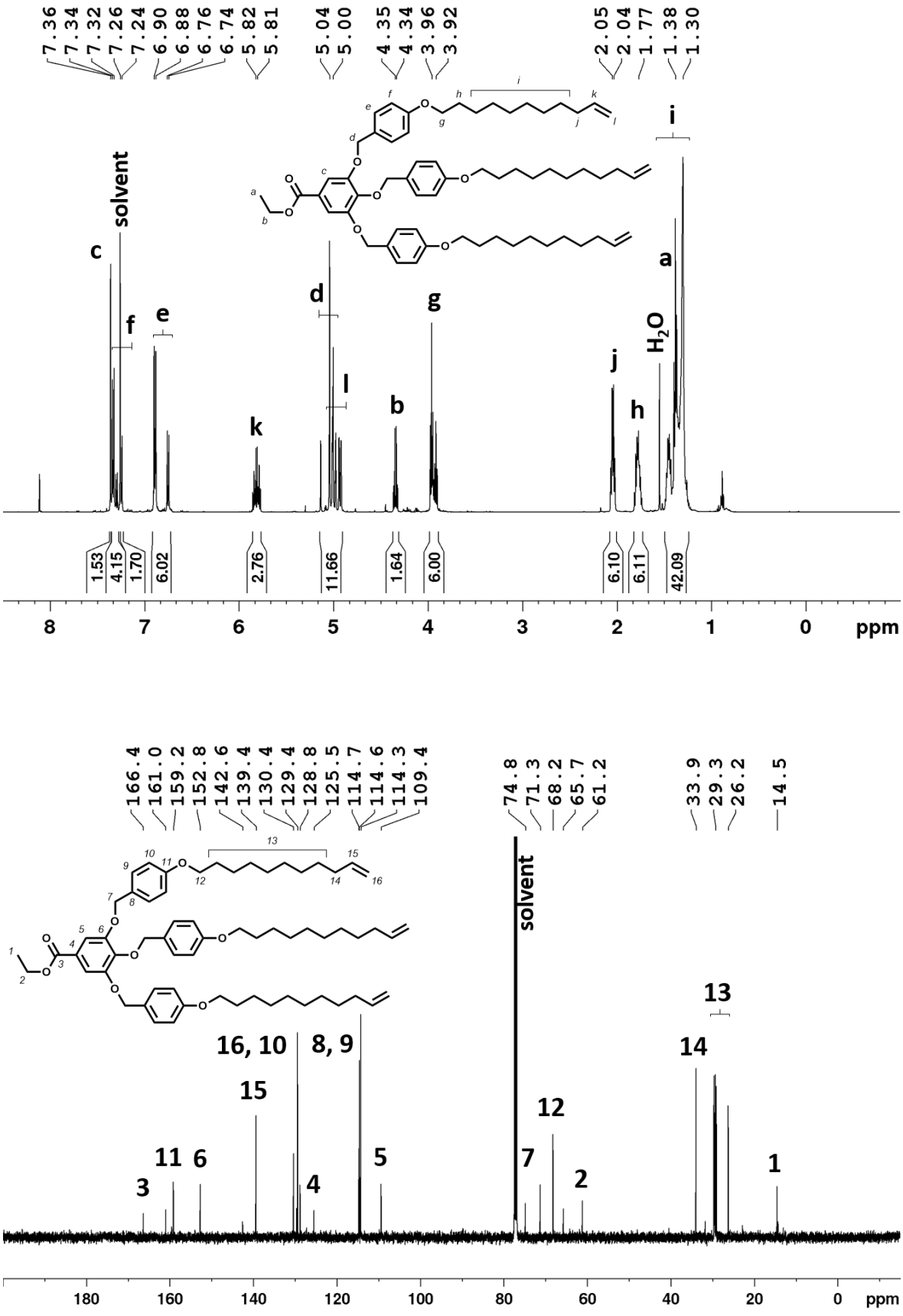

Figure 6.10. ^{1}H and ^{13}C-NMR of **7** in $CDCl_3$.

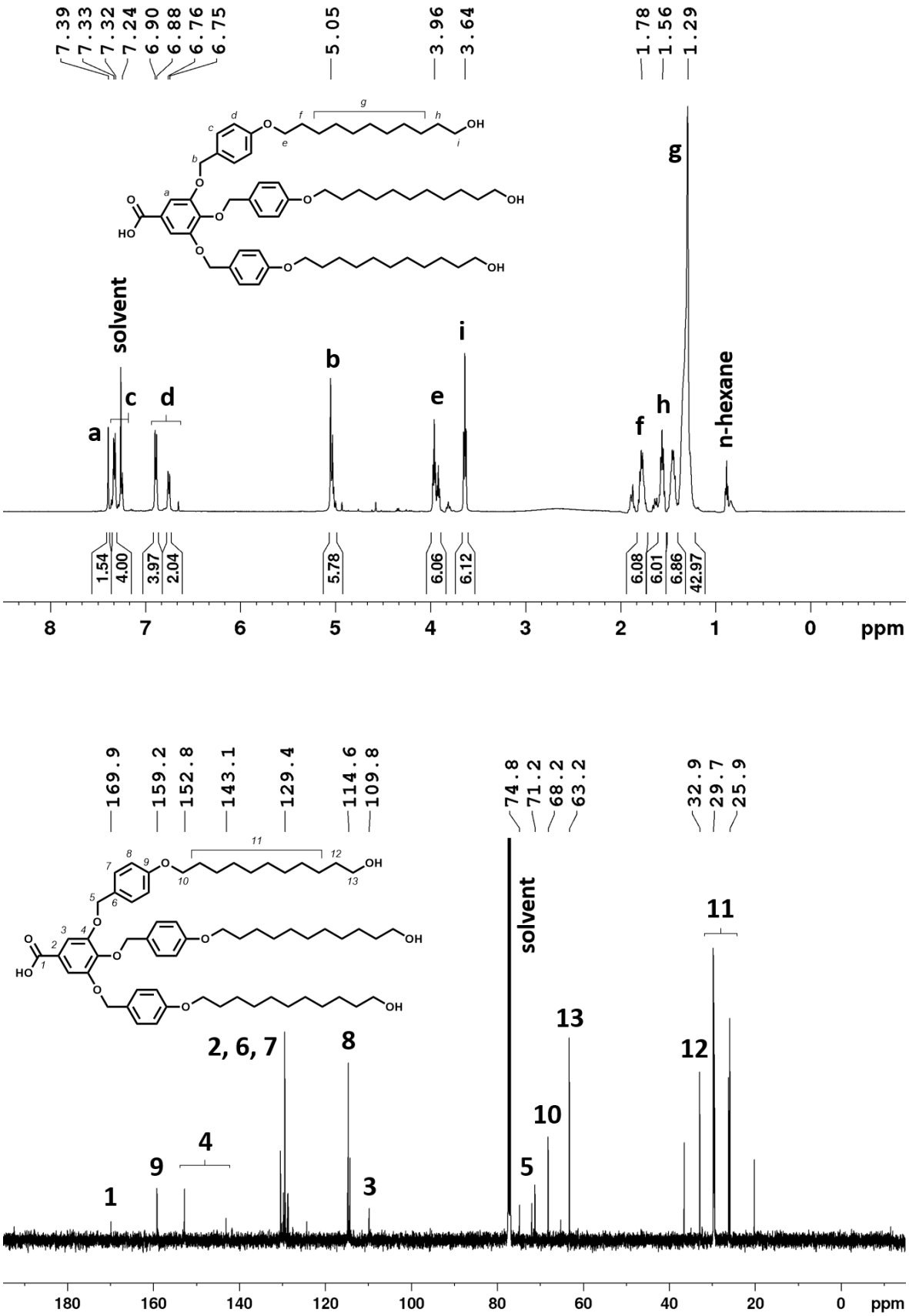

Figure 6.11. ^{1}H and ^{13}C-NMR of **8** in $CDCl_3$.

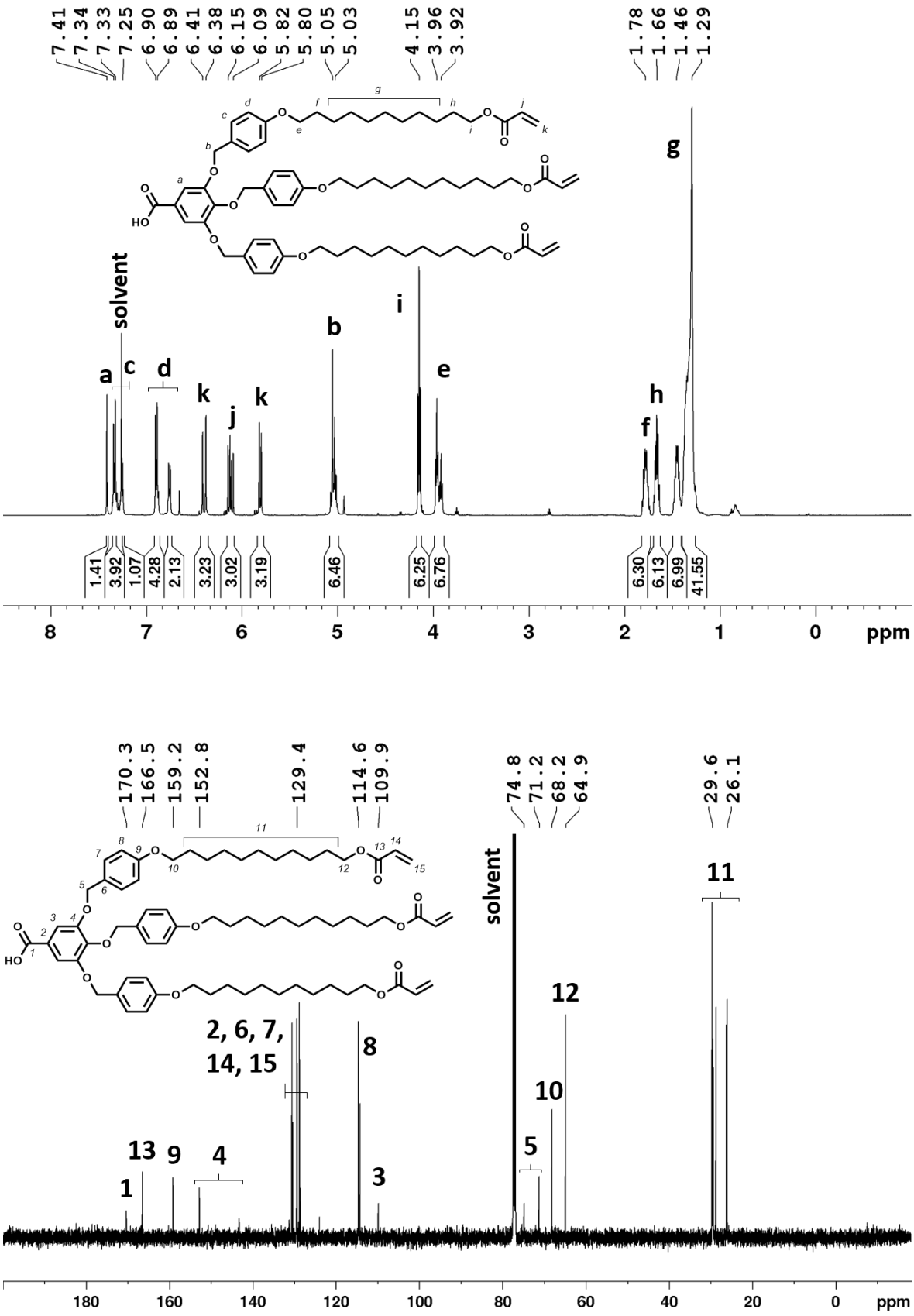

Figure 6.12. ^{1}H and ^{13}C-NMR of **dBzA** in $CDCl_3$.

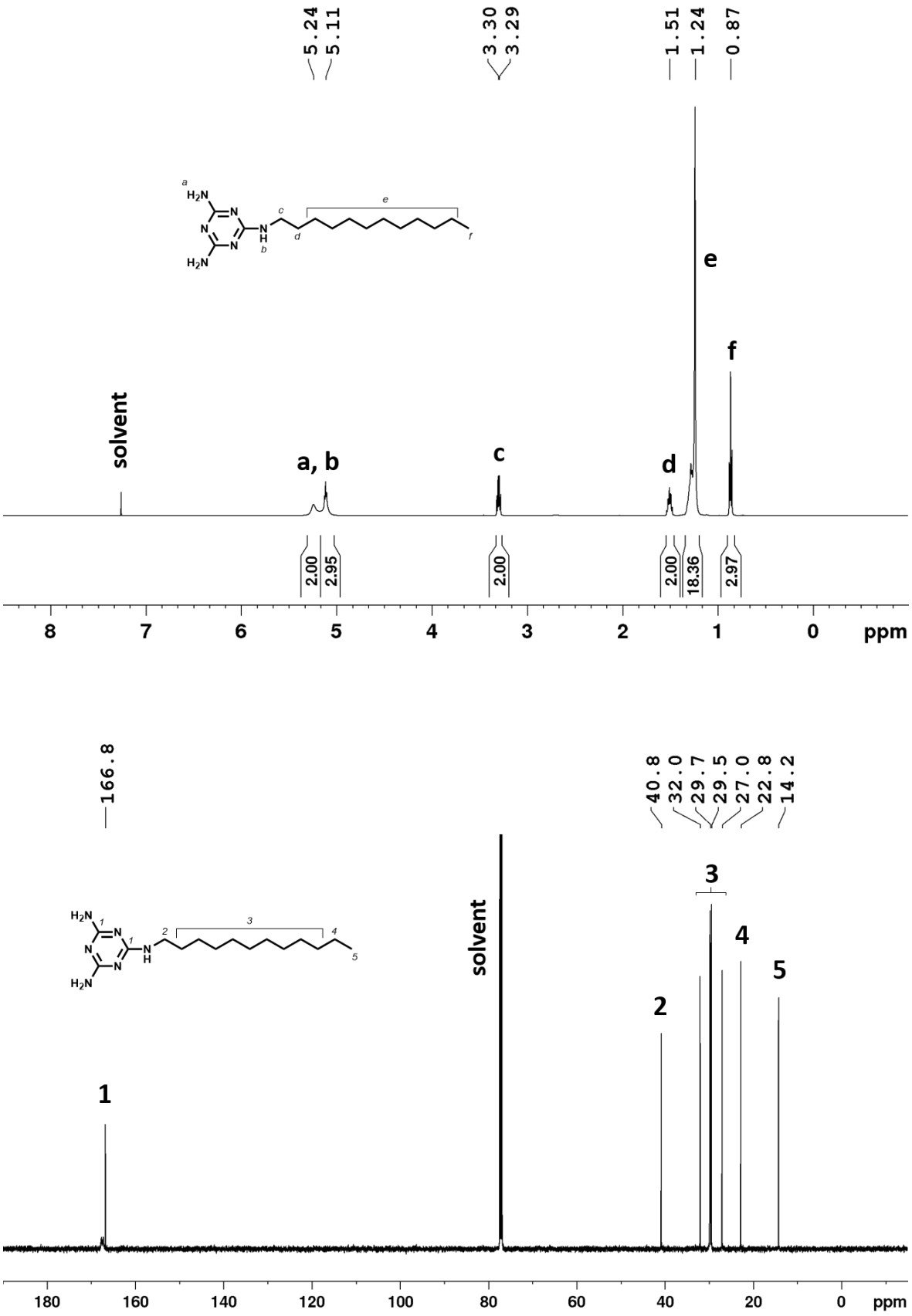

Figure 6.13. ^{1}H and ^{13}C-NMR of **M** in $CDCl_3$.

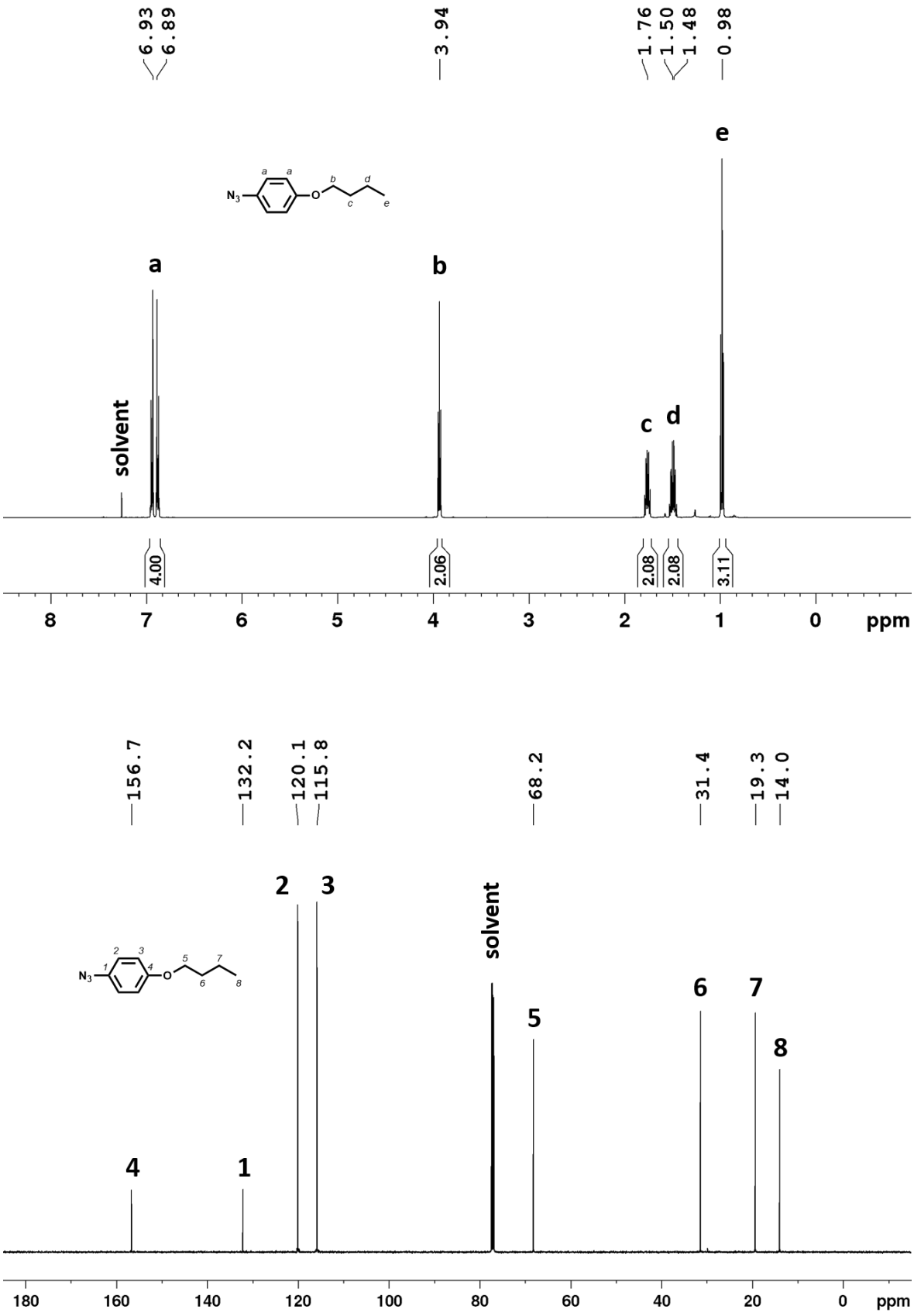

Figure 6.14. ^{1}H and ^{13}C-NMR of **9** in $CDCl_3$.

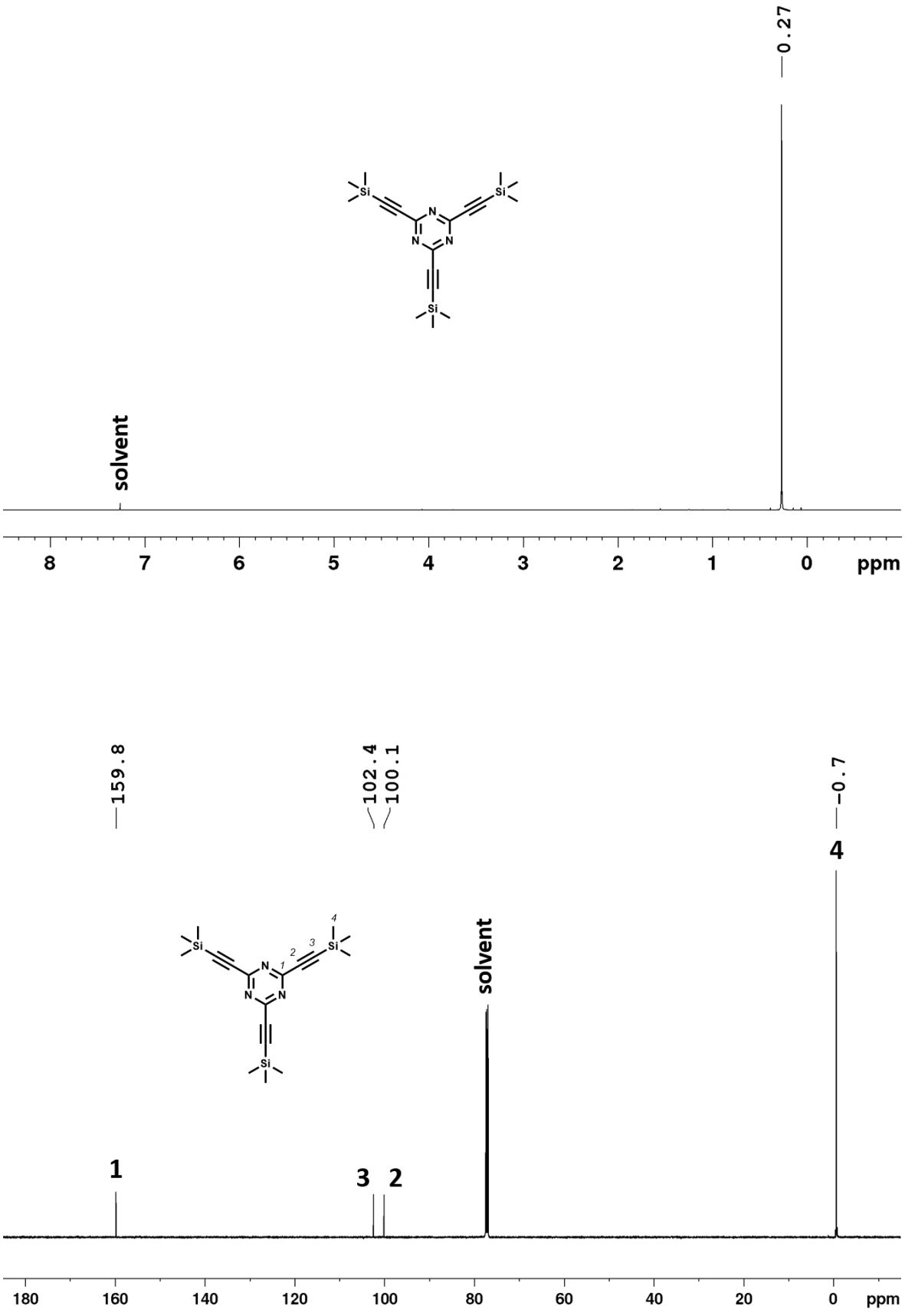

Figure 6.15. ^{1}H and ^{13}C-NMR of **10** in $CDCl_3$.

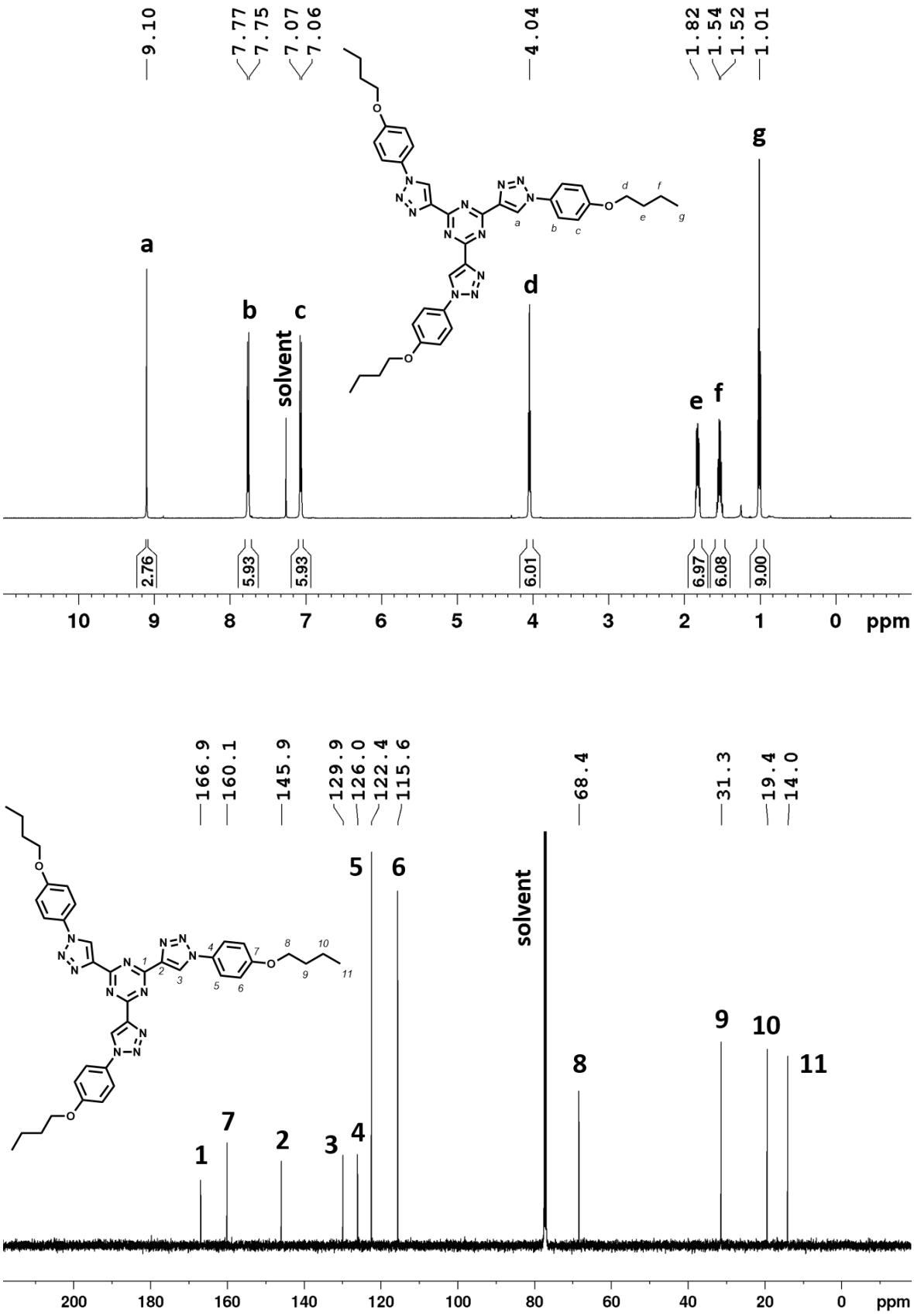

Figure 6.16. ^{1}H and ^{13}C-NMR of **T** in $CDCl_3$.

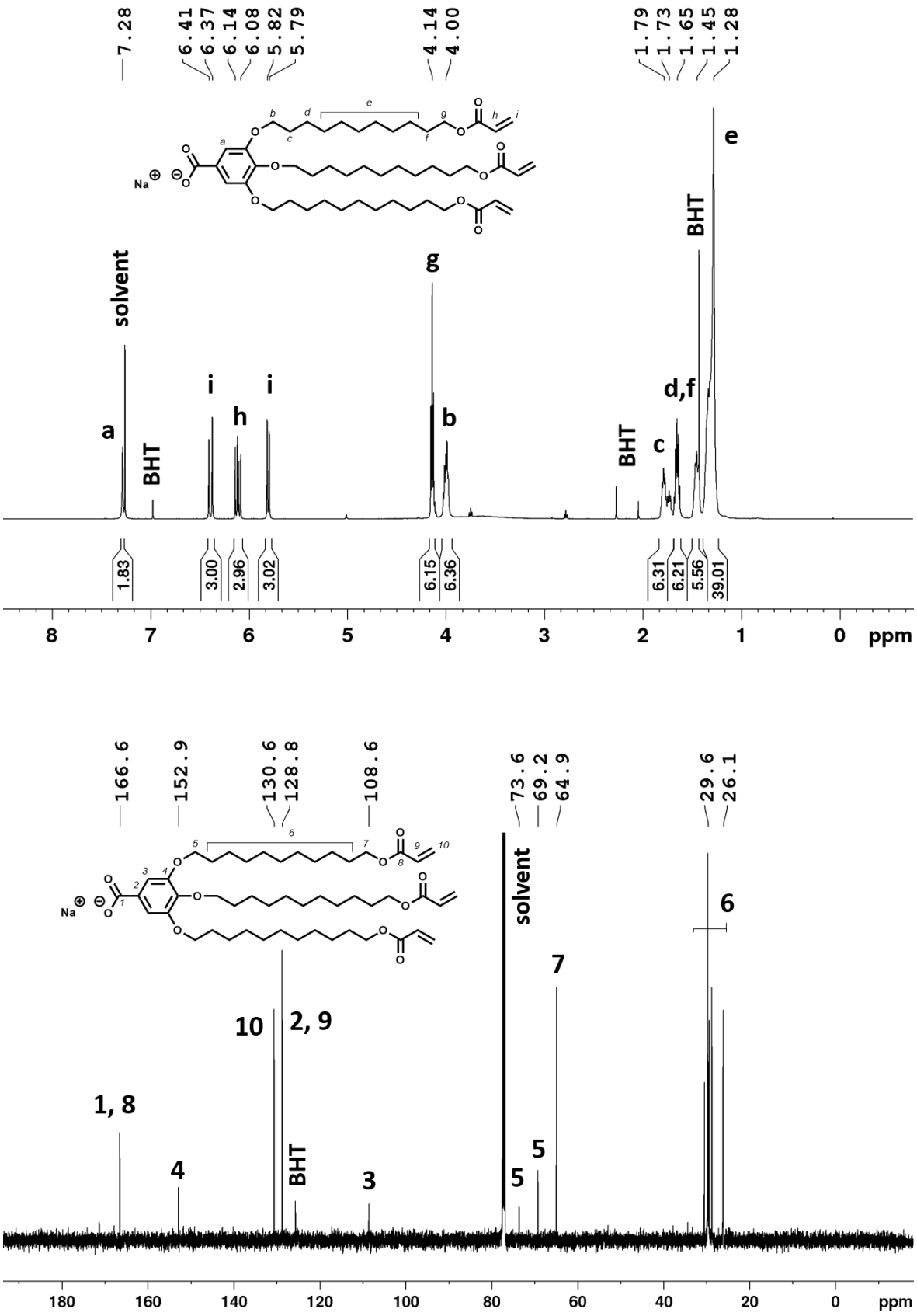

Figure 6.17. ^{1}H and ^{13}C-NMR of **Na:dA** in $CDCl_3$.

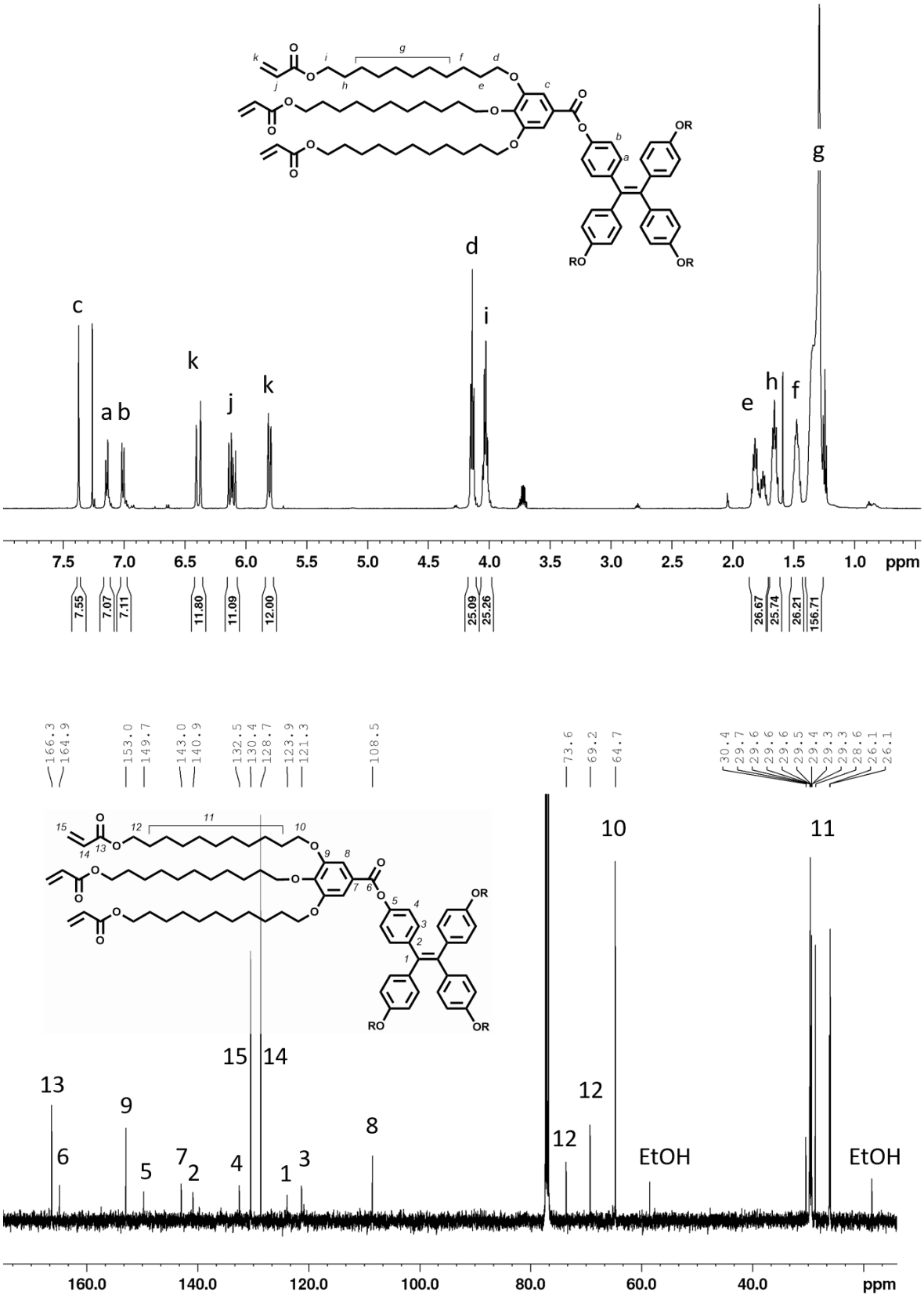

Figure 6.18. ^{1}H and ^{13}C-NMR of **TPE:dA$_4$** in $CDCl_3$.

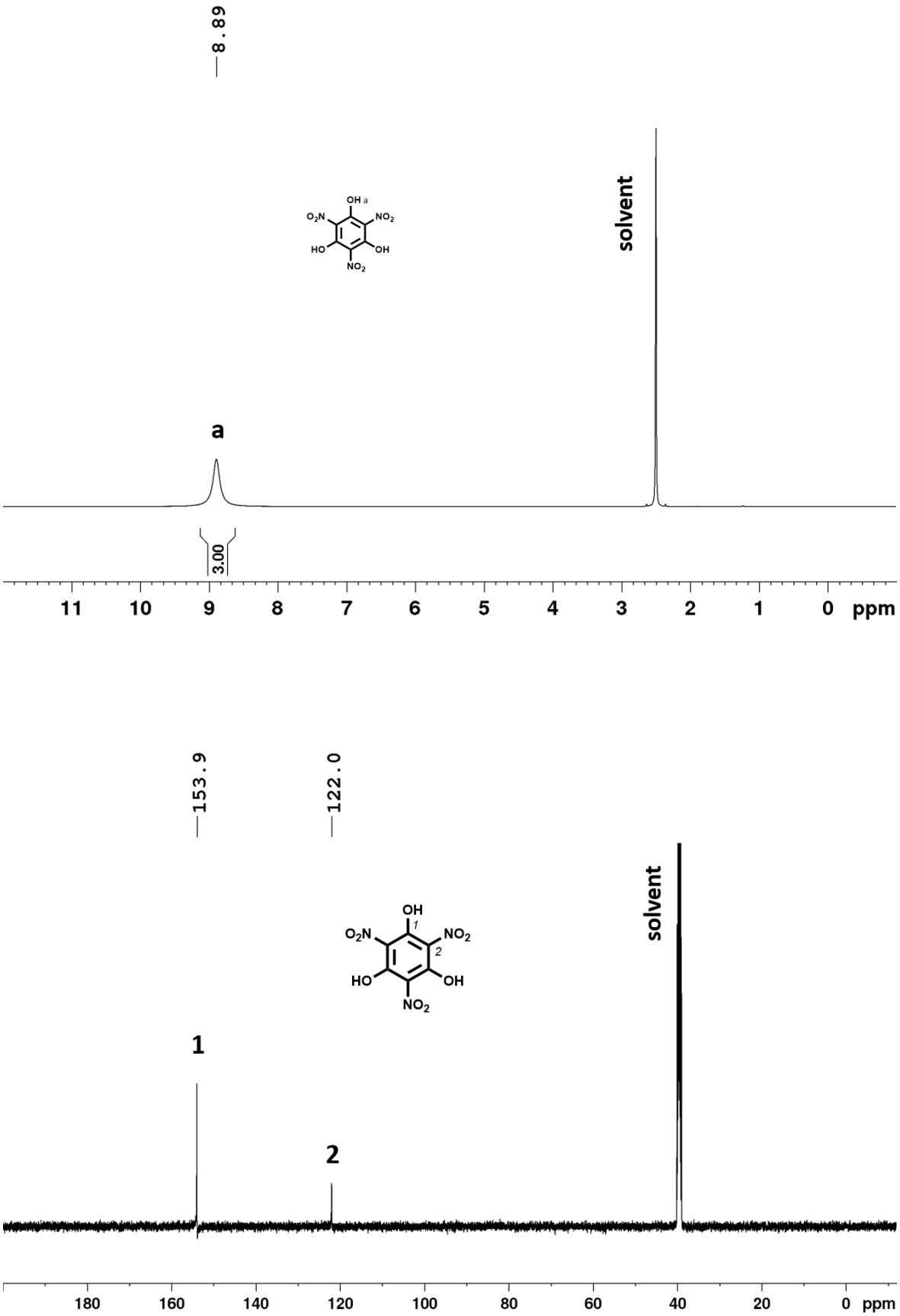

Figure 6.19. ^{1}H and ^{13}C-NMR of **11** in DMSO-d_6.

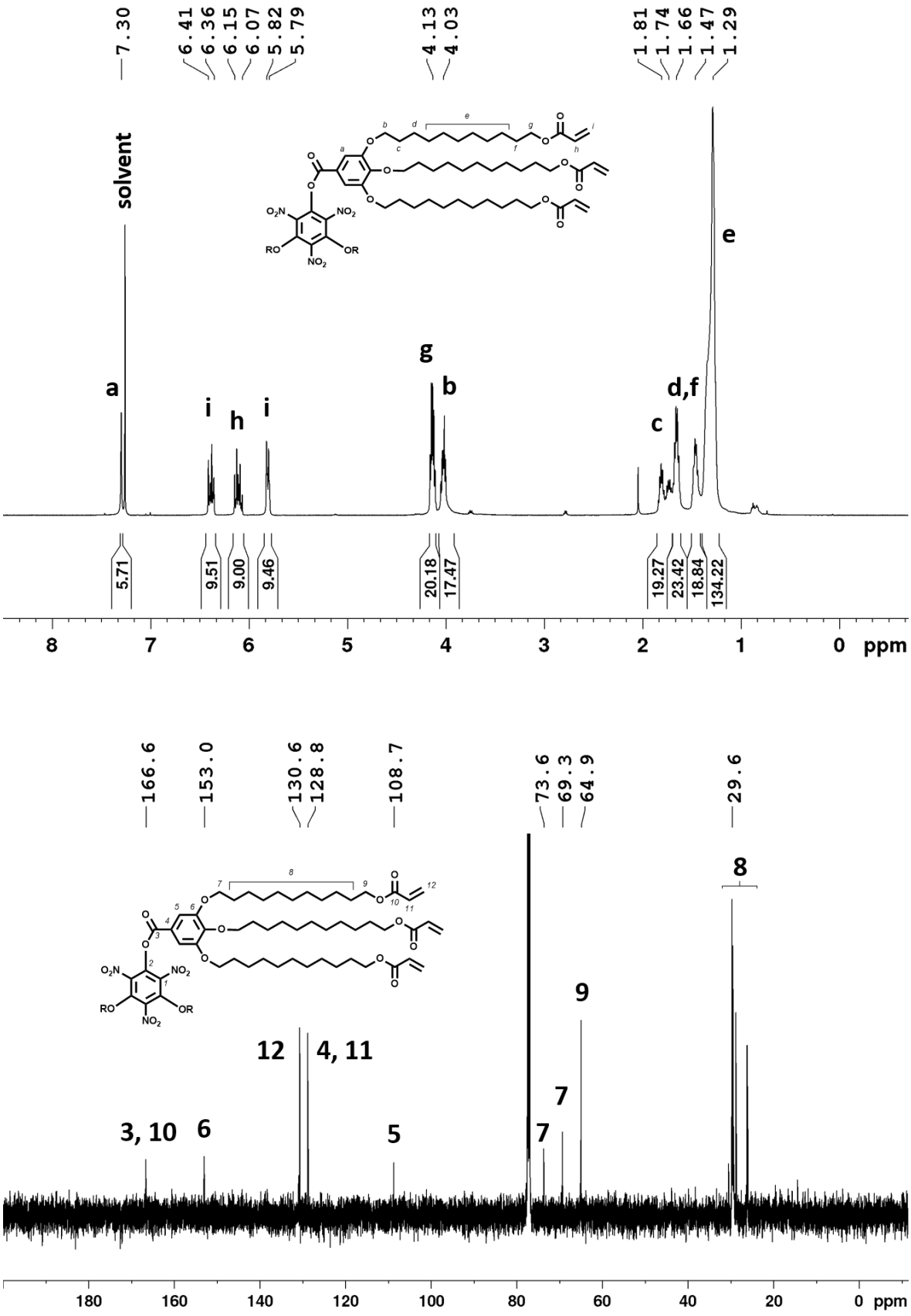

Figure 6.20. ^{1}H and ^{13}C-NMR of **NO2:dA$_3$** in $CDCl_3$.

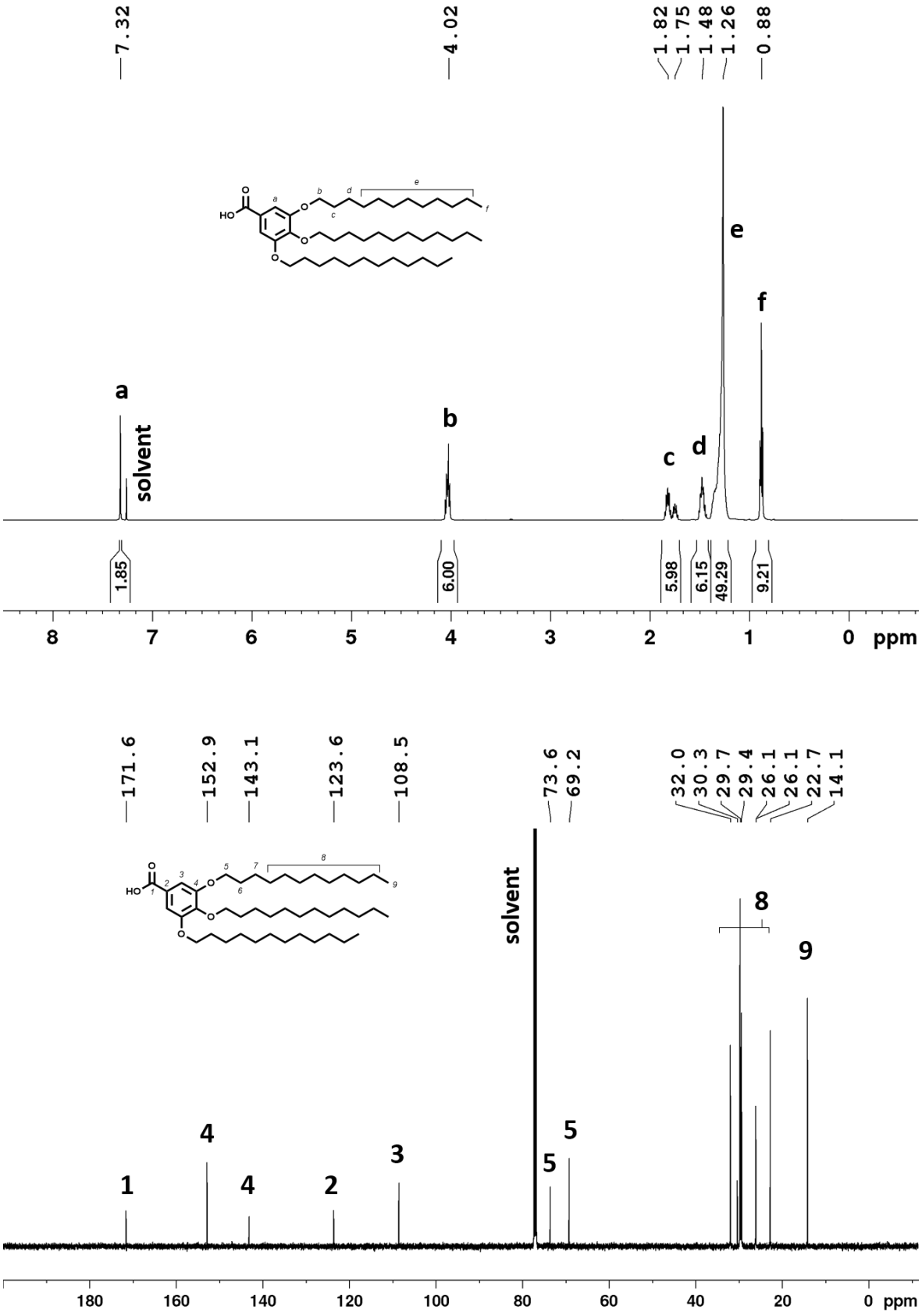

Figure 6.21. ^{1}H and ^{13}C-NMR of **dC12** in $CDCl_3$.

DOSY

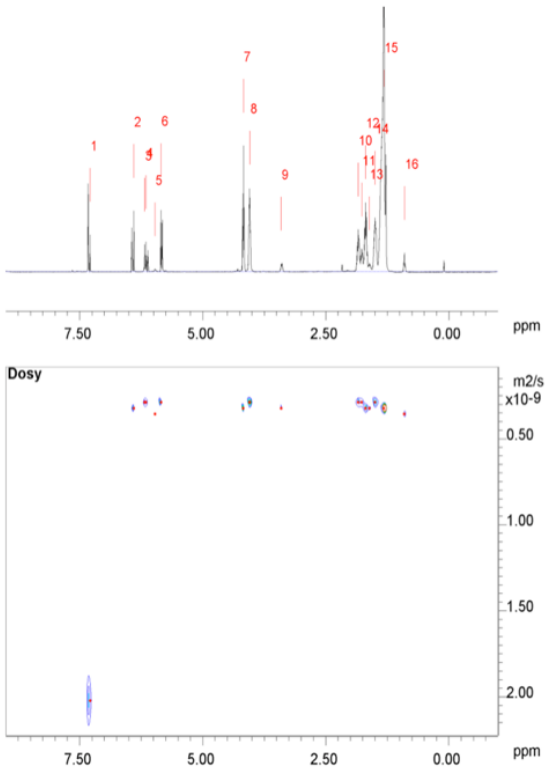

Peak name	F2 [ppm]	D [m2/s]	error
1	7.287	2.04e-09	9.103e-11
2	6.397	3.43e-10	2.417e-12
3	6.177	3.33e-10	4.103e-12
4	6.150	3.30e-10	3.331e-12
5	5.968	3.84e-10	2.824e-11
6	5.846	3.35e-10	2.497e-12
7	4.172	3.46e-10	5.158e-12
8	4.043	3.35e-10	2.014e-12
9	3.401	3.67e-10	8.932e-12
10	1.837	3.33e-10	3.133e-12
11	1.767	3.36e-10	3.897e-12
12	1.686	3.45e-10	1.721e-12
13	1.613	3.62e-10	7.699e-12
14	1.496	3.33e-10	2.682e-12
15	1.315	3.46e-10	1.806e-12
16	0.898	3.78e-10	4.080e-12

Figure 6.22. DOSY of **M:dA$_3$** in $CDCl_3$ (Δ = 0.0599 s, δ = 0.0030 s).

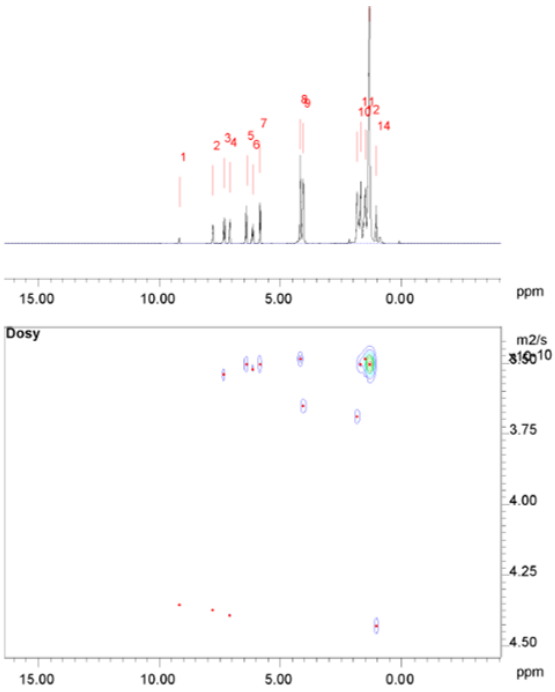

Peak name	F2 [ppm]	D [m2/s]	error
1	9.169	4.37e-10	4.148e-12
2	7.788	4.40e-10	2.100e-12
3	7.335	3.55e-10	2.878e-12
4	7.091	4.41e-10	1.367e-12
5	6.391	3.53e-10	2.829e-12
6	6.145	3.54e-10	5.707e-12
7	5.840	3.53e-10	2.898e-12
8	4.165	3.51e-10	1.528e-12
9	4.051	3.66e-10	1.746e-12
10	1.828	3.70e-10	1.911e-12
11	1.682	3.51e-10	2.087e-12
12	1.488	3.51e-10	1.732e-12
13	1.311	3.53e-10	3.044e-12
14	1.029	4.44e-10	2.933e-12

Figure 6.23. DOSY of **T:dA$_3$** in $CDCl_3$ (Δ = 0.0599 s, δ = 0.0030 s).

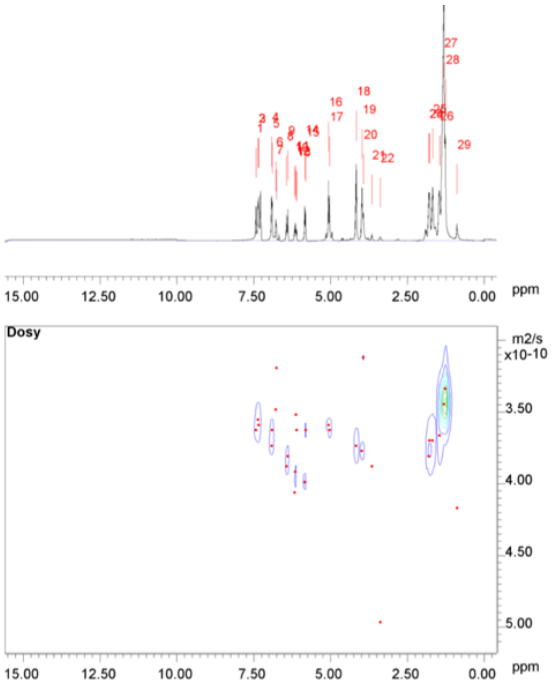

Peak name	F2 [ppm]	D [m2/s]	error
1	7.427	3.65e-10	6.359e-12
2	7.364	3.58e-10	1.003e-11
3	7.344	3.61e-10	1.178e-11
4	6.922	3.77e-10	6.567e-12
5	6.902	3.67e-10	1.017e-11
6	6.783	3.52e-10	8.894e-12
7	6.763	3.24e-10	1.198e-11
8	6.436	3.92e-10	1.033e-11
9	6.393	3.83e-10	1.348e-11
10	6.174	4.10e-10	1.953e-11
11	6.148	3.95e-10	2.659e-11
12	6.130	3.57e-10	3.342e-11
13	6.105	3.66e-10	3.195e-11
14	5.840	4.01e-10	9.980e-12
15	5.815	3.65e-10	1.605e-11
16	5.069	3.64e-10	3.167e-12
17	5.037	3.66e-10	6.658e-12
18	4.168	3.75e-10	9.965e-12
19	3.981	3.81e-10	6.476e-12
20	3.937	3.17e-10	1.534e-11
21	3.658	3.93e-10	1.189e-11
22	3.385	4.99e-10	2.186e-11
23	1.804	3.84e-10	1.177e-11
24	1.787	3.73e-10	1.590e-11
25	1.685	3.73e-10	1.642e-11
26	1.457	3.68e-10	2.287e-11
27	1.316	3.48e-10	1.411e-11
28	1.268	3.38e-10	2.160e-11
29	0.892	4.22e-10	9.777e-12

Figure 6.24. DOSY of **M:dBzA$_3$** in $CDCl_3$ (Δ = 0.0749 s, δ = 0.0030 s).

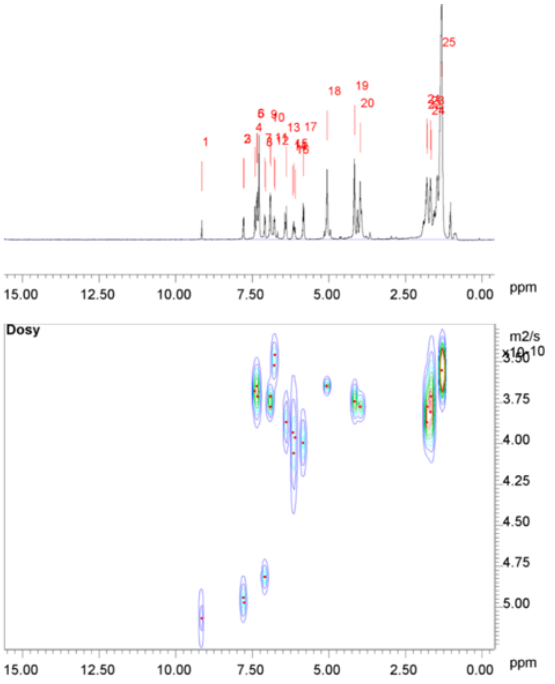

Peak name	F2 [ppm]	D [m2/s]	error
1	9.150	5.09e-10	1.306e-11
2	7.796	4.99e-10	8.458e-12
3	7.774	5.01e-10	7.073e-12
4	7.415	3.70e-10	6.062e-12
5	7.358	3.69e-10	9.236e-12
6	7.338	3.75e-10	1.054e-11
7	7.102	4.84e-10	3.906e-12
8	7.079	4.86e-10	7.228e-12
9	6.921	3.79e-10	5.018e-12
10	6.902	3.75e-10	5.601e-12
11	6.786	3.56e-10	9.047e-12
12	6.767	3.50e-10	8.341e-12
13	6.393	3.90e-10	1.149e-11
14	6.173	3.96e-10	2.337e-11
15	6.148	4.10e-10	2.588e-11
16	6.105	3.99e-10	2.367e-11
17	5.841	4.01e-10	1.206e-11
18	5.063	3.67e-10	2.681e-12
19	4.168	3.79e-10	6.657e-12
20	3.981	3.81e-10	4.817e-12
21	1.804	3.90e-10	9.970e-12
22	1.787	3.81e-10	1.335e-11
23	1.685	3.85e-10	1.414e-11
24	1.667	3.75e-10	2.011e-11
25	1.316	3.60e-10	1.041e-11

Figure 6.25. DOSY of **T:dBzA$_3$** in $CDCl_3$ (Δ = 0.0599 s, δ = 0.0028 s).

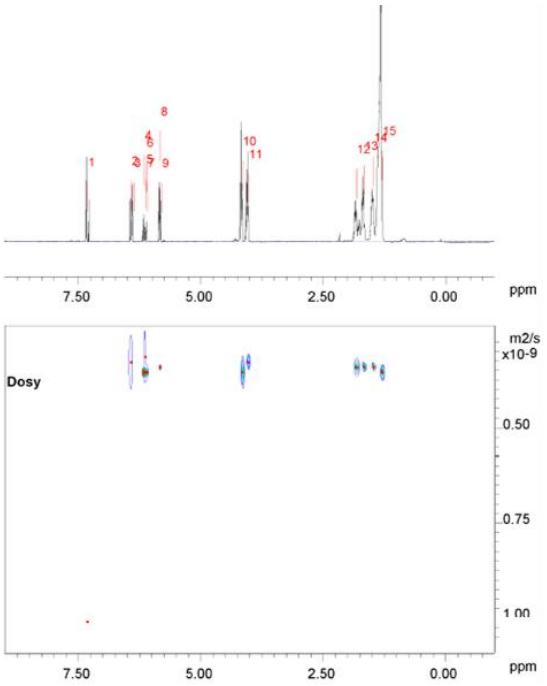

Peak name	F2 [ppm]	D [m2/s]	error
1	7.309	1.02e-09	6.928e-10
2	6.416	3.43e-10	8.359e-11
3	6.372	0.00	0.000
4	6.153	3.63e-10	4.949e-12
5	6.126	3.32e-10	8.846e-11
6	6.109	3.64e-10	6.805e-12
7	6.082	0.00	0.000
8	5.821	3.59e-10	2.666e-12
9	5.794	0.00	0.000
10	4.148	3.68e-10	2.322e-11
11	4.021	3.41e-10	1.452e-11
12	1.815	3.51e-10	9.490e-12
13	1.664	3.61e-10	5.136e-12
14	1.471	3.49e-10	5.754e-12
15	1.293	3.71e-10	8.970e-12

Figure 6.26. DOSY of **dA** in $CDCl_3$ (Δ = 0.0599 s, δ = 0.0030 s).

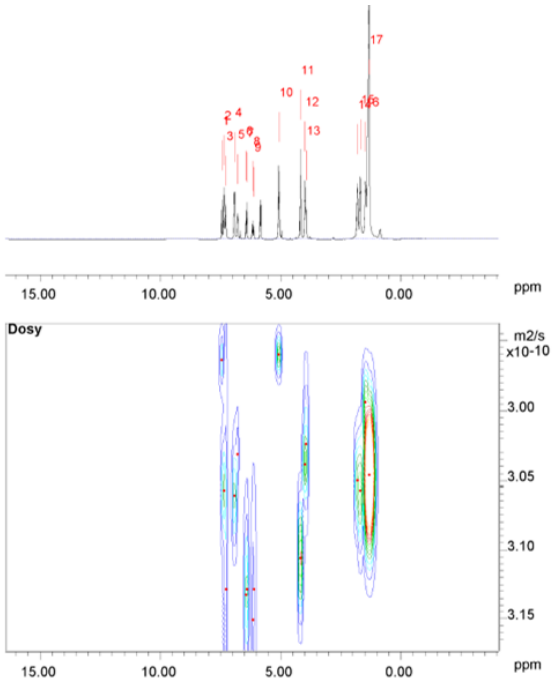

Peak name	F2 [ppm]	D [m2/s]	error
1	7.436	2.97e-10	1.640e-12
2	7.345	3.06e-10	2.848e-12
3	7.266	3.13e-10	1.377e-11
4	6.906	3.07e-10	2.780e-12
5	6.790	3.03e-10	2.293e-12
6	6.436	3.14e-10	2.870e-12
7	6.392	3.13e-10	4.777e-12
8	6.147	3.15e-10	6.916e-12
9	6.104	3.13e-10	8.156e-12
10	5.074	2.96e-10	1.086e-12
11	4.168	3.11e-10	3.069e-12
12	3.984	3.04e-10	1.840e-12
13	3.939	3.03e-10	4.008e-12
14	1.804	3.05e-10	2.523e-12
15	1.684	3.06e-10	3.121e-12
16	1.479	3.00e-10	1.932e-12
17	1.316	3.05e-10	3.574e-12

Figure 6.27. DOSY of **dBzA** in $CDCl_3$ (Δ = 0.0749 s, δ = 0.0030 s).

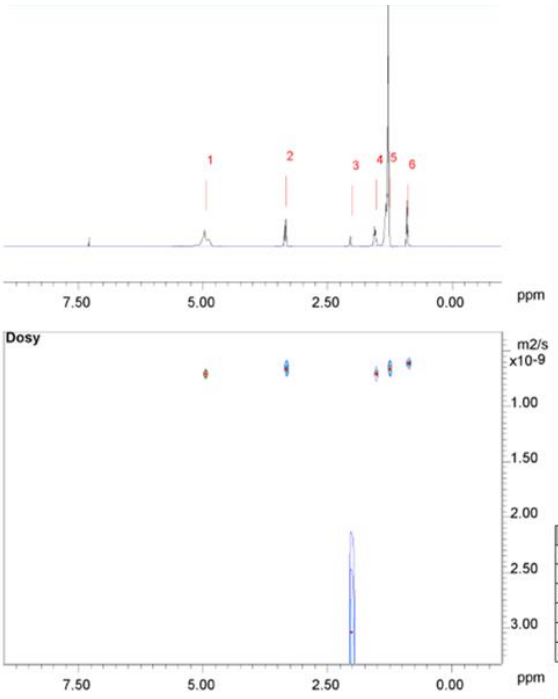

Peak name	F2 [ppm]	D [m2/s]	error
1	4.938	7.71e-10	1.267e-11
2	3.328	7.04e-10	3.225e-11
3	2.013	3.07e-09	5.612e-10
4	1.525	7.36e-10	2.347e-11
5	1.252	7.00e-10	2.746e-11
6	0.874	6.72e-10	2.257e-11

Figure 6.28. DOSY of **M** in $CDCl_3$ (Δ = 0.0599 s, δ = 0.0028 s).

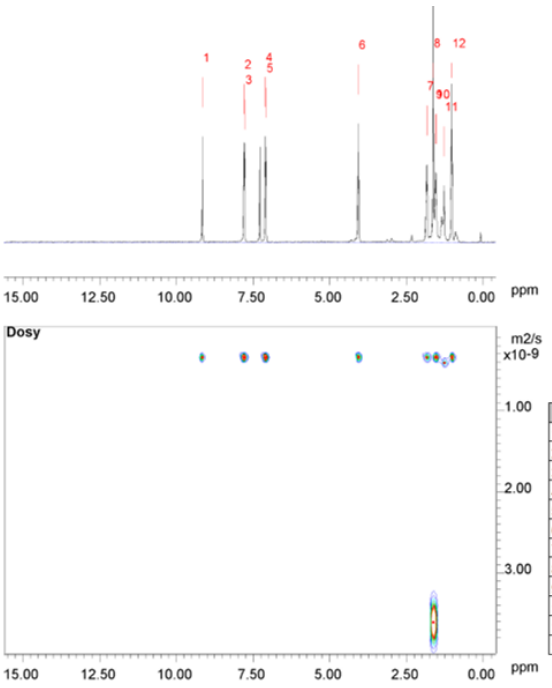

Peak name	F2 [ppm]	D [m2/s]	error
1	9.149	4.25e-10	1.991e-12
2	7.801	4.24e-10	2.339e-12
3	7.779	4.26e-10	1.309e-12
4	7.106	4.26e-10	2.686e-12
5	7.083	4.26e-10	2.959e-12
6	4.074	4.24e-10	2.486e-12
7	1.847	4.30e-10	1.919e-12
8	1.637	3.65e-09	1.576e-10
9	1.567	4.30e-10	5.818e-12
10	1.548	4.24e-10	4.796e-12
11	1.275	4.56e-10	8.299e-12
12	1.033	4.26e-10	1.666e-12

Figure 6.29. DOSY of **T** in $CDCl_3$ (Δ = 0.0599 s, δ = 0.0028 s).

BIBLIOGRAPHY

1. Koons, G. L.; Diba, M.; Mikos, A. G., Materials design for bone-tissue engineering. *Nature Reviews Materials* **2020,** *5* (8), 584-603.
2. Li, J.; Wu, C.; Chu, P. K.; Gelinsky, M., 3D printing of hydrogels: Rational design strategies and emerging biomedical applications. *Materials Science and Engineering: R: Reports* **2020,** *140*, 100543.
3. Radmanesh, S.; Shabangiz, S.; Koupaei, N.; Hassanzadeh-Tabrizi, S. A., 3D printed bio polymeric materials as a new perspective for wound dressing and skin tissue engineering applications: a review. *Journal of Polymer Research* **2022,** *29* (2), 50.
4. Fricain, J.-C.; De Olivera, H.; Devillard, R.; Kalisky, J.; Rémy, M.; Keriquel, V.; Le Nihounen, D.; Gremare, A.; Guduric, V.; Plaud, A., 3D bioprinting in regenerative medicine and tissue engineering. *médecine/sciences* **2017,** *33* (1), 52-59.
5. Baudis, S.; Nehl, F.; Ligon, S. C.; Nigisch, A.; Bergmeister, H.; Bernhard, D.; Stampfl, J.; Liska, R., Elastomeric degradable biomaterials by photopolymerization-based CAD-CAM for vascular tissue engineering. *Biomedical Materials* **2011,** *6* (5), 055003.
6. Camposeo, A.; Persano, L.; Farsari, M.; Pisignano, D., Additive manufacturing: applications and directions in photonics and optoelectronics. *Advanced optical materials* **2019,** *7* (1), 1800419.
7. Hadibrata, W.; Wei, H.; Krishnaswamy, S.; Aydin, K., Inverse Design and 3D Printing of a Metalens on an Optical Fiber Tip for Direct Laser Lithography. *Nano Letters* **2021,** *21* (6), 2422-2428.
8. Kuang, M.; Wang, J.; Bao, B.; Li, F.; Wang, L.; Jiang, L.; Song, Y., Inkjet printing patterned photonic crystal domes for wide viewing-angle displays by controlling the sliding three phase contact line. *Advanced Optical Materials* **2014,** *2* (1), 34-38.
9. Blachowicz, T.; Ehrmann, G.; Ehrmann, A., Optical elements from 3D printed polymers. *e-Polymers* **2021,** *21* (1), 549-565.
10. Jeong, H. Y.; Lee, E.; An, S.-C.; Lim, Y.; Jun, Y. C., 3D and 4D printing for optics and metaphotonics. *Nanophotonics* **2020,** *9* (5), 1139-1160.
11. Jeong, H. Y.; An, S.-C.; Jun, Y. C., Light activation of 3D-printed structures: from millimeter to sub-micrometer scale. *Nanophotonics* **2022,** *11* (3), 461-486.
12. Bunea, A.-I.; Martella, D.; Nocentini, S.; Parmeggiani, C.; Taboryski, R.; Wiersma, D. S., Light-Powered Microrobots: Challenges and Opportunities for Hard and Soft Responsive Microswimmers. *Advanced Intelligent Systems* **2021,** *3* (4), 2000256.
13. Decroly, G.; Toncheva, A.; Blanc, L.; Raquez, J.-M.; Lessinnes, T.; Delchambre, A.; Lambert, P., Programmable Stimuli-Responsive Actuators for Complex Motions in Soft Robotics: Concept, Design and Challenges. *Actuators* **2020,** *9* (4), 131.
14. Lao, Z.; Xia, N.; Wang, S.; Xu, T.; Wu, X.; Zhang, L., Tethered and Untethered 3D Microactuators Fabricated by Two-Photon Polymerization: A Review. *Micromachines* **2021,** *12* (4), 465.

15. Yap, Y. L.; Sing, S. L.; Yeong, W. Y., A review of 3D printing processes and materials for soft robotics. *Rapid Prototyping Journal* **2020,** *26* (8), 1345-1361.
16. Bhattacharjee, N.; Urrios, A.; Kang, S.; Folch, A., The upcoming 3D-printing revolution in microfluidics. *Lab on a Chip* **2016,** *16* (10), 1720-1742.
17. Kang, D.-H.; Louis, F.; Liu, H.; Shimoda, H.; Nishiyama, Y.; Nozawa, H.; Kakitani, M.; Takagi, D.; Kasa, D.; Nagamori, E.; Irie, S.; Kitano, S.; Matsusaki, M., Engineered whole cut meat-like tissue by the assembly of cell fibers using tendon-gel integrated bioprinting. *Nature Communications* **2021,** *12* (1), 5059.
18. Kuntanapreeda, S.; Hess, D., Opening access to space by maximizing utilization of 3D printing in launch vehicle design and production. *Applied Science and Engineering Progress* **2021,** *14* (2), 143-145.
19. Subrin, K.; Bressac, T.; Garnier, S.; Ambiehl, A.; Paquet, E.; Furet, B., Improvement of the mobile robot location dedicated for habitable house construction by 3D printing. *IFAC-PapersOnLine* **2018,** *51* (11), 716-721.
20. Ngo, T. D.; Kashani, A.; Imbalzano, G.; Nguyen, K. T.; Hui, D., Additive manufacturing (3D printing): A review of materials, methods, applications and challenges. *Composites Part B: Engineering* **2018,** *143*, 172-196.
21. Ligon, S. C.; Liska, R.; Stampfl, J.; Gurr, M.; Mülhaupt, R., Polymers for 3D printing and customized additive manufacturing. *Chemical reviews* **2017,** *117* (15), 10212-10290.
22. Wang, J.; Chiappone, A.; Roppolo, I.; Shao, F.; Fantino, E.; Lorusso, M.; Rentsch, D.; Dietliker, K.; Pirri, C. F.; Grützmacher, H., All-in-One Cellulose Nanocrystals for 3D Printing of Nanocomposite Hydrogels. *Angewandte Chemie International Edition* **2018,** *57* (9), 2353-2356.
23. Feng, X.; Yang, Z.; Chmely, S.; Wang, Q.; Wang, S.; Xie, Y., Lignin-coated cellulose nanocrystal filled methacrylate composites prepared via 3D stereolithography printing: Mechanical reinforcement and thermal stabilization. *Carbohydrate polymers* **2017,** *169*, 272-281.
24. Karalekas, D., Study of the mechanical properties of nonwoven fibre mat reinforced photopolymers used in rapid prototyping. *Materials & design* **2003,** *24* (8), 665-670.
25. Chawla, K. K., *Composite materials: science and engineering*. Springer Science & Business Media: 2012.
26. Parandoush, P.; Lin, D., A review on additive manufacturing of polymer-fiber composites. *Composite Structures* **2017,** *182*, 36-53.
27. Fallon, J. J.; McKnight, S. H.; Bortner, M. J., Highly Loaded Fiber Filled Polymers for Material Extrusion: A Review of Current Understanding. *Additive Manufacturing* **2019,** *30*, 100810.
28. Li, Y.; Feng, Z.; Huang, L.; Essa, K.; Bilotti, E.; Zhang, H.; Peijs, T.; Hao, L., Additive manufacturing high performance graphene-based composites: A review. *Composites Part A: Applied Science and Manufacturing* **2019,** *124*, 105483.
29. Sano, Y.; Matsuzaki, R.; Ueda, M.; Todoroki, A.; Hirano, Y., 3D printing of discontinuous and continuous fibre composites using stereolithography. *Additive Manufacturing* **2018,** *24*, 521-527.
30. Ushiba, S.; Shoji, S.; Kuray, P.; Masui, K.; Kono, J.; Kawata, S., Two photon polymerization lithography for 3D microfabrication of single wall carbon nanotube/polymer composites. In *Advanced Fabrication Technologies for Micro/Nano Optics and Photonics VI*, International Society for Optics and Photonics: 2013; Vol. 8613, p 86130Y.

31. Ushiba, S.; Shoji, S.; Masui, K.; Kuray, P.; Kono, J.; Kawata, S., 3D microfabrication of single-wall carbon nanotube/polymer composites by two-photon polymerization lithography. *Carbon* **2013,** *59*, 283-288.
32. Xiong, W.; Liu, Y.; Jiang, L. J.; Zhou, Y. S.; Li, D. W.; Jiang, L.; Silvain, J.-F.; Lu, Y. F., Laser-Directed Assembly of Aligned Carbon Nanotubes in Three Dimensions for Multifunctional Device Fabrication. *Advanced Materials* **2016,** *28* (10), 2002-2009.
33. Tao, Y.; Wei, C.; Liu, J.; Deng, C.; Cai, S.; Xiong, W., Nanostructured electrically conductive hydrogels obtained via ultrafast laser processing and self-assembly. *Nanoscale* **2019,** *11* (18), 9176-9184.
34. Palaganas, N. B.; Mangadlao, J. D.; de Leon, A. C. C.; Palaganas, J. O.; Pangilinan, K. D.; Lee, Y. J.; Advincula, R. C., 3D printing of photocurable cellulose nanocrystal composite for fabrication of complex architectures via stereolithography. *ACS applied materials & interfaces* **2017,** *9* (39), 34314-34324.
35. Li, V. C.-F.; Kuang, X.; Mulyadi, A.; Hamel, C. M.; Deng, Y.; Qi, H. J., 3D printed cellulose nanocrystal composites through digital light processing. *Cellulose* **2019,** *26* (6), 3973-3985.
36. Spiegel, C. A.; Hackner, M.; Bothe, V. P.; Spatz, J. P.; Blasco, E., 4D Printing of Shape Memory Polymers: From Macro to Micro. *Advanced Functional Materials* **2022**, 2110580.
37. Ge, Q.; Sakhaei, A. H.; Lee, H.; Dunn, C. K.; Fang, N. X.; Dunn, M. L., Multimaterial 4D Printing with Tailorable Shape Memory Polymers. *Scientific Reports* **2016,** *6* (1), 31110.
38. Levkin, P. A.; Svec, F.; Fréchet, J. M. J., Porous Polymer Coatings: a Versatile Approach to Superhydrophobic Surfaces. *Advanced Functional Materials* **2009,** *19* (12), 1993-1998.
39. Dong, Z.; Vuckovac, M.; Cui, W.; Zhou, Q.; Ras, R. H. A.; Levkin, P. A., 3D Printing of Superhydrophobic Objects with Bulk Nanostructure. *Advanced Materials* **2021,** *33* (45), 2106068.
40. Dong, Z.; Cui, H.; Zhang, H.; Wang, F.; Zhan, X.; Mayer, F.; Nestler, B.; Wegener, M.; Levkin, P. A., 3D printing of inherently nanoporous polymers via polymerization-induced phase separation. *Nature Communications* **2021,** *12* (1), 247.
41. Nocentini, S.; Parmeggiani, C.; Martella, D.; Wiersma, D. S., Optically Driven Soft Micro Robotics. *Advanced Optical Materials* **2018,** *6* (14), 1800207.
42. Nocentini, S.; Martella, D.; Parmeggiani, C.; Wiersma, D. S., 3D Printed Photoresponsive Materials for Photonics. *Advanced Optical Materials* **2019,** *7* (16), 1900156.
43. Su, A.; Al'Aref, S. J., Chapter 1 - History of 3D Printing. In *3D Printing Applications in Cardiovascular Medicine*, Al'Aref, S. J.; Mosadegh, B.; Dunham, S.; Min, J. K., Eds. Academic Press: Boston, 2018; pp 1-10.
44. Hull, C. W.; Spence, S. T.; Albert, D. J.; Smalley, D. R.; Harlow, R. A.; Steinbaugh, P.; Tarnoff, H. L.; Nguyen, H. D.; Lewis, C. W.; Vorgitch, T. J. Methods and apparatus for production of three-dimensional objects by stereolithography. US4874461, 1991.
45. Petersen, E. E.; Pearce, J., Emergence of home manufacturing in the developed world: Return on investment for open-source 3-D printers. *Technologies* **2017,** *5* (1), 7.
46. Vyavahare, S.; Teraiya, S.; Panghal, D.; Kumar, S., Fused deposition modelling: a review. *Rapid Prototyping Journal* **2020,** *26* (1), 176-201.
47. Mohan, N.; Senthil, P.; Vinodh, S.; Jayanth, N., A review on composite materials and process parameters optimisation for the fused deposition modelling process. *Virtual and Physical Prototyping* **2017,** *12* (1), 47-59.
48. Liu, Z.; Wang, Y.; Wu, B.; Cui, C.; Guo, Y.; Yan, C., A critical review of fused deposition modeling 3D printing technology in manufacturing polylactic acid parts. *The International Journal of Advanced Manufacturing Technology* **2019,** *102* (9), 2877-2889.

49. Gibson, I.; Rosen, D. W.; Stucker, B.; Khorasani, M.; Rosen, D.; Stucker, B.; Khorasani, M., *Additive manufacturing technologies*. Springer: 2021; Vol. 17.
50. Ligon, S. C.; Liska, R.; Stampfl, J. r.; Gurr, M.; Mülhaupt, R., Polymers for 3D printing and customized additive manufacturing. *Chemical reviews* **2017,** *117* (15), 10212-10290.
51. Huang, S. H.; Zhang, L. C.; Han, M., An Effective Error-Tolerance Slicing Algorithm for STL Files. *The International Journal of Advanced Manufacturing Technology* **2002,** *20* (5), 363-367.
52. Szilvśi-Nagy, M.; Mátyási, G., Analysis of STL files. *Mathematical and Computer Modelling* **2003,** *38* (7), 945-960.
53. Zhou, L.-Y.; Fu, J.; He, Y., A Review of 3D Printing Technologies for Soft Polymer Materials. *Advanced Functional Materials* **2020,** *30* (28), 2000187.
54. Conner, B. P.; Manogharan, G. P.; Martof, A. N.; Rodomsky, L. M.; Rodomsky, C. M.; Jordan, D. C.; Limperos, J. W., Making sense of 3-D printing: Creating a map of additive manufacturing products and services. *Additive Manufacturing* **2014,** *1-4*, 64-76.
55. Liu, J.; Gaynor, A. T.; Chen, S.; Kang, Z.; Suresh, K.; Takezawa, A.; Li, L.; Kato, J.; Tang, J.; Wang, C. C. L.; Cheng, L.; Liang, X.; To, A. C., Current and future trends in topology optimization for additive manufacturing. *Structural and Multidisciplinary Optimization* **2018,** *57* (6), 2457-2483.
56. Capanna, R.; Andreani, L., The Rationale of 3D Printing in Oncological Orthopaedics. In *3D Printing in Bone Surgery*, Zoccali, C.; Ruggieri, P.; Benazzo, F., Eds. Springer International Publishing: Cham, 2022; pp 13-23.
57. Shah, R. J.; Lagdive, S. B.; Machchhar, A. H.; Periyanan, K.; Cherian, S., Technique to Fabricate Hollow Maxillary Complete Denture Using 3D Printed Template. *Journal of Prosthodontics* **2020,** *29* (4), 360-363.
58. Goh, G. D.; Agarwala, S.; Goh, G. L.; Dikshit, V.; Sing, S. L.; Yeong, W. Y., Additive manufacturing in unmanned aerial vehicles (UAVs): Challenges and potential. *Aerospace Science and Technology* **2017,** *63*, 140-151.
59. Liu, R.; Wang, Z.; Sparks, T.; Liou, F.; Newkirk, J., 13 - Aerospace applications of laser additive manufacturing. In *Laser Additive Manufacturing*, Brandt, M., Ed. Woodhead Publishing: 2017; pp 351-371.
60. Pervaiz, S.; Qureshi, T. A.; Kashwani, G.; Kannan, S., 3D Printing of Fiber-Reinforced Plastic Composites Using Fused Deposition Modeling: A Status Review. *Materials* **2021,** *14* (16), 4520.
61. Matos, M. A.; Rocha, A. M. A.; Pereira, A. I., Improving additive manufacturing performance by build orientation optimization. *The International Journal of Advanced Manufacturing Technology* **2020**, 1-13.
62. Mostafaei, A.; Elliott, A. M.; Barnes, J. E.; Li, F.; Tan, W.; Cramer, C. L.; Nandwana, P.; Chmielus, M., Binder jet 3D printing—Process parameters, materials, properties, modeling, and challenges. *Progress in Materials Science* **2021,** *119*, 100707.
63. Saroia, J.; Wang, Y.; Wei, Q.; Lei, M.; Li, X.; Guo, Y.; Zhang, K., A review on 3D printed matrix polymer composites: its potential and future challenges. *The International Journal of Advanced Manufacturing Technology* **2020,** *106* (5), 1695-1721.
64. Liu, Z. Y.; Loh, N. H.; Tor, S. B.; Khor, K. A., Characterization of powder injection molding feedstock. *Materials Characterization* **2002,** *49* (4), 313-320.
65. Merhar, J. R., Overview of metal injection moulding. *Metal Powder Report* **1990,** *45* (5), 339-342.

66. Garcia, F. L.; Moris, V. A. d. S.; Nunes, A. O.; Silva, D. A. L., Environmental performance of additive manufacturing process – an overview. *Rapid Prototyping Journal* **2018,** *24* (7), 1166-1177.
67. Govindarajan, S. R.; Xu, Y.; Swanson, J. P.; Jain, T.; Lu, Y.; Choi, J.-W.; Joy, A., A solvent and initiator free, low-modulus, degradable polyester platform with modular functionality for ambient-temperature 3D printing. *Macromolecules* **2016,** *49* (7), 2429-2437.
68. Liu, Q.; Jain, T.; Peng, C.; Peng, F.; Narayanan, A.; Joy, A., Introduction of Hydrogen Bonds Improves the Shape Fidelity of Viscoelastic 3D Printed Scaffolds While Maintaining Their Low-Temperature Printability. *Macromolecules* **2020,** *53* (10), 3690-3699.
69. Widyaya, V. T.; Riga, E. K.; Müller, C.; Lienkamp, K., Submicrometer-Sized, 3D Surface-Attached Polymer Networks by Microcontact Printing: Using UV-Cross-Linking Efficiency To Tune Structure Height. *Macromolecules* **2018,** *51* (4), 1409-1417.
70. Kabb, C. P.; O'Bryan, C. S.; Deng, C. C.; Angelini, T. E.; Sumerlin, B. S., Photoreversible Covalent Hydrogels for Soft-Matter Additive Manufacturing. *ACS Applied Materials & Interfaces* **2018,** *10* (19), 16793-16801.
71. Cazin, I.; Rossegger, E.; Guedes de la Cruz, G.; Griesser, T.; Schlögl, S., Recent Advances in Functional Polymers Containing Coumarin Chromophores. *Polymers* **2021,** *13* (1), 56.
72. Sun, Y. L.; Dong, W. F.; Yang, R. Z.; Meng, X.; Zhang, L.; Chen, Q. D.; Sun, H. B., Dynamically tunable protein microlenses. *Angewandte Chemie International Edition* **2012,** *51* (7), 1558-1562.
73. Sun, Y.-L.; Hou, Z.-S.; Sun, S.-M.; Zheng, B.-Y.; Ku, J.-F.; Dong, W.-F.; Chen, Q.-D.; Sun, H.-B., Protein-based three-dimensional whispering-gallery-mode micro-lasers with stimulus-responsiveness. *Scientific reports* **2015,** *5*, 12852.
74. Igarashi, N.; Onoue, S.; Tsuda, Y., Photoreactivity of amino acids: tryptophan-induced photochemical events via reactive oxygen species generation. *Analytical Sciences* **2007,** *23* (8), 943-948.
75. Kaehr, B.; Shear, J. B., Multiphoton fabrication of chemically responsive protein hydrogels for microactuation. *Proceedings of the National Academy of Sciences* **2008,** *105* (26), 8850-8854.
76. Kaehr, B.; Allen, R.; Javier, D. J.; Currie, J.; Shear, J. B., Guiding neuronal development with in situ microfabrication. *Proceedings of the National Academy of Sciences* **2004,** *101* (46), 16104-16108.
77. Narupai, B.; Nelson, A., 100th Anniversary of Macromolecular Science Viewpoint: Macromolecular Materials for Additive Manufacturing. *ACS Macro Letters* **2020,** *9* (5), 627-638.
78. Nguyen, A. K.; Narayan, R. J., Two-photon polymerization for biological applications. *Materials Today* **2017,** *20* (6), 314-322.
79. Derakhshanfar, S.; Mbeleck, R.; Xu, K.; Zhang, X.; Zhong, W.; Xing, M., 3D bioprinting for biomedical devices and tissue engineering: A review of recent trends and advances. *Bioactive materials* **2018,** *3* (2), 144-156.
80. Hull, C. Apparatus for production of three-dimensional objects by stereolithography. US 4575330 A, 1986.
81. Hill, M. R.; Carmean, R. N.; Sumerlin, B. S., Expanding the Scope of RAFT Polymerization: Recent Advances and New Horizons. *Macromolecules* **2015,** *48* (16), 5459-5469.

82. Zapka, W., *Handbook of Industrial Inkjet Printing: A Full System Approach*. John Wiley & Sons: 2017.
83. Moad, G.; Solomon, D. H., *The chemistry of radical polymerization*. 2 ed.; Elsevier: 2006; p 639.
84. Leggesse, E. G.; Tong, W.-R.; Nachimuthu, S.; Chen, T.-Y.; Jiang, J.-C., Theoretical study on photochemistry of Irgacure 907. *Journal of Photochemistry and Photobiology A: Chemistry* **2017,** *347*, 78-85.
85. Dietliker, K.; Murer, P.; Hüsler, R.; Jung, T. Alpha-hydroxyketones. US9199934B2, 2015.
86. Jockusch, S.; Landis, M. S.; Freiermuth, B.; Turro, N. J., Photochemistry and photophysics of α-hydroxy ketones. *Macromolecules* **2001,** *34* (6), 1619-1626.
87. Fouassier, J.-P.; Lalevée, J., *Photoinitiators for polymer synthesis: scope, reactivity, and efficiency*. John Wiley & Sons: 2012.
88. Gatlik, I.; Rzadek, P.; Gescheidt, G.; Rist, G.; Hellrung, B.; Wirz, J.; Dietliker, K.; Hug, G.; Kunz, M.; Wolf, J.-P., Structure− reactivity relationships in radical reactions: a novel method for the simultaneous determination of absolute rate constants and structural features. *Journal of the American Chemical Society* **1999,** *121* (36), 8332-8336.
89. Jockusch, S.; Turro, N. J., Phosphinoyl radicals: Structure and reactivity. A laser flash photolysis and time-resolved ESR investigation. *Journal of the American Chemical Society* **1998,** *120* (45), 11773-11777.
90. Haas, M.; Radebner, J.; Eibel, A.; Gescheidt, G.; Stueger, H., Recent Advances in Germanium-Based Photoinitiator Chemistry. *Chemistry–A European Journal* **2018,** *24* (33), 8258-8267.
91. Ganster, B.; Fischer, U. K.; Moszner, N.; Liska, R., New photocleavable structures. Diacylgermane-based photoinitiators for visible light curing. *Macromolecules* **2008,** *41* (7), 2394-2400.
92. Moszner, N.; Fischer, U. K.; Ganster, B.; Liska, R.; Rheinberger, V., Benzoyl germanium derivatives as novel visible light photoinitiators for dental materials. *Dental Materials* **2008,** *24* (7), 901-907.
93. Pappas, S. P., Photocrosslinking. **1989**.
94. Hageman, H., Photoinitiators and photoinitiation mechanisms of free-radical polymerisation processes. In *Photopolymerisation and photoimaging science and technology*, Springer: 1989; pp 1-53.
95. Balz, G.; Schiemann, G., Ueber aromatische fluorverbindungen, I.: Ein neues verfahren zu ihrer darstellung. *Berichte der deutschen chemischen Gesellschaft (A and B Series)* **1927,** *60* (5), 1186-1190.
96. Banks, R. E.; Smart, B. E.; Tatlow, J., *Organofluorine chemistry: principles and commercial applications*. Springer Science & Business Media: 2013.
97. Crivello, J. V. In *Cationic polymerization — Iodonium and sulfonium salt photoinitiators*, Berlin, Heidelberg, Springer Berlin Heidelberg: Berlin, Heidelberg, 1984; pp 1-48.
98. Crivello, J. V., The discovery and development of onium salt cationic photoinitiators. *Journal of Polymer Science Part A: Polymer Chemistry* **1999,** *37* (23), 4241-4254.
99. Xing, J.-F.; Zheng, M.-L.; Duan, X.-M., Two-photon polymerization microfabrication of hydrogels: an advanced 3D printing technology for tissue engineering and drug delivery. *Chemical Society Reviews* **2015,** *44* (15), 5031-5039.

100. Stampfl, J.; Liska, R.; Ovsianikov, A., *Multiphoton lithography: Techniques, materials, and applications*. John Wiley & Sons: 2016.
101. Hahn, V.; Messer, T.; Bojanowski, N. M.; Curticean, E. R.; Wacker, I.; Schröder, R. R.; Blasco, E.; Wegener, M., Two-step absorption instead of two-photon absorption in 3D nanoprinting. *Nature Photonics* **2021,** *15* (12), 932-938.
102. Bird, D.; Caravaca, E.; Laquidara, J.; Luhmann, K.; Ravindra, N. M., Formulation of Curable Resins Utilized in Stereolithography. In *TMS 2019 148th Annual Meeting & Exhibition Supplemental Proceedings*, Springer International Publishing: Cham, 2019; pp 1575-1587.
103. van Herk, A. M., Historic Account of the Development in the Understanding of the Propagation Kinetics of Acrylate Radical Polymerizations. *Macromolecular Rapid Communications* **2009,** *30* (23), 1964-1968.
104. Ballard, N.; Asua, J. M., Radical polymerization of acrylic monomers: An overview. *Progress in Polymer Science* **2018,** *79*, 40-60.
105. Jian, Y.; He, Y.; Jiang, T.; Li, C.; Yang, W.; Nie, J., Polymerization shrinkage of (meth)acrylate determined by reflective laser beam scanning. *Journal of Polymer Science Part B: Polymer Physics* **2012,** *50* (13), 923-928.
106. Rostami, N.; Graf, D.; Schranzhofer, L.; Hild, S.; Hanemann, T., Overcoming oxygen inhibition effect by TODA in acrylate-based ceramic-filled inks. *Progress in Organic Coatings* **2019,** *130*, 221-225.
107. Resetco, C.; Hendriks, B.; Badi, N.; Du Prez, F., Thiol–ene chemistry for polymer coatings and surface modification – building in sustainability and performance. *Materials Horizons* **2017,** *4* (6), 1041-1053.
108. Blasco, E.; Wegener, M.; Barner-Kowollik, C., Photochemically driven polymeric network formation: synthesis and applications. *Advanced Materials* **2017,** *29* (15), 1604005.
109. Lee, T. Y.; Carioscia, J.; Smith, Z.; Bowman, C. N., Thiol− Allyl Ether− Methacrylate ternary systems. Evolution mechanism of polymerization-induced shrinkage stress and mechanical properties. *Macromolecules* **2007,** *40* (5), 1473-1479.
110. Chan, J. W.; Shin, J.; Hoyle, C. E.; Bowman, C. N.; Lowe, A. B., Synthesis, thiol− yne "click" photopolymerization, and physical properties of networks derived from novel multifunctional alkynes. *Macromolecules* **2010,** *43* (11), 4937-4942.
111. Oesterreicher, A.; Wiener, J.; Roth, M.; Moser, A.; Gmeiner, R.; Edler, M.; Pinter, G.; Griesser, T., Tough and degradable photopolymers derived from alkyne monomers for 3D printing of biomedical materials. *Polymer Chemistry* **2016,** *7* (32), 5169-5180.
112. Oesterreicher, A.; Ayalur-Karunakaran, S.; Moser, A.; Mostegel, F. H.; Edler, M.; Kaschnitz, P.; Pinter, G.; Trimmel, G.; Schlögl, S.; Griesser, T., Exploring thiol-yne based monomers as low cytotoxic building blocks for radical photopolymerization. *Journal of Polymer Science Part A: Polymer Chemistry* **2016,** *54* (21), 3484-3494.
113. Leonards, H.; Engelhardt, S.; Hoffmann, A.; Pongratz, L.; Schriever, S.; Bläsius, J.; Wehner, M. M.; Gillner, A., Advantages and drawbacks of Thiol-ene based resins for 3D-printing. In *Laser 3D Manufacturing II*, International Society for Optics and Photonics: 2015; Vol. 9353, p 93530F.
114. Wu, G.-H.; Hsu, S.-h., Review: Polymeric-Based 3D Printing for Tissue Engineering. *Journal of Medical and Biological Engineering* **2015,** *35* (3), 285-292.
115. Fairbanks, B. D.; Scott, T. F.; Kloxin, C. J.; Anseth, K. S.; Bowman, C. N., Thiol− Yne photopolymerizations: novel mechanism, kinetics, and step-growth formation of highly cross-linked networks. *Macromolecules* **2009,** *42* (1), 211-217.

116. Lowe, A. B., Thiol-yne 'click'/coupling chemistry and recent applications in polymer and materials synthesis and modification. *Polymer* **2014,** *55* (22), 5517-5549.
117. Senyurt, A. F.; Wei, H.; Hoyle, C. E.; Piland, S. G.; Gould, T. E., Ternary thiol–ene/acrylate photopolymers: Effect of acrylate structure on mechanical properties. *Macromolecules* **2007,** *40* (14), 4901-4909.
118. Reddy, S. K.; Cramer, N. B.; Kalvaitas, M.; Lee, T. Y.; Bowman, C. N., Mechanistic modelling and network properties of ternary thiol–vinyl photopolymerizations. *Australian journal of chemistry* **2006,** *59* (8), 586-593.
119. Wu, X.; Gross, B.; Leuschel, B.; Mougin, K.; Dominici, S.; Gree, S.; Belqat, M.; Tkachenko, V.; Cabannes-Boué, B.; Chemtob, A.; Poly, J.; Spangenberg, A., On-Demand Editing of Surface Properties of Microstructures Made by 3D Direct Laser Writing via Photo-Mediated RAFT Polymerization. *Advanced Functional Materials* **2021,** *32* (14), 2109446.
120. Chen, M.; Gu, Y.; Singh, A.; Zhong, M.; Jordan, A. M.; Biswas, S.; Korley, L. T. J.; Balazs, A. C.; Johnson, J. A., Living Additive Manufacturing: Transformation of Parent Gels into Diversely Functionalized Daughter Gels Made Possible by Visible Light Photoredox Catalysis. *ACS Central Science* **2017,** *3* (2), 124-134.
121. Shi, X.; Zhang, J.; Corrigan, N.; Boyer, C., PET-RAFT facilitated 3D printable resins with multifunctional RAFT agents. *Materials Chemistry Frontiers* **2021,** *5* (5), 2271-2282.
122. Zhang, Z.; Corrigan, N.; Bagheri, A.; Jin, J.; Boyer, C., A Versatile 3D and 4D Printing System through Photocontrolled RAFT Polymerization. *Angewandte Chemie International Edition* **2019,** *58* (50), 17954-17963.
123. Lee, J. B.; Choi, K.-H.; Yoo, K., Innovative SU-8 Lithography Techniques and Their Applications. *Micromachines* **2015,** *6* (1), 1-18.
124. Campo, A. d.; Greiner, C., SU-8: a photoresist for high-aspect-ratio and 3D submicron lithography. *Journal of Micromechanics and Microengineering* **2007,** *17* (6), R81-R95.
125. Juodkazis, S.; Mizeikis, V.; Seet, K. K.; Miwa, M.; Misawa, H., Two-photon lithography of nanorods in SU-8 photoresist. *Nanotechnology* **2005,** *16* (6), 846.
126. Mizeikis, V.; Seet, K. K.; Juodkazis, S.; Misawa, H., Three-dimensional woodpile photonic crystal templates for the infrared spectral range. *Optics letters* **2004,** *29* (17), 2061-2063.
127. McCracken, J. M.; Tondiglia, V. P.; Auguste, A. D.; Godman, N. P.; Donovan, B. R.; Bagnall, B. N.; Fowler, H. E.; Baxter, C. M.; Matavulj, V.; Berrigan, J. D., Microstructured Photopolymerization of Liquid Crystalline Elastomers in Oxygen-Rich Environments. *Advanced Functional Materials* **2019,** *29* (40), 1903761.
128. Bártolo, P. J.; Gibson, I., *Stereolithography: Materials, Processes and Applications*. Springer US: Boston, MA, 2011; p 340.
129. Turro, N. J., Molecular photochemistry. *New York* **1965**, 224.
130. Göppert-Mayer, M., Über Elementarakte mit zwei Quantensprüngen. *Annalen der Physik* **1931,** *401* (3), 273-294.
131. Croissant, J. G.; Zink, J. I.; Raehm, L.; Durand, J. O., Two-photon-excited silica and organosilica nanoparticles for spatiotemporal cancer treatment. *Advanced healthcare materials* **2018,** *7* (7), 1701248.
132. Zheng, L.; Kurselis, K.; El-Tamer, A.; Hinze, U.; Reinhardt, C.; Overmeyer, L.; Chichkov, B., Nanofabrication of High-Resolution Periodic Structures with a Gap Size Below 100 nm by Two-Photon Polymerization. *Nanoscale Research Letters* **2019,** *14* (1), 134.

133. Bártolo, P. J., *Stereolithography: materials, processes and applications*. Springer Science & Business Media: 2011.
134. Gojzewski, H.; Guo, Z.; Grzelachowska, W.; Ridwan, M. G.; Hempenius, M. A.; Grijpma, D. W.; Vancso, G. J., Layer-by-Layer Printing of Photopolymers in 3D: How Weak is the Interface? *ACS Applied Materials & Interfaces* **2020,** *12* (7), 8908-8914.
135. Jigang, H.; Qin, Q.; Jie, W.; Hui, F., Two Dimensional Laser Galvanometer Scanning Technology for Additive Manufacturing. *International Journal of Materials, Mechanics and Manufacturing* **2018,** *6* (5), 332-336.
136. Yoon, T.; Kim, C.-S.; Kim, K.; Choi, J.-r., Emerging applications of digital micromirror devices in biophotonic fields. *Optics & Laser Technology* **2018,** *104*, 17-25.
137. Dudley, D.; Duncan, W.; Slaughter, J., *Emerging digital micromirror device (DMD) applications*. SPIE: 2003; Vol. 4985.
138. Hornbeck, L., *Digital Light Processing for high-brightness high-resolution applications*. SPIE: 1997; Vol. 3013.
139. Tumbleston, J. R.; Shirvanyants, D.; Ermoshkin, N.; Janusziewicz, R.; Johnson, A. R.; Kelly, D.; Chen, K.; Pinschmidt, R.; Rolland, J. P.; Ermoshkin, A., Continuous liquid interface production of 3D objects. *Science* **2015,** *347* (6228), 1349-1352.
140. DeSimone, J. M.; Ermoshkin, A.; Ermoshkin, N.; Samulski, E. T. Continuous liquid interphase printing. US10016938B2, 2018.
141. Maruo, S.; Kawata, S., Two-photon-absorbed photopolymerization for three-dimensional microfabrication. In *Proceedings IEEE The Tenth Annual International Workshop on Micro Electro Mechanical Systems. An Investigation of Micro Structures, Sensors, Actuators, Machines and Robots*, IEEE: 1997; pp 169-174.
142. Wollhofen, R.; Katzmann, J.; Hrelescu, C.; Jacak, J.; Klar, T. A., 120 nm resolution and 55 nm structure size in STED-lithography. *Opt. Express* **2013,** *21* (9), 10831-10840.
143. Müller, P.; Müller, R.; Hammer, L.; Barner-Kowollik, C.; Wegener, M.; Blasco, E., STED-Inspired Laser Lithography Based on Photoswitchable Spirothiopyran Moieties. *Chemistry of Materials* **2019,** *31* (6), 1966-1972.
144. Saha, S. K.; Divin, C.; Cuadra, J. A.; Panas, R. M., Effect of Proximity of Features on the Damage Threshold During Submicron Additive Manufacturing Via Two-Photon Polymerization. *Journal of Micro and Nano-Manufacturing* **2017,** *5* (3), 031002.
145. Mahmood, M. A.; Popescu, A. C., 3D Printing at Micro-Level: Laser-Induced Forward Transfer and Two-Photon Polymerization. *Polymers* **2021,** *13* (13), 2034.
146. Pearre, B. W.; Michas, C.; Tsang, J.-M.; Gardner, T. J.; Otchy, T. M., Fast micron-scale 3D printing with a resonant-scanning two-photon microscope. *Additive Manufacturing* **2019,** *30*, 100887.
147. Monti, J.; Blasco, E., Hierarchical ordering in light-triggered additive manufacturing. *Polymer Chemistry* **2020,** *11* (46), 7316-7329.
148. Del Pozo, M.; Delaney, C.; Bastiaansen, C. W.; Diamond, D.; Schenning, A. P.; Florea, L., Direct Laser Writing of Four-Dimensional Structural Color Microactuators Using a Photonic Photoresist. *ACS nano* **2020,** *14* (8), 9832-9839.
149. Sandford O'Neill, J. J.; Salter, P. S.; Booth, M. J.; Elston, S. J.; Morris, S. M., Electrically-tunable positioning of topological defects in liquid crystals. *Nature Communications* **2020,** *11* (1), 2203.
150. Tartan, C. C.; Sandford O'Neill, J. J.; Salter, P. S.; Aplinc, J.; Booth, M. J.; Ravnik, M.; Morris, S. M.; Elston, S. J., Read on Demand Images in Laser-Written Polymerizable Liquid Crystal Devices. *Advanced Optical Materials* **2018,** *6* (20), 1800515.

151. Tartan, C. C.; Salter, P. S.; Booth, M. J.; Morris, S. M.; Elston, S. J., Localised polymer networks in chiral nematic liquid crystals for high speed photonic switching. *Journal of Applied Physics* **2016,** *119* (18), 183106.
152. Tartan, C.; Salter, P.; Wilkinson, T.; Booth, M.; Morris, S.; Elston, S., Generation of 3-dimensional polymer structures in liquid crystalline devices using direct laser writing. *RSC advances* **2017,** *7* (1), 507-511.
153. Nocentini, S.; Riboli, F.; Burresi, M.; Martella, D.; Parmeggiani, C.; Wiersma, D. S., Three-dimensional photonic circuits in rigid and soft polymers tunable by light. *ACS Photonics* **2018,** *5* (8), 3222-3230.
154. Halevi, O.; Tan, J. M.; Lee, P. S.; Magdassi, S., Hydrolytically Stable MOF in 3D-Printed Structures. *Advanced Sustainable Systems* **2018,** *2* (2), 1700150.
155. Goodby, J. W.; Gray, G. W., Guide to the Nomenclature and Classification of Liquid Crystals. In *Handbook of Liquid Crystals Set*, 1998; pp 17-23.
156. Reinitzer, F., Beiträge zur Kenntniss des Cholesterins. *Monatshefte für Chemie und verwandte Teile anderer Wissenschaften* **1888,** *9* (1), 421-441.
157. Rosen, B. M.; Wilson, C. J.; Wilson, D. A.; Peterca, M.; Imam, M. R.; Percec, V., Dendron-Mediated Self-Assembly, Disassembly, and Self-Organization of Complex Systems. *Chemical Reviews* **2009,** *109* (11), 6275-6540.
158. Malgras, V.; Ji, Q.; Kamachi, Y.; Mori, T.; Shieh, F.-K.; Wu, K. C.-W.; Ariga, K.; Yamauchi, Y., Templated Synthesis for Nanoarchitectured Porous Materials. *Bulletin of the Chemical Society of Japan* **2015,** *88* (9), 1171-1200.
159. Funahashi, M.; Kato, T., Design of liquid crystals: from a nematogen to thiophene-based π-conjugated mesogens. *Liquid Crystals* **2015,** *42* (5-6), 909-917.
160. Gao, L.; Shen, Z.; Fan, X.; Zhou, Q., Mesogen-jacketed liquid crystalline polymers: from molecular design to polymer light-emitting diode applications. *Polymer Chemistry* **2012,** *3* (8), 1947-1957.
161. Lubensky, T. C., Molecular Description of Nematic Liquid Crystals. *Physical Review A* **1970,** *2* (6), 2497-2514.
162. Koide, N., *Liquid Crystal Display Story*. Springer: 2016.
163. Singh, G.; Kumar, S.; Kang, S. W., Structures: Liquid Crystals. In *Reference Module in Materials Science and Materials Engineering*, Elsevier: 2016.
164. Münchinger, A.; Hahn, V.; Beutel, D.; Woska, S.; Monti, J.; Rockstuhl, C.; Blasco, E.; Wegener, M., Multi-Photon 4D Printing of Complex Liquid Crystalline Microstructures by In Situ Alignment Using Electric Fields. *Advanced Materials Technologies* **2022,** *7* (1), 2100944.
165. Yoshida, H.; Nakazawa, G.; Tagashira, K.; Ozaki, M., Self-alignment behaviour of photopolymerized liquid crystal micro-particles in a nematic liquid crystal. *Soft Matter* **2012,** *8* (44), 11323-11327.
166. Spiegel, C. A.; Hippler, M.; Münchinger, A.; Bastmeyer, M.; Barner-Kowollik, C.; Wegener, M.; Blasco, E., 4D Printing at the Microscale. *Advanced Functional Materials* **2019**, 1907615.
167. Mitchell, A.; Lafont, U.; Hołyńska, M.; Semprimoschnig, C., Additive manufacturing—A review of 4D printing and future applications. *Additive Manufacturing* **2018,** *24*, 606-626.
168. Descrovi, E.; Pirani, F.; Rajamanickam, V. P.; Licheri, S.; Liberale, C., Photo-responsive suspended micro-membranes. *Journal of Materials Chemistry C* **2018,** *6* (39), 10428-10434.

169. Zhang, L.; Pan, J.; Gong, C.; Zhang, A., Multidirectional biomimetic deformation of microchannel programmed metal nanowire liquid crystal networks. *Journal of Materials Chemistry C* **2019,** *7* (34), 10663-10671.
170. Ambulo, C. P.; Ford, M. J.; Searles, K.; Majidi, C.; Ware, T. H., 4D-Printable Liquid Metal–Liquid Crystal Elastomer Composites. *ACS Applied Materials & Interfaces* **2021,** *13* (11), 12805-12813.
171. Kotikian, A.; Truby, R. L.; Boley, J. W.; White, T. J.; Lewis, J. A., 3D Printing of Liquid Crystal Elastomeric Actuators with Spatially Programed Nematic Order. *Advanced Materials* **2018,** *30* (10), 1706164.
172. Pozo, M. d.; Sol, J. A. H. P.; van Uden, S. H. P.; Peeketi, A. R.; Lugger, S. J. D.; Annabattula, R. K.; Schenning, A. P. H. J.; Debije, M. G., Patterned Actuators via Direct Ink Writing of Liquid Crystals. *ACS Applied Materials & Interfaces* **2021,** *13* (49), 59381-59391.
173. Kim, K.; Guo, Y.; Bae, J.; Choi, S.; Song, H. Y.; Park, S.; Hyun, K.; Ahn, S.-K., 4D Printing of Hygroscopic Liquid Crystal Elastomer Actuators. *Small* **2021,** *17* (23), 2100910.
174. Ullett, J. S.; Benson-Tolle, T.; Schultz, J. W.; Chartoff, R., Thermal-expansion and fracture toughness properties of parts made from liquid crystal stereolithography resins. *Materials & design* **1999,** *20* (2-3), 91-97.
175. Ullett, J.; Schultz, J.; Chartoff, R., Novel liquid crystal resins for stereolithography–processing parameters and mechanical analysis. *Rapid prototyping journal* **2000,** *6* (1), 8-17.
176. Tabrizi, M.; Ware, T. H.; Shankar, M. R., Voxelated Molecular Patterning in Three-Dimensional Freeforms. *ACS Applied Materials & Interfaces* **2019,** *11* (31), 28236-28245.
177. Li, S.; Bai, H.; Liu, Z.; Zhang, X.; Huang, C.; Wiesner, L. W.; Silberstein, M.; Shepherd, R. F., Digital light processing of liquid crystal elastomers for self-sensing artificial muscles. *Science Advances* **2021,** *7* (30), eabg3677.
178. Gibbons, W. M.; Shannon, P. J.; Sun, S.-T.; Swetlin, B. J., Surface-mediated alignment of nematic liquid crystals with polarized laser light. *Nature* **1991,** *351* (6321), 49-50.
179. Gupta, V. K.; Abbott, N. L., Design of Surfaces for Patterned Alignment of Liquid Crystals on Planar and Curved Substrates. *Science* **1997,** *276* (5318), 1533-1536.
180. Fleisch, M.; Gao, S.; Bošnjaković, D.; Zhang, X.; Rupp, R.; Drevenšek-Olenik, I., Laser-written polymeric scaffolds for micro-patterned liquid crystal alignment. *Liquid Crystals* **2019,** *46* (13-14), 2075-2084.
181. Li, W.; Cui, W.; Zhang, W.; Kastelic, A.; Drevensek-Olenik, I.; Zhang, X., Characterisation of POLICRYPS structures assembled through a two-step process. *Liquid Crystals* **2014,** *41* (9), 1315-1322.
182. Nocentini, S.; Martella, D.; Parmeggiani, C.; Zanotto, S.; Wiersma, D. S., Structured optical materials controlled by light. *Advanced Optical Materials* **2018,** *6* (15), 1800167.
183. Martella, D.; Antonioli, D.; Nocentini, S.; Wiersma, D.; Galli, G.; Laus, M.; Parmeggiani, C., Light activated non-reciprocal motion in liquid crystalline networks by designed microactuator architecture. *RSC advances* **2017,** *7* (32), 19940-19947.
184. Zeng, H.; Martella, D.; Wasylczyk, P.; Cerretti, G.; Lavocat, J. C. G.; Ho, C. H.; Parmeggiani, C.; Wiersma, D. S., High-resolution 3D direct laser writing for liquid-crystalline elastomer microstructures. *Advanced materials* **2014,** *26* (15), 2319-2322.
185. Zeng, H.; Wasylczyk, P.; Parmeggiani, C.; Martella, D.; Wiersma, D. S., Free-form Light Actuators—Fabrication and Control of Actuation in Microscopic Scale. *JoVE (Journal of Visualized Experiments)* **2016,** (111), e53744.

186. Zeng, H.; Wasylczyk, P.; Cerretti, G.; Martella, D.; Parmeggiani, C.; Wiersma, D. S., Alignment engineering in liquid crystalline elastomers: Free-form microstructures with multiple functionalities. *Applied Physics Letters* **2015,** *106* (11), 111902.
187. Zeng, H.; Wasylczyk, P.; Parmeggiani, C.; Martella, D.; Burresi, M.; Wiersma, D. S., Light-fueled microscopic walkers. *Advanced Materials* **2015,** *27* (26), 3883-3887.
188. Xu, G.; Li, S.; Liu, C.; Wu, S., Photoswitchable Adhesives Using Azobenzene-Containing Materials. *Chemistry – An Asian Journal* **2020,** *15* (5), 547-554.
189. Yu, Y.; Nakano, M.; Ikeda, T., Photomechanical Effects in Azobenzene-Containing Polymer Systems. *Journal of Synthetic Organic Chemistry, Japan* **2004,** *62* (5), 471-479.
190. White, T. J., Photomechanical effects in liquid crystalline polymer networks and elastomers. *Journal of Polymer Science Part B: Polymer Physics* **2018,** *56* (9), 695-705.
191. Martella, D.; Nocentini, S.; Nuzhdin, D.; Parmeggiani, C.; Wiersma, D. S., Photonic microhand with autonomous action. *Advanced Materials* **2017,** *29* (42), 1704047.
192. Chen, L.; Dong, Y.; Tang, C.-Y.; Zhong, L.; Law, W.-C.; Tsui, G. C.; Yang, Y.; Xie, X., Development of direct-laser-printable light-powered nanocomposites. *ACS applied materials & interfaces* **2019,** *11* (21), 19541-19553.
193. Hashemi, S.; Jagodič, U.; Mozaffari, M.; Ejtehadi, M.; Muševič, I.; Ravnik, M., Fractal nematic colloids. *Nature communications* **2017,** *8* (1), 1-9.
194. He, Z.; Lee, Y.-H.; Chanda, D.; Wu, S.-T., Adaptive liquid crystal microlens array enabled by two-photon polymerization. *Optics Express* **2018,** *26* (16), 21184-21193.
195. Chandrasekhar, S.; Sadashiva, B. K.; Suresh, K. A., Liquid crystals of disc-like molecules. *Pramana* **1977,** *9* (5), 471-480.
196. Brooks, J. D.; Taylor, G. H., The formation of graphitizing carbons from the liquid phase. *Carbon* **1965,** *3* (2), 185-193.
197. Zimmer, J.; White, J., Disclinations in the carbonaceous mesophase. *Molecular Crystals and Liquid Crystals* **1977,** *38* (1), 177-193.
198. Bisoyi, H. K.; Kumar, S., Discotic nematic liquid crystals: science and technology. *Chemical Society Reviews* **2010,** *39* (1), 264-285.
199. Shimogaki, T.; Dei, S.; Ohta, K.; Matsumoto, A., Columnar mesophases constructed by hierarchical self-organization of rod-like diacetylene molecules. *Journal of Materials Chemistry* **2011,** *21* (29), 10730-10737.
200. Bisoyi, H. K.; Li, Q., Stimuli directed alignment of self-organized one-dimensional semiconducting columnar liquid crystal nanostructures for organic electronics. *Progress in Materials Science* **2019,** *104*, 1-52.
201. Lugger, J. A.; Mulder, D. J.; Bhattacharjee, S.; Sijbesma, R. P., Homeotropic self-alignment of discotic liquid crystals for nanoporous polymer films. *ACS Nano* **2018,** *12* (7), 6714-6724.
202. Feng, X.; Tousley, M. E.; Cowan, M. G.; Wiesenauer, B. R.; Nejati, S.; Choo, Y.; Noble, R. D.; Elimelech, M.; Gin, D. L.; Osuji, C. O., Scalable fabrication of polymer membranes with vertically aligned 1 nm pores by magnetic field directed self-assembly. *ACS Nano* **2014,** *8* (12), 11977-11986.
203. Kumar, S., *Chemistry of discotic liquid crystals: from monomers to polymers*. CRC press: 2016.
204. Heiney, P. A., Structure and Physical Properties of Columnar Liquid Crystals. In *Handbook of Liquid Crystals*, 2014; pp 1-47.

205. Laschat, S.; Baro, A.; Steinke, N.; Giesselmann, F.; Hägele, C.; Scalia, G.; Judele, R.; Kapatsina, E.; Sauer, S.; Schreivogel, A.; Tosoni, M., Discotic Liquid Crystals: From Tailor-Made Synthesis to Plastic Electronics. *Angewandte Chemie International Edition* **2007,** *46* (26), 4832-4887.
206. Feng, X.; Nejati, S.; Cowan, M. G.; Tousley, M. E.; Wiesenauer, B. R.; Noble, R. D.; Elimelech, M.; Gin, D. L.; Osuji, C. O., Thin polymer films with continuous vertically aligned 1 nm pores fabricated by soft confinement. *ACS Nano* **2016,** *10* (1), 150-158.
207. Feng, X.; Kawabata, K.; Kaufman, G.; Elimelech, M.; Osuji, C. O., Highly selective vertically aligned nanopores in sustainably derived polymer membranes by molecular templating. *ACS Nano* **2017,** *11* (4), 3911-3921.
208. Godbert, N.; Crispini, A.; Ghedini, M.; Carini, M.; Chiaravalloti, F.; Ferrise, A., LCDiXRay: a user-friendly program for powder diffraction indexing of columnar liquid crystals. *Journal of Applied Crystallography* **2014,** *47*, 668-679.
209. Echigo, T.; Kimata, M.; Maruoka, T., Crystal-chemical and carbon-isotopic characteristics of karpatite (C24H12) from the Picacho Peak Area, San Benito County, California: Evidences for the hydrothermal formation. *American Mineralogist* **2007,** *92* (8-9), 1262-1269.
210. Cox, E.; Cruickshank, D.; Smith, J. A. S., The crystal structure of benzene at -3°C. *Proceedings of the Royal Society of London. Series A. Mathematical and Physical Sciences* **1958,** *247* (1248), 1-21.
211. Frampton, C.; Knight, K.; Shankland, N.; Shankland, K., Single-crystal X-ray diffraction analysis of pyrene II at 93 K. *Journal of Molecular Structure* **2000,** *520* (1-3), 29-32.
212. El Sayed, M. T., Synthetic Routes to Electroactive Organic Discotic Aromatic Triazatruxenes. *Journal of Heterocyclic Chemistry* **2018,** *55* (1), 21-43.
213. Sergeyev, S.; Pisula, W.; Geerts, Y. H., Discotic liquid crystals: a new generation of organic semiconductors. *Chemical Society Reviews* **2007,** *36* (12), 1902-1929.
214. Guo, F.; Hurt, R., Supramolecular Synthesis of Graphenic Mesogenic Materials. *Macromolecular Chemistry and Physics* **2012,** *213* (10-11), 1164-1174.
215. Ikeda, M.; Takeuchi, M.; Shinkai, S., Unusual emission properties of a triphenylene-based organogel system. *Chemical Communications* **2003,** (12), 1354-1355.
216. Staffeld, P.; Kaller, M.; Ehni, P.; Ebert, M.; Laschat, S.; Giesselmann, F., Improved Electronic Transport in Ion Complexes of Crown Ether Based Columnar Liquid Crystals. *crystals* **2019,** *9* (2), 74.
217. Kaller, M.; Tussetschläger, S.; Fischer, P.; Deck, C.; Baro, A.; Giesselmann, F.; Laschat, S., Columnar Mesophases Controlled by Counterions in Potassium Complexes of Dibenzo[18]crown-6 Derivatives. *Chemistry – A European Journal* **2009,** *15* (37), 9530-9542.
218. Kaller, M.; Laschat, S., Liquid Crystalline Crown Ethers. In *Liquid Crystals: Materials Design and Self-assembly*, Tschierske, C., Ed. Springer Berlin Heidelberg: Berlin, Heidelberg, 2012; pp 109-192.
219. Ahmida, M.; Larocque, R.; Ahmed, M. S.; Vacaru, A.; Donnio, B.; Guillon, D.; Eichhorn, S. H., Halide effect in electron rich and deficient discotic phthalocyanines. *Journal of Materials Chemistry* **2010,** *20* (7), 1292-1303.
220. Axenov, K. V.; Laschat, S., Thermotropic Ionic Liquid Crystals. *Materials* **2011,** *4* (1), 206-259.
221. Giroud-Godquin, A.-M.; Maitlis, P. M., Metallomesogens: Metal Complexes in Organized Fluid Phases. *Angewandte Chemie International Edition in English* **1991,** *30* (4), 375-402.

222. Vinayakumara, D.; Kumar, S.; Prasad, S. K.; Adhikari, A. V., Self-assembly of taper-and wedge-shaped maleimide derivatives: Synthesis and structure-property relationship. *Journal of Molecular Liquids* **2019,** *284*, 765-772.
223. Feringán, B.; Romero, P.; Serrano, J. L.; Giménez, R.; Sierra, T., Supramolecular Columnar Liquid Crystals Formed by Hydrogen Bonding between a Clicked Star-Shaped s-Triazine and Benzoic Acids. *Chemistry – A European Journal* **2015,** *21* (24), 8859-8866.
224. Feringán, B.; Cerdá, J.; Diosdado, B.; Aragó, J.; Ortí, E.; Giménez, R.; Sierra, T., On the Structure and Chiral Aggregation of Liquid Crystalline Star-Shaped Triazines H-Bonded to Benzoic Acids. *Chemistry – A European Journal* **2020,** *26* (66), 15313-15322.
225. Alvarez, L.; Barberá, J.; Puig, L.; Romero, P.; Serrano, J.; Sierra, T., Supramolecular chirality of columnar mesophases consisting of H-bonded complexes of melamine and polycatenar benzoic acids. *Journal of Materials Chemistry* **2006,** *16* (38), 3768-3773.
226. Barberá, J.; Puig, L.; Romero, P.; Serrano, J. L.; Sierra, T., Strict Steric Requirements for the Formation of Helical Mesophases Consisting of H-Bonded Supramolecules. *Chemistry of Materials* **2005,** *17* (14), 3763-3771.
227. Lee, H. K.; Lee, H.; Ko, Y. H.; Chang, Y. J.; Oh, N. K.; Zin, W. C.; Kim, K., Synthesis of a nanoporous polymer with hexagonal channels from supramolecular discotic liquid crystals. *Angewandte Chemie* **2001,** *113* (14), 2741-2743.
228. Gray, D. H.; Hu, S.; Juuang, E.; Gin, D. L., Highly ordered polymer–inorganic nanocomposites via monomer self assembly: In situ condensation approach. *Advanced Materials* **1997,** *9* (9), 731-736.
229. Fendler, J. H., Atomic and molecular clusters in membrane mimetic chemistry. *Chemical Reviews* **1987,** *87* (5), 877-899.
230. Paleos, C. M., Polymerization in organized systems. *Chemical Society Reviews* **1985,** *14* (1), 45-67.
231. Ringsdorf, H.; Schlarb, B.; Venzmer, J., Molecular Architecture and Function of Polymeric Oriented Systems: Models for the Study of Organization, Surface Recognition, and Dynamics of Biomembranes. *Angewandte Chemie International Edition in English* **1988,** *27* (1), 113-158.
232. Devadiga, D.; T.N., A., Liquid Crystal-Based Water Treatment Membranes. *Advanced Materials Interfaces* **2022,** *9* (7), 2101276.
233. Guo, L.-X.; Liu, Y.-H.; Wang, L.; Wang, M.; Lin, B.-P.; Yang, H., Hydrogen-bonding induced melamine-core supramolecular discotic liquid crystals. *Journal of Materials Chemistry C* **2017,** *5* (35), 9165-9173.
234. Nie, Z.-Z.; Zuo, B.; Liu, L.; Wang, M.; Huang, S.; Chen, X.-M.; Yang, H., Nanoporous Supramolecular Liquid Crystal Polymeric Material for Specific and Selective Uptake of Melamine. *Macromolecules* **2020,** *53* (11), 4204-4213.
235. Avilés Moreno, J. R.; López González, J. J.; Partal Ureña, F.; Vera, F.; Ros, M. B.; Sierra, T., Study of the Photoinduced Supramolecular Chirality in Columnar Liquid Crystals by Infrared and VCD Spectroscopies. *The Journal of Physical Chemistry B* **2012,** *116* (16), 5090-5096.
236. Barberá, J.; Puig, L.; Romero, P.; Serrano, J. L.; Sierra, T., Propeller-like Hydrogen-Bonded Banana−Melamine Complexes Inducing Helical Supramolecular Organizations. *Journal of the American Chemical Society* **2006,** *128* (13), 4487-4492.
237. Janietz, D.; Kohlmeier, A., Hydrogen-Bonded Block Mesogens with Fluorinated Molecular Fragments. *Molecular Crystals and Liquid Crystals* **2009,** *509* (1), 39/[781]-46/[788].

238. Miguel-Coello, A. B.; Bardaji, M.; Coco, S.; Donnio, B.; Heinrich, B.; Espinet, P., H-bonded adducts of [2, 4, 6-{(C10H21O) 3C6H2NH} 3C3N3] with [LnM {PPh2 (C6H4CO2H)}] displaying Columnar Mesophases at Room Temperature. *Inorganic Chemistry* **2014,** *53* (20), 10893-10902.
239. Bhattacharjee, S.; Lugger, J. A.; Sijbesma, R. P., Pore size dependent cation adsorption in a nanoporous polymer film derived from a plastic columnar phase. *Chemical Communications* **2018,** *54* (68), 9521-9524.
240. Li, C.; Cho, J.; Yamada, K.; Hashizume, D.; Araoka, F.; Takezoe, H.; Aida, T.; Ishida, Y., Macroscopic ordering of helical pores for arraying guest molecules noncentrosymmetrically. *Nature communications* **2015,** *6* (1), 1-10.
241. Xia, M.; Chen, Y.; Chen, Z.; Yu, W.; Cheng, H.; Feng, C.; Ni, H.; Wang, B.; Zhao, K.; Hu, P., 1, 2, 3-Triazole lamellar liquid crystal and its non-covalent palladium complex dimer: structure, mesomorphism and self-assembly properties. *Liquid Crystals* **2021,** *49* (1), 1-13.
242. Lee, S. J.; Jho, J. Y.; Lee, J. H., Supramolecular Discotic Columnar Liquid Crystals Built through Single Hydrogen Bonding between Carboxylic Acid and Pyridine Moieties. *Molecular Crystals and Liquid Crystals* **2015,** *621* (1), 169-174.
243. Lee, J. H.; Lee, S. J.; Jho, J. Y., Room temperature supramolecular columnar liquid crystals formed by hydrogen bonding of isoquinoline derivatives. *Phase Transitions* **2014,** *87* (7), 656-665.
244. Lee, S. J.; Jho, J. Y.; Lee, J. H., Preparation of Stable Anisotropic Films with Columnar Order from Polymerizable Star-shaped Supramolecular Liquid Crystals. *Molecular Crystals and Liquid Crystals* **2015,** *621* (1), 175-181.
245. Jber, N. R.; Karam, N. H.; Al-Dujaili, A. H., Supramolecular columnar discotic nematic liquid crystal by hydrogen bonding: Synthesis and characterization. *Molecular Crystals and Liquid Crystals* **2018,** *675* (1), 29-38.
246. Ishihara, S.; Furuki, Y.; Hill, J. P.; Ariga, K.; Takeoka, S., Homeotropic alignment of dendritic columnar liquid crystal induced by hydrogen-bonded triphenylene core bearing fluoroalkyl chains. *Journal of Nanoscience and Nanotechnology* **2014,** *14* (7), 5130-5137.
247. Feng, X.; Kawabata, K.; Cowan, M. G.; Dwulet, G. E.; Toth, K.; Sixdenier, L.; Haji-Akbari, A.; Noble, R. D.; Elimelech, M.; Gin, D. L., Single crystal texture by directed molecular self-assembly along dual axes. *Nature materials* **2019,** *18* (11), 1235-1243.
248. Imran, O. Q.; Kim, N. K.; Bodkin, L. N.; Dwulet, G. E.; Feng, X.; Kawabata, K.; Elimelech, M.; Gin, D. L.; Osuji, C. O., Nanoscale Thickness Control of Nanoporous Films Derived from Directionally Photopolymerized Mesophases. *Advanced Materials Interfaces* **2021,** *8* (5), 2001977.
249. Marmur, A., A guide to the equilibrium contact angles maze. In *Contact angle wettability and adhesion*, 2009; Vol. 6.
250. Wenzel, R. N., RESISTANCE OF SOLID SURFACES TO WETTING BY WATER. *Industrial & Engineering Chemistry* **1936,** *28* (8), 988-994.
251. Cassie, A. B. D.; Baxter, S., Wettability of porous surfaces. *Transactions of the Faraday Society* **1944,** *40*, 546-551.
252. Baxter, S.; Cassie, A. B. D., 8—The water repellency of fabrics and a new water repellency test. *Journal of the Textile Institute Transactions* **1945,** *36* (4), T67-T90.
253. Cao, L.; Hu, H.-H.; Gao, D., Design and Fabrication of Micro-textures for Inducing a Superhydrophobic Behavior on Hydrophilic Materials. *Langmuir* **2007,** *23* (8), 4310-4314.
254. Darmanin, T.; Guittard, F., Recent advances in the potential applications of bioinspired superhydrophobic materials. *Journal of Materials Chemistry A* **2014,** *2* (39), 16319-16359.

255. Hodgson, G.; Passmore, M.; Skarysz, M.; Garmory, A.; Paolillo, F., Contact angle measurements for automotive exterior water management. *Experiments in Fluids* **2021,** *62* (5), 119.
256. Li, S.; Huang, J.; Chen, Z.; Chen, G.; Lai, Y., A review on special wettability textiles: theoretical models, fabrication technologies and multifunctional applications. *Journal of Materials Chemistry A* **2017,** *5* (1), 31-55.
257. Nagappan, S.; Park, S. S.; Ha, C.-S., Recent Advances in Superhydrophobic Nanomaterials and Nanoscale Systems. *Journal of Nanoscience and Nanotechnology* **2014,** *14* (2), 1441-1462.
258. Fürstner, R.; Barthlott, W.; Neinhuis, C.; Walzel, P., Wetting and Self-Cleaning Properties of Artificial Superhydrophobic Surfaces. *Langmuir* **2005,** *21* (3), 956-961.
259. Mertaniemi, H.; Jokinen, V.; Sainiemi, L.; Franssila, S.; Marmur, A.; Ikkala, O.; Ras, R. H. A., Superhydrophobic Tracks for Low-Friction, Guided Transport of Water Droplets. *Advanced Materials* **2011,** *23* (26), 2911-2914.
260. Zang, D.; Zhu, R.; Zhang, W.; Yu, X.; Lin, L.; Guo, X.; Liu, M.; Jiang, L., Corrosion-Resistant Superhydrophobic Coatings on Mg Alloy Surfaces Inspired by Lotus Seedpod. *Advanced Functional Materials* **2017,** *27* (8), 1605446.
261. Wang, L.; Gong, Q.; Zhan, S.; Jiang, L.; Zheng, Y., Robust Anti-Icing Performance of a Flexible Superhydrophobic Surface. *Advanced Materials* **2016,** *28* (35), 7729-7735.
262. Zhang, P.; Lv, F. Y., A review of the recent advances in superhydrophobic surfaces and the emerging energy-related applications. *Energy* **2015,** *82*, 1068-1087.
263. Kim, J. U.; Lee, S.; Kim, T.-i., Recent Advances in Unconventional Lithography for Challenging 3D Hierarchical Structures and Their Applications. *Journal of Nanomaterials* **2016,** *2016*, 7602395.
264. Lasagni, A. F., *How laser-based fabrication methods can be used to produce multifunctional surfaces*. SPIE: 2022; Vol. 11988.
265. Li, X.-M.; Reinhoudt, D.; Crego-Calama, M., What do we need for a superhydrophobic surface? A review on the recent progress in the preparation of superhydrophobic surfaces. *Chemical Society Reviews* **2007,** *36* (8), 1350-1368.
266. Paraskevopoulou, P.; Chriti, D.; Raptopoulos, G.; Anyfantis, G. C., Synthetic Polymer Aerogels in Particulate Form. *Materials* **2019,** *12* (9), 1543.
267. Fricke, J.; Emmerling, A., Aerogels. *Journal of the American Ceramic Society* **1992,** *75* (8), 2027-2035.
268. Tetik, H.; Wang, Y.; Sun, X.; Cao, D.; Shah, N.; Zhu, H.; Qian, F.; Lin, D., Additive Manufacturing of 3D Aerogels and Porous Scaffolds: A Review. *Advanced Functional Materials* **2021,** *31* (45), 2103410.
269. Stellacci, F.; Bauer, C. A.; Meyer-Friedrichsen, T.; Wenseleers, W.; Marder, S. R.; Perry, J. W., Ultrabright supramolecular beacons based on the self-assembly of two-photon chromophores on metal nanoparticles. *Journal of the American Chemical Society* **2003,** *125* (2), 328-329.
270. Ding, J. H.; Gin, D. L., Catalytic Pd nanoparticles synthesized using a lyotropic liquid crystal polymer template. *Chemistry of materials* **2000,** *12* (1), 22-24.
271. Beginn, U.; Zipp, G.; Möller, M., Synthesis and Characterization of Tris-Methacrylated 3,4,5-Tris[(alkoxy)benzyloxy]benzoate Derivatives. *Chemistry – A European Journal* **2000,** *6* (11), 2016-2023.

272. Lugger, J. A. M.; Sijbesma, R. P., Easily Accessible Thermotropic Hydrogen-Bonded Columnar Discotic Liquid Crystals from Fatty Acid– Tris-Benzoimidazolyl Benzene Complexes. *ChemistryOpen* **2016,** *5* (6), 580-585.
273. Michael, A.; Auf, U. D. E. V. D., Acetylendicarbonsäuremethylester. *J. prakt. Chem* **1893,** *48*, 94-95.
274. Kolb, H. C.; Finn, M.; Sharpless, K. B., Click chemistry: diverse chemical function from a few good reactions. *Angewandte Chemie International Edition* **2001,** *40* (11), 2004-2021.
275. Fujisawa, S.; Kadoma, Y.; Yokoe, I., Radical-scavenging activity of butylated hydroxytoluene (BHT) and its metabolites. *Chemistry and Physics of Lipids* **2004,** *130* (2), 189-195.
276. Blasco, E.; Tuten, B. T.; Frisch, H.; Lederer, A.; Barner-Kowollik, C., Characterizing single chain nanoparticles (SCNPs): a critical survey. *Polymer Chemistry* **2017,** *8* (38), 5845-5851.
277. Emsley, J., Very strong hydrogen bonding. *Chemical Society Reviews* **1980,** *9* (1), 91-124.
278. Suzuki, Y.; Sakamoto, T.; Yoshio, M.; Kato, T., Development of functional nanoporous membranes based on photocleavable columnar liquid crystals – Selective adsorption of ionic dyes. *European Polymer Journal* **2020,** *134*, 109859.
279. Concellón, A.; Schenning, A. P.; Romero, P.; Marcos, M.; Serrano, J. L., Size-selective adsorption in nanoporous polymers from coumarin photo-cross-linked columnar liquid crystals. *Macromolecules* **2018,** *51* (6), 2349-2358.
280. Krebs, M. R. H.; Bromley, E. H. C.; Donald, A. M., The binding of thioflavin-T to amyloid fibrils: localisation and implications. *Journal of Structural Biology* **2005,** *149* (1), 30-37.
281. Feringán, B.; Folcia, C. L.; Termine, R.; Golemme, A.; Granadino-Roldán, J. M.; Navarro, A.; Serrano, J. L.; Giménez, R.; Sierra, T., Inspecting the Electronic Architecture and Semiconducting Properties of a Rosette-Like Supramolecular Columnar Liquid Crystal. *Chemistry – A European Journal* **2018,** *24* (66), 17459-17463.
282. Pisula, W.; Kastler, M.; Wasserfallen, D.; Pakula, T.; Müllen, K., Exceptionally Long-Range Self-Assembly of Hexa-peri-hexabenzocoronene with Dove-Tailed Alkyl Substituents. *Journal of the American Chemical Society* **2004,** *126* (26), 8074-8075.
283. Luo, J.; Xie, Z.; Lam, J. W. Y.; Cheng, L.; Chen, H.; Qiu, C.; Kwok, H. S.; Zhan, X.; Liu, Y.; Zhu, D.; Tang, B. Z., Aggregation-induced emission of 1-methyl-1,2,3,4,5-pentaphenylsilole. *Chemical Communications* **2001,** (18), 1740-1741.
284. Mei, J.; Leung, N. L. C.; Kwok, R. T. K.; Lam, J. W. Y.; Tang, B. Z., Aggregation-Induced Emission: Together We Shine, United We Soar! *Chemical Reviews* **2015,** *115* (21), 11718-11940.
285. Hu, R.; Leung, N. L. C.; Tang, B. Z., AIE macromolecules: syntheses, structures and functionalities. *Chemical Society Reviews* **2014,** *43* (13), 4494-4562.
286. Förster, T.; Kasper, K., Ein Konzentrationsumschlag der Fluoreszenz des Pyrens. *Zeitschrift für Elektrochemie, Berichte der Bunsengesellschaft für physikalische Chemie* **1955,** *59* (10), 976-980.
287. v. Bünau, G., J. B. Birks: Photophysics of Aromatic Molecules. Wiley-Interscience, London 1970. 704 Seiten. Preis: 210s. *Berichte der Bunsengesellschaft für physikalische Chemie* **1970,** *74* (12), 1294-1295.
288. Mei, J.; Hong, Y.; Lam, J. W. Y.; Qin, A.; Tang, Y.; Tang, B. Z., Aggregation-Induced Emission: The Whole Is More Brilliant than the Parts. *Advanced Materials* **2014,** *26* (31), 5429-5479.

289. Tang, Y.; Tang, B., *Principles and Applications of Aggregation-Induced Emission*. 2019.
290. Leung, N. L. C.; Xie, N.; Yuan, W.; Liu, Y.; Wu, Q.; Peng, Q.; Miao, Q.; Lam, J. W. Y.; Tang, B. Z., Restriction of Intramolecular Motions: The General Mechanism behind Aggregation-Induced Emission. *Chemistry – A European Journal* **2014,** *20* (47), 15349-15353.
291. Schultz, A.; Diele, S.; Laschat, S.; Nimtz, M., Novel columnar tetraphenylethenes via McMurry coupling. *Advanced Functional Materials* **2001,** *11* (6), 441-446.
292. Richard, J., Lithography. Introduction to Microelectronic Fabrication. Upper Saddle River: Prentice Hall: 2002.
293. Rizvi, S., *Handbook of photomask manufacturing technology*. CRC Press: 2018.
294. Yang, L.; Mayer, F.; Bunz, U. H.; Blasco, E.; Wegener, M., Multi-material multi-photon 3D laser micro-and nanoprinting. *Light: Advanced Manufacturing* **2021,** *2*, 296-312.
295. Han, D.; Yang, C.; Fang, N. X.; Lee, H., Rapid multi-material 3D printing with projection micro-stereolithography using dynamic fluidic control. *Additive Manufacturing* **2019,** *27*, 606-615.
296. Ceylan, H.; Yasa, I. C.; Sitti, M., 3D Chemical Patterning of Micromaterials for Encoded Functionality. *Advanced Materials* **2017,** *29* (9), 1605072.
297. Richter, B.; Pauloehrl, T.; Kaschke, J.; Fichtner, D.; Fischer, J.; Greiner, A. M.; Wedlich, D.; Wegener, M.; Delaittre, G.; Barner-Kowollik, C.; Bastmeyer, M., Three-Dimensional Microscaffolds Exhibiting Spatially Resolved Surface Chemistry. *Advanced Materials* **2013,** *25* (42), 6117-6122.
298. Claus, T. K.; Richter, B.; Hahn, V.; Welle, A.; Kayser, S.; Wegener, M.; Bastmeyer, M.; Delaittre, G.; Barner-Kowollik, C., Simultaneous Dual Encoding of Three-Dimensional Structures by Light-Induced Modular Ligation. *Angewandte Chemie International Edition* **2016,** *55* (11), 3817-3822.
299. Jackman, R. J.; Duffy, D. C.; Ostuni, E.; Willmore, N. D.; Whitesides, G. M., Fabricating Large Arrays of Microwells with Arbitrary Dimensions and Filling Them Using Discontinuous Dewetting. *Analytical Chemistry* **1998,** *70* (11), 2280-2287.
300. Neto, M. D.; Stoppa, A.; Neto, M. A.; Oliveira, F. J.; Gomes, M. C.; Boccaccini, A. R.; Levkin, P. A.; Oliveira, M. B.; Mano, J. F., Fabrication of Quasi-2D Shape-Tailored Microparticles using Wettability Contrast-Based Platforms. *Advanced Materials* **2021,** *33* (14), 2007695.
301. Yang, Y.; Xu, L.-P.; Zhang, X.; Wang, S., Bioinspired wettable–nonwettable micropatterns for emerging applications. *Journal of Materials Chemistry B* **2020,** *8* (36), 8101-8115.
302. Kumar, A.; Whitesides George, M., Patterned Condensation Figures as Optical Diffraction Gratings. *Science* **1994,** *263* (5143), 60-62.
303. Wang, Z.; Cui, H.; Li, S.; Feng, X.; Aghassi-Hagmann, J.; Azizian, S.; Levkin, P. A., Facile Approach to Conductive Polymer Microelectrodes for Flexible Electronics. *ACS Applied Materials & Interfaces* **2021,** *13* (18), 21661-21668.
304. Feng, W.; Ueda, E.; Levkin, P. A., Droplet Microarrays: From Surface Patterning to High-Throughput Applications. *Advanced Materials* **2018,** *30* (20), 1706111.
305. Yang, Q.; Lu, Z.; Zhou, J.; Miao, K.; Li, D., A novel method for improving surface finish of stereolithography apparatus. *The International Journal of Advanced Manufacturing Technology* **2017,** *93* (5), 1537-1544.
306. Venuvinod, P. K.; Ma, W., *Rapid prototyping: laser-based and other technologies*. Springer Science & Business Media: 2004.

307. Chen, H.; Zhu, R.; Zhu, J.; Wu, S.-T., A simple method to measure the twist elastic constant of a nematic liquid crystal. *Liquid Crystals* **2015,** *42* (12), 1738-1742.
308. Liang, Y.; Frederik, M.; Uwe, H. F. B.; Eva, B.; Martin, W., Multi-material multi-photon 3D laser micro- and nanoprinting. *Light: Advanced Manufacturing* **2021,** *2*, 296-312.
309. Liu, G.; Petrosko, S. H.; Zheng, Z.; Mirkin, C. A., Evolution of Dip-Pen Nanolithography (DPN): From Molecular Patterning to Materials Discovery. *Chemical Reviews* **2020,** *120* (13), 6009-6047.
310. Lee, H.; Dellatore Shara, M.; Miller William, M.; Messersmith Phillip, B., Mussel-Inspired Surface Chemistry for Multifunctional Coatings. *Science* **2007,** *318* (5849), 426-430.
311. Ryu, J. H.; Messersmith, P. B.; Lee, H., Polydopamine Surface Chemistry: A Decade of Discovery. *ACS Applied Materials & Interfaces* **2018,** *10* (9), 7523-7540.
312. Barclay, T. G.; Hegab, H. M.; Clarke, S. R.; Ginic-Markovic, M., Versatile Surface Modification Using Polydopamine and Related Polycatecholamines: Chemistry, Structure, and Applications. *Advanced Materials Interfaces* **2017,** *4* (19), 1601192.
313. Kang, S. M.; You, I.; Cho, W. K.; Shon, H. K.; Lee, T. G.; Choi, I. S.; Karp, J. M.; Lee, H., One-Step Modification of Superhydrophobic Surfaces by a Mussel-Inspired Polymer Coating. *Angewandte Chemie International Edition* **2010,** *49* (49), 9401-9404.
314. Prieto-López, L. O.; Herbeck-Engel, P.; Yang, L.; Wu, Q.; Li, J.; Cui, J., When Ultimate Adhesive Mechanism Meets Ultimate Anti-Fouling Surfaces—Polydopamine Versus SLIPS: Which One Prevails? *Advanced Materials Interfaces* **2020,** *7* (18), 2000876.
315. De Jesus, M. C.; Fu, Y.; Weiss, R. A., Conductive polymer blends prepared by in situ polymerization of pyrrole: A review. *Polymer Engineering & Science* **1997,** *37* (12), 1936-1943.
316. Gunasekara, D. S. W.; Niu, X.; Lqbal, W.; He, Y.; Liu, H., Pyrrole Coating with In Situ Polymerization for Piezoresistive Sensor Development - A Review. *Macromolecular Research* **2022,** *30* (3), 153-162.
317. Shipway, A. N.; Katz, E.; Willner, I., Nanoparticle Arrays on Surfaces for Electronic, Optical, and Sensor Applications. *ChemPhysChem* **2000,** *1* (1), 18-52.
318. Huang, J.; Kim, F.; Tao, A. R.; Connor, S.; Yang, P., Spontaneous formation of nanoparticle stripe patterns through dewetting. *Nature Materials* **2005,** *4* (12), 896-900.
319. Ye, X.; Qi, L., Two-dimensionally patterned nanostructures based on monolayer colloidal crystals: Controllable fabrication, assembly, and applications. *Nano Today* **2011,** *6* (6), 608-631.
320. Barad, H.-N.; Kwon, H.; Alarcón-Correa, M.; Fischer, P., Large Area Patterning of Nanoparticles and Nanostructures: Current Status and Future Prospects. *ACS Nano* **2021,** *15* (4), 5861-5875.
321. Smith, R. C.; Fischer, W. M.; Gin, D. L., Ordered Poly(p-phenylenevinylene) Matrix Nanocomposites via Lyotropic Liquid-Crystalline Monomers. *Journal of the American Chemical Society* **1997,** *119* (17), 4092-4093.
322. Shimada, K.; Sugawara, A.; Korenaga, T.; Kawashima, H., Total Synthesis and Structural Elucidation of Two Unusual Non-Methylene-Interrupted Fatty Acids in Ovaries of the Limpet Cellana toreuma. *Lipids* **2017,** *52* (12), 1019-1032.
323. Kelly, S. M., Ferroelectric Liquid Crystals. Part 9. Laterally substituted phenyl benzoates incorporating a trans-1,4-disubstituted cyclohexane ring. *Helvetica Chimica Acta* **1989,** *72* (3), 594-607.
324. King, A. O.; Negishi, E.; Villani Jr, F. J.; Silveira Jr, A., A general synthesis of terminal and internal arylalkynes by the palladium-catalyzed reaction of alkynylzinc reagents with aryl halides. *The Journal of Organic Chemistry* **1978,** *43* (2), 358-360.

325. Sonoda, M.; Inaba, A.; Itahashi, K.; Tobe, Y., Synthesis of differentially substituted hexaethynylbenzenes based on tandem Sonogashira and Negishi cross-coupling reactions. *Organic letters* **2001,** *3* (15), 2419-2421.
326. Broer, D. J.; Boven, J.; Mol, G. N.; Challa, G., In-situ photopolymerization of oriented liquid-crystalline acrylates, 3. Oriented polymer networks from a mesogenic diacrylate. *Die Makromolekulare Chemie: Macromolecular Chemistry and Physics* **1989,** *190* (9), 2255-2268.
327. Seo, J.-M.; Noh, H.-J.; Jeong, H. Y.; Baek, J.-B., Converting Unstable Imine-Linked Network into Stable Aromatic Benzoxazole-Linked One via Post-oxidative Cyclization. *Journal of the American Chemical Society* **2019,** *141* (30), 11786-11790.